Characterization and Modeling of Forged ZK60 Mg Alloys under Quasi-static and Fatigue Loadings

by

Seyyed Mohamad Hasan Karparvarfard

A thesis
presented to the University of Waterloo
in fulfillment of the
thesis requirement for the degree of
Doctor of Philosophy
in
Mechanical and Mechatronics Engineering

Waterloo, Ontario, Canada, 2020

Examining Committee Membership

The following served on the Examining Committee for this thesis. The decision of the Examining Committee is by majority vote.

External Examiner	J. BRIAN JORDON Associate Professor
Supervisor(s)	HAMID JAHED Professor
Internal Member	MARY WELLS Professor
Internal Member	CLIFFORD BUTCHER Assistant Professor
Internal-external Member	HASSAN BAAJ Associate Professor

AUTHOR'S DECLARATION

This thesis consists of material all of which I authored or co-authored: see Statement of Contributions included in the thesis. This is a true copy of the thesis, including any required final revisions, as accepted by my examiners.

I understand that my thesis may be made electronically available to the public.

Statement of Contributions

The content of the thesis in chapters 3-5 have been taken from manuscripts which have been published. As a result, a number of co-authors have contributed to the current work whose individual contributions are as follows:

Prof. Hamid Jahed: Supervised and mentored all the research work. He has helped with planning the experiments, discussing the results, and reviewing the final manuscripts for publication.

Dr. Seyed Behzad Behravesh: acted to provide technical and editorial feedback for the research work and manuscripts in the chapters 3-5.

Dr. Sugrib Kumar Shaha: acted to help preparing samples for microstructural imaging in chapter 3 and provided pole figures for texture measurements in chapters 3-5. He also provided editorial feedback for all final manuscripts.

Dr. Amirhossein Pahlevanpour: acted to do some of the fatigue experiment works in chapter 5 and co-authored the final manuscript of the published article.

Dr. Bruce Williams: acted as the main researcher in CanmetMATERIALS and supervised both the open-die and close-die forging processes. He also provided editorial feedback for chapters 3 and 4.

Abstract

In response to impending changes to the environmental regulations on the vehicles' gas consumption rate, the transportation sector is motivated toward the widespread adoption of lightweight materials in the manufacturing of its products. Magnesium (Mg) alloys, being the lightest commercial metals available in the industry, can play an integral role in this scope with offering huge mass saving comparing to aluminum and steel. With the development of multi-material vehicle architecture concept in the automotive industry philosophy, ultra-light materials such as Mg alloys should be exploited in the component in which they perform the best. For vehicle parts which are driven by fatigue, e.g., suspension control arm, wrought Mg is a suitable candidate as a substitute for the current structural metals, due to its excellent fatigue performance in addition to opening mass saving windows.

Of the commercially available Mg alloys, ZK- series, and in particular, ZK60 Mg alloys, have shown superb mechanical properties and formability. Moreover, amongst several prevalent industrial manufacturing techniques, forging is of particular interest because it has shown its promise to produce components with complex geometry and high strength. However, the mechanical behavior of forged ZK60 has been largely unknown so far. The current research work has aimed to fill this gap by characterizing the mechanical behavior of forged ZK60. The focus has been to establish a link between the material, structure and performance. The discovery-level knowledge, established through this project, develops a better understanding of the fatigue performance of this alloy and provides a wealth of mechanical performance data on this material in order for industry to make better use of it in real-world applications.

Initially, the effects of open-die forging on the mechanical behavior of cast ZK60 was studied. A partially recrystallized microstructure with sharp basal texture was developed in the material. Also, the porosity volume was dramatically reduced after the forging. As a result, the tensile yield strength and elongation were increased by 21% and 72%, respectively. Under cyclic loadings, the forged material exhibited a better response in both the low cycle fatigue (LCF) and high cycle fatigue (HCF) regimes in the light of its higher ductility and strength, and lower content of porosities and intermetallic particles, which can play as crack nucleation

sites. The fracture surfaces of the samples tested at various strain amplitudes were analyzed using the scanning electron microscope (SEM), and different crack initiation mechanisms were identified. At low strain amplitudes, corresponding to the HCF regime, persistent slip bands (PSB) and second-phase intermetallic particles were defined as the major causes of crack initiation, whilst at high strain amplitudes, ascribed to the LCF lives, the interactions between twin-twin bands besides twin-dislocation were recognized as the key reasons for cracking.

Next, the quasi-static and strain-controlled fatigue characteristics of ZK60 extrusion have been investigated along different directions, namely, the extrusion direction (ED), the radial direction (RD), and 45° with respect to the extrusion direction (45°), in the scope of process-structure-property-performance relationships. In contrast to the asymmetric quasi-static behavior of extrusion direction, radial and 45° directions manifested symmetric responses. Also, ED samples showed higher strength compared to the other two directions. The strain-controlled fatigue performance of ZK60 extrusion was insensitive to the material direction in the LCF regime. However, in the HCF regime, ED displayed fatigue responses superior to the RD and 45°. The texture measurement indicated a sharp basal texture along ED. Also, microstructural analyses revealed binary microstructure, explaining the ED's asymmetric behavior and higher strength comparing to the other directions. Higher tensile mean stress and less dissipated plastic energy per cycle for the ED samples, acting as two competing factors, were the principal reasons for ED's identical fatigue response to that of RD and 45° in the LCF regime. The fracture surface in the ED direction was dominated by twin lamellae and profuse twinned grains, whereas that in RD was dominated by slip bands. Lastly, Smith-Watson-Topper and Jahed-Varvani models were employed to predict the fatigue lives along all directions using a single set of material parameters. The energy-based model yielded acceptable predictions for ZK60 extrusion with anisotropic behavior.

Finally, the multiaxial fatigue characteristics of as-extruded and close-die "I-beam" extruded-forged ZK60 were investigated. Quasi-static tension and shear tests in addition to uniaxial, pure shear, and multiaxial cyclic tests under variety of loading paths as well as texture measurements and microstructural analysis were delivered to characterize the material's behavior and understand the effects of forging on the performance of the alloy. It was

discovered that the imparted thermo-mechanical process modified the initial sharp basal texture in the flanges of the I-beam. Secondly, following forging, the microstructures in the two flanges of the I-beams were similar. Furthermore, following the quasi-static tests, it was revealed that the axial behavior of the forging was superior to that of the starting extruded material, whereas the shear responses were comparable. Multiaxial fatigue tests demonstrated that non-proportionality does not change the fatigue life tremendously; however, it does affect the shear response remarkably. It was concluded that at low shear strain amplitudes that the shear strain is accommodated by slipping, the multiaxial behavior is somewhat dominated by the axial component. The microstructure of both undeformed and deformed samples after 20% shear strain under quasi-static loading was studied using the EBSD technique. The deformed sample showed considerable amount of $\{10\bar{1}2\}$ tensile twins in the microstructure; hence, the developed texture plays an integral role in the material's shear behavior under large strains where appreciable extension twin occurs. Finally, an energy-based fatigue model was employed that effectively explains the different damage contributions by the axial and torsional loadings at different strain amplitudes, and accurately predicts the proportional and non-proportional multiaxial fatigue lives for both as-extruded and forged alloys.

Acknowledgements

I would like to express my sincere gratitude to my supervisor, Prof. Hamid Jahed, for the opportunity to work on this project and for his invaluable support and guidance.

My heartfelt gratitude goes to my family, especially my parents, parents-in-law, sister and brother-in-law for their boundless love, encouragement and support through my education and the PhD career.

I owe my special thanks to my beloved wife, my beautiful **Bahar**, whose unconditional love, understanding, patience, and inspiration made it possible to finish this research work.

I would like to thank Dr. Mazda Kompani and his great family for their heartfelt kindness and support here in Canada. Mr. and Ms. Kompani acted like real parents to me and I will always owe them.

I would also like to thank Dr. Seyed Behzad Behravesh and Dr. Sugrib Shaha for their exceptional guidance and suggestions throughout the research work. I also express my gratitude to Dr. Amir Pahlevanpour for his precious thoughts and discussions, and to Dr. Paresh Prakash for his valuable collaboration for performing the EBSD analysis.

The financial support of the Natural Sciences and Engineering Research Council of Canada, the Automotive Partnership Canada (APC) program under APCPJ 459269-13 grant with contributions from Multimatic Technical Centre, Ford Motor Company, and Centerline Windsor is acknowledged. The author would also like to thank Jonathan McKinley and Lucian Blaga of CanmetMATERIALS for the forgings.

To my beloved family

&

my dear wife, Bahar

Table of Contents

List of Figures

List of Tables

Chapter 1
Introduction

1.1 Motivation

A drastic increase in the global annual mean surface air temperature since the mid-20th century is reported by NASA [1]. The emission of greenhouse gases such as CO_2, CH_4, N_2O, resulting from the human activity has revealed itself to be the dominant cause of this global warming (Figure 1).

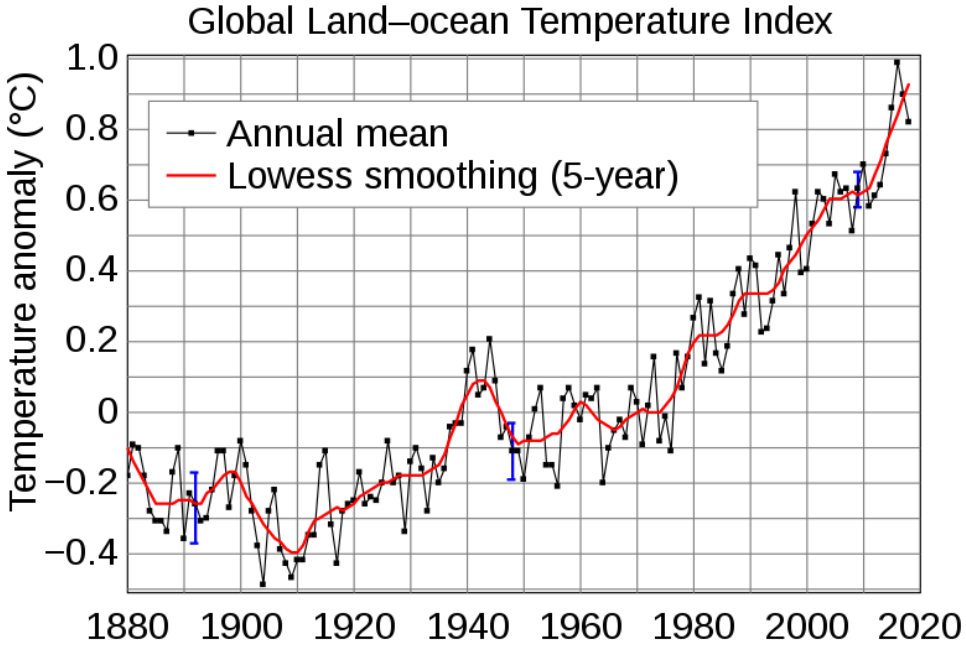

Figure 1. Global average surface temperature from 1880 to 2018 [1]

According to the United States Environmental Protection Agency (EPA) [2] (Figure 2), in North America the transportation sector accounts for almost 30% of the total greenhouse gas emission. This has led to a push by regulatory bodies and manufacturers to cut down on the vehicular emissions. The EPA and the American National Highway Traffic Safety Administration (NHTSA) legislated a fleet-wide automotive fuel economy objective of 54.5 miles per gallon (mpg), equivalent to 4.32 L/100km, by 2025 in 2012 and reaffirmed the law in 2016 [3][4]. To accomplish this aggressive target, automotive manufacturers are investing heavily in the “active” solutions such as hybridization as well as the “passive” technologies

like lightweighting. The concept of lightweighting is reducing the curb weight of the vehicles by implementing alloys which are lighter than the traditionally used aluminum (Al) and steel. This translates to reducing the volume and number of required batteries in the hybrid cars as well as cutting down on the fuel consumption rate of the gas vehicles. Besides the primary fuel economy benefits, lightweighting brings in secondary advantages in the gas vehicles, too; i.e., a lighter car needs smaller engine and transmission and braking systems to produce the same amount of torque and acceleration. It is reported that a 10% decrease in the vehicles' curb mass alongside better aerodynamic characteristics can accomplish 5.7%-7.4% reduction of emission [5]–[7]. This translates to saving huge amount of gas liters considering that over 17 million motor vehicles are annually produced in North America; hence, weight reduction is an important step in improving the automobile fuel economy.

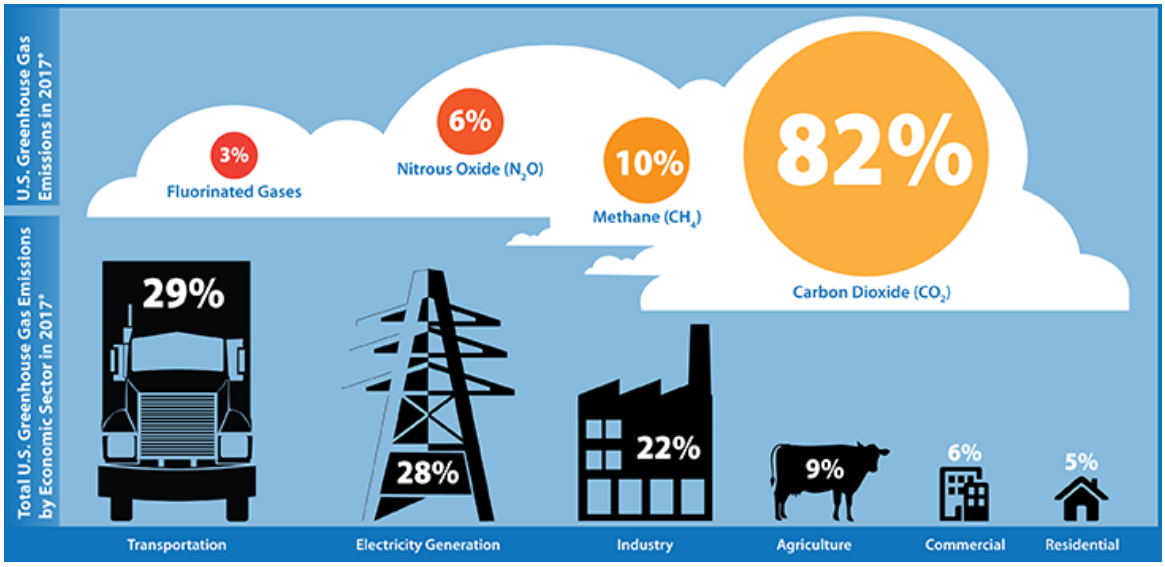

Figure 2. Break down of greenhouse gas emission by sector [2]

Toward this aim, the global automotive sector has undergone advanced research in the area of adopting lightweight materials in the manufacturing of vehicles with a such material being magnesium (Mg). Mg is the lightest commercial structural metal available in industry. It is 33% lighter than Al and 75% lighter than steel. Its low density brings in high specific strength and specific stiffness for this alloy. Also, Mg has good thermal conductivity. The attractiveness of Mg alloys also lies in good recyclability (requiring only 5-10 percent of the

required energy for the manufacturing of the primary part), nontoxicity, and being a biologically safe metal, all of which make Mg a "green" material [8][9]–[11].

Volkswagen was the pioneer in applying Mg in one of its earlier models. Porsche also adopted Mg in the engine block of its products in 1928 [12]. More recently, Porsche used Mg sheets in manufacturing the roof panel of Porsche911 GT2 RS, too; the multi-material vehicle architecture is an emerging concept that involves combining lightweighting alloys with stronger alloys in the structural parts in which they perform the best. This concept opens new frontiers for the usage of Mg in vehicles. Lately, Audi has employed the idea in its Audi A8 series by mixing and matching steel, aluminum, carbon-fiber, and Mg in the construction of the vehicle's chassis. Volkswagen was another company that has recently employed this concept in manufacturing VW XL1. This diesel-powered hybrid car has carbon-fiber body, supplemented by magnesium and aluminum, rides on Mg wheel, and has the magnificent fuel economy of 100 km on 1 liter of diesel fuel! Generally, the average usage of Mg in the automotive industry has grown by 10-15 percent annually over the past 15 years [13]; However, the usage of Mg still falls short of what is needed to meet the automotive fuel economy target in the near future. In particular, the application of Mg should be broadened beyond its current use, which is either in non-load-bearing components and housing parts, or in very low production vehicles, to the load-bearing components in high production automobiles. The main challenges with Mg alloys are their low formability in the room temperature due to its specific crystallographic structure and being a highly corrosive material.

Die casting is the prevalent processing method of Mg alloys for its economic advantages [3][14][15]. However, this manufacturing technique brings in abundant of defects and porosities in the microstructure of the material that adversely affect the mechanical behavior [16]. Therefore, for structural applications, wrought Mg alloys are introduced, which have shown superior mechanical properties and fatigue behavior compared to the cast alloys [17][18][19][20]. They also exhibit better corrosion resistance in the light of their finer crystallographic grains [21]. Moreover, it is recognized by the forging industries that the forging process can be a worthwhile technique where components can be made in a wide variety of shapes and complexities [22]. Therefore, a multidisciplinary research project was

initiated at the University of Waterloo in collaboration with industrial partners and governmental research laboratories, namely, Multimatic Inc., Ford Motor Company, CenterLine (Windsor) Ltd, and CanmetMATERIALS laboratory, to investigate the potential application of thermo-mechanically processed Mg alloys in an automotive fatigue-critical component. Three forgeable Mg alloys were provided by Luxfer MEL Technologies, previously known as Magnesium Elektron North America Inc., in both as-cast and as-extruded starting conditions. Due to the limited available knowledge about the mechanical behavior of forged Mg alloys in the literature, the project started with open-die forging at a high temperature, and subsequently was expanded to the investigations on the close-die forging at low temperatures. This project develops a discovery-level understanding of the fatigue performance of these three different Mg alloys and provides a wealth of mechanical performance data on these alloys in order for industry to make better use of them in real-world applications such as in the control arm of vehicles.

1.2 Research Objectives

As mentioned above, a project was established to develop the basic knowledge required to successfully replace the existing materials in load-bearing automotive components with wrought Mg alloys. In particular, the focus in this project is to replace cast aluminum front lower control arm (FLCA) of a high-volume production passenger car with ultra-lightweight Mg fabricated components. The current undertaking is on studying the effects of thermo-mechanical forging process on the properties of Mg ZK60 alloys. To this end, the focus is in the scope of establishing a fundamental link between the material structure, process, and performance. In addition, the research is focusing on discovering the drives behind any changes observed in the mechanical behavior after conducting the thermo-mechanical process. Lastly, modeling the fatigue behavior of the alloy is targeted in this research. To achieve these goals, the following research objectives are pursued:

1.2.1 To characterize the quasi-static and cyclic behavior of cast ZK60 before and after open-die forging

The first step of the project belongs to developing the knowledge pertaining to forming Mg alloys and investigating the influence of the forging process on the material's performance. To this end, as-cast ZK60 billets were successfully forged using open-die platens. Quasi-static and fully reversed fatigue tests are delivered on the pre- and post-forged standard samples to study the contributions of the forging process to the material's mechanical properties. In addition, microstructural analysis, texture measurement and fracture surface examinations are conducted to track down the mechanisms underlying the failure and comprehend the drives for the material's behavior in the forged state.

1.2.2 To characterize and model the mechanical behavior of ZK60 extrusion in different directions

The final FLCA will be fabricated by forging extrusion billets. Hence, it is important to understand the mechanical behavior of ZK60 extrusion along different directions. Toward this aim, quasi-static and cyclic tests are performed on the samples extracted along three different directions. Differences in behavior are then linked to the texture induced in the as-received material in a material-structure-performance context. Also, the fatigue life along different directions are effectively predicted using an energy-based and a strain-based fatigue model.

1.2.3 To investigate the effects of close-die forging on the fatigue behavior of ZK60 extrusion

Load-bearing components such as FLCA are subjected to multiaxial loading during their service life. Thereby, it is important to characterize the mechanical behavior of Mg alloys under multiaxial loading. Close-die forging at a relatively low temperature of 250° C has been performed on the extrusion billets. Different loading paths, including quasi-static tension and shear loading in addition to cyclic axial, cyclic shear, as well as proportional and non-proportional multiaxial fatigue tests are considered to enhance the fulfillments of research objective #2. Also, due to the lack of knowledge regarding the drives behind the shear failure

mechanism in the Hexagonal Close Packed (HCP) crystal structure materials, the texture and microstructure evolution during the shear loading is investigated. Lastly, different fatigue models are employed that effectively explains different damage contributions by the axial and shear loadings at different strain amplitudes and accurately predicts the proportional and non-proportional fatigue lives.

1.2.4 Thesis overview

This thesis comprises a collection of three papers published in prestigious international journals in the area of material science and fatigue and fracture, and an article to be submitted for publication in an international journal.

Chapter 2 begins with the literature revolving around Mg and in particular ZK60. The effects of forming processes on the fatigue behavior of ZK60 is reviewed. Subsequently, the available knowledge in the literature regarding forging of ZK60 and the influence of the process on the material's structure is discussed. Also, the results of the available multiaxial fatigue tests on Mg alloys are presented. Lastly, the chapter finishes with reviewing the concepts associated with the fatigue life prediction models employed in this research.

Chapter 3 outlines the detailed methodology exploited din this research work. A complete discussion is provided on the forging process, and the specimen geometries and preparations. Test apparatus and procedure, as well as the details surrounding texture measurement and microstructure analysis are described.

Chapter 4, which is published in the International Journal of Material Science and Technology, presents the microstructure, texture and quasi-static characteristics of open-die forged ZK60 cast. The microstructure and texture evolution during the forging process is studied and a structural link between the material's structure and its properties is established.

Chapter 5, which is published in the International Journal of Fatigue, studies the cyclic behavior of ZK60 cast prior and after the open die forging process. The effects of microstructure change and the induced texture on the fatigue response are discussed. Also, thorough post-failure fractography analyses on the cast and forged samples are conducted to

discern the mechanisms underlying the fatigue behavior in ZK60. Lastly, an energy-based fatigue life model is employed which closely estimates the life.

Chapter 6, which is published in the International Journal of Materials and Design, looks at the quasi-static and cyclic behavior of ZK60 extrusion in three different directions: extrusion (ED), radial (RD), and 45° to the extrusion direction (45°). In contrast to the ED, the other two directions show symmetric responses. Also, fatigue performances of different directions are investigated in the low cycle fatigue (LCF) and high cycle fatigue (HCF) regimes. Any differences in the mechanical behaviors will then be linked to the material's microstructure and texture. Lastly, the modified Smith-Watson-Topper (SWT) and Jahed-Varvani (JV) models are employed to predict the fatigue lives along all the directions.

Chapter 7 consists of an article ready for submission to the International Journal of Fatigue and includes the relevant data from another journal paper which is an ongoing work throughout the larger project. This chapter studies the multiaxial cyclic behavior of extruded-forged ZK60 Mg alloy. Quasi-static tension and shear tests in addition to cyclic axial, cyclic pure shear, and cyclic combined axial-torsional experiments are conducted at different strain amplitudes and phase angles on both as-extruded and forged materials. The microstructure and texture of fractured samples under quasi-static shear test is studied and compared to that of starting alloy to discern the shear failure mechanisms. Also, the effects of forging on the fatigue response of extruded ZK60 is presented. The load multiaxiality effects on the cyclic behavior of ZK60 alloys are presented afterwards. In particular, a thorough study on the interaction of axial and shear loadings during the multiaxial fatigue response is presented, and it is shown that the material's behavior is somewhat dominated by the axial loading when the dominant mechanism along shear is slipping. Lastly, the obtained shear fatigue properties are exploited together with those achieved in chapter 5 for axial loading to model the multiaxial fatigue response of both extruded and forged materials.

Lastly, chapter 8 summarizes the conclusions and the scientific contributions of the current work. It also proposes the recommendations for future works in this area.

Chapter 2
Background and literature review

2.1 Magnesium and in Particular ZK60

In the past, magnesium was widely utilized in World War I and World War II. Nevertheless, later it gained automotive applications rather than military usages. Volkswagen was the pioneer to adopt magnesium on its Beetle models. However, magnesium automotive applications petered out due to practical issues, which would happen when higher performance was required [9]. Under the new strict regulations for the fuel consumption rate of vehicles, nonetheless, lightweight materials have driven great interest for use in cars in the last decade. Owing to its very low density, magnesium has been of interest of researches once again.

Magnesium has a density of 1.738 gr/cm^3, which is about a quarter that of steel and two thirds that of aluminum. This low density delivers a superior stiffness-to-weight ratio for magnesium among the commercial metals available in industry [23]. Decent castability, prudent weldability, availability and recyclability can be listed as other major benefits of magnesium [9][24].

Among poor mechanical properties, limited cold workability is a problem, and this stems from magnesium's crystal structure. Magnesium has a hexagonal closed-pack (hcp) crystal structure which provides it with a limited number of slip systems at room temperature. According to the Taylor criterion, five independent deformation modes are required to accommodate induced strains during a homogenous deformation for a polycrystalline material [25]. At lower temperatures, basal, prismatic, and pyramidal slip planes are active, but the lower strength required for basal slip almost always will result in a strong basal texture formation during deformation. If basal slip is hindered, then twinning systems can also be activated at lower temperatures [26][27][28]. In materials like magnesium with $c/a < \sqrt{3}$, the $\{10\bar{1}2\}$ twin is activated by c-axis tension or compression along the direction perpendicular to the c-axis. Additional slips systems are activated at elevated temperatures improving formability and facilitating plastic deformation.

Magnesium alloys have been successfully developed for use in the production of sound forgings with moderately complex features. Three alloy systems are of particular interest for forging: 1) the AZ series aluminum-zinc alloys, 2) the ZK series zinc-zirconium alloys, and 3) the WE yttrium-rare earth alloys. In general, ZK series magnesium alloys, in particular the ZK60 grade, have good formability [29], [30]. They also reveal a superb strength due to precipitations and grain refining effects of Zr [31], [32]. By increasing the rare element (RE) content, the as cast microstructure is refined gradually. The second phase particles in ZK60 tend to distribute along grain boundary. The extrusion microstructure is also refined where the average grain size reaches 8−12 μm for the alloys with high RE-content. Fine grain and few fine dispersed second phase can enhance the impact toughness of magnesium alloys effectively [33]. Therefore, ZK60 alloy was attractive to the research community. The texture evolution of as-extruded AZ-series and ZK60 after performing the equal channel angular extrusion (ECAE) process had also been studied by Agnew et al. [34]. They mentioned that AZ31 and AZ80 Alloys demonstrate basal slip dominated deformation with a small balanced contribution of the non-basal $< a >$ and $< c + a >$ slip modes, whereas the ZK60 alloy shows a significant contribution from the non-basal $< c + a >$ slip mechanism (in addition to basal slip).

2.2 Characterization of Mechanical Behavior of ZK60 Mg Alloy under quasi-static and Cyclic Loading

To exploit magnesium in load-bearing components, mechanical behavior characterization and especially understanding the fatigue response is fundamental. Toward this, it is imperative to understand the deformation mechanisms involved in Mg alloys.

Twinning is an integral phenomenon associated with the cyclic behavior of wrought magnesium alloys. In fact, owing to the hexagonal crystallographic microstructure of magnesium, twinning can play a significant role in Mg's mechanical behavior. At room temperature, twinning may help this material to satisfy the Taylor criterion in the light of the fact that non-basal slip modes are recognizably a hard deformation mode; hence, twinning would be the only active mode serving straining along the c-axis [35]. For magnesium alloys

with $c/a < \sqrt{3}$, the $\{10\bar{1}2\}<10\bar{1}1>$ extension twin can accommodate extensions along the c-axis of the hexagonal lattice, but not contractions along the same direction. This deformation mode yields in the rotation of the grains' basal pole by ~86.3°, as shown in Figure 3. As a result, in reverse loading, detwinning might happen with the tension loading along the c-axis of twinned grains. Furthermore, most wrought magnesium alloys are displaying a textured grain morphology that brings about a tension-compression asymmetric behavior stemming from this polar nature of twinning (deformation is allowed merely in one direction rather than in both directions that happens in dislocation slips). Therefore, to understand the fatigue response of wrought magnesium alloys, it is essential to have an understanding of twinning/ detwinning effects in these alloys.

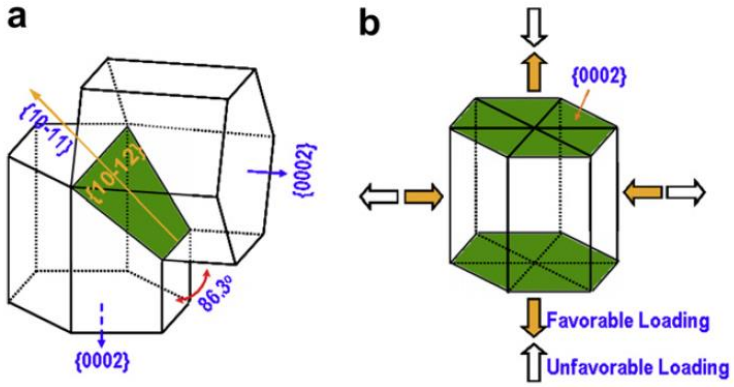

Figure 3. Schematic of $\{10\bar{1}2\}<10\bar{1}1>$ extension twinning in magnesium alloys (a) 86.3° grain rotation; (b) applied loads direction with respect to the c-axis [36]

Twinning has been the topic of a number of studies [37][38][39][40]. These studies reported that twinning and detwinning appear alternatively in fatigue loading. Wu et al. [36] investigated the cyclic twinning–detwinning behavior in ZK60 extrusion using in situ neutron diffraction measurement. They observed two distinct hysteresis loops for the loadings along the extrusion (ED) and transverse directions (TD), normal to the ED, as shown in Figure 4.

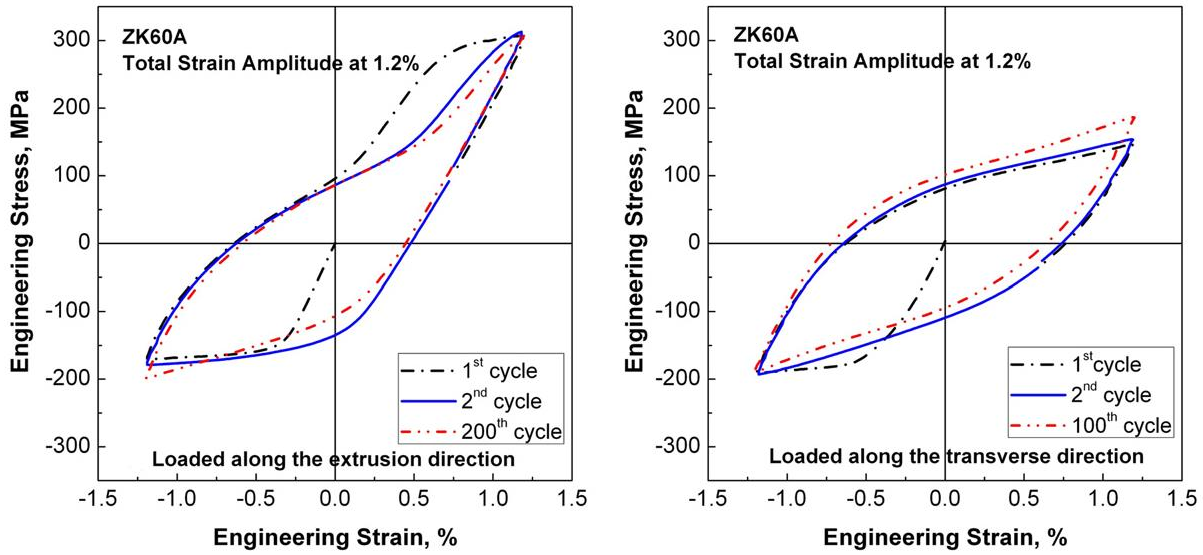

Figure 4. Hysteresis loops of ZK60 at 1.2% straining along (a) ED and (b) TD direction [36]

In Figure 4, the initial loading is compressive; hence, when loading is along the ED, extension twinning can occur, whereas the symmetric hysteresis along the TD attests a slip-dominant deformation. Furthermore, based on Figure 4 (a), once twinning has occurred, a typical strain hardening plateau is seen in the curve which is an indication of the low hardening rate of twinning. On the other hand, upon reversal, detwinning is initially happening. However, once detwinning is exhausted, a rapid strain hardening is observed in the loop originating from non-basal slips and compression twinning dominated deformation.

It is noted that in the second cycle, yielding is happening sooner. As a result, more twins will be formed in the second compression loading, but the compressive peak in this reversal is roughly the same as the one in the first cycle. Again, it implies a very low strain hardening due to the formation of twins. Finally, in the tensile reversal, the inflection point can be detected in higher strain values, since more twins exist in the microstructure. This is in agreement with the results observed by Xiong et al. in [41]. Wu et al. confirmed their observations by in situ neutron diffraction measurement. A normalized intensity evolution of basal poles during the first few cycles is represented in Figure 5. Two detector banks were located such that their recorded diffraction patterns would be an indicative of the volume fraction of parent grains and twinned ones. Bank 2 is placed in an angle so that it corresponds

to the fraction of twinned grains. Therefore, the more the peak value, the more twin in the microstructure.

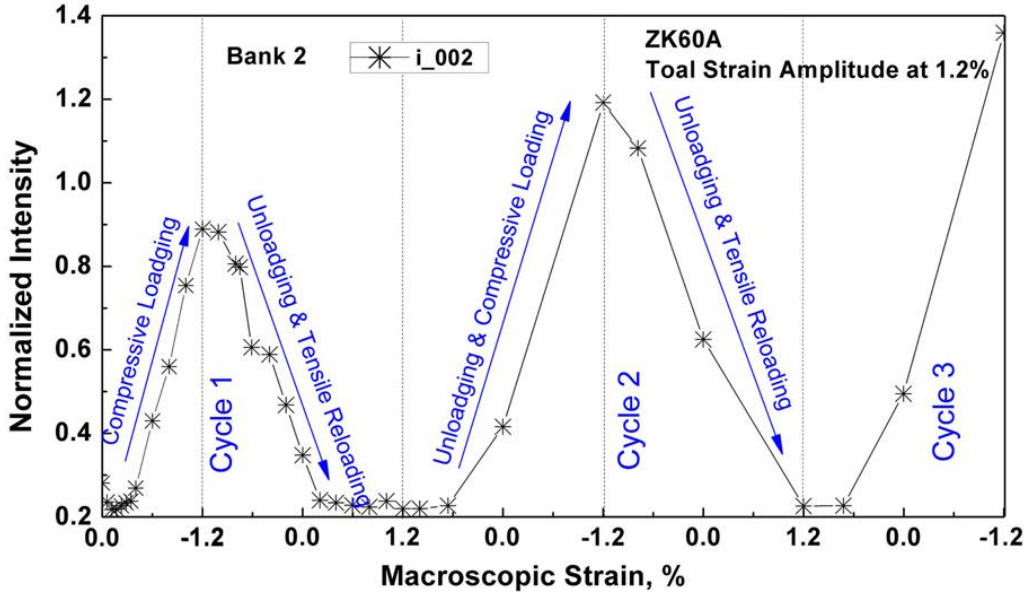

Figure 5. Normalized intensity evolution of basal poles for the first few cycles (Bank 2 is placed so that it collects the radiation from twinned grains) [36]

Figure 5 agrees well with the conclusions made from the hysteresis loops. In the initial stages that deformation is elastic, no bulk twin nucleation can be detected till strain value of ~0.2%. Upon yielding, the intensity increases indicating that bulk twinning is happening. During unloading, intensity value drops swiftly signifying that detwinning is triggered by lower stress values. This is because twins and parent grains ought to have some internal stresses that activate detwinning. Aside from this, it should be noted that once detwinning is exhausted, the resulting orientation is hard with respect to the tensile deformation by basal slips. Therefore, it demands to accommodate the strain by non-basal slips and possible compression twins. In cycle two, as expected, a higher intensity is observed, and it needs more straining to have intensity value back to the background.

Yu et al. [42] investigated the quasi-static and cycle fatigue behavior of as-extruded ZK60 along extrusion direction. Figure 6 depicts the result of quasi-static experiments.

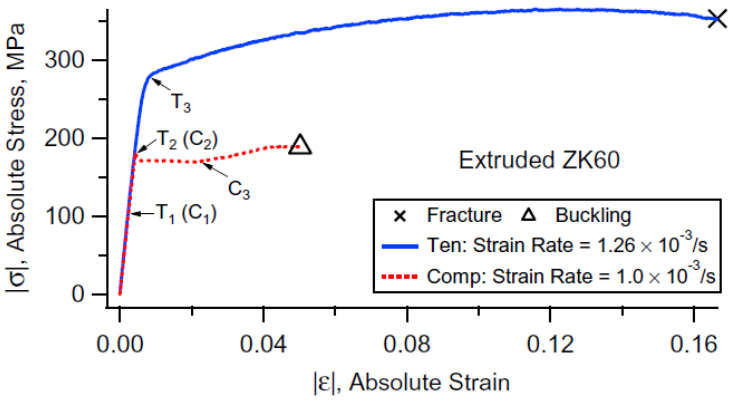

Figure 6. Quasi-static tension and compression of ZK60 extrusion [42]

In this figure, point T1 corresponds to the termination of elastic regime. Beyond T1, the curve flows nonlinearly with very high but slowly decreasing strain hardening rate up to the stress of 180 MPa at point T2. During this stage of deformation, basal slip is activated by few grains which induces micro-yielding. After T2, pronounced yielding asymmetry is observed along tension and compression. The plateau part in the compression curve (red line) corresponds to the initiation of tension twins. Following the plastic plateau, low but slightly increasing strain hardening rate is displayed, and twin formation rate is reducing. Meanwhile, non-basal twins can be activated in the twinned area, and strain hardening is owing to the non-basal slips and the interaction between dislocation slips and twin formation. On the other hand, in tension, stress flow continues its high but slightly decreasing strain hardening behavior till T3 which is 0.2% offset tensile yield stress. After T3, it is reported that few twins can be formed in some favorably oriented grains.

To study the cyclic response, fully reversed strain-controlled fatigue tests were performed at various strain amplitudes. It was observed that the shape of hysteresis loops highly depends on the applied strain amplitude [42]. When the strain amplitude was higher that 0.5%, an asymmetric hysteresis with a sigmoidal shape in the tensile part was obtained owing to the activation of non-basal slips following the exhaustion of detwinning. It was also concluded that after exhaustion of detwinning, a fraction of twinned grains still exits in the microstructure. Therefore, with increasing cycle number, more “residual twins” will be retained. These residual twins block the dislocation movements in the following cycles and

cause a positive mean stress in the material which affects the fatigue behavior adversely. For strain amplitudes between 0.4% and 0.5%, hysteresis loops were asymmetric in the first few cycles corroborating that twinning-detwinning is happening. However, in the following cycles, the hysteresis loop would tend to be symmetric which provides the evidence that no more twinning-detwinning is happening. A moderate mean stress was exhibited in the material due to the initial asymmetric fatigue behavior. Finally, for strain amplitudes lower than 0.4%, it was stated that an elastic symmetric hysteresis loop could be observed; consequently, no mean stress is induced, and the dominant deformation mode is basal slip along both directions. SEM images of the overall macroscopic fatigue fracture surface profiles revealed a tensile cracking for the early growth of cracks. Moreover, it was stated that twinning process plays a dominate role in the crack initiation mechanism at high strain amplitudes.

The fatigue data for extruded ZK60 obtained from the fully reversed strain-controlled tension–compression tests along the extrusion direction was used to develop a fatigue model. It was discovered that while a single three-parameter equation cannot be used to model the whole strain-life curve, SWT model describes it nicely which is consistent with the SEM analysis result, namely early crack growth of ZK60 at the investigated strain amplitudes is characterized by tensile cracking. However, later Xiong and Jiang [43] did cyclic fully reversed strain controlled tests at higher strain amplitudes, and discovered that at strain amplitudes higher than 3%, fracture occurs under compression loading rather than tension. Accordingly, SWT model is unable to predict the fatigue life at those high strain amplitudes. A kink point at strain of 3% in the strain-life curve manifests the variation in the fracture mechanism (Figure 7). Quasi-static tests were conducted likewise; however, this time the effects of pre-compression and pre-tension loadings on the quasi-static tension and compression behavior were also studied. When the material was subjected to tension prior to compression loading, non-basal slips would weaken the texture. As a result, twinning would be triggered at a higher stress value under compression. In contrast, once the material was first compressed to high strain values, yielding occurred earlier. The reason is that in this case, grains are orientated most abundantly along the c-axis. Therefore, bulk detwinning can be activated by tension loading, and yielding will be due to detwinning rather than slip.

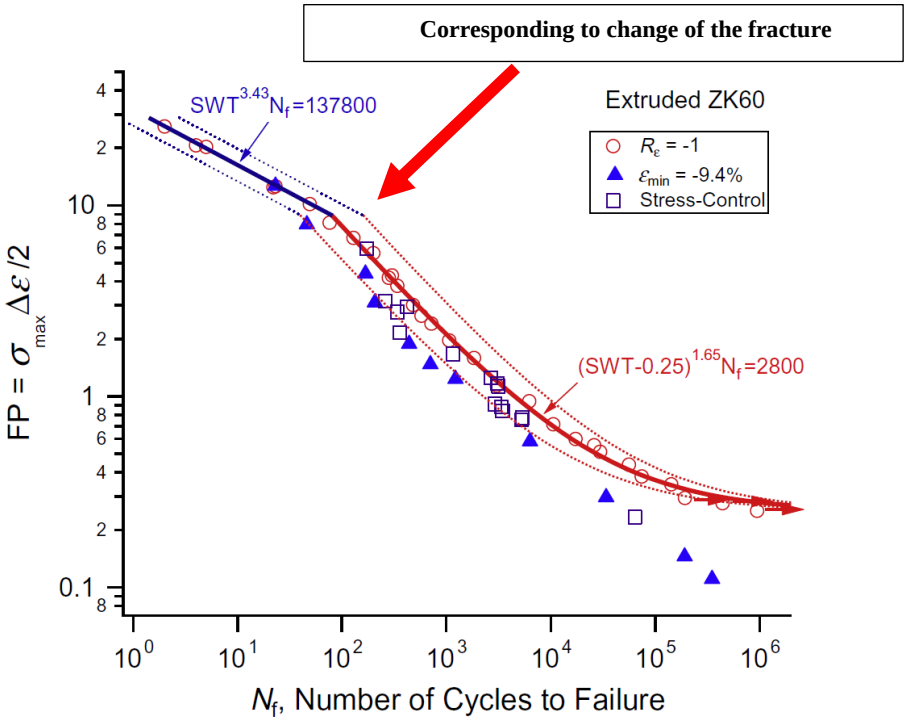

Figure 7. SWT parameter vs. fatigue life of ZK60 under strain-controlled tests [43]

Fully reversed strain controlled cyclic tests revealed similar results to those of previous study that there exists a threshold point below which slip dominates the plastic deformation, whereas strain amplitudes higher than this value brings about twinning-detwinning process. Also, three distinct deformation types could be identified in the context of induced mean stress, as seen in Figure 8 (a). When strain amplitude is below 0.35%, slip modes, mostly basal slip, dominate the plastic deformation. Thus, hysteresis loops are symmetric, and no mean stress can be recognized. For strain amplitudes between 0.35% and 0.8%, partial twinning/ detwinning is occurring; i.e. twinning is not exhausted in compressive reversal, but detwinning will be exhausted under tensile reversal, and the non-basal slip modes will drive the deformation; consequently, a high tensile stress peak will be achieved, and a positive mean stress exhibits in the material. Type three corresponds to the case that both twinning and detwinning will exhaust during compressive and tensile reversals, respectively. After exhaustion, non-basal slips dominate the deformation and a sigmoidal shape can be observed under both tension and compression loading (Figure 8, b). Moreover, as seen in Figure 8 (a),

mean stress decreases with increasing the strain amplitude. The result might be the influence of micro cracks happening. The role of twinning/ detwinning was also studied in [41], and similar dependency was observed on the strain amplitude value.

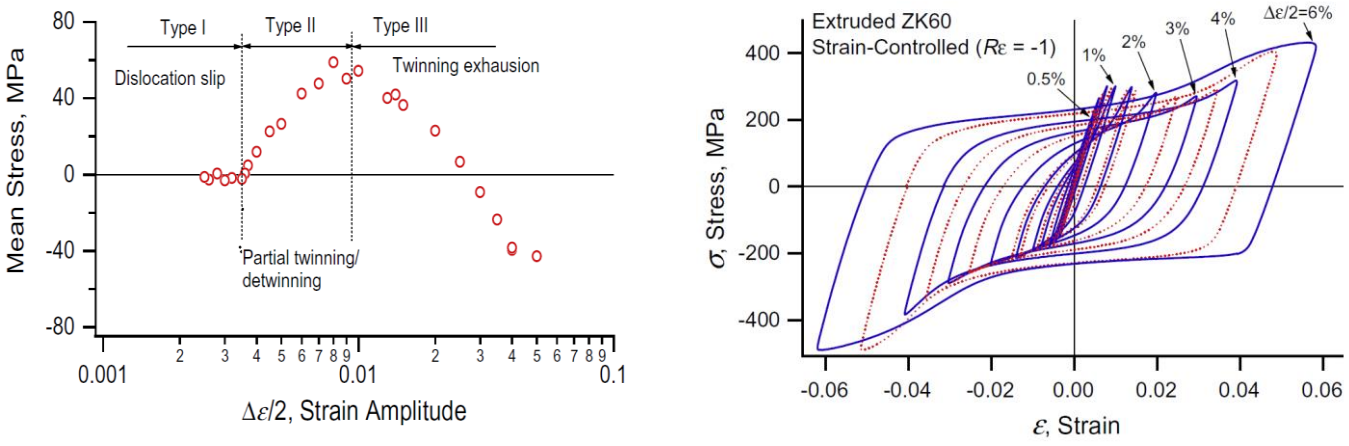

Figure 8. (a) Induced mean stress vs. strain amplitude and (b) hysteresis loops under strain controlled fully reversed cyclic tests [43]

In another study, Dong et al. [44] investigated the effect of heat treatment on the fatigue behavior of extruded ZK60 which is beyond the scope of this research. Nevertheless, it was observed that heat treatment improves the strength under quasi-static loading, but it has marginal effect on the fatigue life. In another study, Liu et al. [45] did study on the high cycle fatigue life (HCF) behavior of extruded ZK60. Fatigue tests were taken under rotary beam loading at different stress amplitudes. A fatigue strength of 140 MPa was reported based on these tests. Moreover, the SEM images of fracture surfaces revealed typical cleavage features consisting lots of lamellar cleavage planes. Furthermore, fatigue experiments were performed on the specimens whose microstructure was pre-revealed by etching. The results of light optical microscopy (LOM) showed that intermetallic phases are playing a major role in crack initiation.

Most of the literature data thus far have been focused on investigating the mechanical behavior of extruded or rolled magnesium alloy. Especially, the mechanical behavior of ZK60 extrusion is investigated mainly along the extrusion direction. Therefore, characterizing the possible anisotropic quasi-static and cyclic response of ZK60 extrusion is a great opportunity

for scientific contribution. Furthermore, there are other manufacturing techniques such as forging that demand more detailed studies. In fact, the thermomechanical effects introduced by forging is a research area that lacks proper attention so far. The next section will review studies focusing on ZK60 at the forge condition.

2.3 Literature on Forged ZK60

The leading manufacturing process of Mg alloy parts is die casting [9], [14][15]. However, the existence of casting defects like porosities, dry oxides, and inclusions limits the alloy strength which prevents the extensive applications in the as-cast state. Studies such as [46][47] show that magnesium alloys in wrought conditions exhibit refined grains, better strength, higher deformability, and longer fatigue life offering better opportunities for the magnesium alloys applications as a structural material. Extrusion, which forms strong basal texture and bimodal grains, is one of the common manufacturing processes for the wrought Mg alloys [45-49]. Recently, ECAP process which causes severe plastic deformation (SPD) is introduced, which refines the microstructures and weakens the texture of the magnesium alloys [50-52]. However, this process cannot be used for manufacturing body parts with complex geometries. Among other manufacturing processes, forging is the most efficient technique where the structural parts are produced in a near net shape. However, there is the requirement to demonstrate that forged non rare-earth Mg alloys meet the demands of microstructure refinement with the improvement of mechanical properties [50][51].

Multi directional forging (MDF) has been employed on magnesium alloys after cast, extruded, and rolled states for the refining of microstructure and texture modification which improved the mechanical properties including the tensile and fatigue properties. Wu et al. [52] studied the effect of high strain rate multiple forging (HSRMF) on homogenized commercial semi-continuous casting ZK60 magnesium alloy. They reported that after homogenization, the majority of eutectic compounds are dissolved into the α-Mg matrix. Owing to the coarse grains microstructure (~100 μm), grain boundary sliding hardly could happen to accommodate the plastic deformation; however, during MDF, twins are induced and rotational dynamic

recrystallization occur which forms honeycomb-like coarse and island-like ultrafine dynamic recrystallize (DRX) grains resulting in the improvement of ductility and tensile strength.

Vasilev et al. [53] evaluated the fatigue performance of as-cast ZK60 after carrying out multiaxial isothermal forging (MIF). According to this study, a bimodal microstructure containing about 80% recrystallized fine grains (3-6 μm) with elongated grains (~1 mm long and ~50 μm thick) were present in the microstructure after the process. Also, MIF yielded in the improvement of both the HCF endurance limit and the LCF life. This improvement was ascribed to the better ductility (~3 times better) and higher strength (~40%) after MIF confirmed by the quasi-static tests. However, the effect of other important factors, i.e. texture and secondary phases distribution, was not considered in the research.

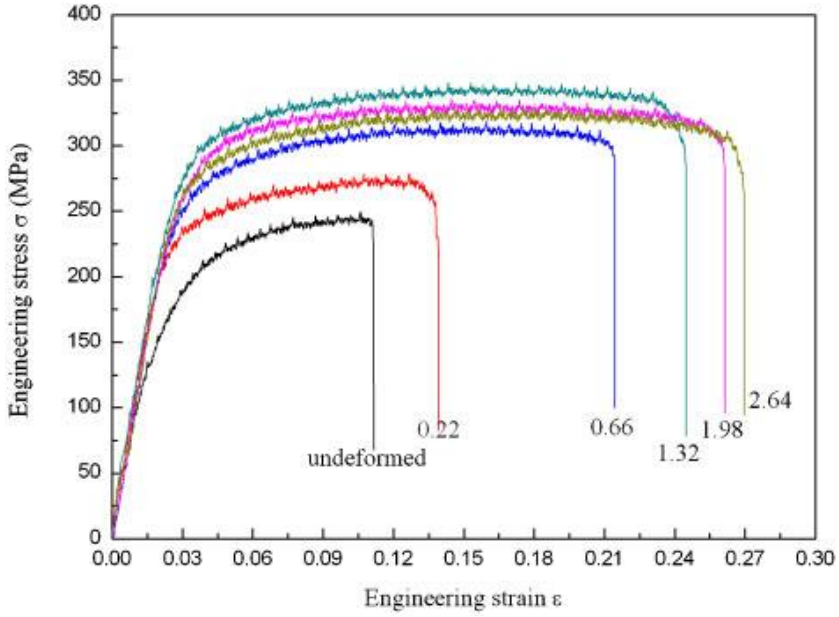

Figure 9. Flow curves of high strain rate multiple forged samples at different accumulated strains [52]

Nugmanov et al. [54] studied the effect of MIF under decreasing temperature conditions in the range of 400° C to 200° on the texture of hot-pressed ZK magnesium alloy rod. It was reported that during the first pass at 400° C, texture did not alter significantly, corresponding to the minor change in the yield strength and its anisotropy. However, the next passes of forging led to texture weakening, thereby reducing the strength anisotropy.

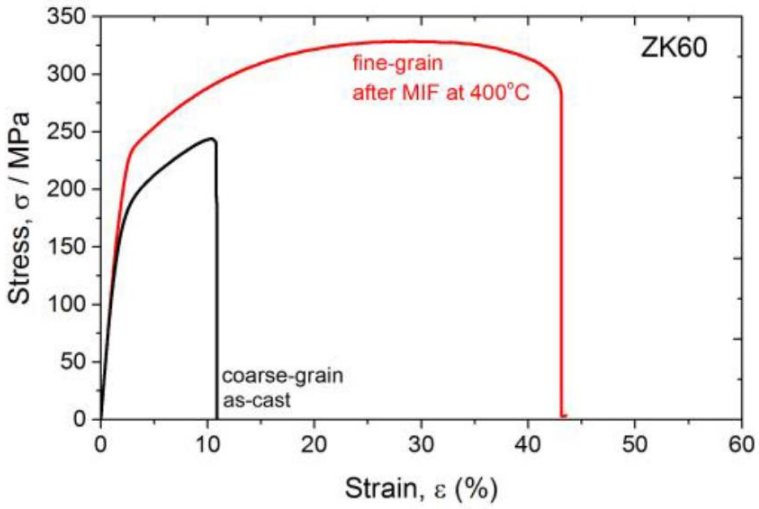

Figure 10. Quasi-static tensile stress-strain curves for the reference coarse grain and MIF-processed fine-grain ZK60 alloy [53]

Tao et al. [55] investigated the microstructure evolution of ZK60 magnesium alloy prepared by the multi-axial forging and partial remelting route in the semi-solid state. The research aimed at studying the improvement of mechanical properties of thixoforming ZK60 which is beyond the objectives of the proposed research (Thixoforming is a semi-solid metal process route that alloys are formed in the semi-solid state to near net shape components). However, microstructural analysis in this study revealed an island-shaped Mg-Zn eutectic components next to grain boundaries for the as-cast ZK60, while the microstructure of the alloy after three passes of forging was filled with elongated and unrecrystallized grains and intermetallic particles vertical in the compression direction.

The research surrounding the characterization of forged ZK60 have been focusing on the effects of the process on the material's structure. However, a link to correlate the material's structure and performance is lacked. Hence, a great opportunity exists in establishing a link between the material-structure-performance, which is the focus and a scientific contribution of this thesis.

Looking more specifically at the effects of forging on the mechanical behavior of ZK60, Moldovan et al. delivered a rudimentary investigation on the mechanical properties of extruded-forged ZK60 and AZ80 by performing stress-controlled fatigue tests [56]. They

reported that inclusions, porosities, and coarse intermetallic particles are the key reasons of failure. EDX measurement confirmed the presence of Mg-Zn and Mg-Zn-Zr on the fracture surfaces.

There are also some studies on the MDF of other magnesium alloys reporting that mechanical properties will be improved as a result of the process. Miura et al. [57] investigated the effect of multi-directional multi-step forging on the mechanical properties of AZ61 alloy, and discovered that the cumulative strain pertaining to the forging process yielded grain refinement pronouncedly, which resulted in the drastic improvement of ductility. In another study [58], it was stated that multidirectional forging under decreasing temperature conditions can expedite the evolution of ultra-fine grains leading to a higher ductility.

Forging as a manufacturing technique has received less attention than the other techniques such as rolling, extrusion, and ECAP. Ogawa et al. [59] looked for the appropriate temperature range for the precision forging of ZK60 Mg alloy, through the upset-ability test, and determined the forming limit of the Mg-alloy in terms of the deformation temperature. They reported that when the forming temperature was less than 200 °C, cracks were observed after 39% reduction in the height, while for deforming temperatures between 250 °C and 400 °C, the Mg billet obtained excellent workability. It was also noticed that the deformation temperatures should not be higher than 400 °C to avoid severe oxidation. The oxide layer of magnesium alloys raises the friction extensively.

Matsumoto and Osakada [60] suggested to keep the billet in non-oxidizing atmosphere, or ride off the oxide layer and apply lubricant on both tools and billet in order to reduce the friction and obtain better response during the warm forging of ZK60 at the temperature of 200 to 400 °C [61]. Kwon et al. [62] investigated the forgeability of magnesium alloys in terms of forging temperature, speed, and grain size. They summarized that forging speed is more sensitive than temperature and finer grains are required for successfully forging of magnesium alloys. However, this result was not well-supported with the experimental evidence.

Kurz et al. [63] investigated the behavior of as-extruded ZK60-F Mg during closed die forging, and concluded that at higher deformation rates (300-400 mm/sec), the forging temperature of 340°C is the optimum condition with no crack happening. Furthermore, they

observed that increasing the forging temperature decreases the mechanical strength due to the grain growth but enhances the elongation in consequence of the increased microstructure homogeneity. The results of quasi-static tests along transverse and longitudinal directions revealed an isotropic behavior in terms of strength for ZK60.

Most of the literature data have focused on microstructural studies and the tensile properties or texture measurement of multidirectional forged magnesium alloy. To the author's knowledge, a comprehensive study on the characterization of the mechanical behavior of forged magnesium alloys cast and extrusion, notably ZK60 magnesium alloy, is not reported in the literature. As a matter of fact, it is also not clear how the forging changes the microstructure and texture of the cast and extruded ZK60 magnesium, which is crucial to develop the technology for wide utilization of forged ZK60. Correspondingly, one of the objectives of this study is to address this gap in the literature, namely identifying the influence of open-die and close die forging on the microstructure, crystallographic texture, and mechanical properties of ZK60 magnesium alloy extrusion and cast.

2.4 Multiaxial fatigue behavior

As mentioned before, transportation sector has been attempting to adopt lightweight alloys in the vehicles' components in the light of the necessity to cut down the fuel consumption rates of automobiles. One such material being magnesium (Mg) alloy was found to be a proper candidate for this purpose due to its low density, high specific strength, and excellent machinability. However, Mg's applications have been limited largely to the non-load-bearing components such as seat frames and housing parts [12]. To achieve the abovementioned mass-saving target, Mg's applications need to be broadened to load-bearing parts such as the suspension system, too. On the other hand, such components are subjected to multiaxial loadings during their service life which brings in its own complexities [64][65]. Thereby, it is important to characterize the mechanical behavior of Mg alloys under multiaxial loadings.

One of the most examined features of the multiaxial loading is the materials' sensitivity to the non-proportionality. Non-proportionality of loading leads to the rotation of the principal axes during the load history, which might affect the fatigue life [66]. It was shown in a study by Pejkowski et al that phase angle shifts under the same stress ratio can influence two different materials differently [67].

The multiaxial fatigue behavior characterization of different wrought Mg alloys has recently been investigated. Yu et al. [68] conducted strain controlled proportional and non-proportional multiaxial fatigue tests on an as-extruded AZ61A Mg alloy. They employed the Fatemi-Socie and the modified SWT criteria (see section 2.5) to model the cyclic behavior. It was found that the former model could predict the fatigue life well in the low cycle fatigue regime, but not in the high cycle fatigue regime. They reported that this may stem from the fact that the Fatemi-Socie is a shear-based fatigue parameter, and the criterion is appropriate when material is displaying shear cracking. However, AZ61A exhibited mixed cracking in the low strain amplitudes (i.e. high cycle fatigue regime). Apart from this, it was reported that the modified SWT criterion could estimate the fatigue life satisfactorily

Albinmousa et al. studied the multiaxial fatigue characteristics of AZ31B Mg alloys extrusion in [46][69][70][71][72][73]. They carried out proportional and non-proportional multiaxial fatigue tests in different phase angles. It was found that non-proportionality exhibits additional hardening, but it does not change the fatigue response significantly. This additional hardening is stemming from dislocation-dislocation interactions; they are forced to move along all possible slip planes [74]. Moreover, it was noted that the twinning mode of deformation has a key role in the multiaxial behavior of the alloy. To be more specific, while hysteresis loops obtained from the cyclic torsion tests were symmetric, they tended to be asymmetric under multiaxial loading, as twinning-detwinning was occurring. Apart from these, different fatigue models, namely Fatemi-Socie, SWT, and Jahed-Varvani approaches as damage parameters, were developed to estimate the cyclic life. Due to the intrinsically scalar nature of energy, the energy-based model employed effectively correlated the different damages of axial and torsional loadings to the fatigue life. In [71], Jahed and Albinmousa delivered a study on the multiaxial behavior of wrought magnesium alloys, in particular AZ-, AM-, and ZK-series,

where they did a comprehensive review on the existing literature. They discussed the sustainability of a two-parameter energy-based model (Jahed-Varvani model), and manifested that the model was capable of correlating a total of 354 data points obtained from testing specimens at various loading conditions and loading orientations in a single scatter band. These conditions were: axial, shear, axial with mean strain or mean stress, stress and strain controlled, and multiaxial loadings.

In another study, Xiong et al. [75] investigated the tension-compression asymmetric behavior of AZ31B extrusion under the combined axial-torsional loading. Again, AZ31 was exhibiting a symmetric behavior under cyclic torsion loading, but asymmetry was seen under multiaxial loading with the axial strain amplitude higher than 0.4%. A positive shear mean stress was seen under proportional loading, and a negative shear mean stress could be observed under non-proportional loading. The reason for asymmetric behavior is the fact that higher twin volume fraction leads to a weaker shear resistance. Hence, under proportional loading, as more twins are available in the microstructure at the compressive peak stress than the tensile peak, a positive shear mean stress would be induced. On the contrary, under nonproportional loading, twin volume fraction at the zero axial strain during the tensile reversal (or at the maximum shear strain) is higher than that at the zero axial strain with proceeding a half more cycle (or at the minimum shear strain); consequently, a negative shear mean stress is developed. The authors also employed modified SWT and an energy-based fatigue model [76], and it was shown that both of them could predict the life convincingly.

Reis et al. [77] investigated the low cycle fatigue behavior of as-extruded AZ31B under uniaxial and multiaxial loadings, and proposed a numeric elastoplastic model based on their experiments. To analyze the numeric model, the results were correlated to the Jiang and Sehitoglu plasticity model [78], and it was found that these two models were not consistent in modeling the softening behavior of Mg.

Li et al. [79] studied the multiaxial ratcheting in AZ31B extrusion, and reported the dependency of the ratcheting strain on the shape of multiaxial locus. Moreover, it was noted that the traditional equivalent stress-strain responses cannot be exploited for AZ31B Mg alloys,

for the contribution of different modes of deformation in the axial and torsional modes of loading.

In another study, Castro and Jiang [80] conveyed a new research on the multiaxial fatigue behavior of AZ31 where they evaluated capability of different fatigue models to predict the life and the cracking behavior. The SWT failed to predict the fatigue life accurately, while Fatemi-Socie criterion could estimate the fatigue lives well for all the experiments; by the way, it led to an unacceptable prediction regarding the early cracking growth behavior. Jiang's energy-based model was assessed, and this model predicted both the fatigue life and crack behavior satisfactorily.

Aside from the AZ31B Mg alloy extrusion, the mechanical behavior of AZ61 Mg alloy extrusion was studied by Yu et al. [68]. They performed fully reversed axial, torsional, proportional axial-torsional, and 90° out-of-phase multiaxial cyclic tests, while the proportional and non-proportional tests exhibited the highest and the shortest lives for the same equivalent strain amplitude, respectively.

In another study, Roostaei et al. [81] studied the multiaxial fatigue behavior of AM30 under different phase angles, namely , 0° (in phase), 45°, and 90°. The effect of non-proportionality was observed to be depended on the applied axial strain amplitude. Moreover, the interaction of the axial and torsional loading was studies. Lastly, two critical-plane models and an energy-based model were employed to predict the multiaxial fatigue life.

Gryguc et al. [82] investigated the multiaxial fatigue behavior of as-extruded and closed-die extruded-forged AZ80 Mg alloy. Five different loading paths were employed to understand the mechanical behavior of AZ80 under pure axial, pure shear, and combined axial-shear loadings. The two non-proportional paths exhibited shorter fatigue lives comparing to the other ones. Of all the strain paths investigated, the pure shear one exhibited longitudinal cracking. However, the initial crack growth behavior was predominantly transverse to the axial direction for the other paths.

The one and only research on the multiaxial fatigue behavior of ZK60 is performed by Albinmousa et al. [83]. They studied the mechanical behavior of ZK60-T5 magnesium extrusion under quasi-static tension and cyclic axial, pure shear, and combined multiaxial

loading. It was reported that the cyclic axial response in terms of the shape of the hysteresis loop depends on the applied strain amplitude, whereas the shear response is symmetric with no sign of twinning-detwinning deformation regardless of the applied shear strain amplitude. Furthermore, the multiaxial fatigue tests revealed that multiaxiality and nonproportionality are not detrimental to the fatigue life of heat treated ZK60.

The main attention in multiaxial fatigue research has been dedicated to the AZ- and AM- series. On the other hand, ZK- series Mg alloys have shown superb mechanical behavior due to the presence of Zr as a grain refiner [32][84]. However, the discovery level study in this area is extremely limited. More importantly, the effects of forging as a promising manufacturing technique on the shear and multiaxial fatigue behavior is largely unknown. Furthermore, the interactions of axial and shear loading under multiaxial loading in ZK60 extrusion and forged is undiscovered.

2.5 Fatigue Life Modeling

The successful design of load-bearing components necessitates developing a fatigue model that can predict the life accurately. Several fatigue models have been proposed by researches which can be classified into three main categories, namely stress-based models, strain-based models, and energy-based models. To be more specific, the fatigue damage parameters are formulated such how that the experimental fatigue life is correlated to the stress, strain, or energy associated with a single loading cycle.

The most frequent question in this context would be “Which fatigue model should we use?”. In fact, there is no straight answer to this question. The applicability of each method depends on various factors such as material and loading type. Generally speaking, when there is no prior knowledge regarding the fatigue behavior, some basic questions need to be answered, which are shown in the diagram below.

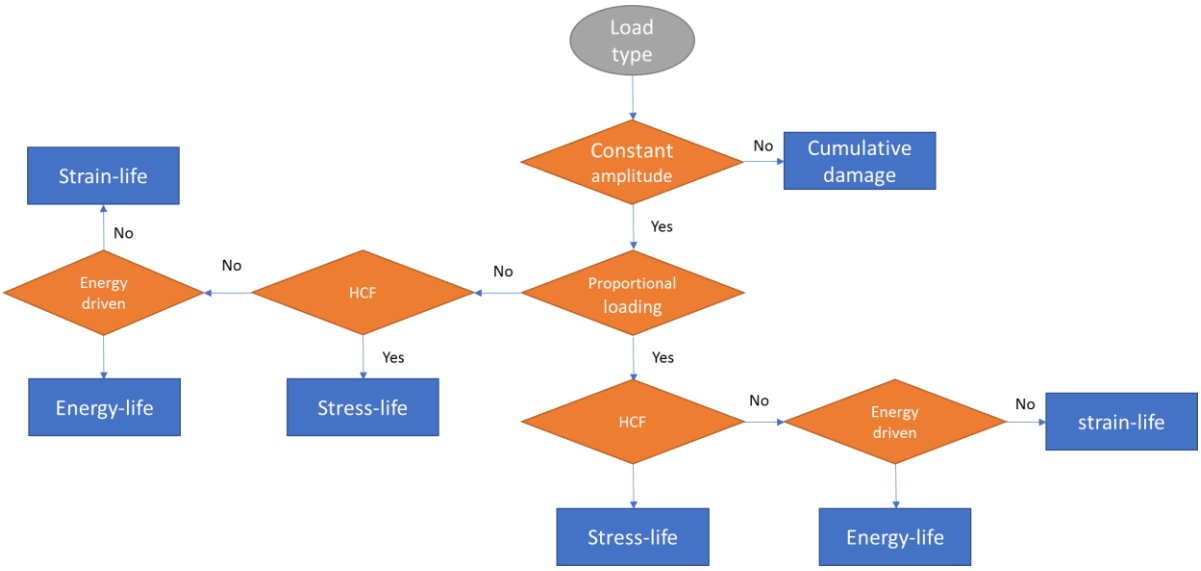

Figure 11. Selection of the fatigue model type

Firstly, one needs to determine whether the loading type is constant amplitude loading or variable amplitude loading. Should that the loading is variable amplitude loading, cumulative fatigue damage features should be considered which is beyond the scope of the current study. A load that is not completely random, but has a sequences of non-constant load cycles can also fall into this category.

Secondly, it is important to determine whether the loading is proportional or non-proportional. Under non-proportional loading, the ordination of the principal stresses or strains change. In another wording, a load on an engineering component in service can be applied on different axis contemporary (multiaxial). When all the components of the stress tensor are in phase, the loading is called proportional, however, under non-proportional loading, the components vary out of phase. Under proportional loading, the direction of the largest stress or strain component that governs the fatigue life is clear. Generally, the stress-based models are suitable to simulate the high cycle fatigue, while the strain-based models are suitable for low-cycle fatigue regime where appreciable plasticity is involved, and the governing factor is the applied strain. Also, stress depends on the geometry of the sample. In contrast, strain does not. Hence, for the sake of material characterization, strain-based models are preferred, and stress-based models can be later employed to design the real component. Therefore, in this

study that focuses on the material characterization in the context of material-structure-performance relationships, strain-based and energy-based models are employed. A very famous and common strain-based model is Coffin-Manson which is presented by Equation 2-1.

$$\frac{\Delta\varepsilon}{2}=\frac{\Delta\varepsilon_e}{2}+\frac{\Delta\varepsilon_p}{2}=\frac{\sigma'_f}{E}(2N)^b+\varepsilon'_f(2N)^c \qquad 2\text{-}1$$

where strain amplitude is resolved into elastic and plastic strain components. At low cycle fatigue regime, the plastic strain is predominant, while at lower strain amplitude pertaining to the high cycle fatigue regime, elastic strain is the leading component [85]. Figure 12 illustrates the equation better.

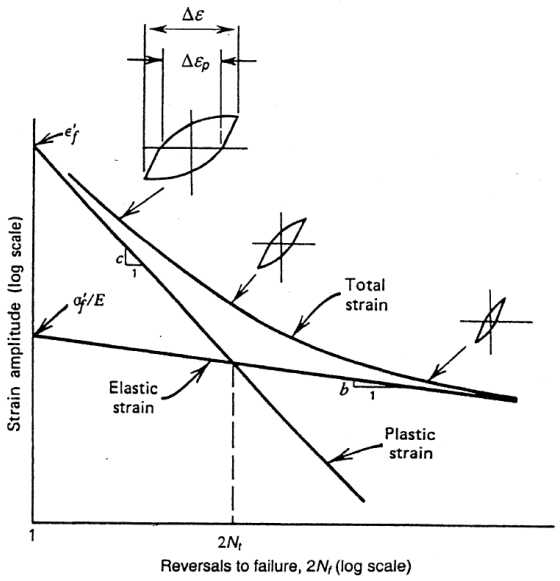

Figure 12. Strain-Life curve showing total, elastic, and plastic strains [85]

A decent fatigue model must account for different fatigue phenomena such as the cyclic hardening and mean stress effect. To consider the mean stress effect, different mean stress correction models have been proposed:

Morrow's equation:

$$\frac{\Delta\varepsilon}{2} = \frac{\sigma'_f - \sigma_m}{E}(2N)^b + \varepsilon'_f (2N)^c \qquad 2\text{-}2$$

Manson-Halford's correction:

$$\frac{\Delta\varepsilon}{2} = \frac{\sigma'_f - \sigma_m}{E}(2N)^b + \varepsilon'_f \left(\frac{\sigma'_f - \sigma_m}{\sigma'_f}\right)^{c/b} (2N)^c \qquad 2\text{-}3$$

Smith-Watson-Topper (SWT):

$$\sigma_{\max}\frac{\Delta\varepsilon}{2} = \frac{(\sigma'_f)^2}{E}(2N)^{2b} + \varepsilon'_f \sigma'_f (2N)^{b+c} \qquad 2\text{-}4$$

where $\sigma_{\max} = \sigma_m + \sigma_a$.

Fatigue failure under multiaxial loading is crucial to be considered, as this kind of loading is very common for components in service. However, multiaxial fatigue loading life estimation is a very complex task in comparison to the uniaxial cases. In fact, the direction of the principal stress or strain changes, and so does the direction of the parameter affecting the fatigue life. To overcome this issue, critical-plane approaches are proposed, of which two of the most common ones are Smith-Watson-Topper (SWT) [86] and Fatemi-Socie [87]. The critical plane in the former is associated with the plane of maximum normal strain, while the latter considers the plane of maximum shear as the critical plane.

SWT [88] was initially defined to estimate the life under uniaxial loading, however, Socie used it in the multiaxial loading analysis that cracked primarily under tensile cracking mode [86]. As above-mentioned, the critical plane is presumed to be the plane of maximum normal strain. The fatigue damage parameter is related to the experimental life via the following equation:

$$\sigma_{n,\max}\frac{\Delta\varepsilon}{2} = \frac{(\sigma'_f)^2}{E}(2N)^{2b} + \varepsilon'_f \sigma'_f (2N)^{b+c} \qquad 2\text{-}5$$

where $\sigma_{n,\max}$ is the maximum normal stress on the critical plane. Later, Jiang and Sehitoglu modified the SWT parameter to better estimate the cracking mode under torsional loading [89]. The parameter that they used is:

$$MSWT\ parameter = 2b\Delta\varepsilon\langle\sigma_{max}\rangle + \frac{1-b}{2}\Delta\tau\Delta\gamma \qquad 2\text{-}6$$

where σ_{max} and $\Delta\tau$ are the maximum normal stress and shear stress range in the half-life cycle on a material plane, respectively. Also, $\Delta\varepsilon$ and $\Delta\gamma$ are normal strain range and shear strain range, respectively, corresponding to the normal stress and shear stress. The symbol $\langle\ \ \rangle$ denotes the MacCauley bracket, which is defined as $\langle x\rangle = 0.5(x + |x|)$. In fact, employing the MacCauley bracket makes sure that no compressive damage is incorporated in the model. Lastly, the parameter b is a material constant which represents the cracking mode and varies from 0 to 1. For b=1, the modified SWT parameter becomes the original parameter defined by Socie. It has been stated that $b \geq 0.5$ suggest tensile cracking mode. On the other hand, b values less than 0.37 suggest the shear cracking behavior, and the values between 0.37 and 0.5 evaluate mixed cracking. Theoretically, the parameter b is determined by setting the pure shear and pure axial responses coincide on a single curve.

Fatemi-Socie parameter is another mostly used strain-based critical plane approach to estimate the fatigue life. According to this parameter formulation, the critical plane is the plane of maximum shear strain. Equation 2-7 describes the model. The left side is the fatigue damage parameter and the right side of the equation is derived in analogy to the Coffin-Manson equation.

$$\frac{\Delta\gamma_{\max}}{2}\left(1+k\frac{\sigma_{n,\max}}{S_{yt}}\right) = \frac{(\tau'_f)^2}{G}(2N)^{b_s} + \gamma'_f(2N)^{c_s} \qquad 2\text{-}7$$

γ_{max} is the maximum shear strain amplitude and $\sigma_{n,max}$ is the maximum normal stress on the principal shear strain plane. k is a material constant that is derived similar to the procedure for determining b in the MSWT model; i.e., the fatigue damage parameter curves for axial and shear loading should be brought together. $S_{y,t}$ is the tensile yield strength under quasi-static loading and G is the shear modulus.

Ling et al. compared different fatigue models mentioned above to predict the life of wrought ZEK100 Mg and compare it with the experimental results [90]. In general, they found good agreement with SWT model that they modified for application in Mg alloys.

2.6 Energy-based Models; Jahed-Varvani Damage Parameter

In some cases, the stress or stain is insufficient to deliver the fatigue modeling. One such cases is materials with anisotropic and asymmetric behavior such as hcp crystal materials like Mg alloys. Energy-based models combine the effects of stress and strain, and are frequently used for such materials in the low-cycle fatigue regime that appreciable amount of plasticity is involved. A significant characteristic of energy is to be a scalar parameter.

In 2006, Jahed and Varvani [91] proposed a damage parameter correlating the fatigue life to the energies due to purely axial and torsional loadings. In this model, the total strain energy density is implemented as the fatigue damage parameter, which is comprised of the elastic and plastic strain energy densities. The latter is the area inside the axial and shear hysteresis loops. The former elastic part is defined as follows:

$$\Delta E_e^+ = \frac{\sigma_{max}^2}{2E} \quad Axial \qquad \Delta E_e^+ = \frac{\tau_{max}^2 + \tau_{min}^2}{2G} \quad Shear \tag{2-8}$$

where σ_{max} is the axial stress at the positive tip of the hysteresis loop, τ_{max} and τ_{min} are the peak and valley stresses of the shear hysteresis loop at the stabilized half-life cycle, and E and G are the elastic axial and shear modulus, respectively. Subsequently, the strain energy density is correlated to the fatigue life for the pure axial and shear tests with a direct-fit approach to a formula like the Coffin-Manson equation.

Two different lives are estimated for axial-torsional loading by equations which are in an analogy to the Coffin-Manson equation:

$$\Delta W_A = E'_e (N_A)^B + E'_f (N_A)^C \tag{2-9}$$

$$\Delta W_T = W'_e (N_T)^{B_s} + W'_f (N_T)^{C_s} \tag{2-10}$$

where ΔW_A and ΔW_T are the energies under purely axial and torsional loading, respectively, and E_e' and W_e' are the energy-based axial and torsional fatigue strength coefficients, respectively. Moreover, E_f' and W_f' are the energy-based axial and torsional fatigue toughness, respectively. All the coefficients and exponents can be calculated similar to the Coffin-Manson equation. Finally, Equation 2-11 is used to obtain the fatigue life in which ΔW_t is the total energy density.

$$N_f = \frac{\Delta W_A}{\Delta W_t} N_A + \frac{\Delta W_T}{\Delta W_t} N_T \qquad 2\text{-}11$$

It is worth mentioning that a new elastic energy density definition based on alternating stress and peak stress is proposed which better accounts for contribution of elastic energy in variable amplitude loading cases and positive stress ratios [92].

Most studies on the fatigue properties of magnesium alloys have employed uniaxial tension-compression loading, and very limited studies have been delivered under multiaxial loading. In 2011, Yu et al. [68] conducted strain controlled proportional and non-proportional multiaxial fatigue tests on an as-extruded AZ61A Mg alloy. They employed the Fatemi-Socie and the modified SWT criteria to model the cyclic behavior. It was found that the former model could predict the fatigue life well in the low cycle fatigue regime, but not in the high cycle fatigue regime. This may stem from the fact that the Fatemi-Socie is a shear-based fatigue parameter, and the criterion is appropriate when material is displaying shear cracking. However, AZ61A exhibited mixed cracking in the low strain amplitudes (i.e. high cycle fatigue regime). Apart from this, it was reported that the modified SWT criterion could estimate the fatigue life satisfactorily.

Albinmousa et al. [46] studied the multiaxial fatigue behavior of AZ31B extrusion under proportional and nonproportional loadings for the first time in 2011. They conducted both in phase and out of phases tests at 45° and 90° phase angle shifts and showed that nonproportionality had no major effect on the fatigue life, but it caused additional hardening. Moreover, while hysteresis loops obtained from the cyclic torsion tests were symmetric, they tended to be asymmetric under multiaxial loading, as twinning-detwinning was occurring.

Apart from these, different fatigue models, namely Fatemi-Socie, SWT, and Jahed-Varvani approaches as damage parameters, were developed to estimate the cyclic life. It was shown that Fatemi-Socie critical plane model and Jahed-Varvani energy models predict the fatigue life of AZ31B within a factor of ±2 persuasively. However, SWT model was incapable of estimating the life under cyclic torsional experiments. Later in 2012 another research was done by Xiong et al. [75] on the multiaxial fatigue behavior of AZ31. Again, AZ31 was exhibiting a symmetric behavior under cyclic torsion loading, but asymmetry was seen under multiaxial loading with the axial strain amplitude higher than 0.4%. A positive shear mean stress was seen under proportional loading, and a negative shear mean stress could be observed under non-proportional loading. The reason for asymmetric behavior is the fact that higher twin volume fraction leads to a weaker shear resistance. Hence, under proportional loading, as more twins are available in the microstructure at the compressive peak stress than the tensile peak, a positive shear mean stress would be induced. On the contrary, under nonproportional loading, twin volume fraction at the zero axial strain during the tensile reversal (or at the maximum shear strain) is higher than that at the zero axial strain with proceeding a half more cycle (or at the minimum shear strain); consequently, a negative shear mean stress is developed. The authors also employed modified SWT and an energy-based fatigue model [76], and it was shown that both of them could predict the life convincingly.

In 2014, Reis et al. [77] investigated the low cycle fatigue behavior of as-extruded AZ31B under uniaxial and multiaxial loadings, and proposed a numeric elastoplastic model based on their experiments. To analyze the numeric model, the results were correlated to the Jiang and Sehitoglu plasticity model [78], and it was found that these two models were not consistent in modeling the softening behavior of Mg.

Later, Albinmousa delivered a study on the effect of multiaxial loading on LCF behavior of AZ31 extrusion [70]. As far as LCF, it was found that phase angle causes additional hardening stemming from dislocation-dislocation interactions; they are forced to move along all possible slip planes [74]. Interestingly, this additional hardening was shown to have no noticeable effect on fatigue life in LCF regime. The total strain energies for the tests were calculated and there was almost no considerable difference between them. In addition, fatigue

life prediction was achieved in this study based on strain- and energy-based models. It was shown that in general all the Fatemi-Socie, SWT, and Jahed-Varvani models were addressing the fatigue life within ±2 scatter bands; however, when the strain-based models were not capable of predicting life when the critical plane was supposed to be the plane of crack propagation observed under optical microscopy. On the hand, the result of energy-based model still was satisfactory, for the total energy damage parameter was not zero owing to including positive elastic shear strain energy and the total axial strain energy densities.

Finally in 2014, Jahed and Albinmousa [71] delivered a study on the multiaxial behavior of wrought magnesium alloys, in particular AZ-, AM-, and ZK-series, where they did a comprehensive review on the existing literature. They discussed the sustainability of a two-parameter energy-based model (Jahed-Varvani model) and manifested that the model was capable of correlating a total of 354 data points obtained from testing specimens at various loading conditions and loading orientations in a single scatter band. These conditions were: axial, shear, axial with mean strain or mean stress, stress and strain controlled, and multiaxial loadings.

Recently, Li et al. [79] investigated the multiaxial behavior of AZ31 extrusion under both strain- and stress controlled tests. Therefore, the phenomenon of ratcheting was also studied besides the previous aspects of research. Experiments showed that the multiaxial ratcheting of AZ31 depends on the shape of loading path and also the applied axial mean stress.

Energy-based models and in particular, the Jahed-Varvani model, have shown their merits in predicating multiaxial fatigue behavior of other wrought Mg alloys as well. Roostaei and Jahed [81] employed this model in predicting multiaxial fatigue life of AM30 extrusion successfully. Also, Gryguc et al. [82] assessed this model's capability in predicting the multiaxial cyclic lives of extruded and forged AZ80 Mg alloy, and the results were satisfactory.

Lastly, Castro and Jiang [80] conveyed a new research on the multiaxial fatigue behavior of AZ31 where they evaluated capability of different fatigue models to predict the life and crack behavior. The SWT failed to predict the fatigue life accurately, while Fatemi-Socie criterion could estimate the fatigue lives well for all the experiments; however, it led to

an unacceptable prediction regarding the crack behavior. Jiang's energy-based model was assessed, and this model predicted both the fatigue life and crack behavior satisfactorily.

It's noteworthy that quantities such as plastic strain, or plastic strain energy incorporated in the fatigue modeling of magnesium alloys require a proper cyclic plasticity model when experiments are not available, especially for multiaxial fatigue. There are only few cyclic plasticity models available for wrought magnesium alloys [93]–[97]. In particular, approximate methods which does not need high-end computations are of great interests [98][99].

As a matter of fact, most studies are dedicated to multiaxial fatigue behavior of AZ31 extrusion. To the author's knowledge, there is no study in the literature on the fatigue behavior of forged magnesium alloy, in particular forge ZK60, under multiaxial loading. Therefore, one of the objectives of this study is to characterize the multiaxial fatigue behavior of this alloy by carrying out various proportional and non-proportional fully reversed strain controlled multiaxial cyclic experiments.

Chapter 3
Methodology

3.1 Introduction

The methodology and experimental details surrounding each chapter of this research work are discussed in the corresponding chapters separately. However, in this chapter, all the details pertaining to the delivered experimental campaign is described together for the convenience of readers. In particular, the forging process, i.e., how the starting materials were thermomechanically processed into variant shapes, is discussed. Also, the details of specimen design and the measurement techniques adopted to fulfill the characterization objectives of this research are presented.

3.2 Material processing and forging

This is a pioneering comprehensive work in developing scientific knowledge regarding the forging of ZK60 Mg alloys and investigating its forging process window. In fact, prior to this research, there existed limited studies pertaining to the forging of Mg alloys. However, their focus was on the applications of forging rather than the effects of forging on the mechanical behavior of Mg alloys. To fill this gap of knowledge, open- and closed-die forging was conducted on as-cast and extrusion billets, and various mechanical tests were performed to characterize the material's behavior before and after forging.

ZK60 cast ingots with the diameter of 300 mm and length of 500 mm was machined to a diameter of 63.5 mm and a length of 200 mm. Then, three billets with a length of 65 mm were machined out of each sample. The upsetting process were conducted isothermally at two different temperatures of 350 °C and 450 °C along the radial direction at a ram speed of 39 mm/min. A graphite lubricant was used to reduce the friction between the materials and the platform. Forging at the lower temperature of 350 °C was not successful, as the sample revealed significant cracks. However, the material forged at 450 °C was crack-free. It was expected that during the slow heating of the billet up to 450 °C, the eutectic phase would be

dissolved into the Mg matrix, which could have led to a better forging response of ZK60 at 450 °C. A schematic of this forging process is presented in Figure 13.

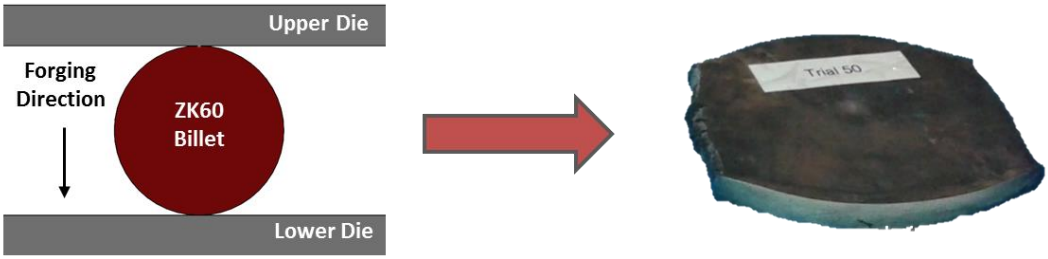

Figure 13. Schematic representation of open-die forging of ZK60 cast billet and the final product

This study employed ZK60 extrusion at its final step to investigate the effects of closed-die forging on the mechanical behavior of the material. The extrusion material was a cylinder with the diameter of 127 mm and length of 400 mm, supplied by Luxfer MEL Technologies. Also, the starting material for the forged alloy was supplied by the same company in the form of cylindrical billets with 300 mm diameter, which were subsequently cut into smaller billets of 65 mm in length and 63.5 mm in diameter. The billets were heated for 3 hours in a furnace to various temperatures between 250° C and 375° C. Then, the billets were placed in a hydraulic press, and isothermally pressed into an I-beam [100] at the ram speed of 20 mm/sec in a single step. Graphite was again the employed lubricant to reduce the friction during the process. Eventually, the forged samples were air-cooled to the room temperature. Figure 14 schematically shows the configuration of the forging dies and the billet, as well as the final forged part.

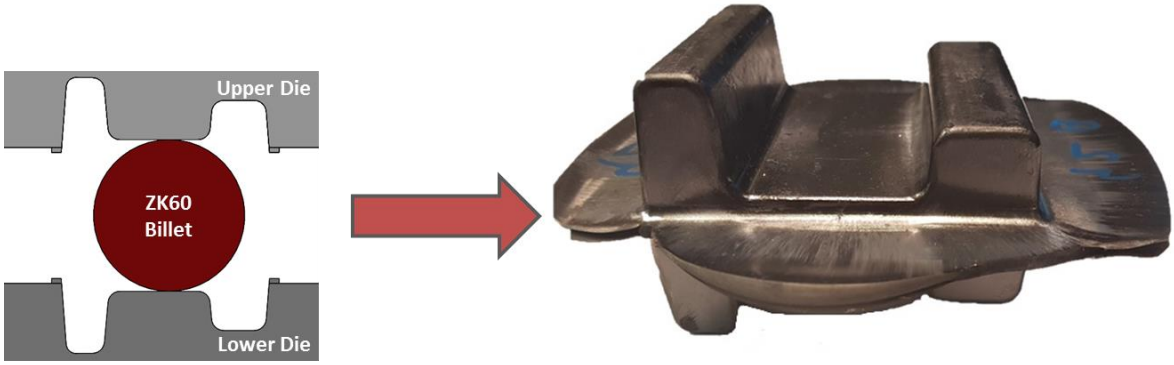

Figure 14. Schematic representation of closed-die forging of ZK60 extrusion billet and the final product

3.3 Specimen geometries and preparations

Dog-bone flat samples for quasi-static tension and cyclic tests and cubic samples for quasi-static compression tests were extracted out of the materials. Moreover, to perform pure shear and multiaxial tests, thin-walled tubular samples with the geometry in accordance with the ASTM E2207 standard [101] were machined out of the as-extruded cylinder billet and closed-die I-beams along the longitudinal direction. Thin-wall samples are employed in these particular tests to ensure the validity of the uniformly distributed shear stress assumption. Also, it is noteworthy that in general, the properties of the samples might be sensitive to the location and orientation of where samples were extracted in the light of thermo-mechanical history of the samples. For instance, in the case of ZK60 extrusion, it is believed that due to the inhomogeneous thermal filed in the material during the extrusion process, the mechanical properties vary radially. Hence, efforts were taken to machine the samples at locations with similar radial distance from the center of the billet. Moreover, the samples were extracted at rational distance from the edges to avoid the edge effects. Lastly, according to the ASTM standard and to reduce the risk of premature failure due to the rough surface, a nominal surface finish of $Ra \leq 0.2\mu m$ was considered for all samples. A summary of sample geometries is illustrated in Figure 15. Also, Figure 16 depicts the location of samples in each sample.

(a) Cubic compression sample:

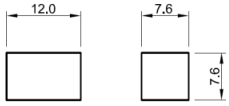

(b) Dog bone tension sample:

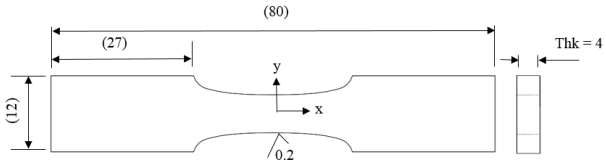

Notes:

1. All dimensions are in millimeters (mm) except the surface roughness, which is in micrometers (μm).
2. Axes x and y are axes of symmetry.

x (mm)	y (mm)	x (mm)	y (mm)
0.00	3.00	7.64	3.37
0.68	3.00	8.38	3.49
1.37	3.00	9.14	3.63
2.05	3.01	9.93	3.82
2.74	3.03	10.69	4.05
3.42	3.04	11.36	4.37
4.11	3.07	11.77	4.71
4.80	3.11	12.01	4.98
5.50	3.15	12.25	5.34
6.20	3.20	12.52	6.00
6.91	3.28	40.00	6.00

(c)

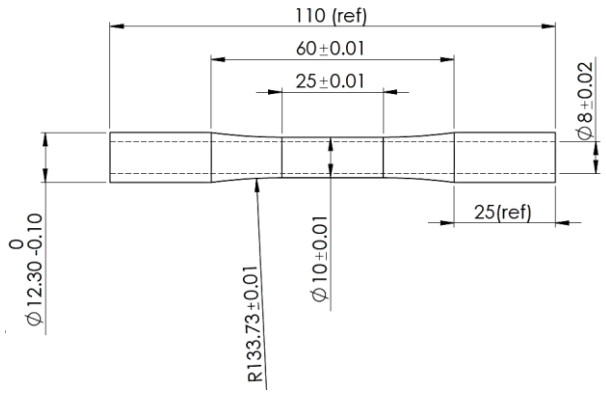

Figure 15. (a) Axial compressive sample; (b) dog-bone samples for axial tensile and cyclic tests; (c) Thin-wall tubular samples for quasi-static and cyclic pure shear, and multiaxial tests

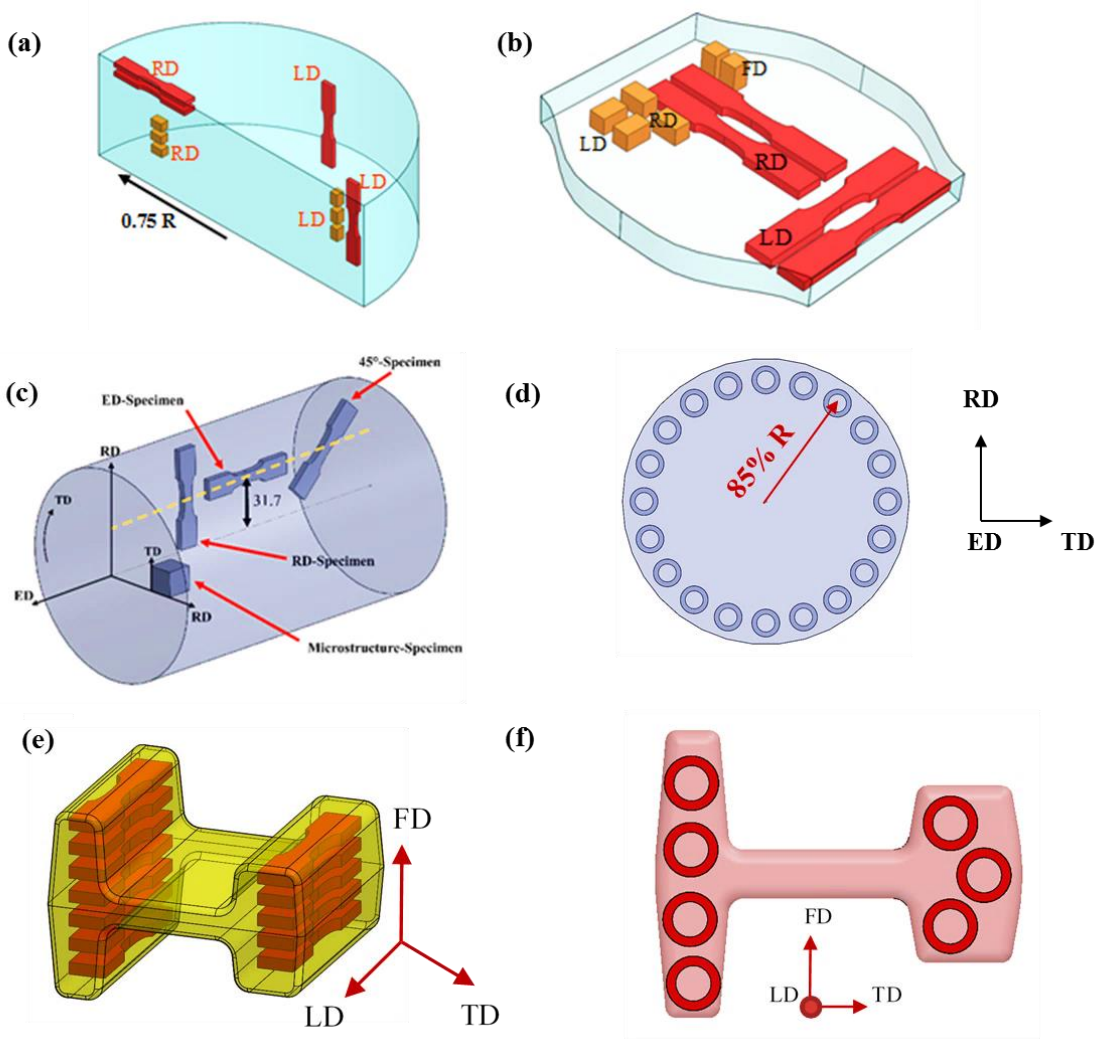

Figure 16. Dog-bone and cubic sample locations in as-cast billet (a), open-die forged sample (b), as-extruded billet (c), and closed-die forged sample (e), and thin-wall tubular samples in ZK60 extrusion (d) and ZK60 extrusion-forge (f)

3.4 Mechanical testing; test apparatus and procedure

All quasi-static tension tests were performed under standard laboratory conditions in displacement-controlled mode using an Instron 8874 servo-hydraulic frame having a capacity of ±25 kN. Compression tests were also performed at room temperature in the same controlling mode as tension testing utilizing MTS 810 machine with a load capacity of ±50 kN. The crosshead speed for both the tension and compression tests was 1 mm/min. Strain was

measured using the ARAMIS 3D Digital Image Correlation (DIC) system with 5-megapixel resolution and a frame rate of 15 fps.

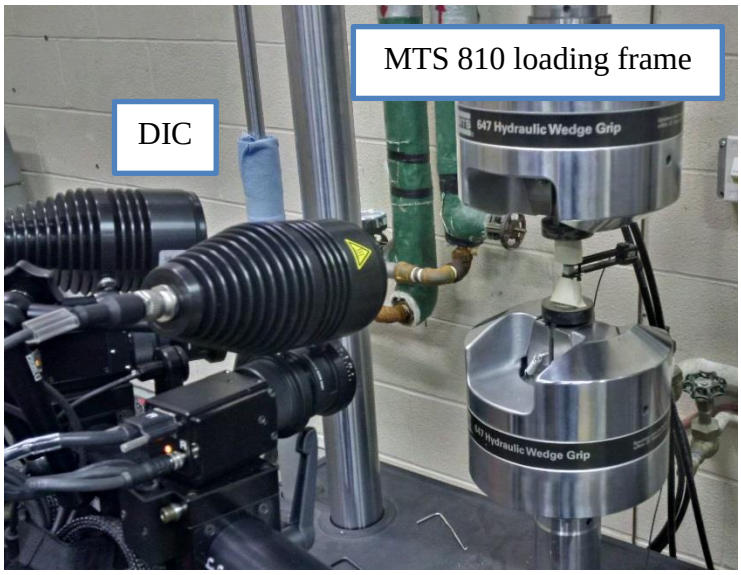

Figure 17. ARAMIS 3D 5MP DIC system

Fatigue tests were carried out under standard laboratory conditions, as per ASTM E606/E6060M-12 standard, using the same Instron 8874 servo-hydraulic frame in strain-controlled mode under fully reversed condition. Strain was controlled using a uniaxial epsilon extensometer with a gauge length of 8 mm and travel distance of ±0.8 mm. The loading frequency was selected between 0.2 and 1 Hz to achieve the same strain rate of 10^{-2} sec^{-1} throughout the fatigue tests. The material's behavior was called stable once changes in tensile and compressive peak loads were not more than 5% in consecutive 500 cycles. Tests would be continued under load-controlled mode after stabilization at a higher frequency of up to 30 Hz and continued up to failure or 10^7 cycles, whichever occurred first. Tests with no failure at 10^7 cycles were stopped and considered as run-out tests. Final failure was taken to be either the final rupture, or 50% drop in the maximum load, whichever came first. Each test was at least duplicated once to ensure the repeatability of the results. The number of test specimens and percent replication was based on ASTM E739-10 standard.

Fully reversed cyclic pure shear tests as well as proportional, 45° and 90° out-of-phase multiaxial experiments were conducted on the same Instron loading frame having axial and

torsional load capacities of ±25 kN and ±100 N.m, respectively, under the standard laboratory conditions. Axial and shear strains were controlled for all the fatigue tests. Strain was being measured using an epsilon biaxial extensometer with the axial and shear strain travels of ±5% and ±1.5°. The frequency during the tests were in the range of 0.1-0.5 Hz, depending on the applied strain amplitude. Higher frequencies were applied for the tests at lower strain amplitudes which exhibit longer fatigue lives. At very small strain amplitudes during the pure shear tests, material's behavior was assumed to be stable should that neither of axial loadings nor torsional loadings change by 5% in 500 cycles. Once the material's behavior was stabilized, the test mode was shifted to the load-controlled, and at higher frequencies up to 10 Hz. The failure criterion was assumed to be either the final rupture, or 50% drop in the maximum load, whichever came first. Moreover, each test was at least once duplicated to verify the reproducibility of the results. Figure 18 delineates the test setup for pure shear and multiaxial loading tests.

Figure 18. Bi-axial test setup, showing the frame and bi-axial extensometer

3.5 Microstructure and texture

For microstructure and texture analysis, the samples were collected from the same locations that samples were machined for the mechanical tests. The samples for microstructural and texture analyses were prepared using up to 1200-grit SiC sandpaper. Samples were then polished with 6-, 3-, 1-, and 0.1-micron diamond pastes with oil-based lubricant on the imperial cloth. Finally, the samples were polished using colloidal silica on the black CHEM pad. An etchant with a chemical composition of 4.2 gr picric acid, 70ml ethanol, 10 ml acetic acid, and 10 ml distilled water was used to etch the sample. The microstructure was examined in unetched and etched conditions using an optical microscope (OM) and a scanning electron microscope (SEM), coupled with energy-dispersive X-ray spectroscopy (EDX). The present phases in the as-cast alloy were identified using Bruker D8-discover equipped with advanced 2D-detector and CuKα1 radiation of X-ray diffractometer (XRD). To collect the diffraction patterns, the following parameters were used: accelerating voltage of 40 kV, current of 40 mA, step size of 15°, and scanned speed of 60s for each step of the 2θ angle, from 25°–95°. The collected diffraction patterns were evaluated using Bruker trademark software "DIFFRAC.EVA".

Figure 19. Bruker D8-Discover XRD machine

Texture measurements were performed using the same XRD machine on polished samples. The experiment was conducted by measuring the incomplete pole figures (PFs) of {0001}, $\{10\bar{1}0\}$, $\{10\bar{1}1\}$, and $\{1\bar{1}02\}$ for tilt angle (Ψ) between 0 ° and 75 °, with a step of 15°, and in axis rotation (Φ) from 0 ° to 360 °, with a step size of 5° in the back-reflection mode. Finally, the complete PFs were calculated based on the measured incomplete PFs using DIFFRAC.Suite: Texture software.

EBSD measurement was delivered on samples failed under quasi-static shear loading in the CanmetMATERIAL center in Hamilton, Canada, using an EDAX EBSD detector, mounted to an FEI NovaSEM-650 (FEG-SEM), at an operating voltage of 20 kV. The step size for the measurement was chosen to be 0.35 µm. The step size was chosen such that a minimum of 25 measurements were done per grain, considering a minimum grain size of 2 µm. The data was post processed using TSL OIM 8.0 software. The data was initially filtered using the grain dilation approach. An orientation difference of 10 degrees or more between adjacent pixels was used to create grain boundaries. For the sake of sample preparation, samples were polished till 3µm diamond paste and then polished with oxide polishing suspensions (OPS) for improving the polishing results. Subsequently, the samples were chemically polished in a 5% Nital solution for 30 seconds. Further details regarding the EBSD setup and data processing can be found in [102].

An overall matrix for all tests performed in this study are depicted in the following tables:

Table 1. Test Matrix for ZK60 cast

As-Cast			
Sample #	**ε_a (%)**	**Orientation**	**Test type**
1	-	-	Texture
2	-	-	Microstrcture
3	-	LD	Tensile Static
4	-	LD	Tensile Static

5	-	LD	Tensile Static
6	-	RD	Tensile Static
7	-	RD	Tensile Static
8	-	RD	Tensile Static
9	-	LD	Compressive Static
10	-	LD	Compressive Static
11	-	LD	Compressive Static
12	-	RD	Compressive Static
13	-	RD	Compressive Static
14	-	RD	Compressive Static
15	-	ND	Compressive Static
16	-	ND	Compressive Static
17	-	ND	Compressive Static
18	0.15	LD	Fatigue
19	0.175	LD	Fatigue
20	0.2	LD	Fatigue
21	0.2	LD	Fatigue
22	0.3	LD	Fatigue
23	0.3	LD	Fatigue
24	0.4	LD	Fatigue
25	0.4	LD	Fatigue
26	0.5	LD	Fatigue
27	0.5	LD	Fatigue
28	0.6	LD	Fatigue
29	0.6	LD	Fatigue
30	0.7	LD	Fatigue
31	0.7	LD	Fatigue
32	0.8	LD	Fatigue
33	0.8	LD	Fatigue
34	0.9	LD	Fatigue
35	0.9	LD	Fatigue

Table 2. Test Matrix for ZK60 cast-forge

Cast-Forged			
Sample #	**ε_a (%)**	**Orientation**	**Test**
1	-	-	Texture
2	-	-	Microstrcture
3	-	LD	Tensile Static
4	-	LD	Tensile Static
5	-	LD	Tensile Static
6	-	RD	Tensile Static
7	-	RD	Tensile Static
8	-	RD	Tensile Static
9	-	LD	Compressive Static
10	-	LD	Compressive Static
11	-	LD	Compressive Static
12	-	RD	Compressive Static
13	-	RD	Compressive Static
14	-	RD	Compressive Static
15	-	ND	Compressive Static
16	-	ND	Compressive Static
17	-	ND	Compressive Static
18	0.2	LD	Uniaxial Fatigue
19	0.22	LD	Uniaxial Fatigue
20	0.25	LD	Uniaxial Fatigue
21	0.25	LD	Uniaxial Fatigue
22	0.3	LD	Uniaxial Fatigue
23	0.3	LD	Uniaxial Fatigue
24	0.4	LD	Uniaxial Fatigue
25	0.4	LD	Uniaxial Fatigue
26	0.5	LD	Uniaxial Fatigue
27	0.5	LD	Uniaxial Fatigue
28	0.7	LD	Uniaxial Fatigue
29	0.7	LD	Uniaxial Fatigue

30	0.9	LD	Uniaxial Fatigue
31	0.9	LD	Uniaxial Fatigue

Table 3. Test Matrix for ZK60 extrusion

Extrusion				
ε_a (%)	**γ_a (%)**	**Orientation**	**Phase angle**	**Test**
-	-	-	-	Texture
-	-	-	-	Microstrcture
-	-	ED	-	Tensile Static
-	-	RD	-	Tensile Static
-	-	45	-	Tensile Static
-	-	ED	-	Compressive Static
-	-	RD	-	Compressive Static
-	-	46	-	Compressive Static
-	-	ED	-	Torsional Static
0.3	-	ED	-	Uni-axial Fatigue
0.4	-	ED	-	Uni-axial Fatigue
0.5	-	ED	-	Uni-axial Fatigue
0.6	-	ED	-	Uni-axial Fatigue
0.7	-	ED	-	Uni-axial Fatigue
0.8	-	ED	-	Uni-axial Fatigue
0.9	-	ED	-	Uni-axial Fatigue
1.0	-	ED	-	Uni-axial Fatigue
1.6	-	ED	-	Uni-axial Fatigue
2.0	-	ED	-	Uni-axial Fatigue
0.2	-	RD	-	Uni-axial Fatigue
0.25	-	RD	-	Uni-axial Fatigue
0.3	-	RD	-	Uni-axial Fatigue
0.4	-	RD	-	Uni-axial Fatigue
0.5	-	RD	-	Uni-axial Fatigue
0.6	-	RD	-	Uni-axial Fatigue
0.7	-	RD	-	Uni-axial Fatigue
0.8	-	RD	-	Uni-axial Fatigue

0.9	-	RD	-	Uni-axial Fatigue
1.0	-	RD	-	Uni-axial Fatigue
1.6	-	RD	-	Uni-axial Fatigue
2.0	-	RD	-	Uni-axial Fatigue
0.3	-	45	-	Uni-axial Fatigue
0.5	-	45	-	Uni-axial Fatigue
1.0	-	45	-	Uni-axial Fatigue
2.0	-	45	-	Uni-axial Fatigue
0.4	-	ED	-	Pure Shear Fatigue
0.4	-	ED	-	Pure Shear Fatigue
0.5	-	ED	-	Pure Shear Fatigue
0.5	-	ED	-	Pure Shear Fatigue
0.7	-	ED	-	Pure Shear Fatigue
0.7	-	ED	-	Pure Shear Fatigue
0.9	-	ED	-	Pure Shear Fatigue
0.9	-	ED	-	Pure Shear Fatigue
1.1	-	ED	-	Pure Shear Fatigue
1.1	-	ED	-	Pure Shear Fatigue
0.7	1.0	ED	0	Multiaxial Fatigue
0.3	0.5	ED	0	Multiaxial Fatigue
0.3	1.0	ED	0	Multiaxial Fatigue
0.6	1.0	ED	0	Multiaxial Fatigue
0.7	0.5	ED	0	Multiaxial Fatigue
0.7	0.5	ED	45	Multiaxial Fatigue
0.3	0.5	ED	45	Multiaxial Fatigue
0.3	1.0	ED	45	Multiaxial Fatigue
0.7	0.5	ED	90	Multiaxial Fatigue
0.3	0.5	ED	90	Multiaxial Fatigue
0.3	1.0	ED	90	Multiaxial Fatigue

Table 4. Test Matrix for ZK60 extrusion-forge

Closed-die forged				
ε_a (%)	**γ_a (%)**	**Location**	**Phase angle**	**Test**
-	-	-	-	Texture
-	-	-	-	Microstrcture
-	-	Long flange	-	Tensile Static
-	-	Short flange	-	Tensile Static
-	-	Web	-	Tensile Static
-	-	Long flange	-	Torsional Static
-	-	Short flange	-	Torsional Static
-	-	Web	-	Torsional Static
0.4	-	Flange	-	Uni-axial Fatigue
0.5	-	Flange	-	Uni-axial Fatigue
0.6	-	Flange	-	Uni-axial Fatigue
0.7	-	Flange	-	Uni-axial Fatigue
0.8	-	Flange	-	Uni-axial Fatigue
0.4	-	Flange	-	Pure Shear Fatigue
0.5	-	Flange	-	Pure Shear Fatigue
0.6	-	Flange	-	Pure Shear Fatigue
0.7	-	Flange	-	Pure Shear Fatigue
0.9	-	Flange	-	Pure Shear Fatigue
0.4	0.5	Flange	0	Multiaxial Fatigue
0.7	0.5	Flange	0	Multiaxial Fatigue
0.4	0.5	Flange	45	Multiaxial Fatigue
0.7	0.5	Flange	45	Multiaxial Fatigue
0.4	0.5	Flange	90	Multiaxial Fatigue
0.7	0.5	Flange	90	Multiaxial Fatigue

Chapter 4

Microstructure, Texture, and Mechanical Behavior Characterization of Hot Forged Cast ZK60 Magnesium Alloy

4.1 Introduction

Concerns over the environmental impacts of fossil fuels have led to the development of aggressive fuel efficiency targets. An effective way to increase fuel efficiency is to decrease vehicle weight by utilizing lightweight metallic materials like magnesium (Mg) and its alloys, which have superb specific strength, good cast-ability, and excellent damping capacity [9], [103], [104]. To date, the use of Mg for automotive applications has mainly been limited to trimming and non-structural members. Expanding the use of Mg to load-bearing components with complex shapes requires a thorough understanding of Mg behavior after manufacturing.

Journal of Materials Science & Technology 33 (2017) 907–918

Contents lists available at ScienceDirect

Journal of Materials Science & Technology

journal homepage: www.jmst.org

Microstructure, texture and mechanical behavior characterization of hot forged cast ZK60 magnesium alloy

S.M.H. Karparvarfard [a], S.K. Shaha [a,*], S.B. Behravesh [a], H. Jahed [a,*], B.W. Williams [b]

[a] Department of Mechanical & Mechatronics Engineering, University of Waterloo, 200 University Ave W, Waterloo, ON N2L 3G1, Canada
[b] CanmetMATERIALS, Natural Resources Canada, 183 Longwood Road South, Hamilton, ON L8P 0A1, Canada

ARTICLE INFO

Article history:
Received 20 October 2016
Received in revised form 31 January 2017
Accepted 31 January 2017
Available online 14 April 2017

Keywords:
Magnesium
Forging
Ductility
Texture
Recrystallization

ABSTRACT

Uniaxial tension and compression tests were conducted to investigate the quasi-static performance of ZK60 Mg alloy in cast, followed by forging at optimum temperature of 450 °C and a ram speed of 39 mm min^{-1}. Microstructure and texture analysis showed that the as-cast alloy exhibited a dendritic structure with casting porosity and random texture. In contrast, the forged alloy exhibited a refined grain structure with a significant reduction in casting porosity, while the texture changed to sharp basal texture. Measured mechanical properties of the forged alloy showed that strength did not change, however, ductility improved by 75%. The analysis of the fracture surface of the forged alloy under tension revealed a ductile fracture with dimple morphology, while the as-cast alloy displayed a brittle fracture with open pores. This demonstrated that the reduction of casting defects and dendritic morphology, as well as the evolution of recrystallized grains, enhanced ductility, while partial dynamic recrystallization through the forging process resulted in only marginal modification of strength in the forged condition.

1. Introduction

Concerns over the environmental impacts of fossil fuels have led to the development of aggressive fuel efficiency targets. An effective way to increase fuel efficiency is to decrease vehicle weight by utilizing lightweight metallic materials like magnesium (Mg) and its alloys, which have superb specific strength, good cast-ability, and excellent damping capacity [1–3]. To date, the use of Mg for automotive applications has mainly been limited to trimming and non-structural members. Expanding the use of Mg to load-bearing components with complex shapes requires a thorough understanding of Mg behaviour after manufacturing.

Mg has a hexagonal closed-pack (hcp) crystal structure with $c/a < \sqrt{3}$, which translates to limited formability at lower temperatures, preventing its widespread use for industrial applications. According to the von Mises criterion, five independent deformation modes are required to accommodate induced strains during homogenous deformation of a polycrystalline material. At lower temperatures, basal, prismatic, and pyramidal slip planes are active, but the lower strength required for basal slip will result in the formation of a strong basal texture during deformation [4,5]. If basal slip is hindered, twinning systems can be activated at lower temperatures. Additional slip systems are activated at elevated temperatures, which improves formability, but lowers the strength of deformation [6,7].

The leading manufacturing process (~90%) of Mg alloy parts is die casting. However, the occurrence of casting defects like porosities, dry oxides, and inclusions, limits alloys strength and thus the suitability of Mg alloys in the as-cast state for industrial applications [8]. Studies have shown that Mg alloys in wrought conditions exhibit refined grains [9,10], better tensile properties, such as strength and deformability [11,12], improved fracture toughness [12], and longer fatigue life [13,14], which expands the opportunities for the use of Mg alloys as structural materials. Extrusion, which forms strong basal texture and bimodal grains, is a common material processing technique for wrought Mg alloys [12–18]. Recently, equal channel angular pressing (ECAP), which causes severe plastic deformation (SPD), has been employed for processing Mg alloys. ECAP refines microstructures and weakens texture of Mg alloys [19,20]. However, these processes cannot be used for manufacturing complex parts. Forging is an efficient technique, in which structural parts are produced in a near net shape [21]. Because of its promise as an effective manufacturing method for Mg alloy microstructure refinement and mechanical property improvement,

* Corresponding authors.
E-mail addresses: skumarsh@uwaterloo.ca (S.K. Shaha), hjahedmotlagh@uwaterloo.ca (H. Jahed).

Figure 20. SMH. Karparvarfard et al., "Microstructure, texture and mechanical behavior characterization of hot forged cast ZK60 magnesium alloy", Journal of Materials Science & Technology, 33(9) (2017): 907-918

Magnesium has a hexagonal closed-pack (hcp) crystal structure with $c/a < \sqrt{3}$, which translates to limited formability at lower temperatures, preventing its widespread use for industrial applications. According to the von Mises criterion, five independent deformation modes are required to accommodate

induced strains during homogenous deformation for a polycrystalline material. At lower temperatures, basal, prismatic, and pyramidal slip planes are active, but the lower strength required for basal slip will almost always result in the formation of a strong basal texture during deformation [105], [106]. If basal slip is hindered, then twinning systems can be activated at lower temperature. Additional slip systems are activated at elevated temperatures, which improves formability [27], [28].

The leading manufacturing process (~90%) of Mg alloy parts is die casting. However, the occurrence of casting defects like porosities, dry oxides, and inclusions limits the alloy's strength and thus the suitability of Mg alloys in the as-cast state for industrial applications [15]. Studies have shown that Mg alloys in wrought conditions exhibit refined grains [19], [107], better tensile properties like strength and deformability [108][48], improved fracture toughness [48], and longer fatigue life [18], [46], which expand the opportunities for the use of Mg alloys as structural materials. Extrusion, which forms strong basal texture and bimodal grains, is a common material processing technique for wrought Mg alloys [12-18]. Recently, equal channel angular pressing (ECAP), which causes severe plastic deformation (SPD), has been employed for processing Mg alloys. ECAP refines microstructure and weakens the texture of the Mg alloys [49][109]. However, these processes cannot be used for manufacturing complex parts. Forging is an efficient technique, in which the structural parts are produced in a near net shape [110]. Because of its promise as an effective manufacturing method for Mg alloy's microstructure refinement and mechanical property improvement, forging is currently of significant interest for industrial applications [50][51].

In general, the Mg ZK series, and ZK60 in particular, have good formability [29], [30]. They also have good strength due to precipitations and grain refining effects of Zr [31], [32]. ZK60 is the forgeable Mg alloy. The effects of microstructure and texture on the mechanical properties of extruded, rolled, and ECAPed ZK60 have been reported extensively in the literature [108], [111]–[113]. Findings of these studies demonstrate that the mechanical properties, especially the ductility, which controls the formability of the ZK60 Mg alloy, improve significantly as a result of the presence of fine grain structures and the modification of the texture of as-cast materials. The texture evolution of as-extruded ZK60 following equal

channel angular extrusion (ECAE) has been studied by Agnew et al. [34]. They observed that while AZ-series Mg alloys pretend to accommodate both $\langle a \rangle$ and $\langle c + a \rangle$ non-basal slips, ZK-series Mg alloys prefer non-basal $\langle c + a \rangle$ slip systems. Multi-steps processing (MSP) or Multi-directional forging (MDF) is becoming a popular material processing technique to enhance the mechanical properties of Mg alloys. The MDF or MSP has been employed on Mg alloys after casting, extrusion, and rolling for refining the microstructure and texture, which leads to the improved tensile and fatigue properties. Wu et al. [52] studied the effect of high strain rate multiple forging (HSRMF) on commercial semi-continuous casting ZK60 Mg alloy. They reported that during MDF, twins are induced, and rotational dynamic recrystallization occurs, which forms honeycomb-like coarse and island-like ultrafine dynamic recrystallized (DRX) grains, resulting in improved ductility and tensile strength. Other studies on the MDF of ZK60 Mg alloys in extruded condition demonstrated the formation of a bimodal microstructure containing about 80% recrystallized fine grains (3–6 μm) with elongated grains (~1 mm long and ~50 μm thick) [55], which significantly improved the ductility and tensile strength [54], and led to the improvement of low cycle and high cycle fatigue properties [53][56]. More recently, researchers achieved superior ductility and strength for ZK60 Mg alloy sheets by a combination of repeated upsetting and forward extrusion [114].

Most of the machine parts in manufacturing industries are forged in one pass instead of multiple passes. However, forging as a manufacturing technique has received less attention than other techniques such as die casting, rolling, and extrusion. Ogawa et al. [59] investigated the appropriate temperature range for precision forging of ZK60, through the upset-ability test and backward extrusion. They reported that at forming temperatures below 200 °C, cracks occurred, resulting in a height reduction of 39% during the upset-ability test. At deforming temperatures between 250 °C and 400 °C, the Mg billet had excellent workability and backward extrusion capability. It was also observed that deformation temperatures should not exceed 400 °C to avoid severe oxidation, which significantly increases friction. Matsumoto and Osakada [60] suggested keeping the billet in a non-oxidizing atmosphere, or riding off the oxide layer by applying lubricant on both the tools and billet to reduce friction during forging at temperatures of 200–400 °C [61]. Kwon et al. [62] investigated the forgeability of Mg alloys

in terms of forging temperature, speed, and grain size. They demonstrated that forging speed is more important than temperature, and finer grains are required for the successful forging of Mg alloys [62]. Researchers have also demonstrated that the tensile strength of forged ZK60 decreases with increasing the forging temperature, while the elongation increases significantly [63],[56] with temperature. However, most of the data presented in the literature are focused on the microstructural studies, followed by the tensile properties of the forged Mg alloys, while less attention has been devoted to the compression behavior of the cast and forged conditions. Moreover, the effect of tensile and/or compressive loading on the microstructure and the texture of as-cast and forged ZK60 Mg alloys has not been comprehensively investigated.

Therefore, the objective of this research was to characterize the microstructure, texture, and mechanical behavior of as-cast ZK60 before and after hot forging. Toward this goal, quasi-static tension and compression tests were carried out before and after forging, and the microstructure and texture were examined before and after the mechanical tests of both as-cast and forged ZK60 Mg alloy.

4.2 Experimental details

4.2.1 Forging of ZK60 Mg alloy

The starting material used in this investigation was a commercial ZK60 Mg alloy cast ingot (chemical composition is presented in Table 5), with a diameter of 300 mm and a length of 500 mm. The ingot was machined to a diameter of 63.5 mm and a length of 200 mm. Finally, each piece was cut into three billets, each with a length of 65 mm, for the forging. The as-cast ZK60 Mg alloy billet was heated over 3.5 hours in an oven at two different temperatures of 350 °C and 450 °C, then transferred to the forging anvil, which was also heated at the same temperatures. The upsetting was performed along the radial direction at a ram speed of 39 mm/min. To reduce the friction between the materials and the platform, a graphite lubricant was used, which also acted as a protective layer to prevent oxidation. Figure 21 shows the forged samples at different temperatures.

Table 5. Chemical composition of as-cast ZK60 Mg alloy (weight %)

Zn	Zr	Others	Mg
5.8	0.61	<0.30	Balance

A significant number of edge cracks were observed in the samples deformed at 350 °C, while the samples deformed at 450 °C were crack-free, with no prominent oxidation. An 80% height reduction was accommodated in the forging process. The lowest melting point of the eutectic phase for ZK60 Mg alloy has been reported to be 339.5 °C [115]. The volume fraction of the eutectic phase was below 3%, which was estimated using "Factsage" software. It was therefore expected that during the slow heating of the billet up to 450 °C for 3.5 hours, the eutectic phase would be dissolved into the Mg matrix, which could have led to a better forging response of ZK60 at 450 °C. Also, a recent study by Hadadzadeh et al. [116] on the same ZK60 cast alloy using a Gleeble® 3500 thermal-mechanical simulation testing system reported no incipient melting in the microstructures. Thus, the sample deformed at 450 °C was selected for further testing in this study.

(a) (b)

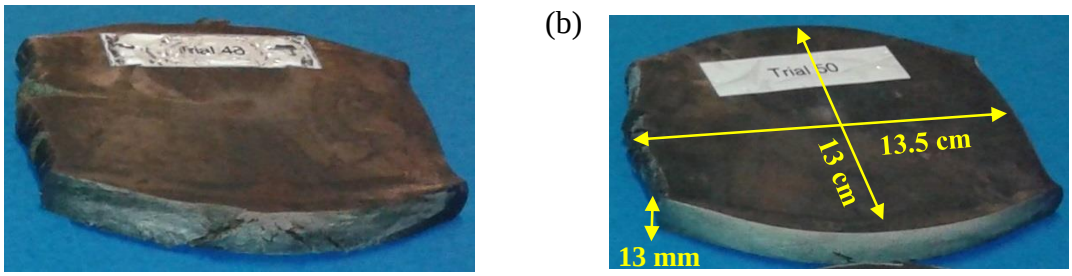

Figure 21. ZK60 sample geometries after forging at (a) 350° C and (b) 450° C. Note that lowering the deformation temperature causes severe edge cracks in the material, as seen in (a).

4.2.2 Microstructure and texture

For microstructure and texture analysis, the samples were collected from the as-cast billet and forged parts. To ensure consistency, all the test samples of the as-cast billet were collected at a distance equivalent to 75 % of the billet radius, and all the forged test samples were extracted from the middle portion of the forged part, away from the curved edges. The samples for microstructural and texture analyses were prepared using up to 1200-grit SiC

sandpaper. After that, the samples were polished with 6-, 3-, 1-, and 0.1-micron diamond pastes with oil-based lubricant on the imperial cloth. Finally, the samples were polished using colloidal silica on the black CHEM pad. An etchant with a chemical composition of 4.2 gr picric acid, 70ml ethanol, 10 ml acetic acid, and 10 ml distilled water was used to etch the sample. The microstructure was examined in unetched and etched conditions using an optical microscope (OM) and a scanning electron microscope (SEM), coupled with energy-dispersive X-ray spectroscopy (EDX). The present phases in the as-cast alloy were identified using Bruker D8-discover equipped with advanced 2D-detector and CuKα1 radiation of X-ray diffractometer (XRD). To collect the diffraction patterns, the following parameters were used: accelerating voltage of 40 kV, current of 40 mA, step size of 15°, and scanned speed of 60s for each step of the 2θ angle, from 25–95°. The collected diffraction patterns were evaluated using Bruker trademark software "DIFFRAC.EVA".

Texture measurements before and after forging tests were performed using the same XRD machine on polished samples. The experiment was conducted by measuring the incomplete pole figures (PFs) of {0001}, $\{10\bar{1}0\}$, $\{10\bar{1}1\}$, and $\{1\bar{1}02\}$ for tilt angle (Ψ) between 0 ° and 75 °, and in axis rotation (Φ) from 0 ° to 360 ° in the back-reflection mode. Finally, the complete PFs were calculated based on the measured incomplete PFs using DIFFRAC.Suite: Texture software.

4.2.3 Tension and compression properties

As illustrated in Figure 22 (a), dog-bone flat samples for tension and cubic samples for compression tests were extracted from as-cast material along the radial (RD) and longitudinal (LD) directions. Similar types of samples were cut from the forged material along different orientations, and were labeled as shown in Figure 22 (b). However, the compression test on the forged material was performed in LD, RD, and forging direction (FD). The dimensions of the tension and compression tests samples are given in Figure 23.

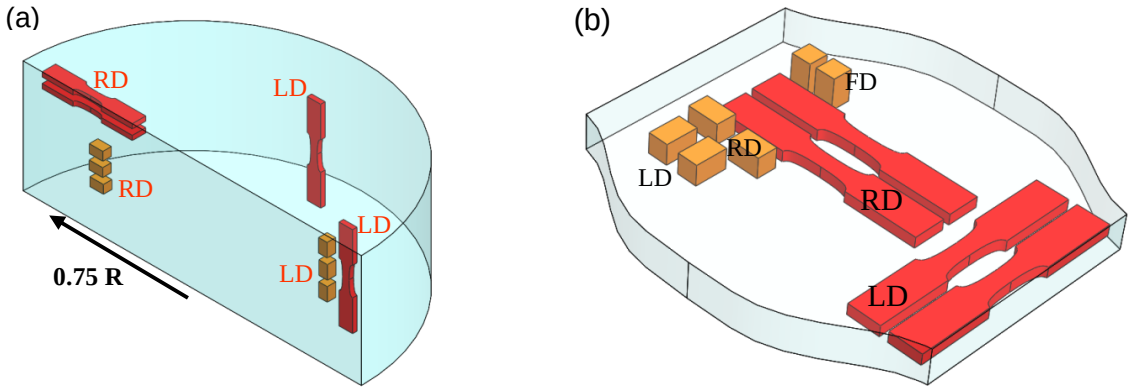

Figure 22. Specimen locations and direction convention; (a) as-cast, (b) forged ZK60 Mg alloy

All quasi-static tension tests were performed under standard laboratory conditions in displacement-controlled mode using an Instron 8874 servo-hydraulic frame having a capacity of ±25 kN. Compression tests were also performed at room temperature in the same controlling mode as tension testing-utilizing MTS 810 machine, with a load capacity of ±50 kN. The crosshead speed for both the tension and compression tests was 1 mm/min. Strain measurement for the tension specimens was performed using an extensometer with a gage length of 10 mm and $\pm$ 1.5 mm travel limits. For compression tests, strain was measured using the ARAMIS 3D Digital Image Correlation (DIC) system with 5-megapixel resolution and a frame rate of 15 fps. After testing, the fracture surfaces were examined by SEM. At least two samples were tested for each testing condition. Samples were also cut and polished along the loading axis to observe the microstructure and texture near the fracture surfaces.

(a) Cubic compression sample:

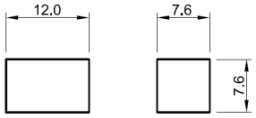

(b) Dog bone tension sample:

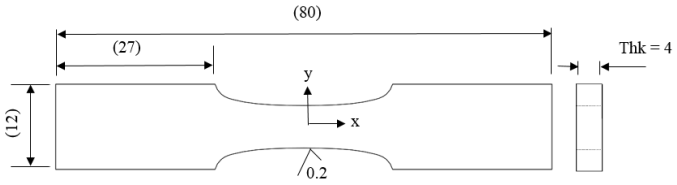

Notes:
1. All dimensions are in millimeters (mm) except the surface roughness, which is in micrometers (μm).
2. Axes x and y are axes of symmetry.

x (mm)	y (mm)	x (mm)	y (mm)
0.00	3.00	7.64	3.37
0.68	3.00	8.38	3.49
1.37	3.00	9.14	3.63
2.05	3.01	9.93	3.82
2.74	3.03	10.69	4.05
3.42	3.04	11.36	4.37
4.11	3.07	11.77	4.71
4.80	3.11	12.01	4.98
5.50	3.15	12.25	5.34
6.20	3.20	12.52	6.00
6.91	3.28	40.00	6.00

Figure 23. Typical specimen geometries for (a) compression tests and (b) tension tests

4.3 Results

4.3.1 Microstructure

Typical OM and SEM microstructures of the as-cast ZK60 Mg alloy in the unetched and etched conditions are shown in Figure 24. The presence of alloying elements in the intermetallics of the alloy is identified using an EDX line scan (Figure 24 (d) and (e)). As seen in Figure 24 (a), the microstructure exhibits casting porosities with intermetallics. A secondary dendritic arm spacing (SDAS) of 23.43±5.32 μm and a grain size of 131.44±25.84 μm was observed in as-cast materials in the etched condition (Figure 24 (b) and (c)).

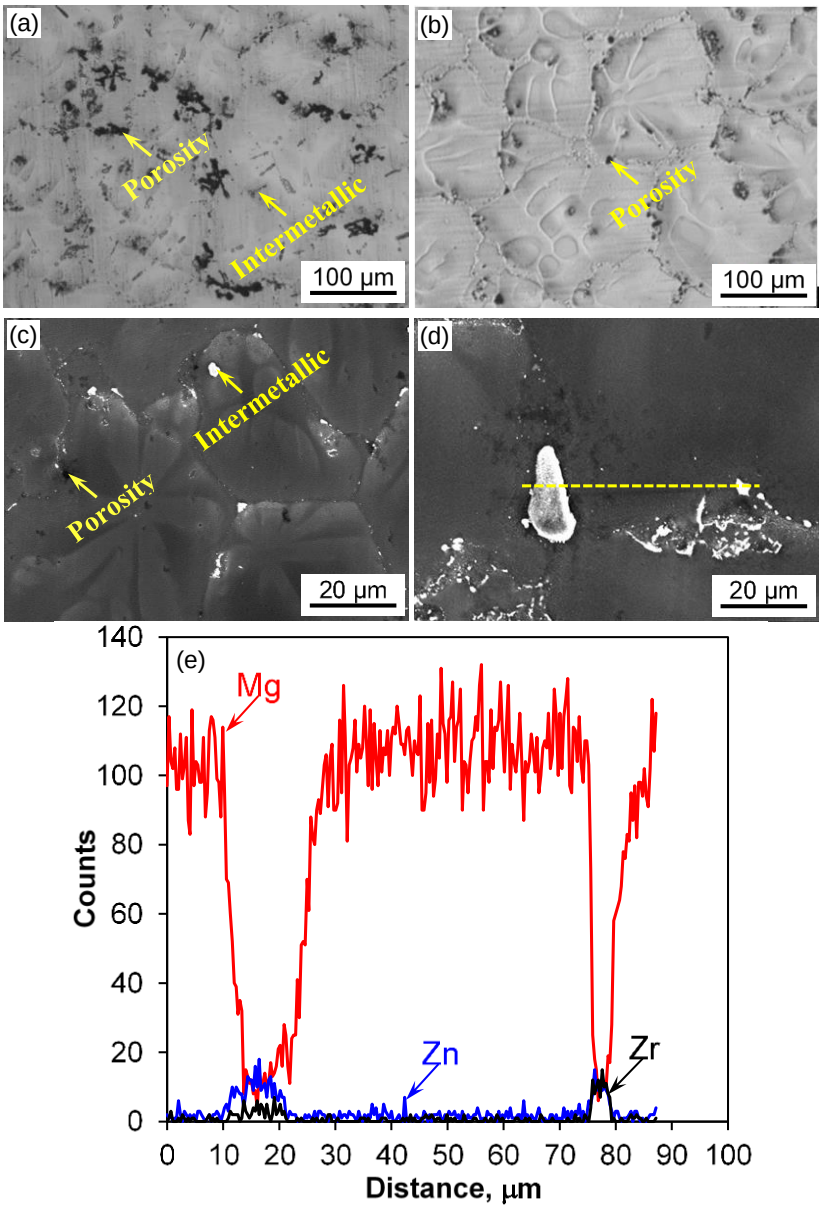

Figure 24. Typical OM (a, b) and SEM (c, d) microstructures of the as-cast ZK60 Mg-alloy in conjunction with EDX (e) line scans exhibiting the presence of intermetallics containing Zn and Zr. The microstructure was taken in (a) unetched and (b) etched conditions

The EDX point analysis revealed that the alloy microstructure consisted of α-Mg dendrites with two intermetallic phases: $MgZn_2$ and Zn_2Zr. The presence of phases in the as-cast alloy was confirmed by the XRD analysis, as illustrated in Figure 25. These intermetallics

were formed in the intergranular and interdendritic region during solidification of the alloy, as seen in Figure 24 (c). Similar types of intermetallics have been reported in the literature for the ZK60 Mg-alloy [115].

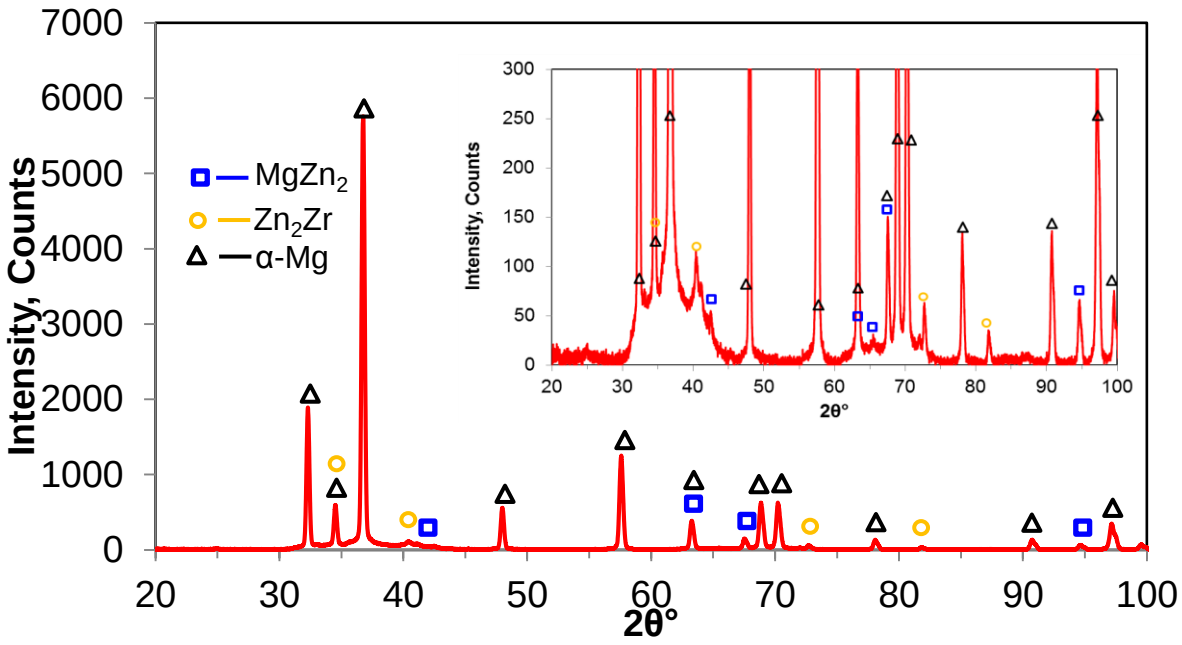

Figure 25. XRD patterns showing the phases present in the ZK60 Mg alloy in as-cast condition. The inserted graph is the magnified view of the y-axis

The microstructural analysis was performed for the forged sample as well. A modified microstructure of the forged ZK60 Mg alloy is shown in Figure 26. It can be seen that the porosity fraction has decreased significantly in the forged alloy (Figure 26 (a)). The forged microstructure in Figure 26 (b) exhibits bimodal grain structure: elongated pancaked type grains surrounded by fine grains (2–5 µm), which are more visible in the magnified image in Figure 26 (c). However, the dendritic marks (shown by the black arrow) are still visible. This could be due to an incomplete DRX during forging at higher temperatures. It has been reported that the presence of the Zr-rich phase in ZK60 Mg alloy causes a pinning effect, which hinders the movement of dislocations and prevents DRX, resulting in an incomplete grain refinement [117]. Similar types of grain structures with incomplete DRX, and a similar pinning effect of

Zr-rich precipitates during hot deformation of the ZK60 Mg alloy have been reported in [118], [119].

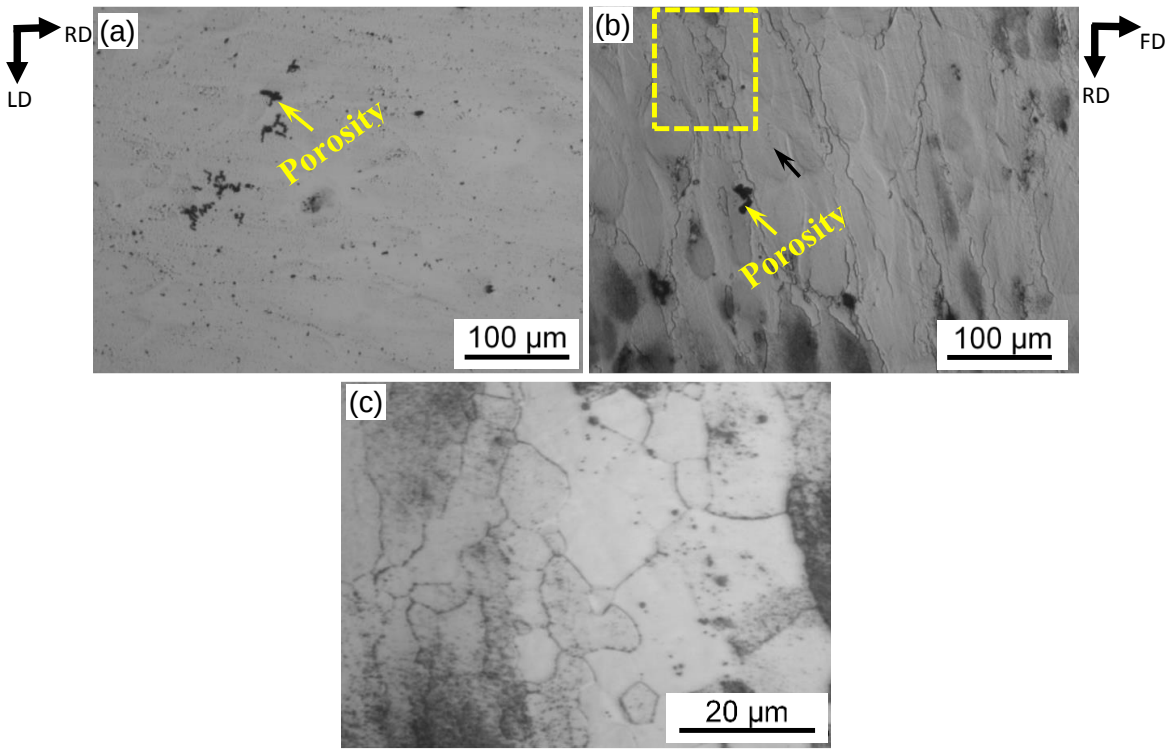

Figure 26. Typical OM microstructures of as-cast followed by forging ZK60 Mg-alloy in (a) unetched and (b, *c*) etched conditions. The location enclosed by yellow box is the magnified view illustrated in (c).

Note: LD-loading direction, FD-forging direction and RD-radial direction.

4.3.2 Texture analysis of cast and forged samples

The as-cast ZK60 Mg alloy, shown in Figure 27 (a), exhibited a random texture with a maximum intensity of 5.08 multiples of random distribution (MRD) in the basal plane of (0002), while the prismatic $(10\bar{1}0)$ poles reach an intensity of 3.46 MRD. Although the PFs show a strong pole density in the as-cast materials, there was no preferred orientation that can be considered as a texture in the material; i.e., the hcp unit cells are randomly distributed in the materials, as shown schematically in Figure 27 (a). In contrast, the forged material obtained a

strong basal texture with a maximum intensity of 5.70 and 2.21 MRD for the basal plane (0002) and the prismatic plane $(10\bar{1}0)$, respectively, depicted in Figure 27 (b).

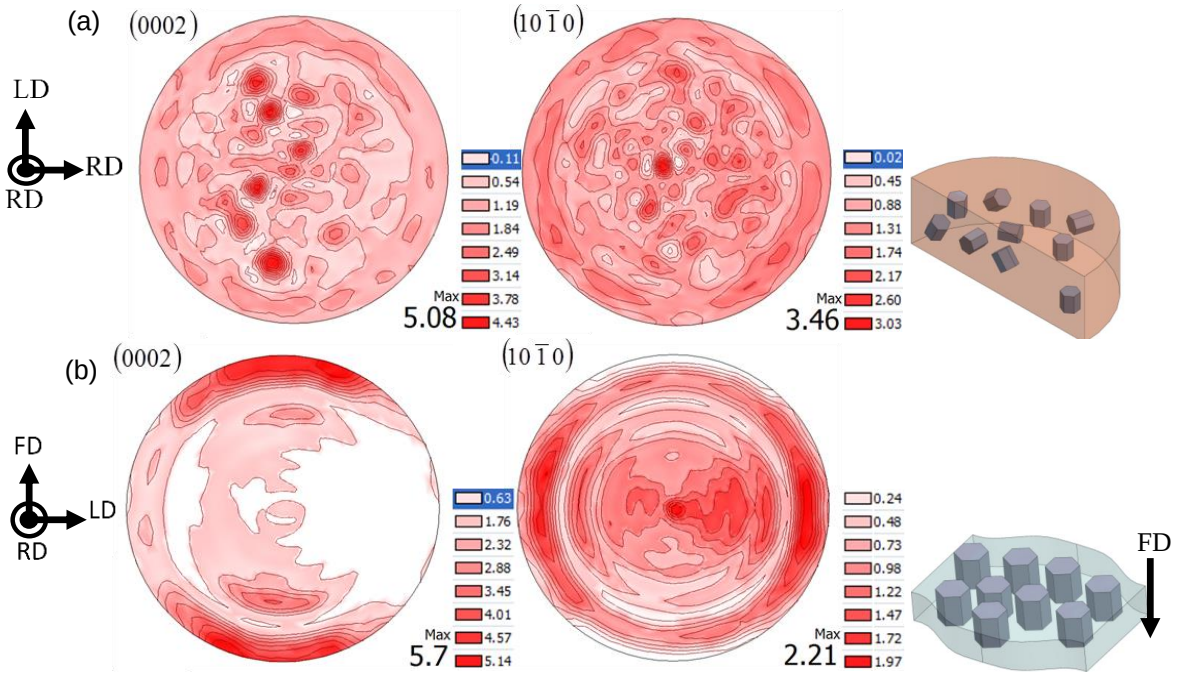

Figure 27. (0002) and $(10\bar{1}0)$ pole figures obtained from the ZK60 Mg alloy in (a) as-cast and (b) forged condition. The schematic illustration shows the orientation of the hcp unit cell in the material

As seen in the schematic illustration, the unit cells in the forged materials are aligned towards the FD and the $(10\bar{1}0)$ poles were observed towards LD, indicating that the prismatic $(10\bar{1}0)$ planes of hcp unit cells in the grains were perpendicular to the FD. As a result, a set of basal textures, i.e., $\{0001\}\langle 2\bar{1}\bar{1}0\rangle$ could be identified in the forged ZK60 Mg alloy.

4.3.3 Quasi-static tension test

The engineering stress–engineering strain plot obtained from the quasi-static tension tests in the as-cast and forged conditions is shown in Figure 28. The quasi-static tension properties are listed in Table 6. The results of this study and of a similar upsetting study [37] (also shown in Table 6) demonstrate that a higher ductility is always achieved after forging, compared to the ductility of as-cast or as-extruded materials. It is evident from Figure 28 that

the tensile behavior is very similar in RD and LD orientations for both as-cast and forged samples. Hence, the yield strengths in tension (YST) and ultimate tensile strengths (UTS) in LD and RD are almost the same. The average YST of the as-cast material was 140 MPa, and the average UTS was 278 MPa. The as-cast material achieved an average elongation of ~15% along the LD, and ~14% along the RD. In comparison, the yield strength and elongation of the forged alloy increased by 21% and 72%, respectively. The YSTs of the forged alloy were 163 MPa and 177 MPa, and the tensile fracture strain values were 26% and 24% in the LD and RD, respectively. However, the UTS after forging was approximately the same as that of the as-cast (285 MPa). The same behavior has also been reported in a study on the effects of warm rolling on the mechanical properties of ZK60 Mg alloy. The ultimate strengths along the rolling direction, 45° to the rolling direction, and the direction perpendicular to rolling direction were the same, while yield strengths along these orientations were different [120].

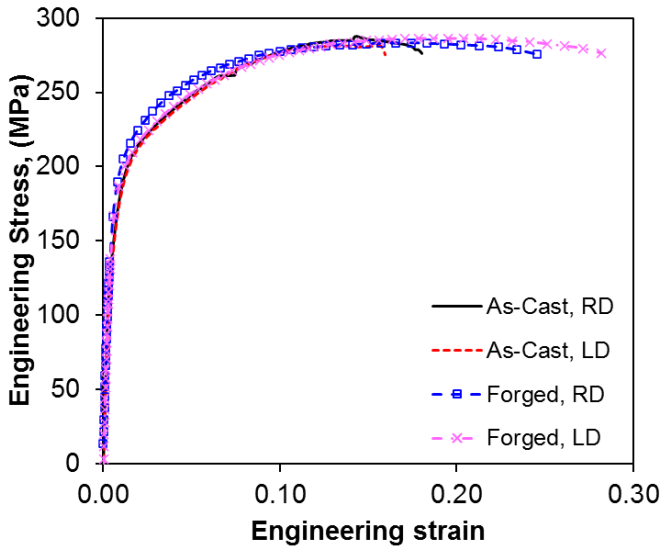

Figure 28. Typical engineering stress–engineering strain curves under tension loading of the ZK60 Mg alloy in as-cast and forged conditions tested at LD and RD and a strain rate of $10^{-3}s^{-1}$

Table 6. Tension quasi-static mechanical properties of as-cast and forged ZK60 Mg alloy along different directions in the present study and published in the literature

	Direction	YST (MPa)	UTS (MPa)	Fracture Strain (%)
As-Cast	LD	138 ± 0	279 ± 3	15 ± 1
	RD	140 ± 1	278 ± 7	14 ± 4
Forged	LD	163 ± 10	286 ± 4	26 ± 3
	RD	177 ± 0	284 ± 1	24 ± 0
Extruded **[37]**	ED	267	331	24.5
	ED	174	326	24
	TD	221	316	11
Upsetting of cast **[37]**	-	224	286	21
Upsetting of extruded **[37]**	ED	168	319	32
	TD	198	290	13

4.3.4 Quasi-static compression behavior

The compression tests were conducted on the as-cast material in the two orthogonal directions of RD and LD, and on the forged material along the RD, LD, and FD. Figure 29 depicts typical engineering stress–strain curves of the as-cast and forged samples tested under compression. The compressive strains and stresses in this figure are reported in their absolute magnitudes. The quasi-static compression properties along different directions are summarized in Table 7. The fracture strain and ultimate compressive strengths (UCS) of as-cast material were the same in the LD and RD directions (~19% and ~353 MPa, respectively). However, the materials achieved a yield strength in compression (YSC) of 109 MPa along the LD, and 118 MPa along the RD. In comparison, the UCS of the forged alloy increased significantly at the expense of a reduction in fracture strain. The YSCs of the forged alloy were 127 MPa, 119 MPa, and 111 MPa along FD, RD, and LD directions, respectively, while the UCSs were 373 MPa, 391 MPa, and 390 MPa, respectively. The fracture strain was between 13% and 15% in

all three directions. It is evident that the compression curves of the as-cast ZK60 material in LD and RD are similar to one another. This is in agreement with the texture measurement results. The basal and non-basal slip systems are dominant during compression of the as-cast material, but in the forged samples, particularly in the RD and LD directions, the stress–strain curves show that additional twinning systems are active and lead to deformation asymmetry.

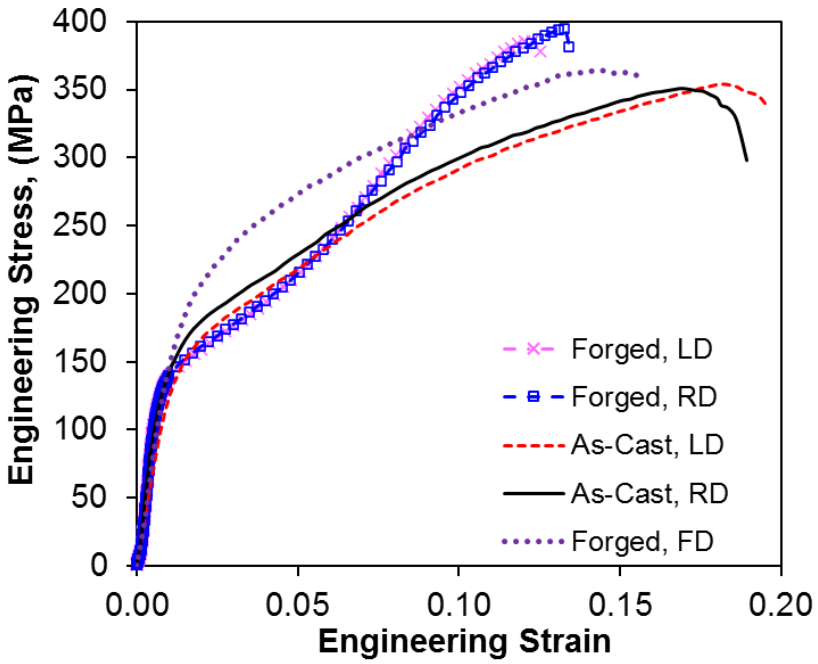

Figure 29. Typical engineering stress– engineering strain curves under compression loading of the ZK60 Mg-alloy in as-cast and forged conditions tested at LD, FD and RD directions and a strain rate of $10^{-3}s^{-1}$

Figure 30 shows the compression engineering stress vs. engineering plastic strain curves of the as-cast materials exhibiting three prominent stages: elastic, plastic with decreasing hardening, and plastic with increasing hardening. The pure elastic behavior saturates at a stress value of 70 MPa, which is lower than that of tension loading. Beyond that, at stress values above 113 MPa, yielding occurs and considerable strain hardening is seen (Figure 30).

Table 7. Quasi-static mechanical properties under compression, as-cast, and forged ZK60

	Direction	YSC (MPa)	UCS (MPa)	Fracture Strain [%]
As-Cast	LD	109 ± 6	352 ± 4	19 ± 0
	RD	118 ±0	354 ± 4	19 ± 1
Forged	LD	111 ± 1	390 ± 6	13 ± 1
	RD	119 ± 1	391 ± 4	14 ± 1
	FD	127 ± 4	373 ± 13	15 ± 0

The strain hardening rate during this stage is decreasing. In contrast, the anisotropic behavior of the forged ZK60 sample is obvious, which is due to the activation of twinning in two directions and idling of that when material is loaded along the FD. Indeed, the texture analysis reveals that the c-axes in hcp crystals are primarily orientated along the FD (Figure 27 (b)). This orientation favors triggering extension-twins $\langle 10\bar{1}2 \rangle$ when the compression load is applied along a direction perpendicular to the c-axis of the hcp unit cell of the grains; i.e., RD and LD. Along RD and LD, when the stress exceeds ~115 MPa, pronounced twinning starts and the curve ultimately becomes concave-up or sigmoidal in shape. As stress increases, non-basal slips can be activated in the twinned areas. Additionally, twin boundaries hinder dislocation movements; consequently, the rate of strain hardening increases. It was also observed that a stress of approximately 300 MPa causes twinning exhaustion. Under this amount of stress, tension twinning does not occur to a significant extent; as a result, the twinning boundary area is minimal and does not significantly obstruct the dislocation movement, which results in a decrease in the strain hardening rate. The cumulative effects of these competing factors: strain hardening due to twin boundaries, strain softening due to new twin formation, and the interaction between the twins and dislocation slips occurring during further compression, have previously been reported [41][42]. It is also important to note that along the FD, yielding occurs at ~127 MPa, accompanying a concave-down curve until fracture

occurs. During this stage, non-basal slip is expected to be the principal deformation mode, and the rate of strain hardening decreases [121].

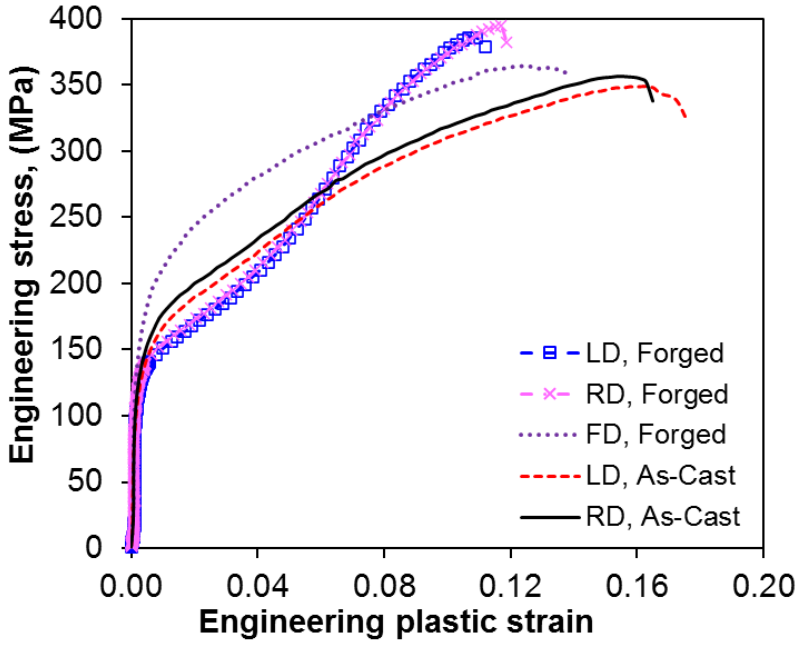

Figure 30. Engineering stress vs. engineering plastic strain under quasi-static compression loading of as-cast ZK60 and forged ZK60

4.3.5 Microstructure and texture after deformation of cast and forged samples

Figure 31 depicts the optical microstructures and the fracture profile, including the crack propagation in the as-cast and forged samples obtained from the tension tests along the LD. There are no visible twins observed in the micrograph. The multiple cracks with voids were formed in both as-cast and forged conditions. However, it is clear that the driving force for fracture in the as-cast sample was the normal stress, since it has failed in the plane of maximum normal stress (normal to uniaxial loading direction), while shear stress has driven a ductile fracture in the forged sample with the fracture plane angled about 45° to the uniaxial tension loading. In the as-cast material, porosities and defects are the likely causes of the crack formation [122][123].

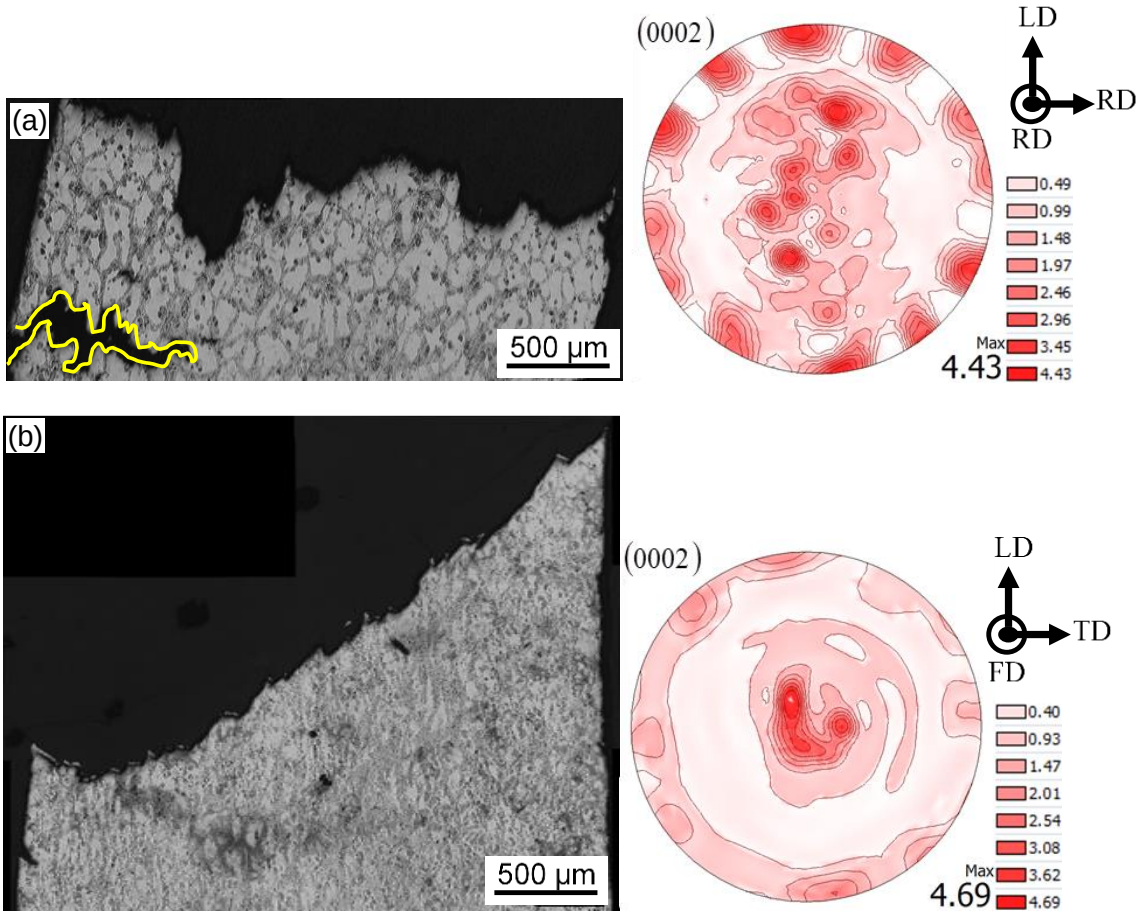

Figure 31. The polished cross section showing the fracture face profile with basal (0002) pole figures of ZK60 Mg alloy obtained from tension testing, (a) as-cast and (b) forged. The enclosed yellow line shows the secondary crack near the fracture surface in the cast materials

Figure 31 (a) exhibits a large secondary crack that has propagated across the grain boundaries (intergranular). This type of crack propagation is a manifestation of brittle fracture, which is seen more clearly in the SEM micrographs in a later section. The microstructures of the polished cross sections of the deformed in compression samples are illustrated in Figure 32. A combination of twin grains and parent grains is evident in the as-cast sample deformed along the LD. In contrast, the microstructure of the sample compressed along the LD exhibits a significant trace of twining, while the sample compressed along the FD shows elongated deformed grains without twining.

The change in texture during tension and compression, obtained from the samples after final fracture, is shown in Figure 31 and Figure 32. In the tensile test sample in the as-cast condition, the basal (0002) presented some concentration of the intensity toward the tensile direction. This means that the *c*-axes of hcp unit cells in some grains, which were favorable for twining, rotated along the loading direction. In contrast, in the forged samples, the maximum basal pole (0002) intensity was in the same orientation, which indicated that the orientation of the unit cell was not favorable for twining deformation. By contrast, the texture results obtained from compression samples show a significant change in orientation of the PFs. As seen in Fig 12 (a), the maximum pole density of the as-cast sample was 8.29 MRD, which is parallel to the LD. This finding suggests that those unit cells were not aligned along the CD, and that after compression all the unit cells in the grains were rotated and achieved a strong basal texture. In contrast, the forged sample compressed along the LD (Figure 32 (b)) obtained a texture intensity rotation of about 90° (unit cells as shown schematically), while the maximum texture intensity of the (0002) pole remained in the same direction for the sample compressed along the FD (Figure 32 (c)). These texture results support the observed stress–strain behavior of the tested samples shown in Figure 28 and Figure 30, where the obtained compression curves in LD exhibited a sigmoidal shape, an indication of twining deformation.

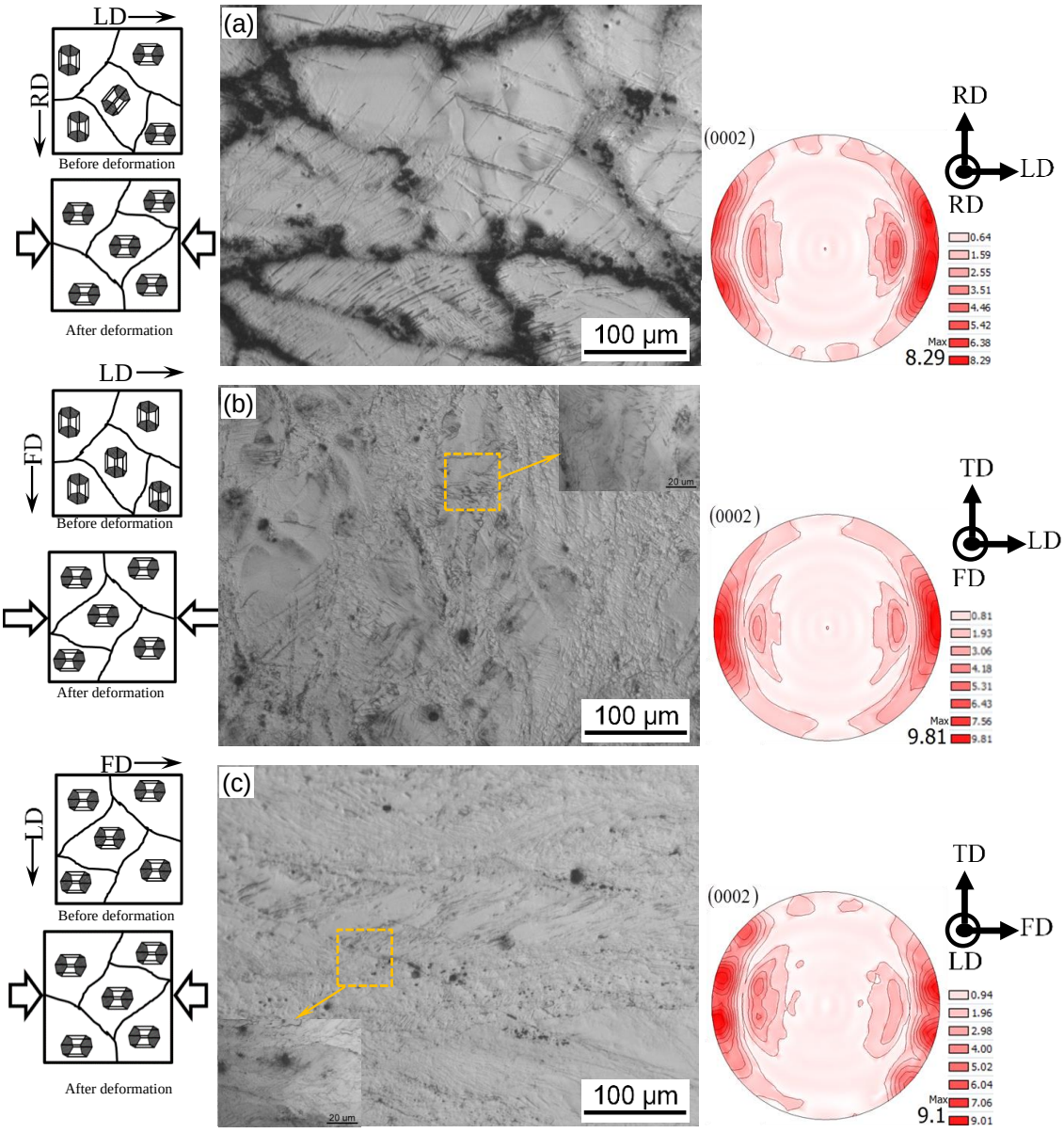

Figure 32. The polished cross section showing the microstructures near the fracture surface with basal (0002) pole figures of ZK60 Mg alloy obtained from compression testing, (a) as-cast, and forged followed by compression along (b) the LD and (c) FD. The enclosed yellow boxes show the location of higher magnified images. Note that the schematic shows the orientation of the unit cells in the grains before and after deformation

4.3.6 Fracture surface analysis

The fractured surfaces obtained during tension testing of the as-cast and forged samples were also examined via SEM, and are illustrated in Figure 33. As seen in Figure 33(a), the intergranular cracks, which are evidence of brittle fracture, are visible in the fracture surface of the as-cast ZK60, while fractographic analysis of the forged samples (Figure 33 (c)) demonstrates a ductile fracture.

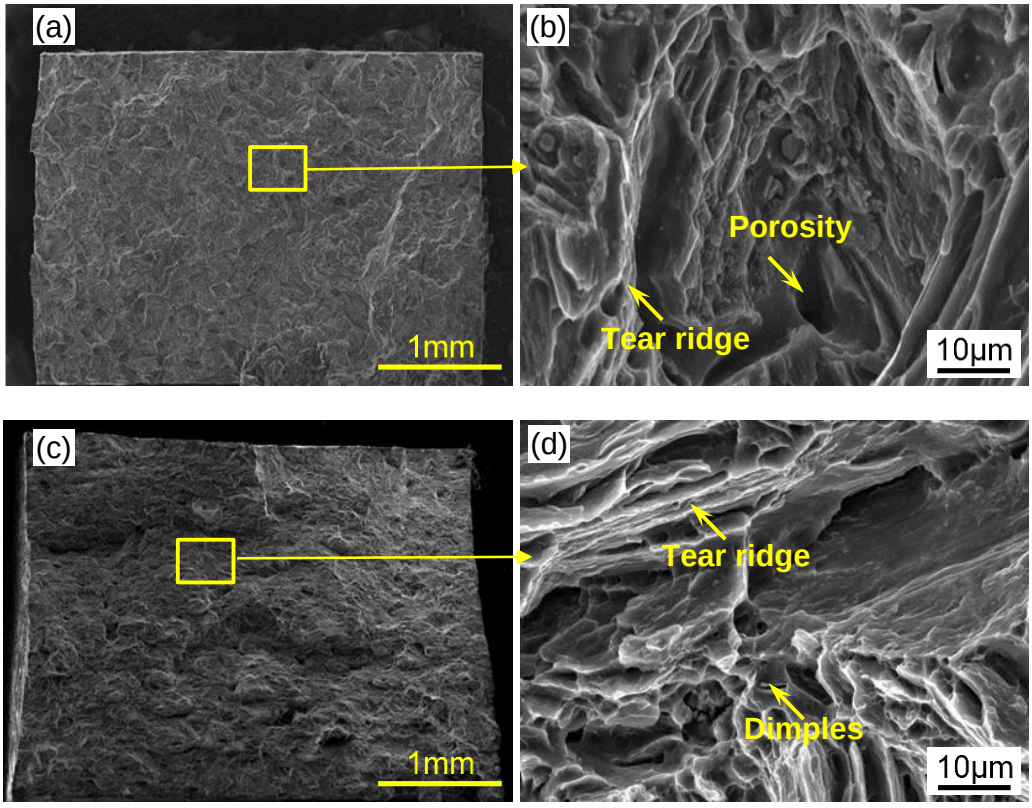

Figure 33. SEM micrographs showing the overall and magnified view of the tensile fracture surface of ZK60 Mg alloy in (a, b) as-cast and (c, d) forging conditions

As seen in Figure 33 (b), the magnified view of the fracture surface of as-cast materials shows large porosity surrounded by a tear ridge of the grains, which influences the alloy ductility. In contrast, there was no visible porosity present in the microstructure of the fracture surface of forged material shown in Figure 33 (d). Instead, dimples with tear ridges, which indicate a

ductile fracture, are identified. It is clear that the forged material has higher ductility compared to the as-cast material.

4.4 Discussion

The above results clearly indicate that the microstructure of as-cast ZK60 Mg alloy was refined by forging at elevated temperatures. The degree of modification in the microstructural features, such as dispersoid phases, grain size, and dendritic structures, is beneficial for the improvement of alloy performance in service. As seen in Figure 28 and Table 6, the forging process contributes to a significant improvement in the YST and ductility, while the UTS remains approximately the same between the as-cast and forged conditions. As discussed earlier, the improvement of alloy tensile properties, especially ductility, depends on the presence of defects in the alloy. Shaha et al. [122] reported that porosities play a significant role in cast alloys. They reported that during tension loading, pores tend to elongate, open, and increase in size, and therefore connect with one another more easily, which increases the potential for crack nucleation and propagation. This in turn may result in a premature fracture and affect the hardening and ductility of the alloy. As illustrated in Figure 24 and Figure 26, the as-cast alloy contains significantly more casting defects, such as pores, compared to the forged alloy, which eventually achieved better tensile ductility. Fractographic analyses also confirmed that porosities severely affect the as-cast alloy's ductility; this was also reported in a study on the effects of heat treatment on the forged Mg-Y-Zr alloy [124]. The authors analyzed the microstructure using X-ray computed tomography (XCT) and concluded that forging can significantly reduce casting porosity. Another potential reason for the lower ductility of the cast material is the presence of coarse intermetallics in the as-cast microstructure. The second phase particles, like intermetallics, also influence the alloy strength. The coarse intermetallics contain defects, which form voids during a deformation. Those voids are interconnected with each other, leading to the final fracture of the cast alloy at a lower strain. It is also believed that the presence of dendritic structures in the cast alloy causes premature fracture. As depicted in Figure 24 (b), the dendritic cell forms a wall between the grains, which cannot sustain a higher level of strain, and leads to a lower ductility. Ulacia

et al. [125] reported that during the hot deformation of Mg-based alloys, different DRX may be observed: discontinuous (DDRX), continuous (CDRX), or rotational dynamic recrystallization (RDRX). The DDRX occurs by nucleating new grains and their growth, while CDRX is obtained at the new high-angle boundaries, as a result of local lattice rotations caused by dislocation accumulation [56]. At the same time, the RDRX is acquired near grain boundaries of the new grains, due to increased dislocation density where the intergranular strain incompatibilities occur. However, differentiating between DDRX and RDRX is quite difficult, since both phenomena occurred at the new grains formed during deformation, and both processes cause grain refinement. Thus, it is believed that during forging, DDRX and RDRX occurred simultaneously, which causes the evolution of finer grains along the boundary of the pancaked elongated grains and reduces the dendritic morphology. The presence of the grain boundaries limits the movement of dislocations. Eventually, improvements in strength and ductility are observed. However, the UTS in the forged condition remains the same, due to incomplete recrystallization. Partially-recrystallized grains after forging have been reported in research on the effects of multi-axial forging on as-cast ZK60 Mg alloy [55], where the microstructure of ZK60 was analyzed after accomplishing three passes of multi-axial forging, and the grains and intermetallic particles were elongated vertical to the final compression loading.

The tension-compression asymmetry of the Mg-based alloys is a very common phenomenon. In this study, it is worth noting that the forged alloy possesses a tension-compression asymmetry (see Figure 34). The asymmetric behavior can be quantified by the following equation:

$$\text{Asymmetry level} = \frac{YST - YSC}{YST} \times 100 \qquad 4\text{-}1$$

Then, the magnitude of tension-compression asymmetry for the forged and as-cast materials will be approximately 28% and 19%, respectively. In the case of forged material, this tension-compression asymmetry is attributed to the formation of a strong basal texture in the forged materials and the polar nature of twinning, i.e., activation of twinning rotated the c-axis about 86.3° to the loading axis [126]. When the compression load is exerted perpendicular to the c-

axis, tension-twinning $\{10\bar{1}1\}\langle 10\bar{1}2\rangle$ is active; however, when the load is in tension, strain hardening is not prevailed by the twin formation. Tension-compression asymmetry is therefore conspicuous in the material's behavior. Furthermore, a discernible tension-compression asymmetry is evident for as-cast ZK60 though its random texture. The asymmetry stems from different slip and twin behavior in tension and compression. The tension-twins are nucleated during the tension test, while compression loading is mostly dominated by the twin growth, and twin initiation occurs to a significant extent at the onset of the test [127], [128]. Vinogradov et al. [129] investigated the asymmetric behavior for as-cast ZK60 and reported that more grains are orientated favorably for tension-twinning in compression than in tension. This is in agreement with the results shown in Figure 34, where a weak sigmoidal shape is visible in the as-cast tension curve.

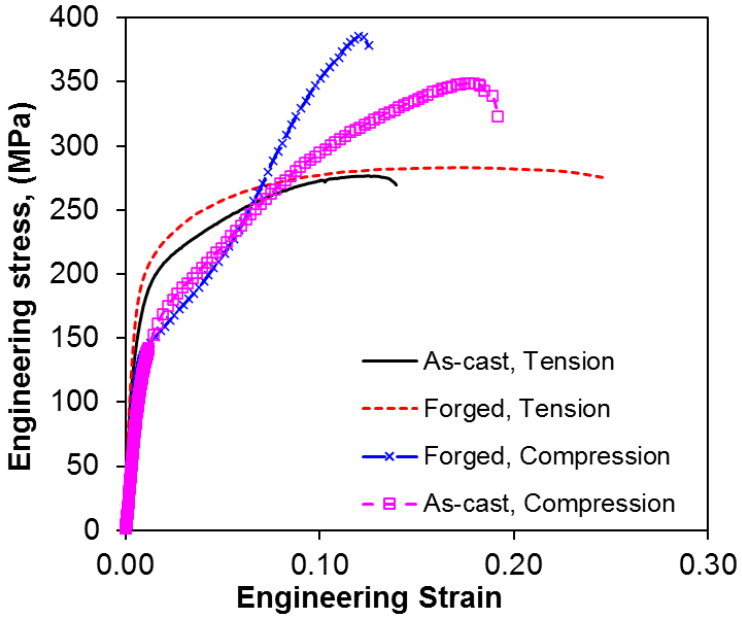

Figure 34. Typical engineering stress–engineering strain curves under tension and compression loading of the ZK60 Mg-alloy in as-cast and forged conditions exhibiting asymmetric behavior in both conditions

Figure 35 represents the strain hardening variation with regards to the strain after the yielding point. As seen in the Figure 35, except for the case of compression loading in the forged sample tested along the FD, the strain hardening rate decreases with an increase in the

strain value. However, when compression loading is applied to the forged sample along LD/RD, the curve consists of 3 stages. First, a rapid decrease occurs, followed by an increase at a strain of ~0.05. This point is ascribed to the inflection point, attesting that twinning deformation is occurring. Stage B terminates at a strain value of ~0.08 where again strain hardening rate is decreasing until fracture occurs. A similar trend has also been reported in AM30 extruded Mg alloy [121].

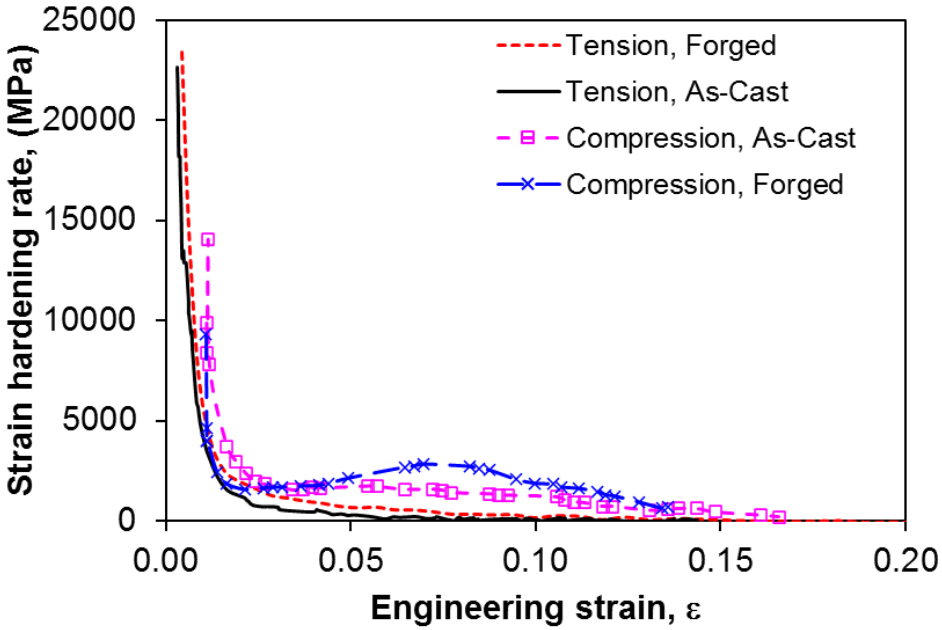

Figure 35. Typical strain hardening rate-engineering strain curves under tension and compression loading of the ZK60 Mg-alloy in as-cast and forged conditions

Lastly, as illustrated in Figure 32 (b, c) and explained earlier, after forging, the c-axes are mainly oriented along the FD, while a random orientation was identified in the as-cast materials. It has been reported that DRX can change the crystal orientation, especially the hcp crystal, which is very prone to the texture formation [130], [131]. This process can be (1) nucleation oriented, or (2) growth oriented. In the former, the majority of new grains are nucleated in the dominant final texture orientation, while in the latter, the growth frequency of grains grown in one direction is higher than that of those grown in random directions [131]. In this study, a nucleation-oriented texture was observed due to both DDRX and RDRX, so the maximum sharpness of texture did not increase significantly. Moreover, according to Doherty

et al. [132], precipitation and second phase particles can inhibit texture revolution by pinning the grain boundaries. As a matter of fact, in the case of ZK60 Mg alloys, $MgZn_2$ and Zn_2Zr are reported to be the key precipitate phases that significantly influence the alloy's behavior [133],[134].

4.5 Conclusion

In the present study, the as-cast ZK60 Mg alloy was forged at elevated temperatures for manufacturing structural parts. From the above results and discussion, the following conclusions can be made:

1. Microstructural analysis revealed that bimodal refined grains with a significant reduction of casting defects were formed during forging. However, the dendritic morphologies still existed after the forging process, demonstrating that completed DRX did not occur.
2. Texture analysis revealed a random texture for the cast material; however, in the case of forged ZK60, grains are orientated toward the FD. As a result, quasi-static compression loading showed both tension-compression asymmetry and anisotropic behavior for the forged ZK60.
3. The yield strength and ductility of the forged ZK60 Mg alloy tested in tension loading increased significantly, while the tensile strength remains about the same. At the same time, the yield strength and ultimate strength in compression increased at the expense of a small decrease in fracture strain.
4. Fracture analysis showed brittle fracture behavior of the as-cast ZK60, while a ductile fracture surface with some dimples and tear ridges were obvious on the fracture surface of the forged samples. This indicates that more plastic deformation is occurring during the test on the forged sample, meaning that material is more ductile.

Chapter 5

Fatigue Characteristics and modeling of Cast and Cast-Forged ZK60 Magnesium Alloy

5.1 Introduction

Since the 1920s, steel has been an integral material utilized in cars [135]. However, environmental concerns have driven new interests for cutting down on the vehicles' mass. It was reported that 10% reduction of the vehicles' weight would lead to the saving of the cars' fuel consumption rates of approximately 5% [14]. Therefore, magnesium (Mg), which is the lightest commercially available metal, has attracted the interest of the automotive industry [9]–[12].

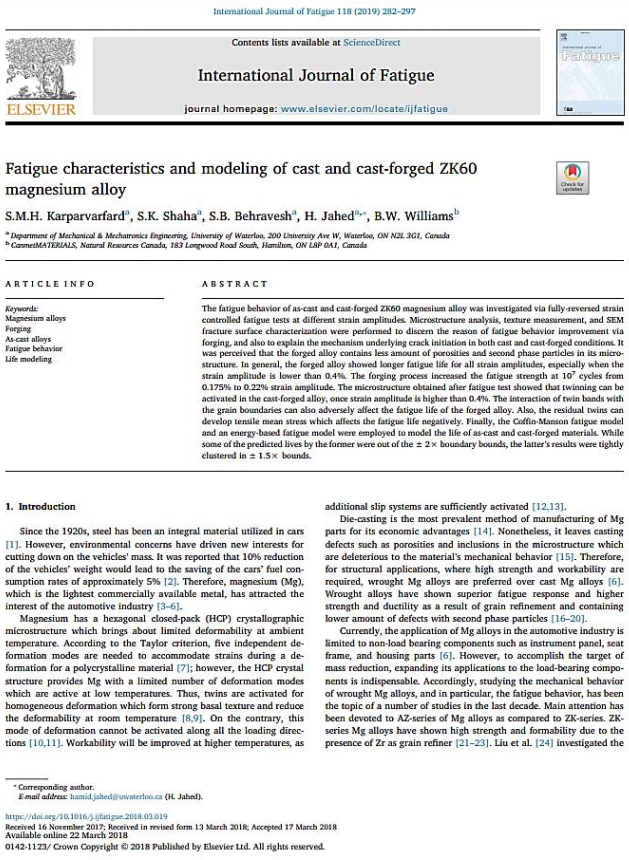

International Journal of Fatigue 118 (2019) 282–297

Contents lists available at ScienceDirect

International Journal of Fatigue

journal homepage: www.elsevier.com/locate/ijfatigue

Fatigue characteristics and modeling of cast and cast-forged ZK60 magnesium alloy

S.M.H. Karparvarfard[a], S.K. Shaha[a], S.B. Behravesh[a], H. Jahed[b,*], B.W. Williams[b]

[a] Department of Mechanical & Mechatronics Engineering, University of Waterloo, 200 University Ave W, Waterloo, ON N2L 3G1, Canada
[b] CanmetMATERIALS, Natural Resources Canada, 183 Longwood Road South, Hamilton, ON L8P 0A1, Canada

ARTICLE INFO

Keywords:
Magnesium alloys
Forging
As-cast alloys
Fatigue behavior
Life modeling

ABSTRACT

The fatigue behavior of as-cast and cast-forged ZK60 magnesium alloy was investigated via fully-reversed strain controlled fatigue tests at different strain amplitudes. Microstructure analysis, texture measurement, and SEM fracture surface characterization were performed to discern the reason of fatigue behavior improvement via forging, and also to explain the mechanism underlying crack initiation in both cast and cast-forged conditions. It was perceived that the forged alloy contains less amount of porosities and second phase particles in its microstructure. In general, the forged alloy showed longer fatigue life for all strain amplitudes, especially when the strain amplitude is lower than 0.4%. The forging process increased the fatigue strength at 10^7 cycles from 0.175% to 0.22% strain amplitude. The microstructure obtained after fatigue test showed that twinning can be activated in the cast-forged alloy, once strain amplitude is higher than 0.4%. The interaction of twin bands with the grain boundaries can also adversely affect the fatigue life of the forged alloy. Also, the residual twins can develop tensile mean stress which affects the fatigue life negatively. Finally, the Coffin-Manson fatigue model and an energy-based fatigue model were employed to model the life of as-cast and cast-forged materials. While some of the predicted lives by the former were out of the ± 2× boundary bounds, the latter's results were tightly clustered in ± 1.5× bounds.

1. Introduction

Since the 1920s, steel has been an integral material utilized in cars [1]. However, environmental concerns have driven new interests for cutting down on the vehicles' mass. It was reported that 10% reduction of the vehicles' weight would lead to the saving of the cars' fuel consumption rates of approximately 5% [2]. Therefore, magnesium (Mg), which is the lightest commercially available metal, has attracted the interest of the automotive industry [3–6].

Magnesium has a hexagonal closed-pack (HCP) crystallographic microstructure which brings about limited deformability at ambient temperature. According to the Taylor criterion, five independent deformation modes are needed to accommodate strains during a deformation for a polycrystalline material [7]; however, the HCP crystal structure provides Mg with a limited number of deformation modes which are active at low temperatures. Thus, twins are activated for homogeneous deformation which form strong basal texture and reduce the deformability at room temperature [8,9]. On the contrary, this mode of deformation cannot be activated along all the loading directions [10,11]. Workability will be improved at higher temperatures, as additional slip systems are sufficiently activated [12,13].

Die-casting is the most prevalent method of manufacturing of Mg parts for its economic advantages [14]. Nonetheless, it leaves casting defects such as porosities and inclusions in the microstructure which are deleterious to the material's mechanical behavior [15]. Therefore, for structural applications, where high strength and workability are required, wrought Mg alloys are preferred over cast Mg alloys [6]. Wrought alloys have shown superior fatigue response and higher strength and ductility as a result of grain refinement and containing lower amount of defects with second phase particles [16–20].

Currently, the application of Mg alloys in the automotive industry is limited to non-load bearing components such as instrument panel, seat frame, and housing parts [6]. However, to accomplish the target of mass reduction, expanding its applications to the load-bearing components is indispensable. Accordingly, studying the mechanical behavior of wrought Mg alloys, and in particular, the fatigue behavior, has been the topic of a number of studies in the last decade. Main attention has been devoted to AZ-series of Mg alloys as compared to ZK-series. ZK-series Mg alloys have shown high strength and formability due to the presence of Zr as grain refiner [21–23]. Liu et al. [24] investigated the

* Corresponding author.
E-mail address: hamid.jahed@uwaterloo.ca (H. Jahed).

https://doi.org/10.1016/j.ijfatigue.2018.03.019
Received 16 November 2017; Received in revised form 13 March 2018; Accepted 17 March 2018
Available online 22 March 2018
0142-1123/

Figure 36. SMH. Karparvarfard et al., "Fatigue characteristics and modeling of cast and cast-forged ZK60 magnesium alloy." International Journal of Fatigue 118 (2019): 282-297.

Magnesium has a hexagonal closed-pack (HCP) crystallographic microstructure which brings about limited deformability at ambient temperature. According to the Taylor criterion, five independent deformation modes are needed to accommodate strains during a deformation for a polycrystalline material [136]; however, the HCP crystal structure provides Mg with a limited number of deformation modes which are active at low temperatures. Thus, twins are activated for homogeneous deformation which form strong basal texture and reduce

the deformability at room temperature[137][35]. On the contrary, this mode of deformation cannot be activated along all the loading directions [39][38]. Workability will be improved at higher temperatures, as additional slip systems are sufficiently activated [130][138].

Die-casting is the most prevalent method of manufacturing of Mg parts for its economic advantages [15]. Nonetheless, it leaves casting defects such as porosities and inclusions in the microstructure which are deleterious to the material's mechanical behavior [16]. Therefore, for structural applications, where high strength and workability are required, wrought Mg alloys are preferred over cast Mg alloys [12]. Wrought alloys have shown superior fatigue response and higher strength and ductility as a result of grain refinement and containing lower amount of defects with second phase particles [18][46][81][19][20].

Currently, the application of Mg alloys in the automotive industry is limited to non-load bearing components such as instrument panel, seat frame, and housing parts [12]. However, to accomplish the target of mass reduction, expanding its applications to the load-bearing components is indispensable. Accordingly, studying the mechanical behavior of wrought Mg alloys, and in particular, the fatigue behavior, has been the topic of a number of studies in the last decade. Main attention has been devoted to AZ-series of Mg alloys as compared to ZK-series. ZK- series Mg alloys have shown high strength and formability due to the presence of Zr as grain refiner [31][32][84]. Liu et al. [45] investigated the tensile and high cycle fatigue (HCF) behavior of extruded and T5 heat treated ZK60 under load-controlled fatigue. They reported that the T5 heat treatment refined the grain structure from bimodal to more equiaxed grains with higher pole figure intensity of fiber texture which basically improved the performance of ZK60; especially the fatigue strength improved from 140 to 150 MPa. Other studies [43][41][42] investigated the cyclic behavior of the extruded ZK60 along the extrusion direction through fully-reversed stress and strain controlled cyclic tests to understand the twining/detwinning activity. They revealed that the activation of twinning and detwinning during the cyclic loading increased with increasing the strain amplitude beyond 4% due to the asymmetric behavior in tension-compression, while the slip was dominated at lower stress/strain amplitude.

Several manufacturing processes have been employed to achieve grain refinement through forming of Mg alloys [19][49][34] [139][140]. Among a wide variety of processing methods, forging is of particular interest because it has shown its promise to produce components with complex geometries [110][100][141]. However, only a few studies have been performed to isolate the contribution of the forging process to the cyclic behavior of Mg alloys. Vasilev et al. [53] carried out a study on the effects of multiaxial isothermal forging (MIF) on the microstructure and fatigue behavior of as-cast ZK60. The results demonstrated that nearly 80% of coarse grains volume fraction was refined after MIF, which causes better fatigue response in both LCF and HCF regimes. However, limited number of studies has been contributed to the effects of forging process on the as-cast Mg alloys in particular as-cast ZK60. Recently, Gryguc et al. [50], [142] and Toscano et al. [47] studied the influence of forging on the mechanical properties, and in particular cyclic response, of AZ80 and AZ31B Mg alloys, respectively. They revealed that a significant grain refinement was achieved in forged components, which improved the fatigue life of the cast or extruded Mg alloy. In another study, the authors have characterized the quasi static tensile and compressive behavior of cast-forged ZK60 [143] and showed ZK60's great potentials to be utilized in load-bearing components of vehicles. However, the fatigue behavior of the forged ZK60 alloy has not yet been comprehensively investigated. In this paper we investigate the fatigue behavior of cast and cast-forged ZK60. Toward this objective, strain controlled fully reversed push-pull fatigue tests have been performed. Texture and microstructural analysis, and SEM fracture surface analysis were carried out to discern the mechanical behavior, and to identify the mechanism underlying crack initiation and failure. Moreover, two common fatigue models were utilized to discuss the obtained fatigue results.

5.2 Materials and Methods

The starting material in the present study was an as-cast ZK60 ingot with the dimensions of 300 mm diameter and 500 mm length. The chemical composition of the alloy is presented in [143]. The ingot was then machined into cylinders with a diameter of 63.5 mm and a length of 65 mm, which were used as forging billets. Each billet was heated at the

temperature of 450°C for 3.5 hours, and transferred to the forging anvil, which was also heated up to the same temperature. The open-die forging process was then performed at the ram speed of 390 mm/min along the radial direction, as shown schematically in Figure 37. As discussed in our previous study [143], the temperature of 450°C was selected for the forging, as it is above the lowest melting temperature of the eutectic phase for ZK60, 339.5°C [115]. It is therefore expected that the second phase particles were dissolved into the matrix, which could lead to a better forging response. Also, Hadadzadeh et al. [144] investigated the same material exploiting a Gleeble® 3500 thermal-mechanical simulation testing system, and observed no incipient melting in the microstructure at 450°C. Regarding the ram speed of 390 mm/min, it should be stated that forging trials had been performed at four different speeds of 0.39 mm/min, 3.9 mm/min, 39 mm/min, and 390 mm/min [145]. It was observed that the mechanical behavior of the materials under compression loading is the same. Hence, for practical purposes, and to save the time and energy, the highest ram speed was chosen for investigation in this study.

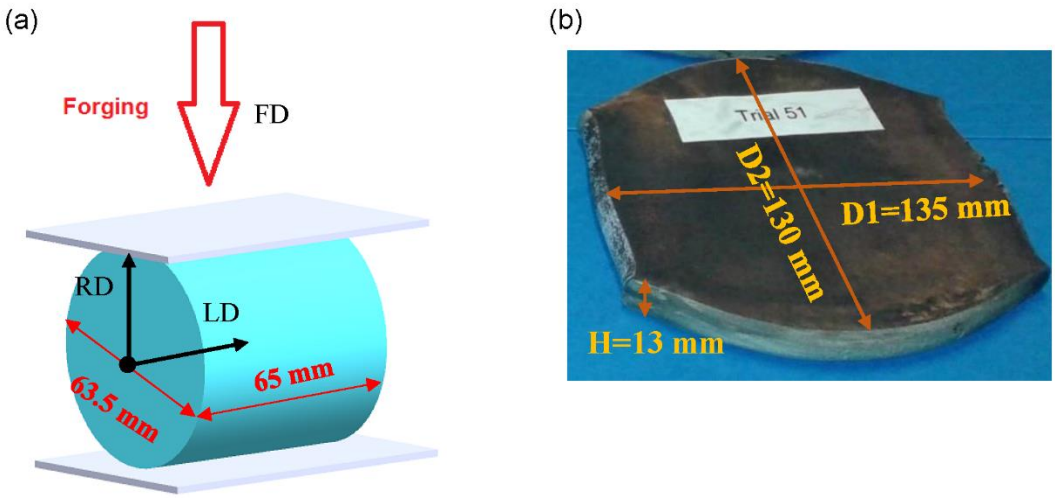

Figure 37. (a) Schematic illustration of the open-die forging process; (b) the final ZK60 sample after forging at 450°C with the ram speed of 390 mm/min

Note: LD-longitudinal direction, RD-radial direction, and FD-forging direction

Microstructures and texture analysis were carried out on samples collected from both as-cast and forged conditions. The samples were initially ground with SiC sandpapers, and later polished with 6, 3, 1, and 0.1-micron diamond pastes. After that, polishing was performed using colloidal silica. Finally, the samples were etched utilizing an acetic-picral etchant. Texture measurement was done with a Bruker D8 Discover X-ray diffractometer equipped with an advanced 2D-detector using CuKα beam radiation at the voltage of 40 kV and current of 40 mA. The obtained diffraction patterns were evaluated using Bruker trademark software DIFFRAC.EVA. Further details about the texture analysis are explained in [141].

Smooth dog-bone samples were machined from the as-cast and forged ZK60 materials. The specimen locations and corresponding labelling are shown in Figure 38 (a) and (b) for the as-cast and forged ZK60, respectively. The as-cast specimens were cut along two different directions, i.e., radial (RD) and longitudinal (LD) directions. To avoid inconsistency, all the samples from the as-cast billet were cut at the distance of the 75% of the billet radius. However, the specimens from the forged material were cut along only one direction, i.e., LD. The FD in Figure 38 (b) represents the forging direction. The specimen geometry can be found in [143].

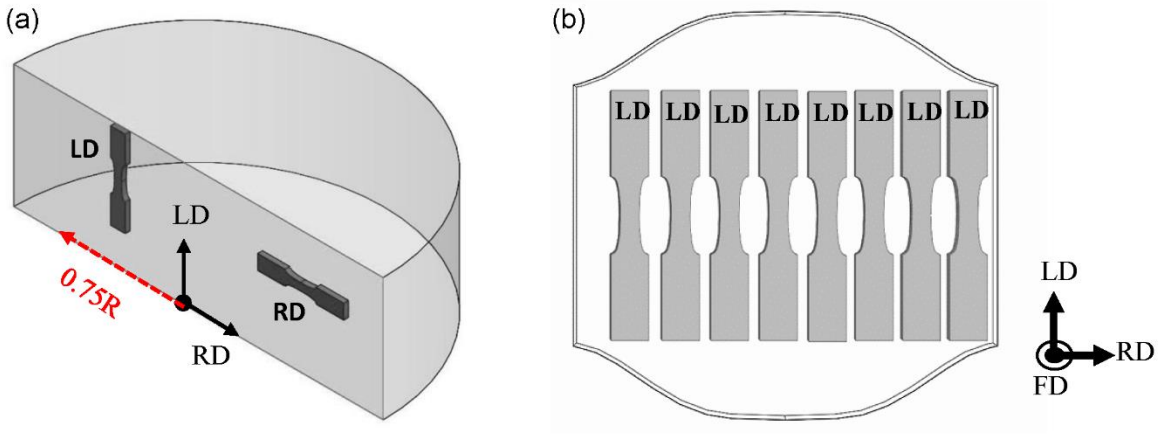

Figure 38. Schematic depiction of the specimen locations and directions in (a) as-cast and (b) forged ZK60

Fatigue tests were performed under standard laboratory condition, as per ASTM E606/E606M-12 standard, using an Instron 8874 servo-hydraulic frame having a load capacity

of ±25 kN. Engineering strain values were measured during the tests using a uniaxial epsilon extensometer with a gauge length of 8 mm and travel distance of ±0.8 mm. All the experiments were conducted under fully revered (R = -1) strain-controlled condition. The loading frequency was selected between 0.2 and 1 Hz to achieve the same strain rate of 10^{-2} sec^{-1} throughout the fatigue tests. At very low strain amplitudes and after the material's behavior was stabilized, the tests were shifted to load controlled mode at a higher frequency of up to 30 Hz and continued up to 10^7 cycles. Tests with no failure at 10^7 cycles were stopped and considered as run-out tests. Fatigue life was assumed to be the life at rupture. Each test was at least once duplicated to verify the reproducibility of the results. The number of test specimens and percent replication was based on ASTM E739-10 standard. Finally, fracture surfaces were analyzed under SEM to describe the mechanism underlying the crack initiation, propagation, and final failure.

5.3 Results and discussion

5.3.1 Texture and microstructure

Figure 39 (a) and (b) depict the microstructure of the as-cast ZK60 in the un-etched and etched conditions, respectively. As seen, the microstructure of ZK60 cast is laden with dendrites and porosities. A secondary dendritic arm spacing (SDAS) of 35±6 µm and a grain size of 104 ±25 µm was observed in the as-cast material. The presence of Zn- and Zr- rich intermetallics ($MgZn_2$ and Zn_2Zr) in the microstructure has already been reported in the literature, detected using EDX line scanning and XRD analysis [115][143]. For the forged material, however, as shown in Figure 39 (c) and (d), grains were finer with the average size of 2–5 µm, and the porosity fraction was reduced significantly. Moreover, the volume fraction of second phase particles was reduced in the microstructure of forged alloy in comparison to the as-cast alloy, since during the forging process some intermetallics dissolve back into the matrix. While 15% volume fraction of the microstructure of as-cast ZK60 contained porosities and second phase particles, that amount was promisingly reduced to 5% for the forged alloy. This can lead to better fatigue response, as intermetallic particles are notable sites for crack initiation due to stress concentration [146]. Porosities can also play a major role in premature

failure. These vacancies can coalesce and make a void leading to a crack that can cause the final fracture [122]. In addition, dendrites can accommodate pores and play as walls between the grains, and decreasing the SDAS results in superior strength of the material [147].

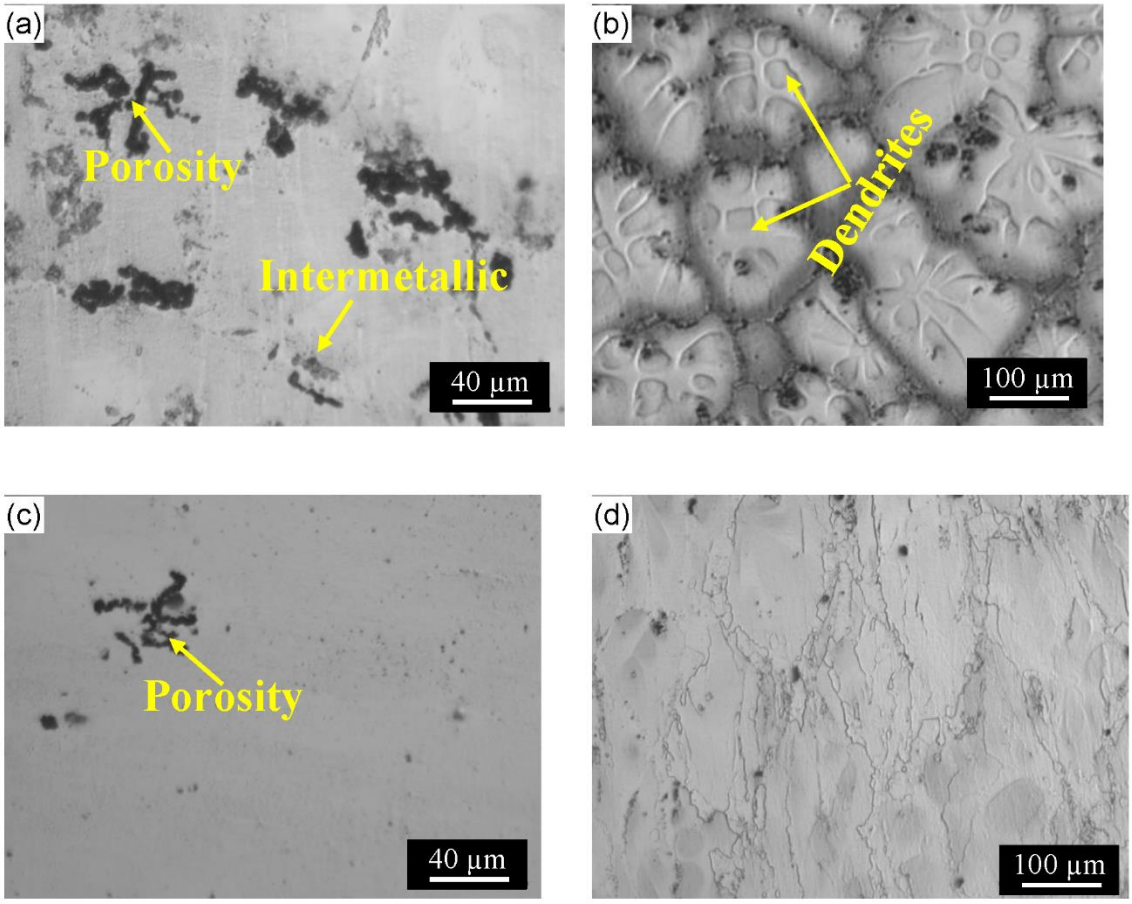

Figure 39. Typical optical microstructures of as-cast ZK60 in unetched (a), and etched conditions (b) and forged ZK60 in unetched (c) and etched conditions (d)

Figure 40 shows the texture measurement results for the as-cast and forged materials. While the as-cast alloy shows a random texture, where grains are not orientated mainly along any specific direction, a strong basal texture can be observed in the forged alloy. Specifically, the pole figures (PF) for the basal (0002) and prismatic $(10\bar{1}0)$ planes indicated a maximum

intensity of 5.7 and 2.21, respectively; thereby, the HCP unit cell of the forged alloy are primarily aligned such that the c-axis is parallel to the forging direction.

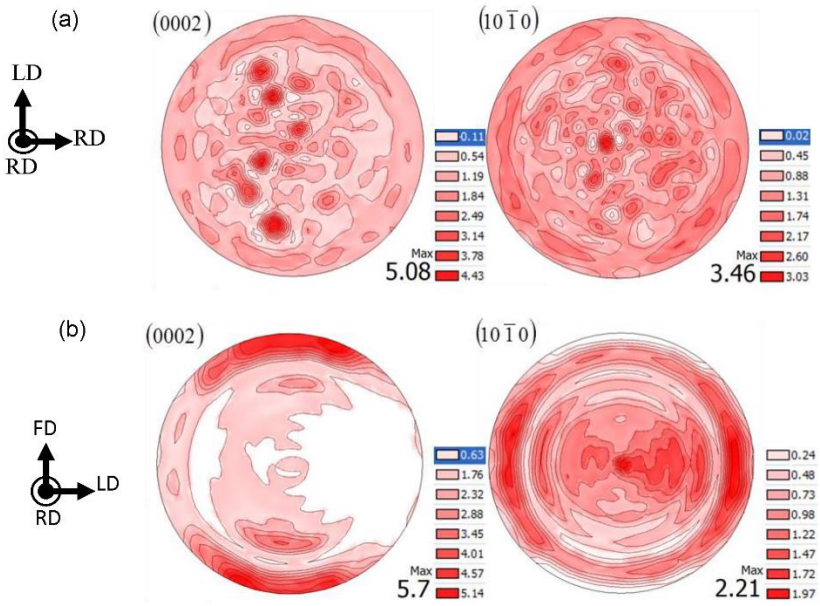

Figure 40. The (0002) basal and $(10\bar{1}0)$ prismatic pole figures (PF) for (a) as-cast ZK60, (b) cast-forged ZK60 Mg alloy [39]

5.3.2 Quasi-static uniaxial tensile behavior

A comprehensive investigation of the quasi-static uniaxial behavior of the as-cast and forged ZK60 alloys has already been delivered in the previous study by the authors [143]. Table 8 shows the tensile properties of the as-cast and forged alloy under uniaxial tensile loading along LD direction. As reported in [143], the quasi-static uniaxial behavior of ZK60 is similar in both, LD and RD directions at both as-cast and forged conditions.

Table 8. Mechanical properties of as-cast and forged ZK60 under quasi-static tensile loading

	0.2% offset yield strength (MPa)	Ultimate tensile strength (MPa)	Fracture strain (%)
As-Cast	138 ± 0	279 ± 3	15 ± 1
Forged	163 ± 10	286 ± 4	26 ± 3

5.3.3 Cyclic behavior

Fatigue tests were performed under strain control mode at different strain amplitudes ranging from 0.15% to 0.9%. Detailed summary of uniaxial cyclic tests is presented in Table 9 which includes the applied strain amplitudes (elastic and plastic strain amplitudes), the total life, the maximum and minimum stresses, and the elastic and plastic strain energy densities for the half-life cycles. Figure 41 depicts the typical engineering stress-strain hysteresis loops for the second and half-life cycles at the total strain amplitudes of 0.3%, 0.5%, and 0.7% for the as-cast and cast-forged conditions. It is noticed that the cyclic behavior of as-cast ZK60 is symmetric during the whole cyclic life at different strain amplitudes (Figure 41 (a), (b), and (c)), 3 distinct types of behavior can be inferred for the forged alloy. They are (i) symmetric (ii) partially symmetric and (ii) asymmetric behavior in hysteresis loops. Firstly, for the strain amplitudes lower than 0.4%, Figure 41 (d), the forged alloy exhibits symmetric hysteresis loop in the second cycle, whereas no plateau in the compression reversal can be seen, which signifies that the twinning is not activated [38][36][148]. Moreover, while marginal strain hardening is occurring during the history of cyclic loading, as the tensile peak stress is increased in the half-life hysteresis, still no sign of twinning is present in the compression reversal. At higher strain amplitude of 0.5%, Figure 41 (e), it is seen that twinning is driving the deformation under compression loading after the strain of ~ -0.3%, and detwinning is active till about the strain of 0.03% in the second cycle. In contrast, the half-life hysteresis loop indicates that the strain is primarily accommodated by the slip mode of deformation, since no zero-work hardening plateau can be seen under compressive loading. It is believed that this

remarkable change in the hysteresis loop shape is owing to the exhaustion of the new extension twinning happening, which is also seen for other wrought Mg alloys at different strain amplitudes [18][42]. Finally, as seen in Figure 41 (f), the second and half-life hysteresis loops at the strain amplitude of 0.7% show sigmoidal shapes indicating the activation of extension twin and detwinning under compressive and tensile loading, respectively. Additionally, an investigation on the evolution of internal stress during the cyclic deformation by $\{10\bar{1}2\}\langle 10\bar{1}1\rangle$ extension twins in the extruded ZK60 reported that the local intergranular stress drives the activation of detwinning [149], thereby detwinning along the c-axis is starting in the reverse tensile loading with small external stress at the stress of ~ -100 MPa.

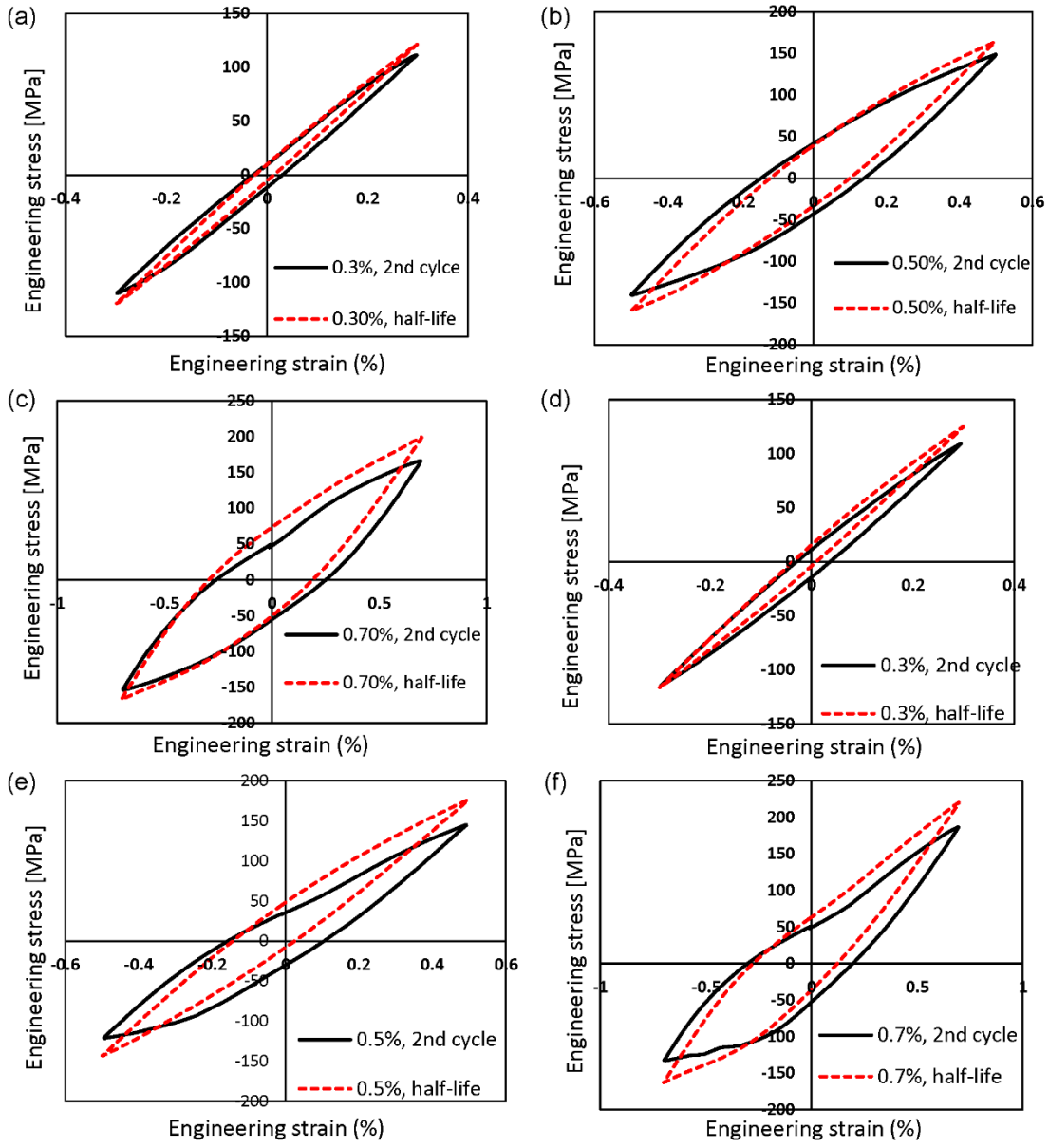

Figure 41. Typical engineering stress-engineering strain hysteresis loops for the as-cast (a, b, c) and forged (d, e, f) ZK60 Mg alloy at different total strain amplitudes of 0.3% (a, d), 0.5% (b, e), and 0.7% (c, f)

Figure 42 shows the half-life hysteresis loops for the as-cast ZK60 for different strain amplitudes. It is noted that the shape of hysteresis loops as well as the peak stresses are

symmetric in tension and compression reversals. This behavior is an evidence of slip being the dominant plastic deformation [41][150], which is attributed to the random texture in the cast Mg alloy. To be more specific, returning to the texture measurement (Figure 40 (a)), ZK60 cast has no preferred unit cell orientation inside its microstructure. Therefore, extension twins will not take over during low deformation. Nevertheless, the hysteresis loop at the strain amplitude of 0.9% tends to be marginally sigmoidal shape, which is evidence for the mild activation of extension twins and detwinning at higher deformation levels. In fact, in a randomly textured material, some grains would have an orientation that is favorable for activation of twinning. As a result, at high strain amplitudes, some twining might happen for which the hysteresis loop would be sigmoidal; however, the hysteresis loop is still symmetric at the strain amplitude of 0.9%, as the amount of twinning may not be significant. Comparing with the half-life hysteresis loops in as-cast condition (Figure 42), the forged half-life hysteresis loops (Figure 43) exhibit asymmetric behavior above the strain amplitude of 0.4%. As seen in Figure 43, the hysteresis loops are almost symmetric up to the strain amplitude of 0.4% in terms of both the shape of hysteresis loop and the peak stresses. However, at the strain amplitudes higher than 0.4%, the hysteresis loops tend to be asymmetric. Such an asymmetric behavior stems from the strong basal texture developed during the forging process. According to Figure 38 (b) and Figure 40 (b), tensile loading on the fatigue specimen (along LD) applies contraction along the c-axis of HCP unit cells, then no twining occurs. However, compressive loading brings about extension along the c-axis, thereby twining takes over [36]. The twinning deformation is often characterized by very low hardening rates [148]. Thus, the strain hardening rate decreases by increasing the strain amplitude. On the other hand, under tensile loading, detwinning occurs inside the twinned grains which also accompanies with low strain hardening rate [151]. By contrast, following the detwinning exhaustion, strain hardening rate increases dramatically. The increase in the hardening rate is attributed to the new orientation of HCP unit cells inside the grains of the alloy after detwinning that causes the activation of higher order non-basal slip systems, which has significantly higher critical resolved shear stress (CRSS), and compression twinning systems [25][152][153].

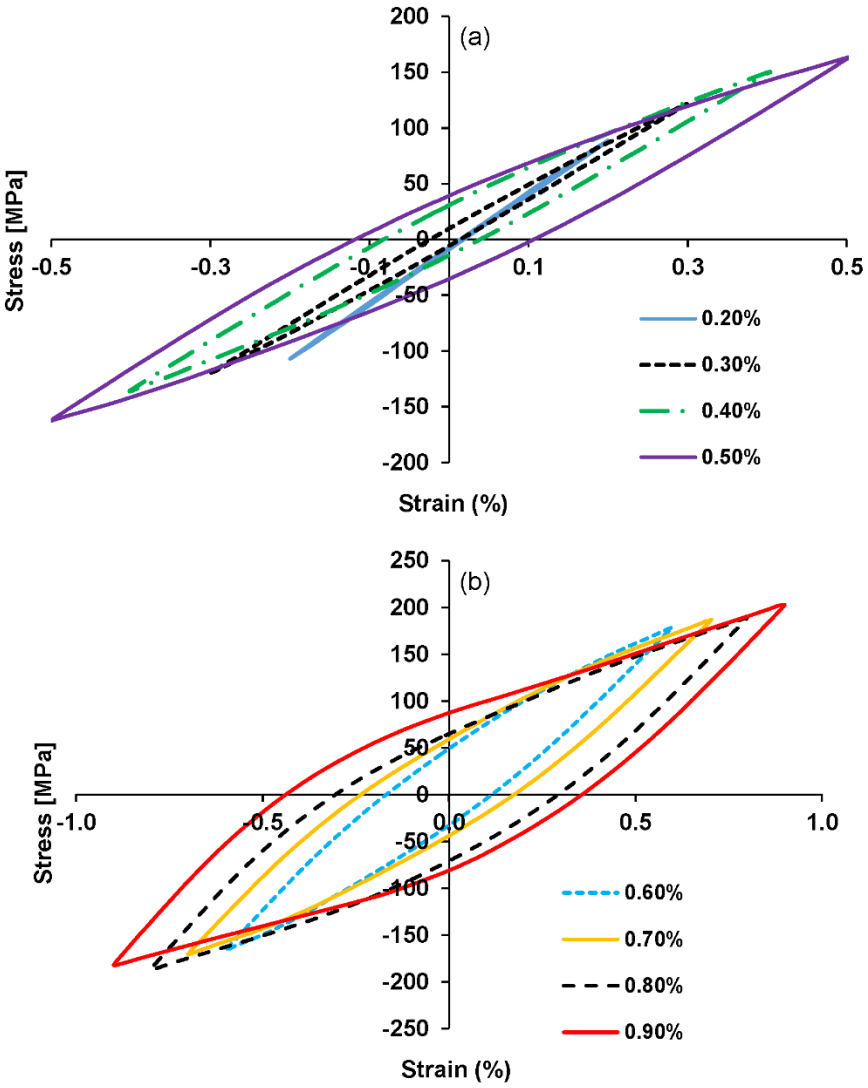

Figure 42. Half-life hysteresis loops for as-cast ZK60 obtained from fully reversed strain-controlled fatigue tests at different strain amplitudes of (a) 0.2 -0.5% and (b) 0.6-0.9%

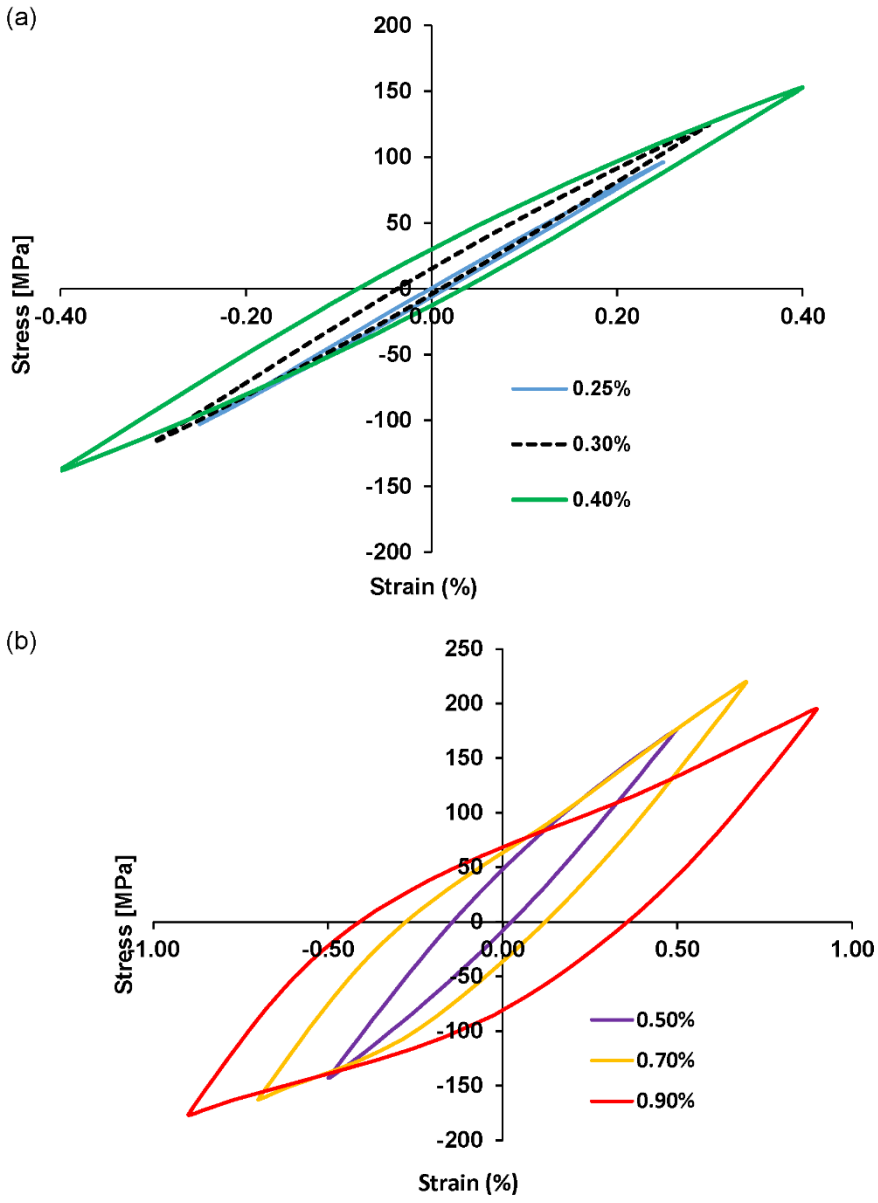

Figure 43. Half-life hysteresis loops for forged ZK60 obtained from fully reversed strain-controlled fatigue tests at different strain amplitudes of (a) 0.2 -0.4% and (b) 0.5-0.9%

Figure 44 presents the cyclic tension and cyclic compression curves for the as-cast and cast-forged ZK60. The curves were obtained by connecting the peak stresses of the half-life

hysteresis loops at different strain amplitudes. The tensile and compressive peak stresses for the as-cast alloy were almost similar in comparison to the forged alloy. For the forged alloy, however, the tensile peak stresses were higher than the compressive ones for strain amplitudes higher than 0.4%. This concurs well with Figure 42 and Figure 43 where symmetric and asymmetric cyclic behaviors were observed for the as-cast and forged samples, respectively.

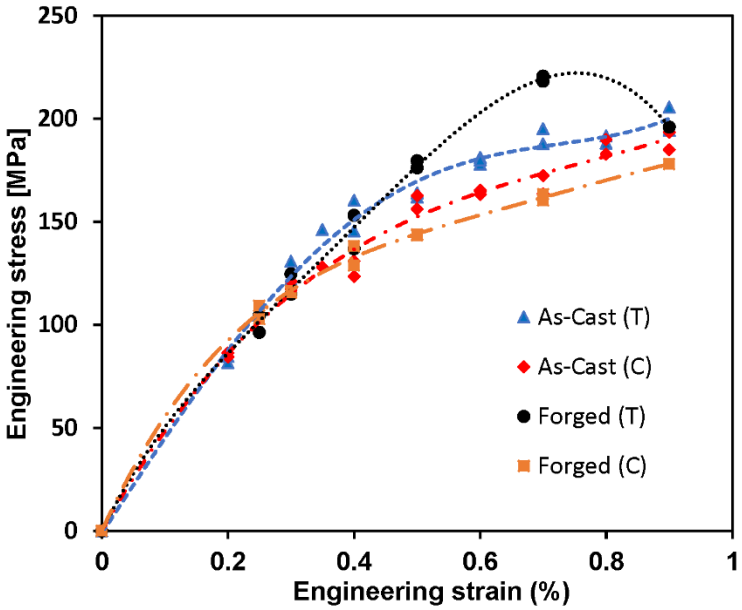

Figure 44. Cyclic behavior of as-cast and forged ZK60 obtained by connecting the peak stresses of the half-life hysteresis loops at different strain amplitudes

Note: T is for tensile peaks on and C is for compressive peaks

The tensile quasi-static and cyclic behavior of as-cast and cast-forged alloys are depicted in Figure 45. It is noticed that at low strain values, the quasi-static and cyclic behaviors are approximately the same; however, with increasing the strain values, the cyclic curves become harder than the quasi-static curves, which confirms the cyclic hardening behavior for the two materials. Figure 46 (a) and (b) also show the evolution of stress amplitude during strain-controlled test for the as-cast and forged ZK60, respectively. For the both conditions, as-cast and forged, the stress amplitude is almost constant at lower strain amplitudes up to 0.3%. However, stress amplitude has an increasing trend for higher strain amplitudes, which

demonstrates cyclic hardening behavior. The variation of stress amplitude with the number of cycles has already been studied for extruded ZK60 [41]. The results for the extruded alloy were the same as the results of this study for the forged alloy. The stress amplitude did not change up to strain amplitude of 0.35%, it started to increase for the strain amplitudes of 0.4% and higher. It was also reported that increasing the loading cycles increased the dislocation density which act as barriers against the movement other dislocation which builds up the resistance to plastic deformation resulting in cyclic hardening [126][154]. Moreover, at higher strain amplitudes, and in particular for the forged alloy, twining is an active mode of deformation under compression loading. Twin deformations in the compressive reversal are partially reversed in the subsequent tensile reversal, but some residual twins remain. The interactions of dislocation-twin besides twin-twin brings about the strain hardening [36][126][155].

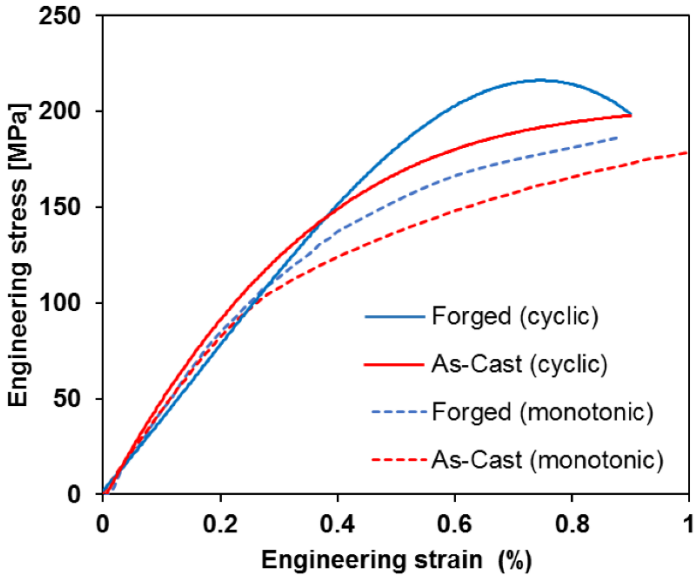

Figure 45. Comparison of the cyclic tensile and quasi-static tensile behavior for as-cast and forged ZK60

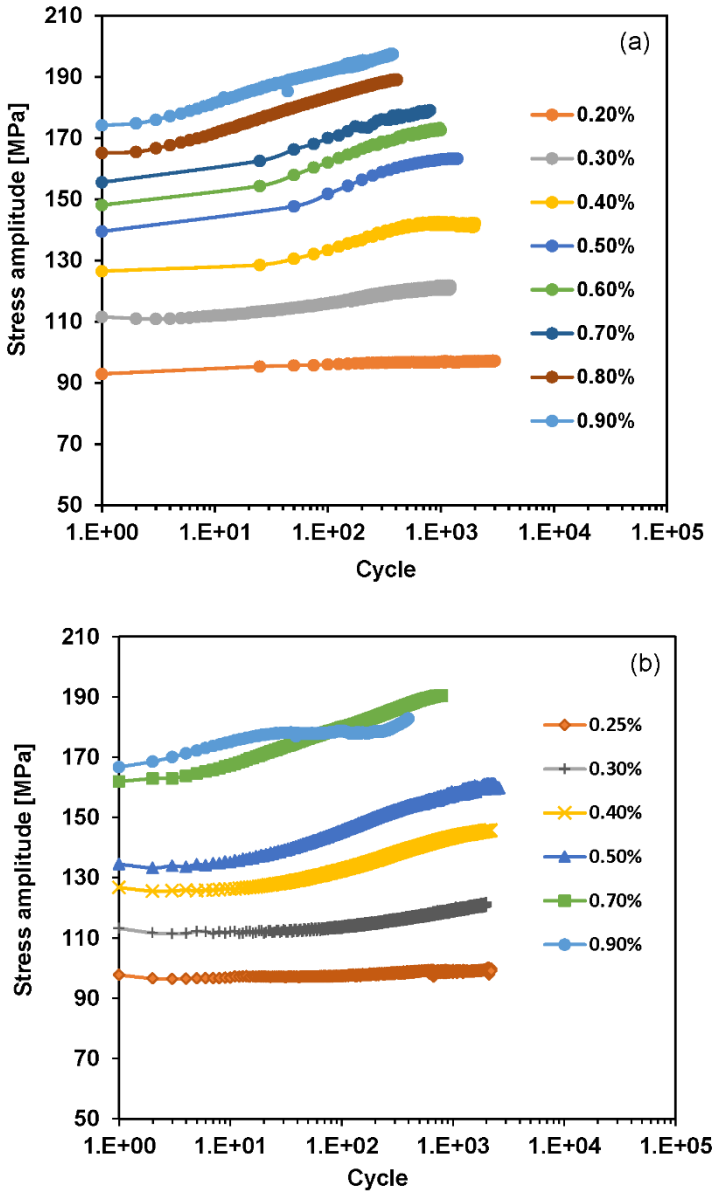

Figure 46. The variation of stress amplitude vs. number of cycles for (a) as-cast and (b) forged ZK60 under different strain amplitudes

Figure 46 (b) shows a drop in the stress amplitude at the strain amplitude of 0.9%. Also, in both Figure 44 and Figure 45, a decrease in the tensile peak stress is observed at the total strain amplitude of 0.9%. This behavior might be due to the micro-cracks formation near grain

boundaries and twin tips, as has been previously observed for pure Mg [155]. With increasing strain amplitude, and accordingly the applied load, some micro-cracks may initiate inside the microstructure reducing the material's ability to endure tensile loading. On the contrary, the compressive peak stress has increased at the strain amplitude of 0.9% (as seen in Figure 44), which can be due to crack closure occurring. Hence, micro-cracks deteriorate the strength of material under tension but not under compression. Aside from this, the drop in the maximum tensile peak had already been seen for extruded ZK60 Mg alloy after the strain amplitude of 0.8% [41][42].

The number of cycles to failure, N_f, against the applied total strain amplitudes ($\Delta\varepsilon_t/2$) for the ZK60 Mg alloy in as-cast and forged conditions is depicted in Figure 47, along with some data available in literature for extruded ZK60 [43]. The as-cast alloy obtained lower fatigue life to that of the forged ZK60 Mg alloy at high strain amplitudes and significantly lower life compared to the forged alloy at low strain amplitudes. Also, the extruded ZK60 shows shorter fatigue life for the similar testing condition. It should be mentioned that the fatigue life is always higher in forged samples compared to the extruded materials above a total strain amplitude of 0.4%. Additionally, a couple of run-out tests were run to assess the strain amplitude leading to 10^7 cycles (run-out). The run-out life was achieved at the total strain amplitude of 0.175% for the as-cast alloy, while the forged ZK60 could endure higher strain amplitude of 0.22%, which confirms the improvement of HCF response. It is reported that the high cycle fatigue life is controlled by the strength of materials [53][156]. Therefore, it is believed that higher strength of the forged alloy compared to the as-cast alloy can lead to the superior fatigue strength in the HCF regime. Additionally, the presence of intermetallics in the microstructure can cause stress concentration, which facilitates crack nucleation. As explained earlier, the forged ZK60 contained less amount of porosities and intermetallics, which can contribute to the longer HCF life [156]. On the other hand, for strain amplitudes higher than 0.4%, twinning is active for the forged alloy due to the strong developed basal texture (as seen in Figure 40 (b)). Twinned lamellas can be a zone for crack initiation leading into a premature fracture happening [155]. Moreover, the tension-compression asymmetry stemming from the induced texture (and not hydrostatic stress as is in the case of strength differential effect of

high strength metals [157]) brings about tensile mean stress which affects the fatigue life adversely. Therefore, the similar fatigue lives for as-cast and forged ZK60 in the LCF regime might be due to combination of different factors: i) improvement of fatigue response as a result of grain refinement and lower density of porosities and intermetallics, ii) the adverse effects of strong basal texture induced during the forging process.

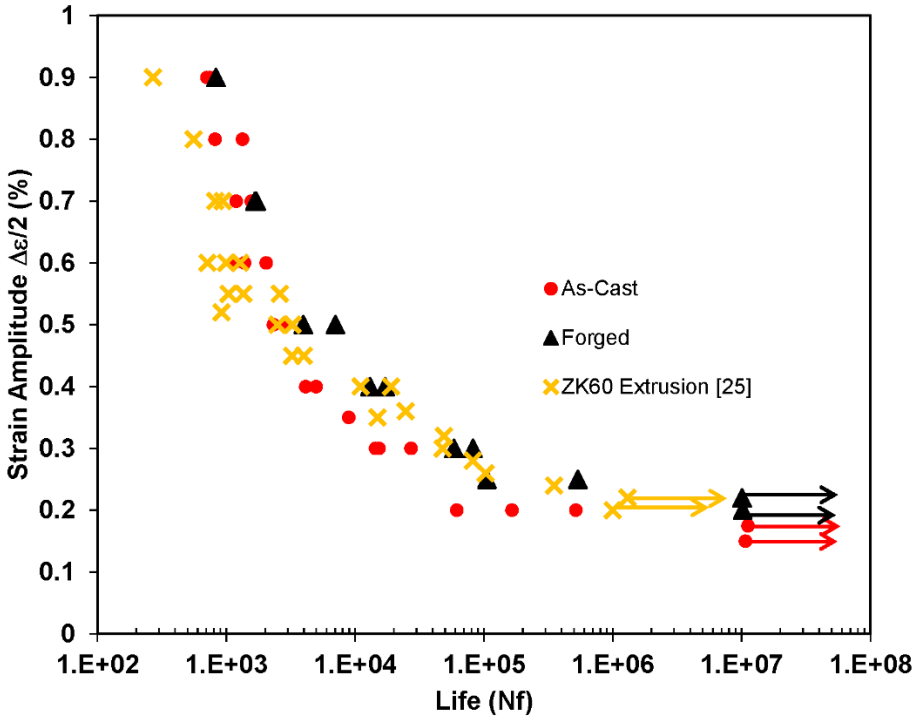

Figure 47. Strain-life data obtained from fully reversed strain-controlled cyclic tests for cast and cast-forged ZK60

Table 9. Cyclic tests summary for the half-life cycle for as-cast and forged ZK60 Mg alloy

Specimen condition	Strain amplitude (%)	Elastic strain amplitude (%)	Plastic strain amplitude (%)	Max stress [MPa]	Min stress [MPa]	Life	Elastic strain energy density [MJ/m3]	Plastic strain energy density [MJ/m3]
As-cast	0.9	0.439	0.461	198	-197	750	0.44	1.95
	0.9	0.428	0.472	203	-183	709	0.46	1.95
	0.8	0.420	0.380	191	-188	1338	0.40	1.47
	0.8	0.421	0.379	192	-186	818	0.41	1.48
	0.7	0.407	0.293	187	-167	1563	0.39	0.99
	0.7	0.398	0.302	187	-171	1194	0.39	0.99
	0.6	0.391	0.209	185	-167	1388	0.38	0.67
	0.6	0.384	0.216	179	-166	2040	0.36	0.67
	0.5	0.359	0.141	164	-160	2858	0.30	0.49
	0.5	0.363	0.137	164	-163	2321	0.30	0.49
	0.4	0.315	0.085	160	-123	4149	0.28	0.24
	0.4	0.314	0.086	149	-134	4996	0.25	0.23
	0.3	0.271	0.029	122	-121	14417	0.17	0.07
	0.3	0.269	0.031	128	-114	15299	0.18	0.07
	0.3	0.256	0.044	114	-117	27137	0.15	0.06
	0.2	0.184	0.016	81	-84	516579	0.07	0.01
	0.2	0.190	0.010	85	-87	165385	0.08	0.01
	0.175	0.175	0.000	73	-74	>10000000	0.06	0.00
	0.15	0.150	0.000	66	-64	>10000000	0.05	0.00
Forged	0.9	0.416	0.484	197	-179	832	0.43	1.81
	0.7	0.420	0.280	220	-161	1707	0.54	1.01
	0.7	0.427	0.273	221	-164	1674	0.54	0.99
	0.5	0.359	0.141	180	-144	3976	0.36	0.37
	0.5	0.355	0.145	176	-143	7041	0.34	0.38
	0.4	0.324	0.076	154	-139	13090	0.26	0.28
	0.4	0.295	0.105	138	-130	17152	0.21	0.28
	0.3	0.256	0.044	125	-116	58490	0.17	0.11
	0.3	0.268	0.032	115	-117	82445	0.15	0.11
	0.25	0.238	0.012	105	-110	105616	0.12	0.03
	0.25	0.221	0.029	97	-104	536971	0.10	0.03
	0.22	0.220	0.000	92	-93	>10000000	0.09	0.00
	0.2	0.200	0.000	88	-88	>10000000	0.09	0.00

5.3.4 Fracture surface analysis

SEM images of the fatigue fracture surface of as-cast and cast-forged samples at two strain amplitudes of 0.5% and 0.9% are presented in Figure 48. Fatigue crack initiation (FCI), fatigue crack growth (FCG), and final fracture (FF) areas are demarcated as the main features of the fracture surface. It is clear that the forged samples tested at different strain amplitudes shows multiple FCI sites while the as-cast sample exhibits lower number of FCI sites. In general, increasing the strain amplitudes, the FCG zone decreased which is the indication of shorter fatigue life as seen in Figure 47. At the same time, a wider FCG zone can be detected on the fracture surface of the forged sample compared to the as-cast sample indicating the longer fatigue life of the forged sample. This can be due to the fact that the microstructure of the forged alloy contains finer grains and also that less volume fraction of porosities and inclusions exists in the material (Figure 39). Figure 49 depicts the crack initiation site of the as-cast alloy at higher magnifications. Most of the cracks have initiated from the open surface area as a consequence of the extrusion/intrusion of the slip bands formation, known as persistent slip band (PSB), or casting porosities. These porosities can join and make voids leading to a crack formation. At the same time, the interactions between grains and PSB, which are made by cyclic irreversible slips, are reported to be a major drive for crack initiation in different metals, especially in HCF regime [158][159][160]. However, other studies [161] also stated that in the LCF regime, crack initiation and propagation proceed along PSB through dendritic cells in the as-cast alloys as well. Figure 50 shows the crack initiation sites of the forged alloy at the similar two total strain amplitudes at higher magnifications. As shown in Figure 50 (b), oxide layers are observed on the FCI sites. It is also noticed that the matrix was delaminated and formed a step like morphology during crack propagation. In addition, secondary cracks were also noticed in the matrix which is an indication of strengthening of the matrix (Figure 50 (d)). As seen in Figure 51, micro-cliffs, step like morphologies parallel to the fatigue cracks, and fatigue striation (FS) are the main characteristics which are marked by arrows of the FCG zone. It is well established that the fatigue cracks are propagating perpendicular to the FS and parallel to the micro-cliffs [162].

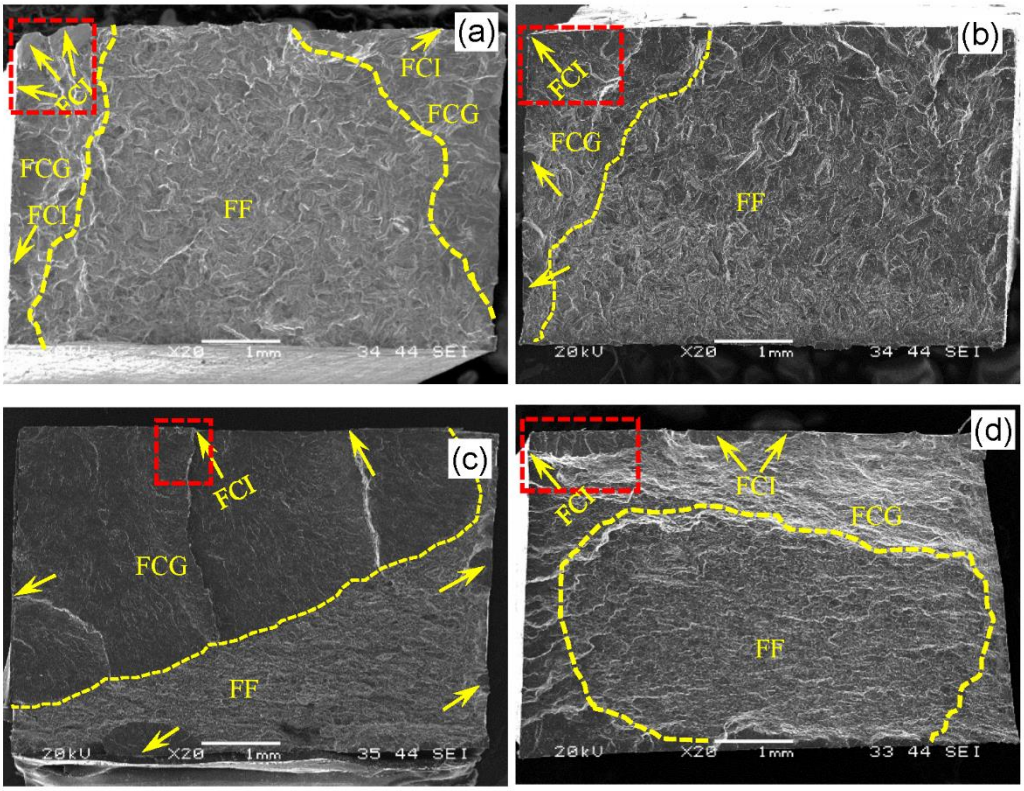

Figure 48. SEM images of fatigue fracture surfaces of ZK60 Mg alloy at different strain amplitudes (a) as-cast at ε_a =0.5%, (b) as-cast at ε_a =0.9%, (c) forged at ε_a =0.5%, and (d) forged at ε_a =0.9% (Yellow arrows indicate the position of FCI sites, and the dashed lines represent the boundary between the FCG and the FF zones)

Each striation mark denotes the fatigue crack propagation in each cycle. It is noticed that the FS marks on the fracture surface of the forged alloy are finer than those on the surface of as-cast alloy under the same strain amplitude. For instance, at the total strain amplitude of 0.5%, the average distance between the striations on the fracture surface of as-cast ZK60 is ~1.2 μm, while the forged material exhibits FS with average distance of ~0.65 μm. This corresponds well with the longer fatigue life of the forged alloy. At the same time, it is noticed that with increasing the strain amplitude (Figure 51 (b) and Figure 51 (d)), FS marks become coarser

(~2.6 µm and 0.9 µm between the striations for the as-cast and forged ZK60, respectively, at the total strain amplitude of 0.9%) because more cracks opening lead to greater plasticity on each cycle.

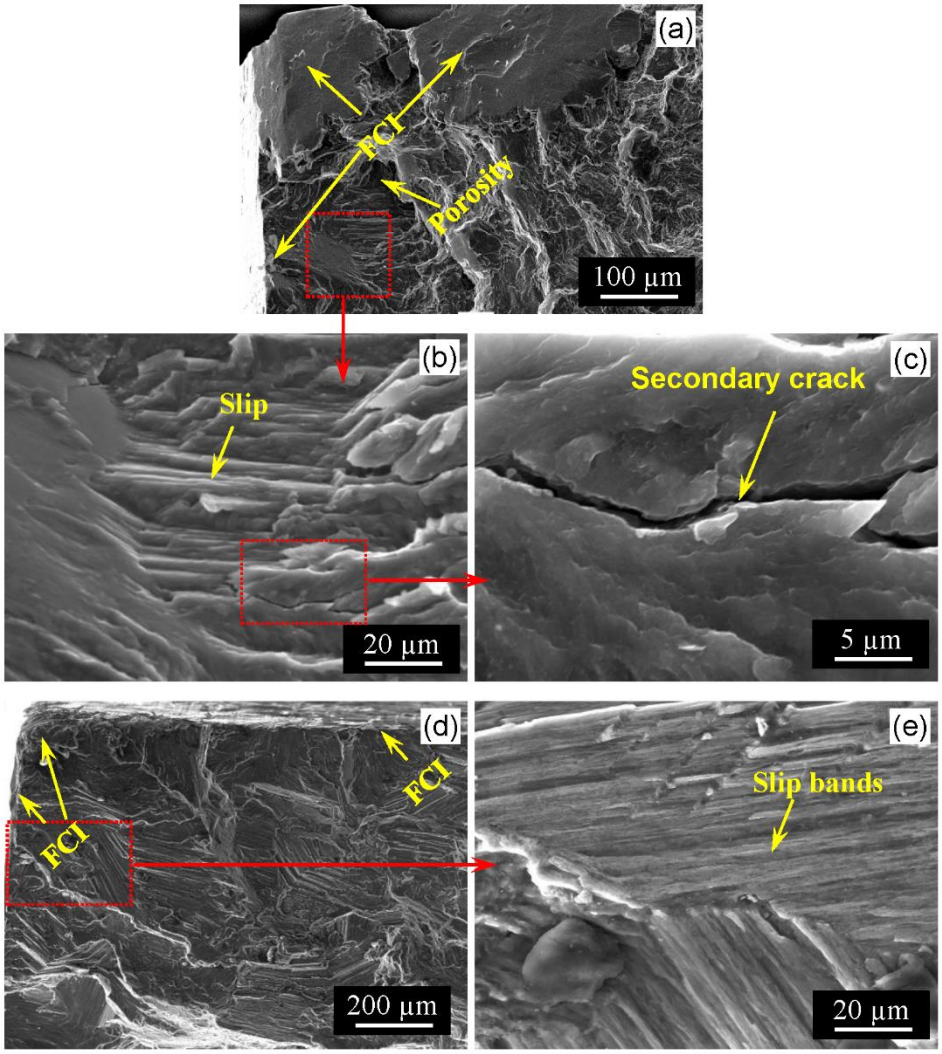

Figure 49. SEM images of FCI locations in as-cast ZK60 tested at strain amplitudes of ε_a =0.5% (a-c), and ε_a =0.9% (d, e)

Figure 52 represents the magnified FF zones on the fatigue fracture surface of the as-cast and forged ZK60. It is worth to mention that FF area for all testing conditions show tensile like

morphology as illustrated in [143]. As depicted in Figure 52, the as-cast alloy resembles a quasi-cleavage surface with some dimples besides tear ridges. In contrast, more dimples can be observed on the fracture surface of the forged alloy. This is in correlation with the result obtained under tensile quasi-static results (Table 8) that the forged alloy exhibits higher ductility.

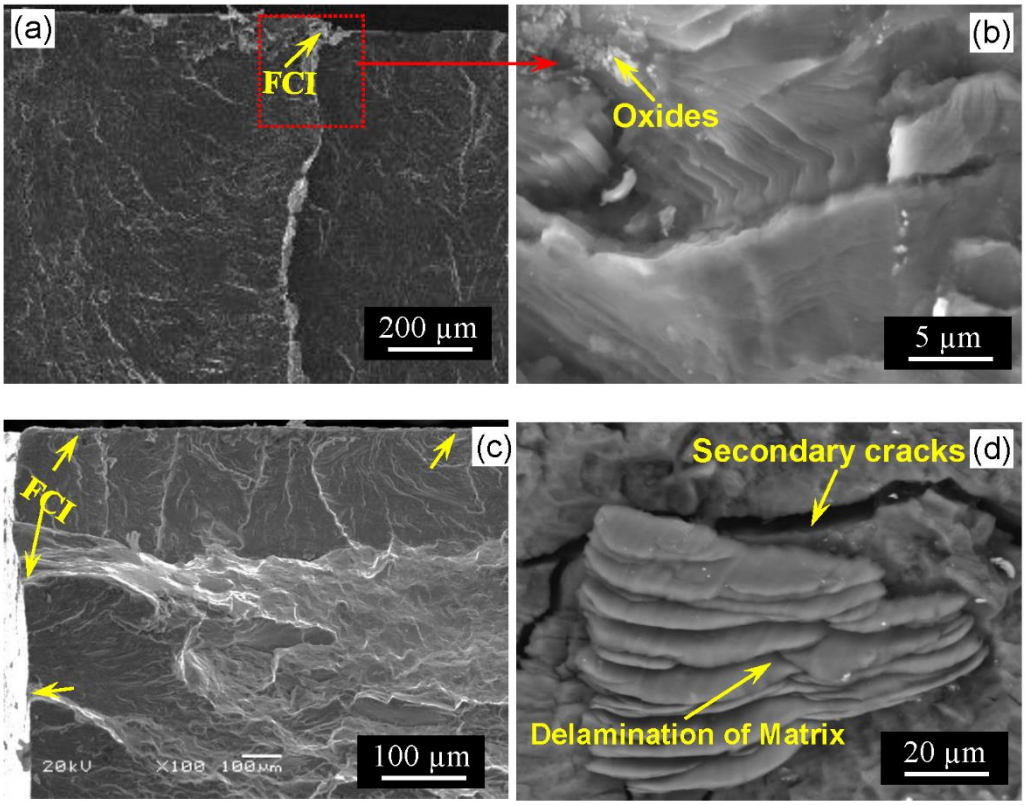

Figure 50. SEM images of fatigue fracture surfaces for cast forged ZK60 tested at a strain amplitude of 0.5% (a, b) and 0.9% (c, d) showing the crack initiation sites with (d) secondary cracks and delamination of the matrix

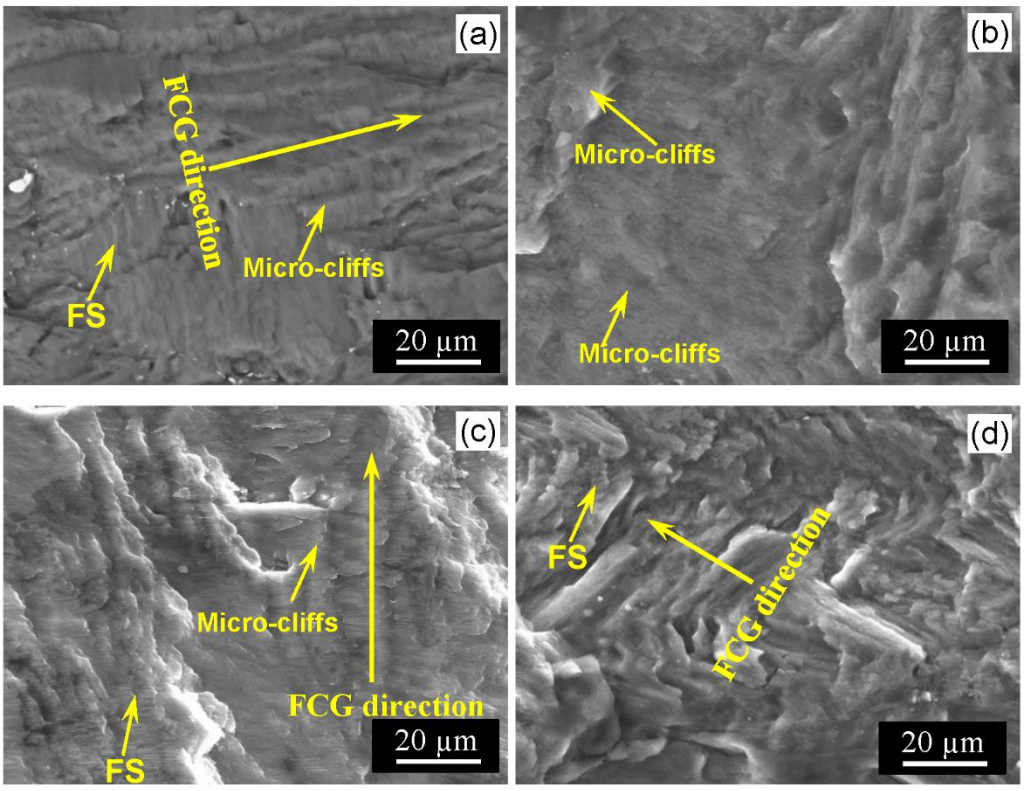

Figure 51. SEM images of the FCG regions of ZK60 under different strain amplitudes (a) as-cast at ε_a =0.5%, (b) as-cast at ε_a =0.9%, (c) forged at ε_a =0.5%, and (d) forged at ε_a =0.9%

At the same time, the SEM images at the FF evident that intermetallics played a great roll in fatigue life (Figure 53). As discussed earlier that the volume fraction of intermetallics in the as-cast sample is higher than the forged sample (Figure 39). As displayed in Figure 53 (a, b), the identified intermetallics on the fracture surfaces of as-cast samples tested at the different stress amplitude of 0.5% and 0.9% were $ZnZr_2$ and $MgZn_2$, which exhibits multiple cracks were the potential sites of the nucleation of cracks results premature failure and shorter the fatigue life. In contrast, the fracture surfaces of forged samples (Figure 53 (c, d)) tested at the similar strain amplitudes shows less volume fraction of the intermetallic (only $ZnZr_2$) results lower nucleation sites for the cracks leading to the longer fatigue life. The combined action of grain refinement, modification of texture and strengthening of the matrix by dissolving the

intermetallics (solid solution strengthening) and reducing the defects has caused the forged sample to obtain longer fatigue life compared to the as-cast ZK60. Similar type of fatigue life enhancement was observed in cast forged AZ31B [47].

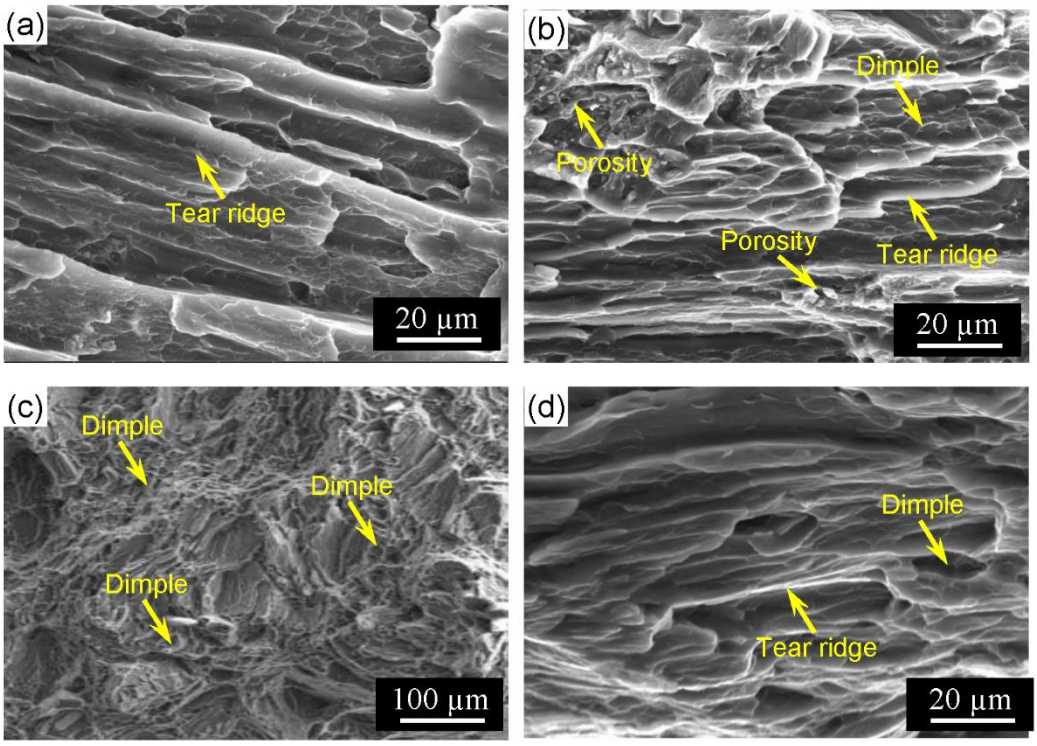

Figure 52. SEM images of the FF regions of ZK60 under different strain amplitudes (a) as-cast at ε_a =0.5%, (b) as-cast at ε_a =0.9%, (c) forged at ε_a =0.5%, and (d) forged at ε_a =0.9%

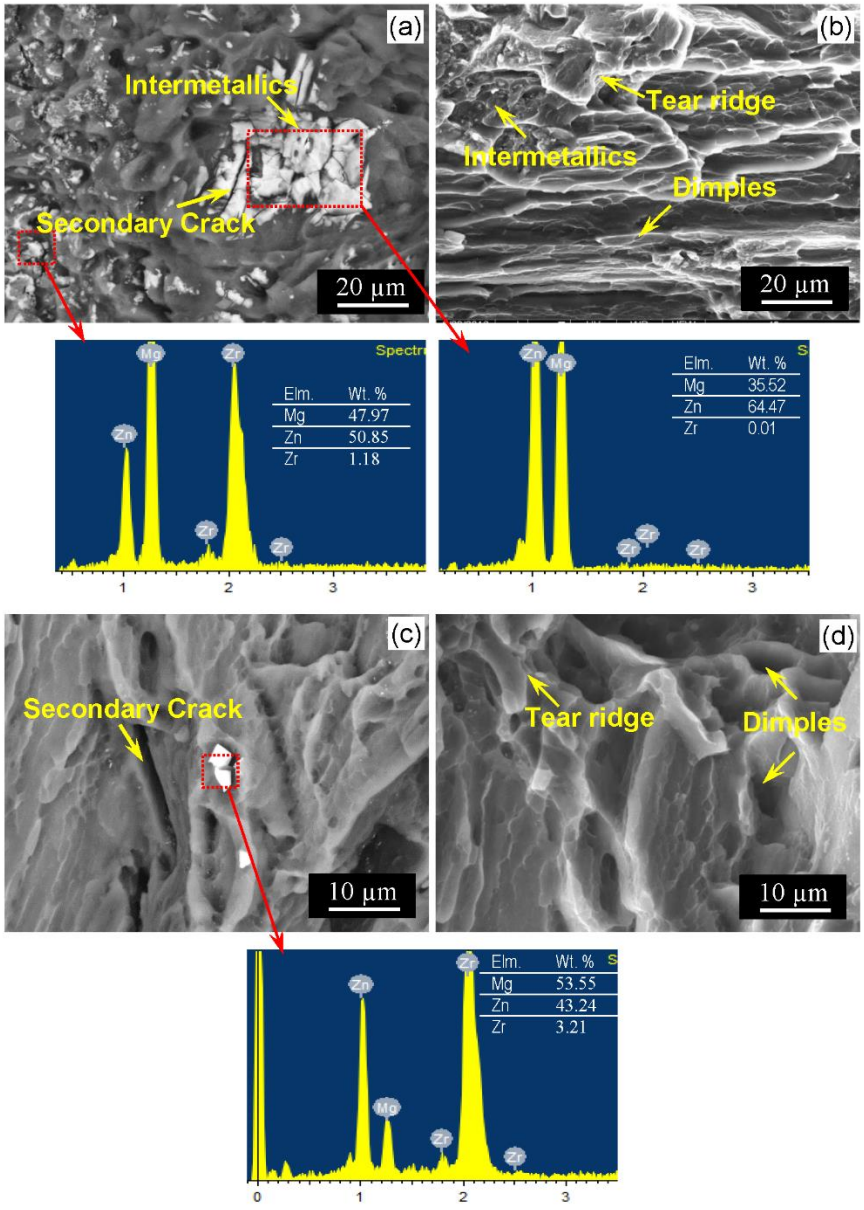

Figure 53. SEM images with EDX spectrums of the FF regions of ZK60 under different strain amplitudes (a) as-cast at ε_a =0.5%, (b) as-cast at ε_a =0.9%, (c) forged at ε_a =0.5%, and (d) forged at ε_a =0.9%

5.3.5 Fatigue modeling

Fatigue is the primary failure mechanism in most engineering components; hence, the accurate prediction of the fatigue life of an in-service component is of critical importance. Several fatigue models were established to predict the fatigue life leading to the fatigue damage per cycle and compared with the experimental obtained fatigue life data [70], [71], [163], [164]. The suggested models are either stress- strain- or energy-based. In this study, the stress based approached may not be suitable for modelling the ZK60 alloy subjected to strain-controlled fatigue testing [165]. At the same time, the well-established fatigue models presently available in literature were either for isotropic materials, or for other forms of wrought Mg alloys (such as rolling or extrusions) with different characteristics than the current forged ZK60 alloy. Therefore, the present study adopted the following models to describe the cyclic behavior of the studied ZK60 alloy.

The strain-life response of metals is often modeled by Coffin-Manson-Basquin (Morrow's) equation [166][167]. The elastic strain and plastic strain amplitudes are defined by the Basquin and Coffin-Manson equations, respectively as:

$$\varepsilon_{a,elastic} = \frac{\sigma_f'}{E}(2N_f)^b \quad 5\text{-}1$$

$$\varepsilon_{a,plastic} = \varepsilon_f'(2N_f)^c \quad 5\text{-}2$$

where, $\varepsilon_{a,elastic}$ and $\varepsilon_{a,plastic}$ are the elastic and plastic strain amplitudes, respectively. E is the modulus of elasticity, which is approximately 45 GPa for ZK60 Mg alloy [71] and close to the average modulus of elasticity obtained from cyclic tests, and N_f is the fatigue life. σ_f' and b are the fatigue strength coefficient and fatigue strength exponent, respectively, and ε_f' and c are fatigue ductility coefficient and fatigue ductility exponent, respectively. The total strain amplitude, ε_a, is then obtained from:

$$\varepsilon_a = \frac{\sigma_f'}{E}(2N_f)^b + \varepsilon_f'(2N_f)^c \quad 5\text{-}3$$

Eq. (1) and (2) were employed to calculate the Coffin-Manson Parameters which are listed in Table 10. Figure 54 represents the fatigue life predicted by the Coffin-Manson model

versus the life obtained from the experiments. According to this figure, the majority of data points are located between the factor of 2 bound lines. However, two data points corresponding to $\varepsilon_a = 0.25\%$ lay outside this domain.

Table 10. Coffin-Manson parameters for the as-cast and cast-forged ZK60 magnesium alloy

fatigue parameter	As-cast ZK60	Forged ZK60
σ_f' (MPa)	442	510
b	-0.12	-0.12
ε_f'	0.31	0.37
c	-0.62	-0.59

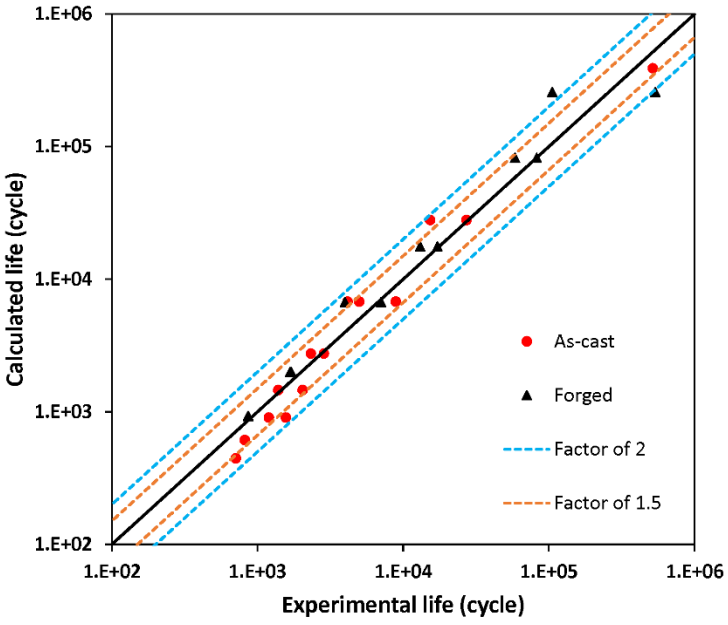

Figure 54. Predicted life vs. experimental life for as-cast and forged ZK60 Mg alloy using the Coffin-Manson model

The Jahed-Varvani model (JV) [91] [168] was also employed in this study to predict the fatigue life of as-cast and forged ZK60. The JV model relates the fatigue life to a measure of strain energy, as opposed to the Coffin-Manson model relating the life to strain amplitude.

The JV model accounts for the mean stress effects. Because energy is a scalar parameter, the strain energy corresponding to different stress/strain components can be manipulated algebraically, without the concern of different material orientation or loading direction [71]. According to this model, the total strain energy density is expressed by two terms: i) the positive elastic strain energy density, ΔE_e^+, and ii) the plastic strain energy density, ΔE_p [169]. The former part which accounts for the effect of mean stress can be calculated by Eq. 4, where σ_{max} is the tensile peak stress of the hysteresis loop. In addition, the plastic strain energy density is calculated from the area inside the half-life hysteresis loop.

$$\Delta E_e^+ = \frac{\sigma_{max}^2}{2E} \qquad 5\text{-}4$$

Figure 55 displays the schematic of the total energy density obtained from the half-life hysteresis loop.

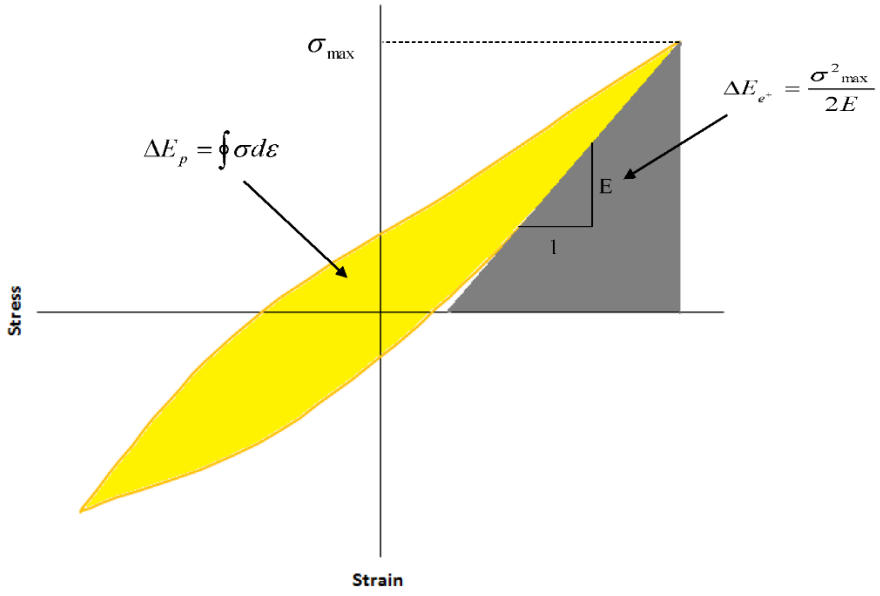

Figure 55. Schematic illustration of positive elastic and plastic strain energy densities [74]

The strain energy density is then related to the fatigue life as:

$$\Delta E = E_e'(2N_f)^B + E_f'(2N_f)^C \quad 5\text{-}5$$

where E_e', B, E_f', and C are the fatigue strength coefficient, the fatigue strength exponent, the fatigue toughness coefficient, and the fatigue toughness exponent, respectively. The values of these parameters are calculated and listed in Table 11.

Figure 56 displays the correlation between the predicted fatigue life and the experimentally obtained fatigue life of the as-cast and forged materials. As can be seen, the majority of the data points are banded within the lines of factor of 1.5 which shows the promise of JV model to predict the fatigue life of as-cast and forged ZK60 under uniaxial loading.

There was more scatter seen in the Coffin-Manson results due to the fact that Coffin-Manson equation does not account for the mean stress effect, whereas mean stress is generated during fully reversed strain-controlled tests due to asymmetry. However, in the JV model, as indicated previously, the elastic part of the total strain energy density accounts for the means stress effect.

Table 11. The energy parameters of JV fatigue model for the tested as-cast and cast-forged ZK60 magnesium alloy

fatigue parameter	As-cast ZK60	Forged ZK60
E_e' (MJ/m^3)	4.20	4.30
B	-0.30	-0.27
E_f' (MJ/m^3)	1525.50	290.60
C	-0.92	-0.70

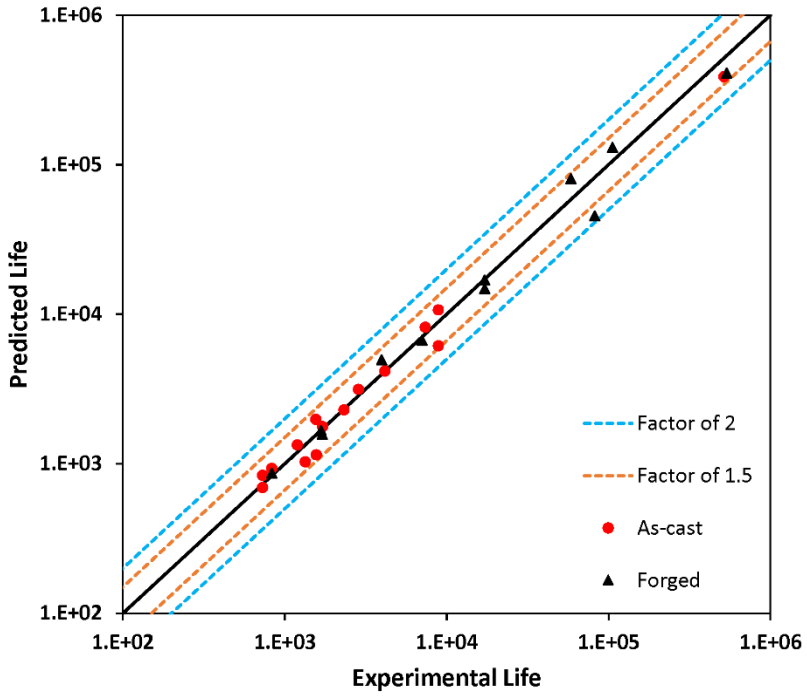

Figure 56. Predicted life versus the experimental life for as-cast and forged ZK60 Mg alloy using the JV fatigue model

5.4 Conclusion

In the present study, the cyclic behavior of as-cast and cast-forged ZK60 was studied at different strain amplitudes. From the above results and discussion, the following conclusions are made:

1. While as-cast ZK60 displays symmetric hysteresis loops at different strain amplitudes, the shape of hysteresis loops for the forged material depends on the applied strain amplitude. For the strain amplitudes lower than 0.4%, the shape of the hysteresis loops is symmetric and dislocation slip governs the deformation. At the strain amplitude of 0.4%-0.5%, twinning is activated under the compression reversal and detwinning occurs during the subsequent tension reversal during the first few cycles; therefore, the hysteresis loop shape is sigmoidal. However, the half-life hysteresis loop is symmetric, as no more twinning/ detwinning is happening. For strain amplitudes more than 0.5%,

the applied stress is large enough to make twinning/ detwinning occurring during the whole life as a result of the basal texture, thereby the half-life hysteresis loop as well as the second cycle hysteresis loop is asymmetric.

2. In general, forged ZK60 is exhibiting superior fatigue strength compared to the as-cast alloy owing to the grain refinement happening in the forged material and lower amount of porosities and second-phase particles inside its microstructure.
3. Different mechanisms of crack initiation for the forged material are proposed. At high cycle fatigue regime, persistent slip bands (PSB) and intermetallics are the major cause of crack nucleation. On the other hand, for the strain amplitudes higher than 0.4%-0.5%, that twinning is occurring, the interaction between twin-twin bands besides twin-dislocation can also form cracks leading to final fracture.

The Coffin-Manson fatigue model and the energy-based JV model were assessed in terms of the fatigue life prediction for the as-cast and forged ZK60. Both models yielded predictions with the 2x band, however, due to consideration of mean stress through elastic strain energy density, the JV model predictions were confined within 1.5x band.

Chapter 6

Anisotropy in the Quasi-static and Cyclic Behavior of ZK60 Extrusion: Characterization and Fatigue Modeling

6.1 Introduction

Light-weighting is one of the pivotal steps toward fuel consumption reduction in vehicles and consequent environmental preservation. Magnesium (Mg) alloys, as the lightest engineering metal, could contribute to this process. However, they should be well characterized in order to elucidate their properties for the automotive industry [14]. In spite of the wide implementation of Mg alloys in many non-structural automotive components, their current application in load-bearing sections is limited [12]. To expand their application in load-bearing components, it is of key importance to investigate Mg alloys' behavior under both static and cyclic loading.

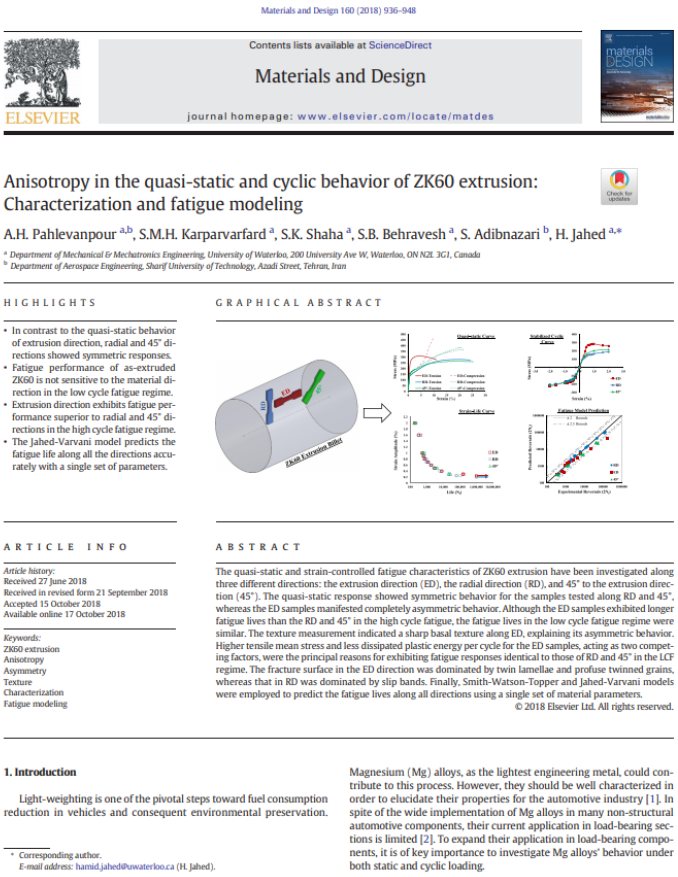

Materials and Design 160 (2018) 936-948

Contents lists available at ScienceDirect

Materials and Design

journal homepage: www.elsevier.com/locate/matdes

Anisotropy in the quasi-static and cyclic behavior of ZK60 extrusion: Characterization and fatigue modeling

A.H. Pahlevanpour [a,b], S.M.H. Karparvarfard [a], S.K. Shaha [a], S.B. Behravesh [a], S. Adibnazari [b], H. Jahed [a,*]

[a] Department of Mechanical & Mechatronics Engineering, University of Waterloo, 200 University Ave W, Waterloo, ON N2L 3G1, Canada
[b] Department of Aerospace Engineering, Sharif University of Technology, Azadi Street, Tehran, Iran

HIGHLIGHTS

- In contrast to the quasi-static behavior of extrusion direction, radial and 45° directions showed symmetric responses.
- Fatigue performance of as-extruded ZK60 is not sensitive to the material direction in the low cycle fatigue regime.
- Extrusion direction exhibits fatigue performance superior to radial and 45° directions in the high cycle fatigue regime.
- The Jahed-Varvani model predicts the fatigue life along all the directions accurately with a single set of parameters.

GRAPHICAL ABSTRACT

ARTICLE INFO

Article history:
Received 27 June 2018
Received in revised form 21 September 2018
Accepted 15 October 2018
Available online 17 October 2018

Keywords:
ZK60 extrusion
Anisotropy
Asymmetry
Texture
Characterization
Fatigue modeling

ABSTRACT

The quasi-static and strain-controlled fatigue characteristics of ZK60 extrusion have been investigated along three different directions: the extrusion direction (ED), the radial direction (RD), and 45° to the extrusion direction (45°). The quasi-static response showed symmetric behavior for the samples tested along RD and 45°, whereas the ED samples manifested completely asymmetric behavior. Although the ED samples exhibited longer fatigue lives than the RD and 45° in the high cycle fatigue, the fatigue lives in the low cycle fatigue regime were similar. The texture measurement indicated a sharp basal texture along ED, explaining its asymmetric behavior. Higher tensile mean stress and less dissipated plastic energy per cycle for the ED samples, acting as two competing factors, were the principal reasons for exhibiting fatigue responses identical to those of RD and 45° in the LCF regime. The fracture surface in the ED direction was dominated by twin lamellae and profuse twinned grains, whereas that in RD was dominated by slip bands. Finally, Smith-Watson-Topper and Jahed-Varvani models were employed to predict the fatigue lives along all directions using a single set of material parameters.

1. Introduction

Light-weighting is one of the pivotal steps toward fuel consumption reduction in vehicles and consequent environmental preservation. Magnesium (Mg) alloys, as the lightest engineering metal, could contribute to this process. However, they should be well characterized in order to elucidate their properties for the automotive industry [1]. In spite of the wide implementation of Mg alloys in many non-structural automotive components, their current application in load-bearing sections is limited [2]. To expand their application in load-bearing components, it is of key importance to investigate Mg alloys' behavior under both static and cyclic loading.

* Corresponding author.
E-mail address: hamid.jahed@uwaterloo.ca (H. Jahed).

Figure 57. A.H. Pahlevanpour, SMH. Karparvarfard et al., "Anisotropy in the quasi-static and cyclic behavior of ZK60 extrusion: Characterization and fatigue modeling." *Materials & Design* 160 (2018): 936-948.

The hexagonal close-packed (HCP) crystal structure of Mg brings about a strong basal texture in its wrought alloys [24]. As they undergo forming processes, such as rolling and extrusion, the basal planes will be lined up parallel to the working direction. This intense

crystallographic texture will make the $\{10\bar{1}2\}$ pyramidal twin the dominant deformation mechanism under certain loading directions where tension along the c-axis is triggered [170]–[172]. Reversing the load will reorient the twinned crystals toward their initial state; this process is known as detwinning. Twinning-detwinning engenders highly distorted asymmetrical hysteresis loops, mainly in the twinning-induced regions [173], [174]. The directional dependency of twinning-detwinning renders not only the quasi-static tension and compression behaviors but also the fatigue properties of wrought Mg alloys, and so has been widely investigated for such alloys [139], [164], [175], [176].

Anisotropy in Mg alloys can affect the fatigue strength differently in the high-cycle fatigue (HCF) and low-cycle fatigue (LCF) regimes. Sajuri et al. [177] reported that the HCF strength of AZ61 extrusion along the extrusion direction (ED) in stress-controlled experiments is higher than that in the transverse direction (TD) and 45° to the ED. The same characteristic was observed under controlled strain by Jordon et al. [178] for AM30 extrusion in the HCF regime, even though for LCF, loading along ED yields lower life to failure than along TD. Roostaei and Jahed [18] investigated the effect of loading direction on the LCF fatigue characteristics of AM30 extrusion. They reported that TD specimens failed in higher lives when identical strain amplitude is applied to both TD and ED specimens. In contrast, Wang et al. [179] found the opposite while testing ED against TD samples under the strain-control state for ZA81M extrusion, a result they attributed to strengthened twinning deformation as well as to the higher detrimental tensile mean stresses in TD. Xiong and Jiang [180], while experimentally scrutinizing the LCF behavior of AZ80 rolled in four different orientations found that deformation mechanism alteration at a certain strain level affects the material's fatigue resistance with respect to the loading direction. The AZ80 samples in the rolling direction (RD) have the longest life of all other directions for strain amplitudes of less than 0.4%, but increasing the strain to higher values causes the 30° and 60° inclined samples with respect to the rolled plane to exhibit higher fatigue strength.

ZK60, the material under study in this paper, exhibits exceptional strength and ductility due to its alloying elements [181]. However, despite these characteristics, only limited studies have investigated its fatigue characteristics in extrusion form. Xiong et al. [41], [43] and Yu et

al. [42] have studied LCF and cyclic plastic deformation, and Wu et al. [36] explored twinning–detwinning behavior of ZK60 extrusion along the ED. These studies reported asymmetry in both the quasi-static behavior and the cyclic hysteresis loops. In more recent study by Xiong et al. [182], characterizing ZK60 under quasi-static loading along ED and TD revealed intensive anisotropy in the stress-strain response of the material. The reviewed literature discloses a lack of knowledge on the HCF behavior of ZK60 along directions other than ED.

Numerous fatigue damage criteria have been developed and reviewed over the last two decades [183]–[192]. However, most of these criteria have been developed and calibrated for isotropic materials, with dislocation slip being the dominant deformation mechanism. Due to slip dislocation, intergranular and transgranular cracking along the slip lines are the primary cracking behavior under cyclic loading for isotropic material [193]. However, the twinning-detwinning deformation mechanism adds micro-cracking on the twin boundaries as a third mode in Mg alloys [193]. This additional deformation mechanism and its detrimental effects should be reflected in the fatigue damage models proposed for Mg and its alloys. The scalar inherence of energy allows the simple manipulation of the energy values corresponding to the axial and shear components of stress/strain tensors. This feature suggests that strain energy is a good candidate for fatigue damage representation in anisotropic materials. Jahed and Varvani proposed a fatigue model based on the strain energy dissipated in each cycle of loading and on the dominant cracking mechanisms [91]. This model has been widely employed in many related types of research on Mg alloys [17], [18] exhibiting promising results. They improved the capability of the original model to make it applicable to non-proportional loading by adopting Garud's incremental cyclic plasticity model [168], [194]. This extended model has shown promising life estimation for AZ31B under proportional and non-proportional loading in research by Albinmousa and Jahed [46]. Roostaei and Jahed showed that the Smith-Watson-Topper (SWT) and Jahed-Varvani JV parameters yield acceptable life prediction for AM30 extrusion along the different loading directions [18].

Smith–Watson–Topper (SWT) was introduced as a critical plane approach for modeling material in which fatigue cracks are initiated and grew predominantly under tensile loading [88]. Tensile cracking developed in ZK60 extrusion along ED was implied by a single

curve description of the SWT parameter in less than 1.5% strain amplitudes [42]. A similar justification was provided to explain imprecise SWT life estimation when the strain amplitude was increased to larger than or equal to 3.5%, the amplitudes where ED samples fail under compressive loading [43].

This present investigation, therefore, begins with the microscopic characterization of ZK60 extrusion. The cyclic behavior of the material, including its strain-life and stabilized strain-stress response together with fractographic observations, will be presented and rigorously discussed with reference to three different directions: namely, ED, RD, and 45° to ED (45°). Finally, the merits of SWT as a critical plane and JV as an energy-based model will be assessed based on their capability of mimicking experimental data.

6.2 Material and experimental details

6.2.1 Material and specimen

The material investigated in this study, ZK60A Mg alloy in the form of an extruded cylindrical billet with a 127mm diameter, has the chemical composition of Zn 5.5%, Zr 0.71%, other 0.3%, and the balanced weight percent of Mg. The static and fatigue specimens' geometry is depicted in Figure 58 (a) and (b). In order to investigate the anisotropy effect of loading directions, specimens were extracted along three distinctive directions, labeled ED, RD, and 45°, such that gage sections were located at the same radius for all samples. The reference cylindrical coordinate system for specimen extraction relative to the extruded billet is illustrated in Figure 58 (c). ED, RD, and TD denote the extrusion, radial, and tangential directions, respectively.

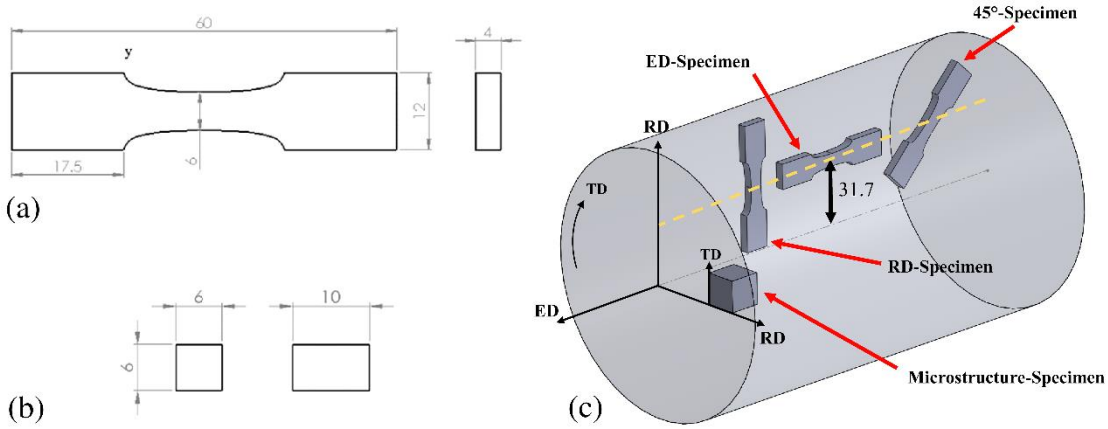

Figure 58. (a) Static tension and fatigue test specimens' geometry, (b) Static compression test specimen geometry, and (c) Reference cylindrical coordinate system for sample extraction (Dimensions are in "mm")

6.2.2 Experimental procedures

For microstructural observation, samples were prepared through the following standard metallographic procedure. First, they were ground using silicon carbide papers with grit No. up to 1200 and polished sequentially with 6-, 3-, 1- and 0.1-micron diamond pastes. In order to reveal the grain/twin boundaries, etchant made of 4.2 g picric acid, 70 ml ethanol, 10 ml acetic acid, and 10 ml distilled water was applied to the sample surface.

The crystallographic texture was characterized by means of X-ray diffraction employing Bruker D8 Discover X-ray diffractometer equipped with an advanced 2D-detector. The characterization started with incomplete pole figures measurement in the back-reflection mode applying CuKα radiation at 40 kV-40 mA. The complete pole figures were calculated using DIFFRAC.texture software.

Quasi-static tests were conducted on Instron 8872 servo-hydraulic axial test frame with 25kN load capacity at the ambient temperature. Dog-bone and cuboid samples were used for the static tension and static compression tests, respectively. In these tests, displacement was controlled in order to maintain the strain rate at 0.015 mm/mm/min in accordance with ASTM E8 [195], while the strain was measured using digital image correlation (DIC) technique.

Fully reversed strain-controlled fatigue tests were performed on the same Instron test frame. These tests were conducted at different strain amplitudes, (R=-1) ranging from 0.2 to 2 %, with at least two trials at each amplitude. The test frequency was selected based on the applied strain amplitude, varying from 0.1 Hz to 10 Hz, to guarantee precise control of the sinusoidal waveform of the strain. The strain was measured by Instron extensometer with a 10 mm gauge length and ±1 mm travel. The fatigue failure was set at 50% drop in the peak tensile force of the stabilized cycle or the final fracture and the test is considered run-out if the sample survives for more than 1 million cycles. Selected fracture samples were analyzed using scanning electron microscope (SEM) to understand the fracture mechanisms.

6.3 Results

6.3.1 Microstructure analysis

The microstructural examination of ZK60 extrusion, shown in Figure 59Error! Reference source not found., disclosed the twin-free bimodal grains, i.e., sizable elongated and small equiaxed grains. Similar microstructural characteristics have been reported for this material [42], [196].

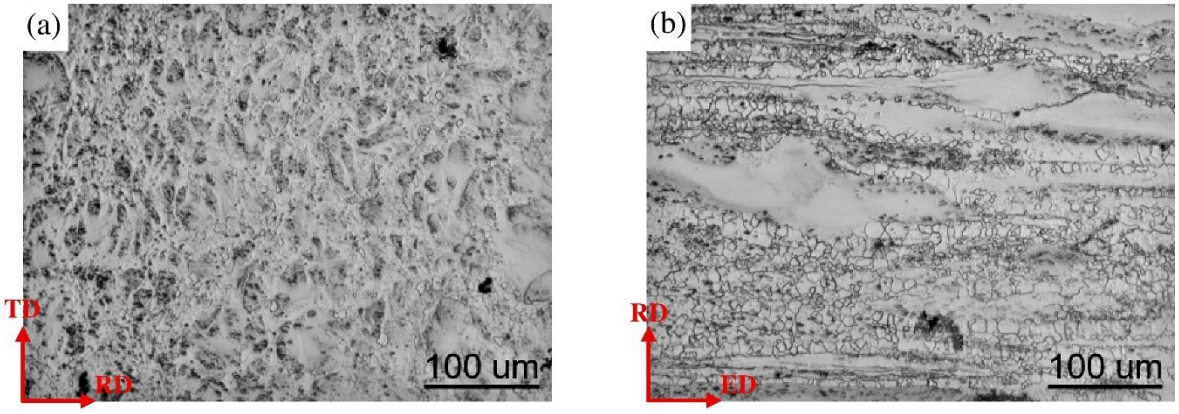

Figure 59. Typical microstructure of ZK60 extrusion: (a) TD-RD plane and (b) RD-ED plane

The pole figures, plotted for both RD-TD and ED-RD planes in Figure 60, revealed that the majority of the c-axes are oriented approximately perpendicular to the ED, but not necessarily parallel to the RD or TD. The crystallographic orientation matches those observed in earlier studies on ZK60 extrusion [182], [196]. This can favor $\{10\bar{1}2\}$ extension-twinning under compression loading in ED samples [36], [182]. The effect of this texture on quasi-static and cyclic behaviors will be thoroughly discussed later.

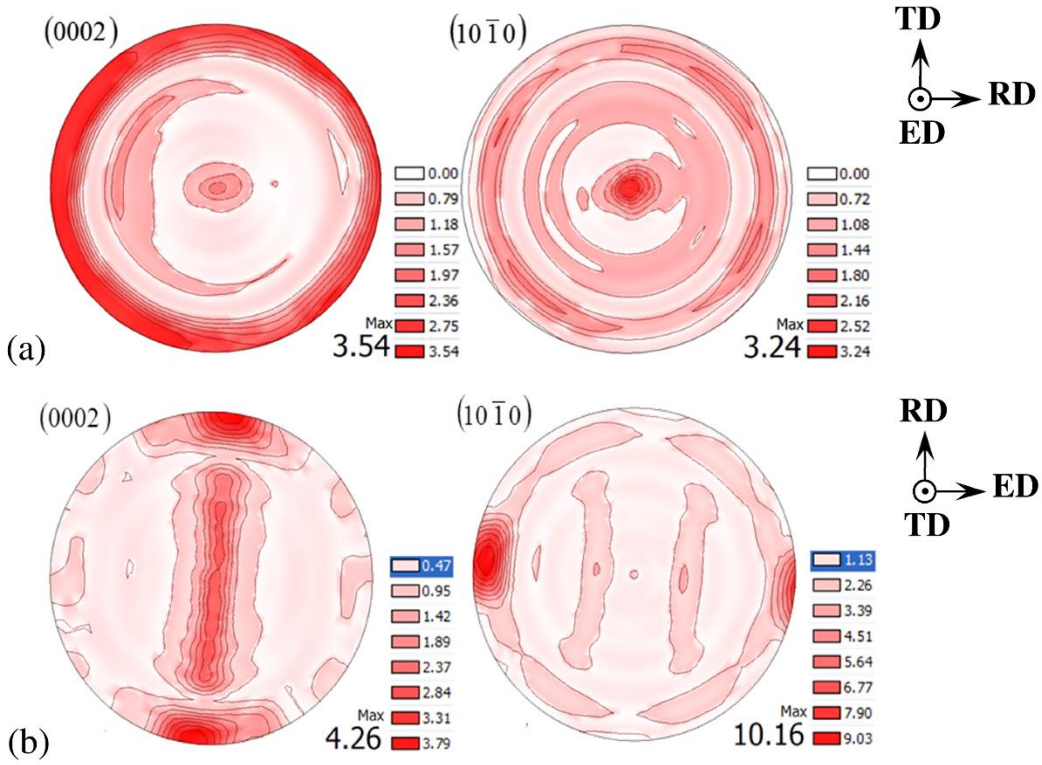

Figure 60. (0002) and (10$\bar{1}$0) pole figures of ZK60 extrusion obtained from: (a) TD-RD plane and (b) ED-RD plane

6.3.2 Quasi-static tension and compression behavior

Figure 61 illustrates the engineering stress-strain curves for ZK60 extrusion under quasi-static tensile and compressive loadings along different directions. It is seen that the tensile and compressive yield strengths along ED are 251 MPa and 128 MPa, respectively. In contrast, similar yield strengths are observed along the other two directions, i.e., the average

yield strengths of 130 MPa and 136 MPa, along RD and 45°, respectively. Table 12 summarizes the quasi-static mechanical properties of the material along these directions. Two tests were averaged to get the value for each property. The ductility along ED is less than that along RD and 45°, which is in agreement with the texture results, indicating that the c-axes of the grains are perpendicular to the ED. Hence, a smaller number of slip modes can be activated to accommodate the strain.

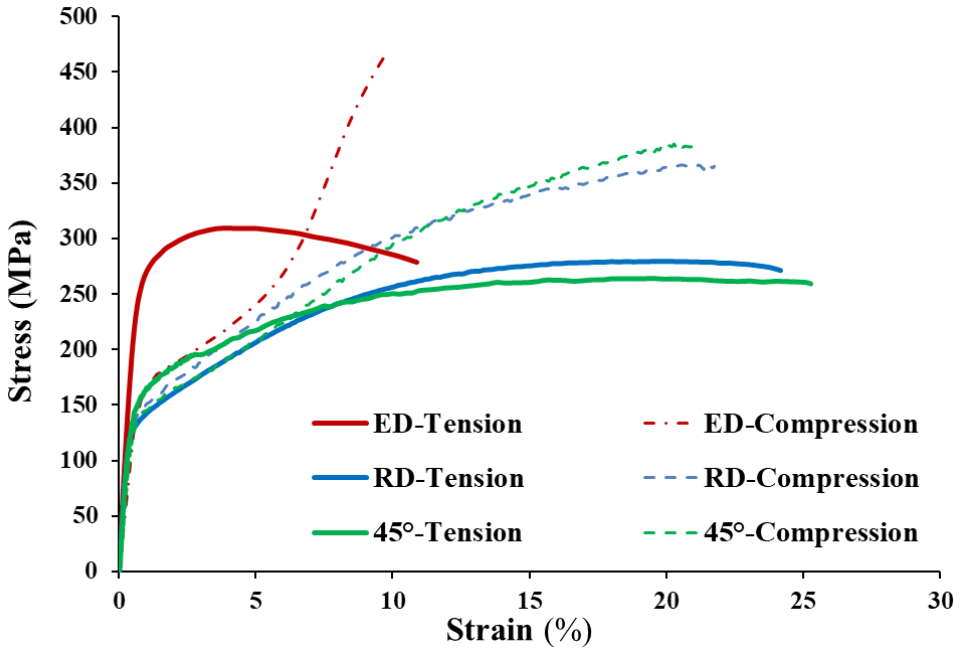

Figure 61. Quasi-static behavior under tensile and compressive loading for ED, RD, and 45°

Table 12. Quasi-static mechanical properties of ZK60 extrusion along different directions (The numbers in the parentheses are standard deviations)

Mechanical properties	ED	RD	45°
Module of elasticity [GPa]	43 (1)	45 (0)	42 (1)
Tensile yield strength [MPa]	251 (0)	128 (0)	149 (2)
Tensile ultimate strength [MPa]	309 (1)	279 (1)	264 (1)
Ductility (%)	11 (0)	23 (1)	26 (0)
Compressive yield strength [MPa]	128 (10)	132 (4)	123 (5)
Compressive ultimate strength [MPa]	449 (15)	357 (9)	388 (3)

6.3.3 Cyclic behavior

6.3.3.1 Extrusion direction

Figure 62 depicts the typical engineering stress-strain hysteresis loops of the stabilized cycles for total strain amplitudes between 0.2% and 2% for the ZK60 extrusion along ED. It is observed that the hysteresis loops for the strain amplitudes lower than 0.5% are not sigmoidal. In contrast, increasing the strain amplitudes to more than 0.5% brings about a sigmoidal-shape hysteresis loop. Such asymmetry indicates the activation of twinning and detwinning upon compressive and tensile reversals, respectively [38].

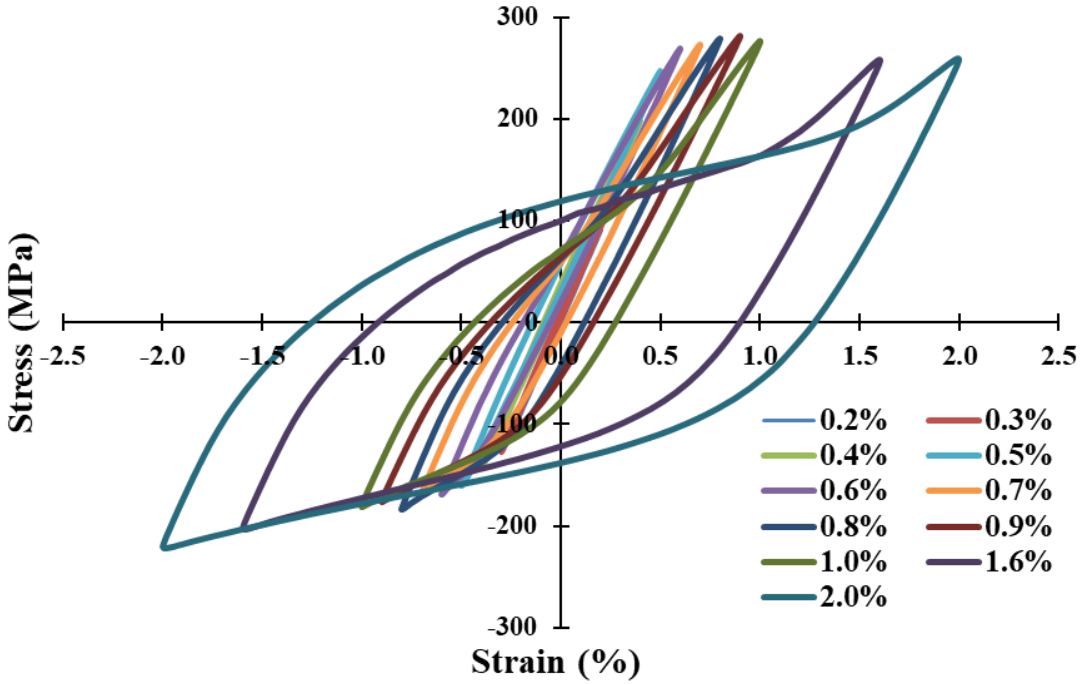

Figure 62. Typical engineering stress-strain hysteresis loops of the stabilized cycle for ED ranging from 0.2% to 2% strain amplitudes

To be more specific, the evolutionary change of hysteresis loops from the second cycle to the stabilized cycle is depicted in Figure 63. One of four distinct behaviors is applicable depending on the applied strain amplitude: (i) symmetric without twinning, (ii) partially

asymmetric, (iii) asymmetric, and (iv) “leading-to-symmetric” behavior. First, at low strain amplitudes (lower than 0.4%), the stabilized hysteresis loops are symmetric, implying that the stress is insufficient to activate extension-twinning under compression loading [148]. At such low strain amplitudes, the deformation mechanism is controlled by the gliding of dislocations [36]. Moreover, marginal cyclic hardening is observed in Figure 63 (a), probably due to the increased density of dislocations with the increasing number of cycles [154]. For the strain amplitudes of 0.5%, Figure 63 (b), the hysteresis loop at the second cycle is asymmetric in tension and compression reversals, denoting that twin and detwin deformations are active. Activation of the extension twin in a compression reversal results in an 86.3° rotation in crystal orientation [128]. Therefore, the twinned grains are likely to detwin during the subsequent tension reversal [36]. Nevertheless, the twinned grains in the compression reversal are not fully detwinned in the following tension reversal, leading to the formation of residual twins and cyclic hardening [46]. However, the hysteresis loop at the stabilized cycle exhibits no sign of twinning dominance, and therefore the slip of dislocations is accommodating the applied strain. It is believed that this change in the deformation behavior is due to the exhaustion of the new extension twin. This behavior has already been observed in ZK60 [42] and AM30 [18] along ED.

As the applied strain amplitude is increased (to more than 0.5%), Figure 63 (c), the stresses during compressive reversals are high enough to activate the extension-twinning. The twinned grains formed under compression are partially detwinned in the next tensile reversal, resulting in residual twins. These residual twins build up resistance to the plastic deformation in the wake of their interactions with dislocations and twinned grains which brings about cyclic hardening [36][126].

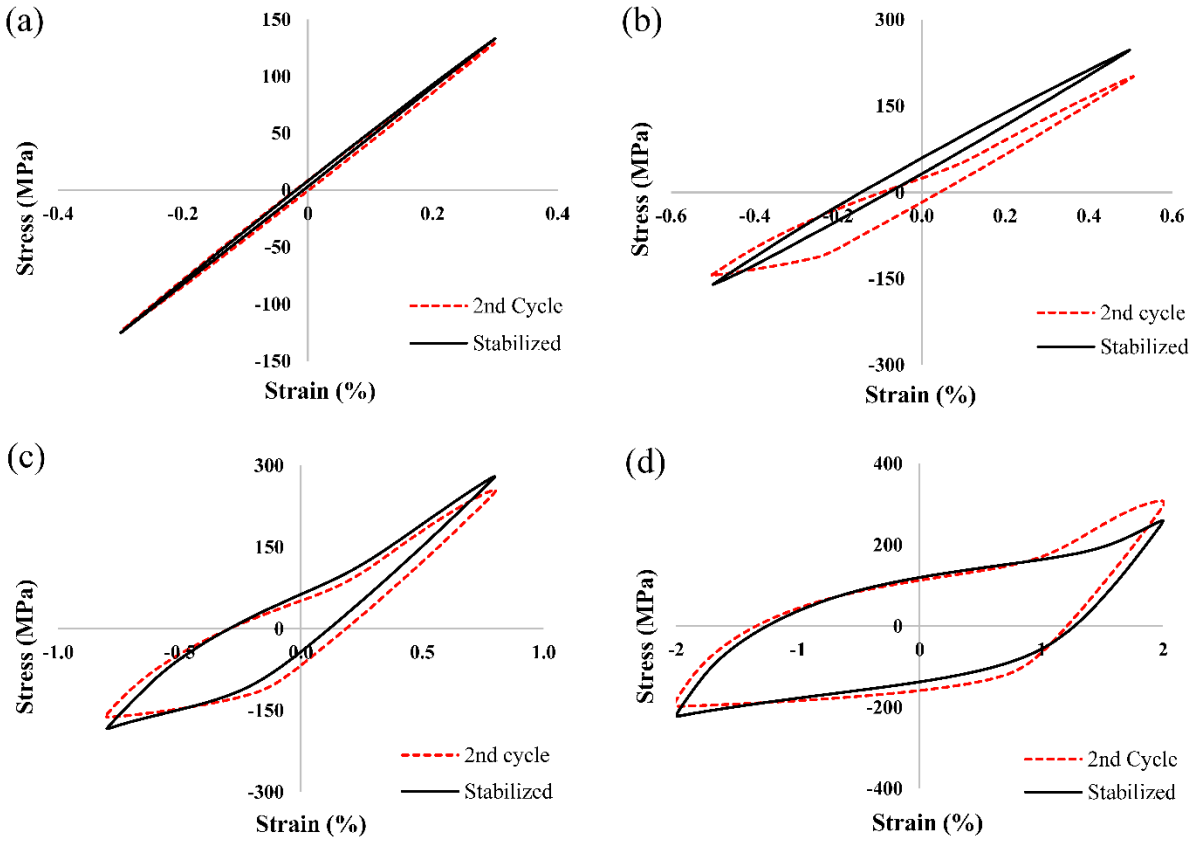

Figure 63. Evolution of hysteresis loops for 2nd and stabilized cycles along ED at different strain amplitudes: (a) 0.3%, (b) 0.5%, (c) 0.8%, and (d) 2%

Lastly, when the strain amplitude reaches to as large as 2%, Figure 63 (d), twinning governs the plastic deformation in the compressive reversal of the first few cycles. During the tensile reversal, detwinning occurs inside the twinned grains, and after detwinning exhausts, non-basal slips accommodate strain [180]. As a result, the hysteresis loop for the second cycle is sigmoidal for the tensile reversal. However, as the number of cycles increases, the compressive reversal also tends to the sigmoidal shape, as twinning is exhausted before the end of compressive reversal. The subsequent concave-down curve is as a result of the competitive twinning and slip mechanisms [41]. In contrast, the tensile reversal demonstrates cyclic softening, which is due to the incessant formation of micro-cracks in the first few cycles with limited growth at such a high strain amplitude. These micro-cracks alleviate deformation under tension which would be generally hindered by residual twin. As a result, less tension is

required to achieve the intended strain level leading to the softening behavior. In contrast, the micro-cracks are closed under compression and consequently cannot accommodate the deformation [155]. It is also reported that the annihilation and rearrangement of dislocations can cause this softening [36]. As a result of cyclic hardening in the compressive reversals and cyclic softening in the tensile reversals, hysteresis loops tend to be tension-compression symmetric. Similar behavior has been observed in AM30 extrusion for strain amplitudes greater than 1.5% [18].

6.3.3.2 Radial direction

Typical engineering stress-strain hysteresis loops along RD for ZK60 extrusion are plotted in Figure 64 at different strain amplitudes ranging from 0.2% to 2%. At all strain amplitudes, the hysteresis loops are roughly symmetric, unlike those in the ED. Slip is the dominant deformation mechanism at small strain amplitudes; however, twinning is also happening at high strain amplitudes ($\varepsilon_a \geq 1.6\%$) and forms sigmoidal-shape hysteresis loops. It is also observed that the peak stresses in the compression reversals are larger than those in the tension ones. As indicated in Figure 65, there is no such a difference between the second hysteresis and the stabilized one along RD. This is because of the lack of residual twins in this direction, the reason of which will be discussed later. Thus, larger compressive peak stresses comparing to the tensile ones stem from the quasi-static behavior. Returning to section 3.1 and Table 1, it was stated that along RD, the compression yield strength is greater than the tension yield; thereby, higher peak stress is eventually achieved under compression reversal.

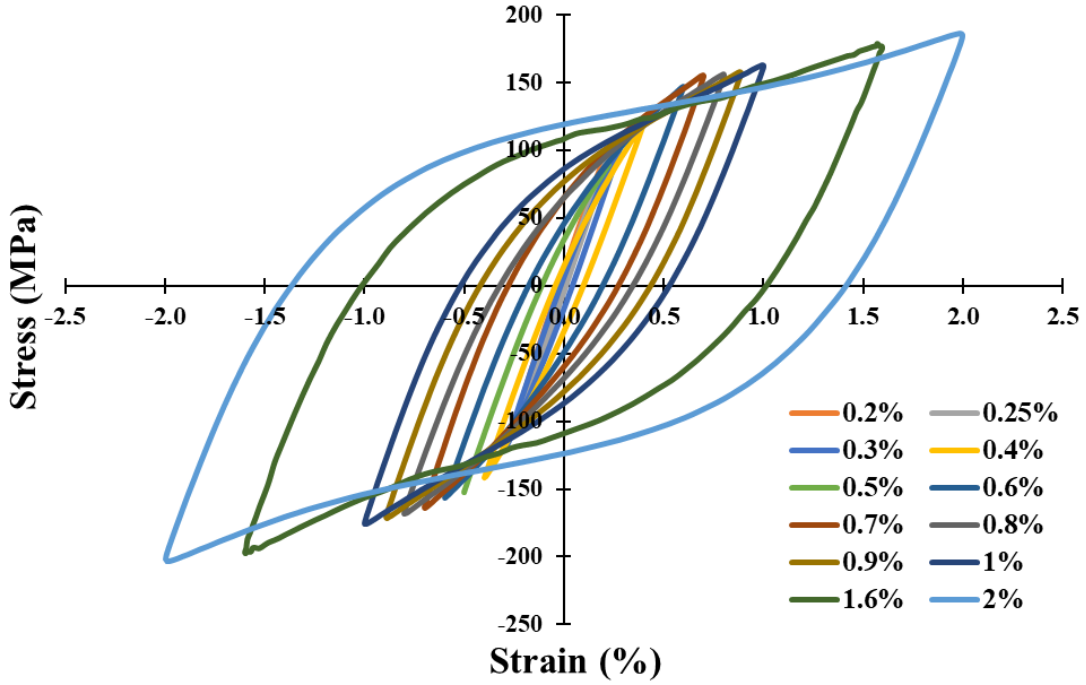

Figure 64. Typical engineering stress-strain hysteresis loops of the stabilized cycle for RD ranging from 0.2% to 2% strain amplitudes

According to Figure 65, at the strain amplitude of 1%, the second and stabilized hysteresis loops do not show a remarkable decrease of hardening rate under compressive reversal, indicating that twinning is not happening massively. In fact, the crystal orientations in some grains favor the activation of extension-twinning under both reversals, and consequently, detwinning partially reorients the twinned grains under both tension and compression loading. As a result, few residual twins remain in the microstructure; hence, slight strain hardening occurs both in tension and compression reversals due to the twin-twin and twin-dislocation interactions. On the other hand, as the strain amplitude is increased to 2%, the non-basal slip modes are activated in addition to the twinning and detwinning, which results in the sigmoidal hysteresis loop. However, for the reason mentioned before, only a limited number of residual twins remain in the microstructure. Marginal cyclic hardening can be observed by comparing the stabilized and second cycle hysteresis loops.

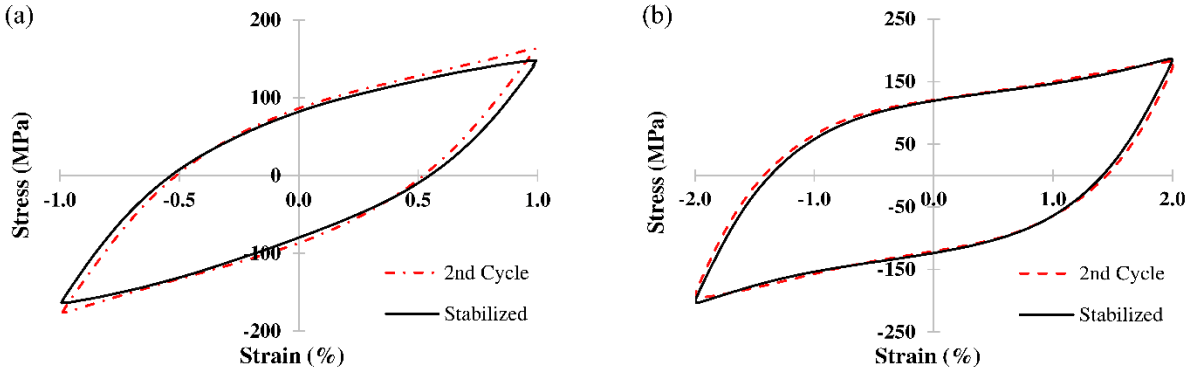

Figure 65. Evolution of hysteresis loops for 2nd and stabilized cycles along RD at the strain amplitude of (a) 1% and (b) 2%

6.3.3.3 45° Direction

Figure 66 shows the typical engineering stress-strain hysteresis loops along 45° for ZK60 extrusion at strain amplitudes ranging from 0.3% to 2%. The stabilized fatigue response, like the one along RD, does not show a low-hardening section under compressive and tensile reversals up to the strain amplitude of 1%. However, the sigmoidal behavior along 45° differs from that along RD, i.e., the peak stresses and strain hardening are slightly higher in tension reversals. This, again like RD, is stemming from the quasi-static behavior of 45°.

Hysteresis loop evolution along 45° is shown in Figure 67. As seen in Figure 67 (a), the hysteresis loop evolution along 45° at the strain amplitude of 1% is similar to that along RD; i.e., very marginal cyclic hardening is observed under both tension and compression loading. However, at the strain amplitude of 2%, Figure 67 (b), the behavior is more similar to that in the ED direction; i.e., after the first few cycles, cyclic softening on the tensile side and cyclic hardening on the compressive side can be seen. However, in the case of 45°, softening is not as severe as that along ED.

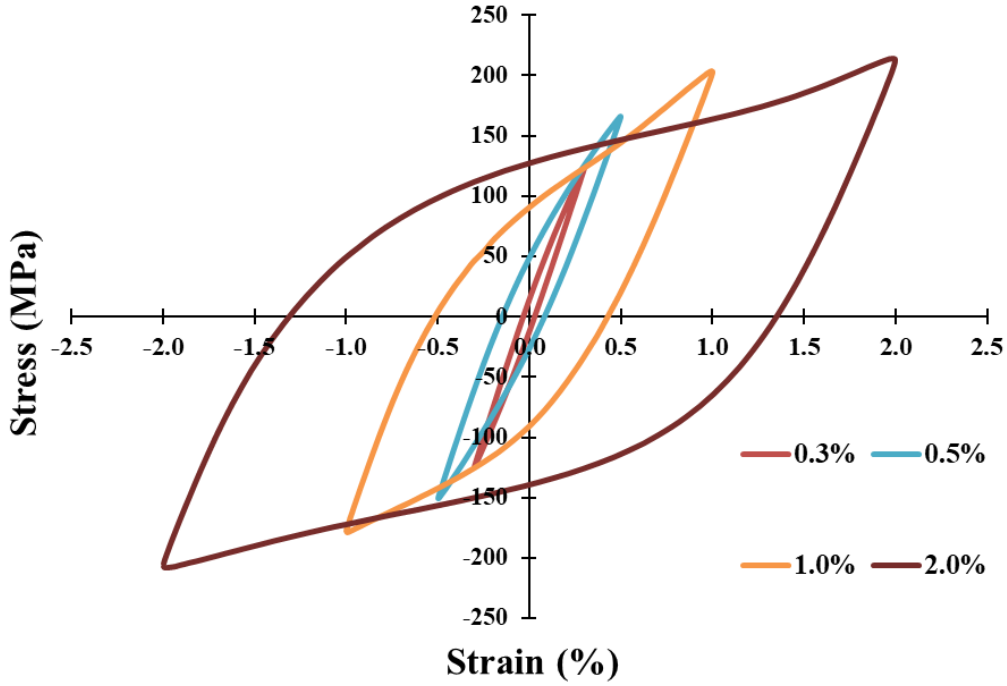

Figure 66. Typical engineering stress-strain hysteresis loops of the stabilized cycle for 45° direction ranging from 0.3% to 2% strain amplitudes

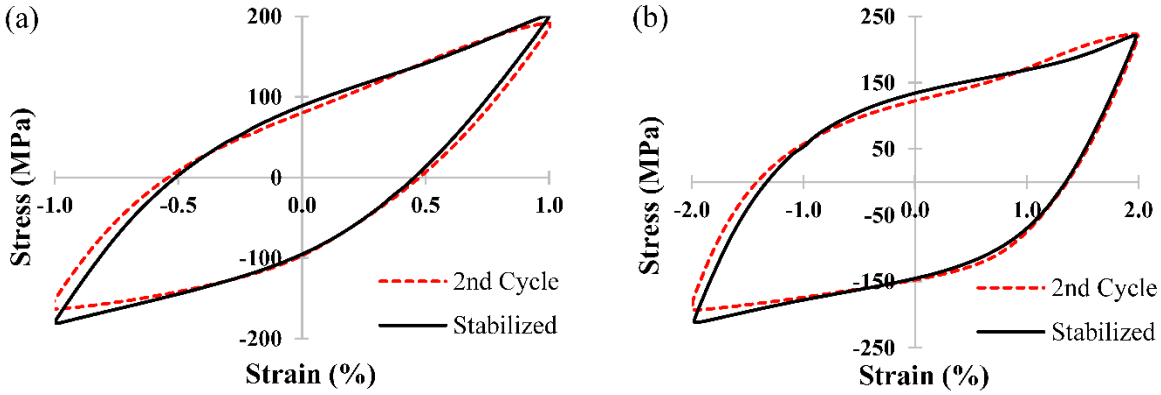

Figure 67. Evolution of hysteresis loops for 2nd and stabilized cycles along 45° direction at the strain amplitudes of (a) 1% and (b) 2%

6.3.4 Strain-life curve

The strain-life (ε_a-N) curves for ZK60 extrusion along different directions are depicted in Figure 68. It is noteworthy that both the 45° and RD samples are displaying the same life at different strain amplitudes. Moreover, comparing the fatigue responses along RD and ED, it is noted that the lives are similar for the strain amplitudes of 0.4% and higher (the low cycle fatigue regime). However, in the high cycle fatigue regime (strain amplitudes of 0.3% and lower), the cyclic respond depends on the material direction. For instance, while the fatigue life at the strain amplitude of 0.3% along RD is ~ 27000 cycles, that for ED is improved to ~ 100,000 cycles. While the run-out test for ED happened at the strain amplitude of 0.25%, RD samples exhibited an average life of 90,000 cycles at the same strain amplitude. The run-out test for RD was achieved at 0.2%. The reasons for the similar fatigue performance in the low cycle fatigue (LCF) for all directions, but not in the high cycle fatigue (HCF) will be discussed later.

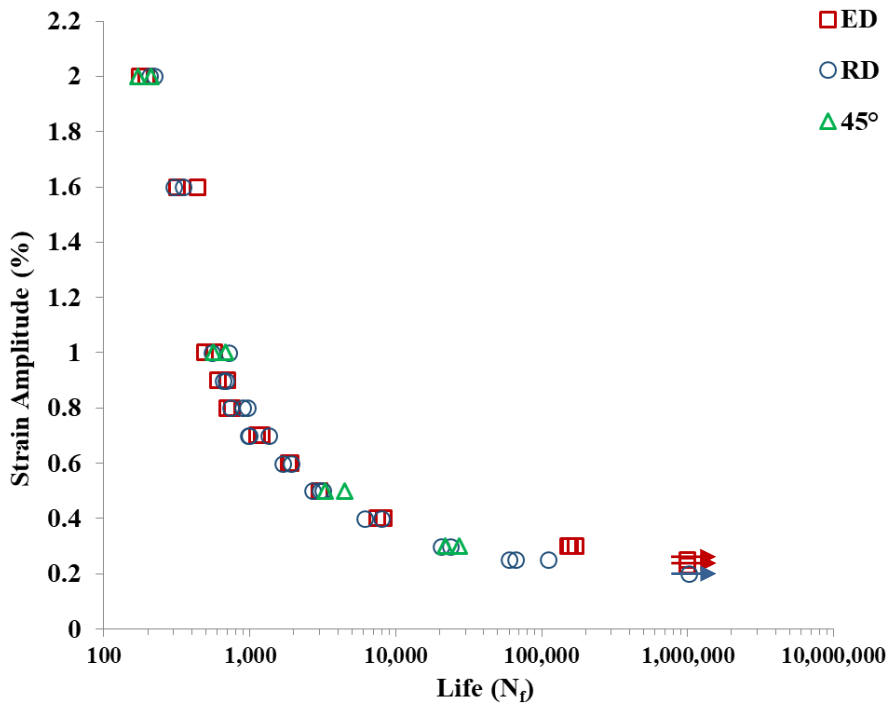

Figure 68. A comparison of strain-life (ε_a-N) curves obtained from different directions for the ZK60 extrusion

6.3.5 Fatigue fracture surfaces

The SEM images of the fatigue fracture surface of ED, RD, and 45° samples at two strain amplitudes of 0.3% and 2% are presented in Figure 69. Multiple crack initiation sites (marked by yellow arrows) are visible for all directions at the higher strain amplitude, whereas crack initiation sites are fewer at the lower strain amplitude. The fatigue failure (FF) area is distinguished from the fatigue crack growth (FCG) zone by dashed lines, and generally, at lower strain amplitudes, the FCG area is larger, manifesting a longer fatigue life. Yellow arrows indicate the position of crack initiation sites.

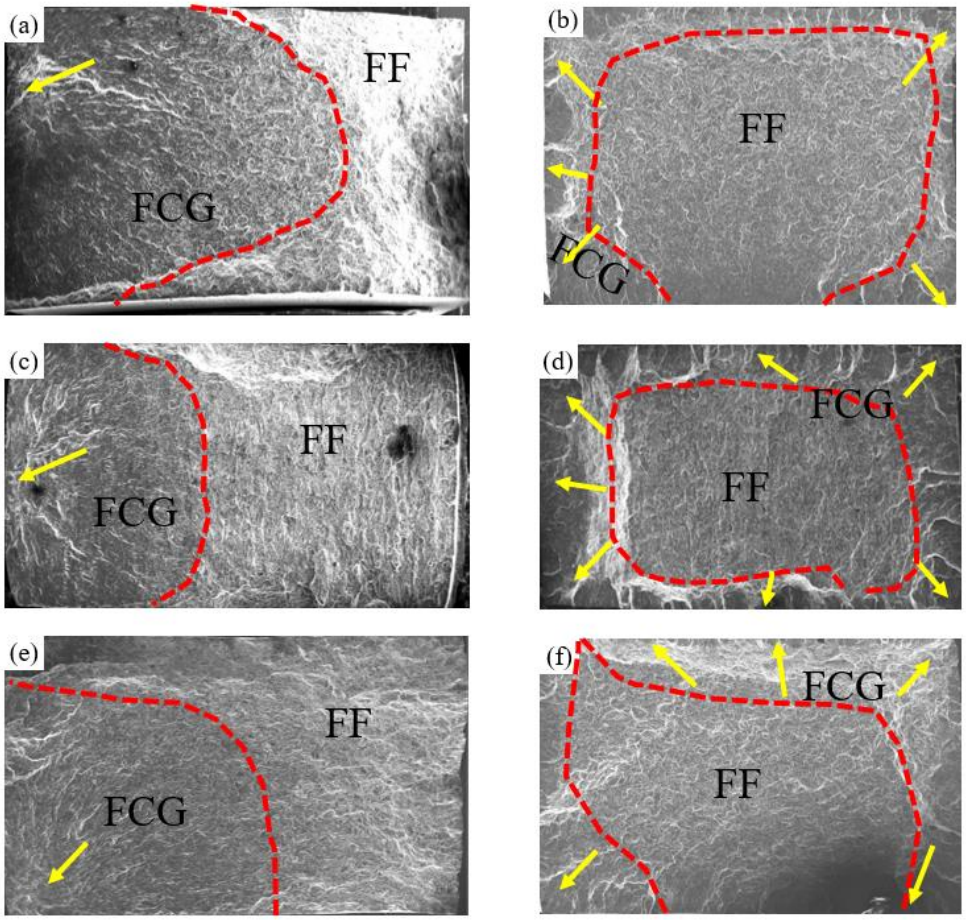

Figure 69. SEM images of fatigue fracture surfaces of ZK60 extrusion Mg alloy at different strain amplitudes along different directions: (a) ED at ε_a =0.3%, (b) ED at ε_a =2%, (c) RD at ε_a =0.3%, (d) RD at ε_a =2%, (e) 45° at ε_a =0.3%, and (f) 45° at ε_a =2%

The fracture surfaces at higher magnifications are shown for the strain amplitude of 2% along different directions in Figure 70. Twin lamellae are observed on the fracture surface of ED samples, whereas RD fracture surface reveals slip bands (SB).

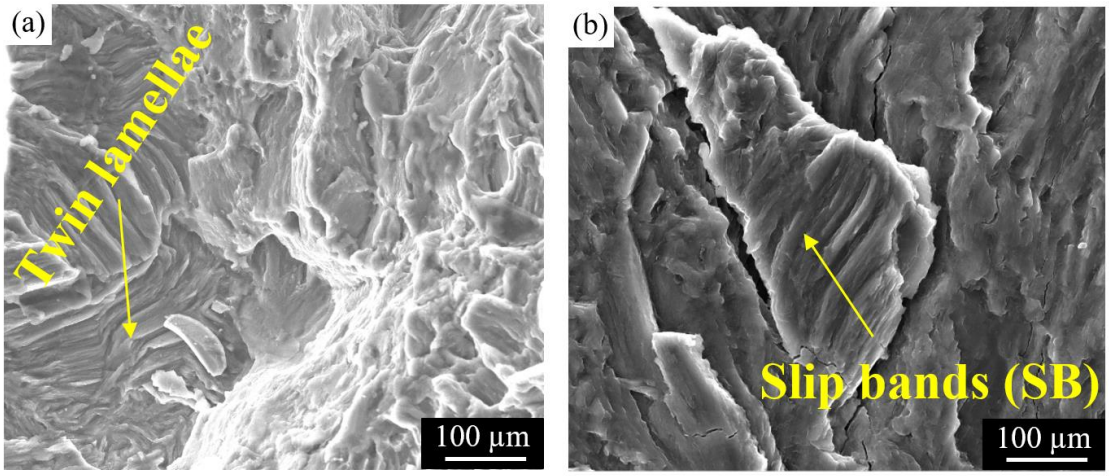

Figure 70. SEM images of the fracture surface of ZK60 extrusion at the total strain amplitude of 2% showing twin lamellae and slip bands on the (a) ED sample and (b) RD sample

Figure 71 illustrates the FCG zone of ZK60 at the total strain amplitudes of 0.3% and 2%. Fatigue striations (FS) marks are denoted on the images. Each striation mark represents the propagation of the fatigue crack in one cycle. Hence, the finer the marks, the longer the fatigue life. While the average distance between the FS marks for the ED sample under strain amplitude of 0.3% was 0.6±0.16 µm, the RD and 45° samples exhibited striations with an average distance of 1.92±0.3 µm, which is a testimony to the longer fatigue life along ED. In contrast, the average distance along FS marks along ED, RD, and 45° directions under strain amplitude of 2% were 2.14±0.04 µm, 2.01±0.09 µm, and 2.21±0.43 µm, asserting the similar lives in the LCF regime.

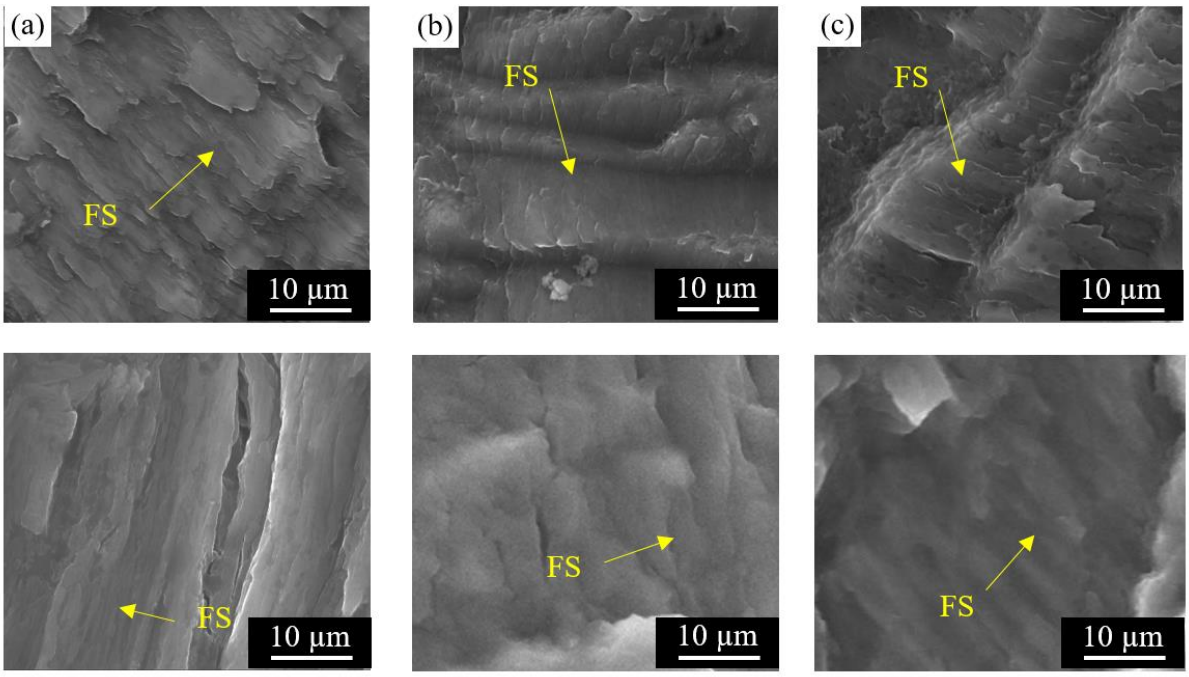

Figure 71. Fatigue crack growth at the total strain amplitudes of 0.3% (Top) and 2% (Bottom) for (a) ED, (b) RD, and (c) 45° samples

Lastly, to be more specific, the microstructure of the fatigue fractured samples tested at the strain amplitude of 2% along (a) ED and (b) RD are shown in Figure 72. Profuse twinned grains are observed in the microstructure along ED; however, the twinned area in the RD sample was significantly lower. This is in agreement with the hysteresis loops obtained in section 6.3.3, in that the ones for ED samples were less symmetric, as twinning was more dominant.

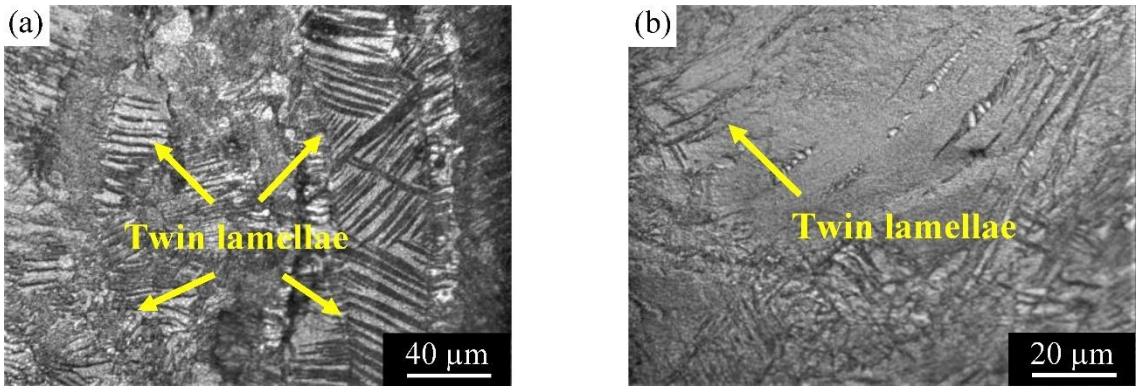

Figure 72. Microstructure illustrating the traces of twin on the polished cross-section of the fatigue-tested samples near the fracture surface, obtained at a strain amplitude of 2% along (a) ED and (b) RD

6.4 Discussion

6.4.1 Deformation behavior

The development of hysteresis responses along different directions during the fatigue tests was discussed in the previous sections. The mechanical behavior of the material is highly associated with the crystallographic texture, which controls the active modes of deformation. It is well-established that $\{10\bar{1}2\}$ extension-twin can accommodate plastic strain in HCP crystal structures when the applied loading is either tensile along the c-axes of the grains, or compressive perpendicular to the c-axes [36]. This polar nature of twinning brings about evident tension-compression asymmetric behavior in wrought Mg alloys [143]. For ZK60 extrusion, along ED, extension-twinning drives the deformation only under compressive loading. However, for the radial and 45° directions, twinning can happen under both tensile and compressive reversals. Consequently, in each reversal, some of the grains' orientation favors the activation of twinning, while the other pre-twinned grains tend to detwin. Therefore, hysteresis loops along these directions are less asymmetric compared to ED.

Figure 73 depicts the cyclic tension and compression behaviors of ZK60 along the three directions. The plots are constructed from the peak stresses of the stabilized hysteresis loops. It is noted that both the cyclic tension and cyclic compression curves for 45° are located

between the curves of ED and RD. This observation suggests that the deformation mechanism, as a macroscopic consequence of texture, along the 45° direction is a combination of the activated mechanisms along ED and RD.

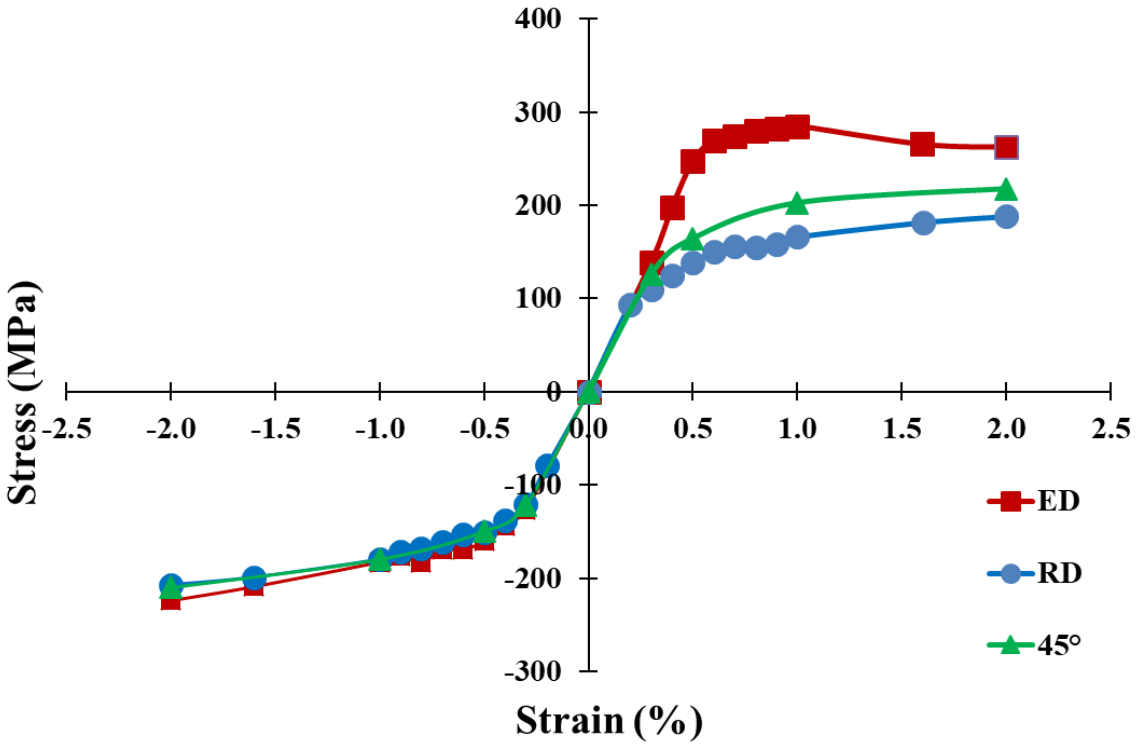

Figure 73. Cyclic tension and compression behaviors along ED, RD, and 45°

In Figure 74, the term Asymmetric Ratio (AR) = $\frac{TS-CS}{TS+CS}$ refers to the level of asymmetry, where TS and CS are the tensile peak stress and compressive peak stress, respectively. For a symmetric cyclic behavior, the asymmetry level equals zero, whereas the positive and negative levels of asymmetry reveal higher tensile peak stress and higher compressive peak stress, respectively. Asymmetry is clearly evident along ED up to the strain amplitude of 1%, but then decreases drastically, probably due to the formation of micro-cracks, and consequently reduces the tensile peak stress. The annihilation and rearrangement of dislocations, which together can decrease the post-detwinning dislocation-based flow, can also cause this softening, as reported in the literature [41][36][155][47].

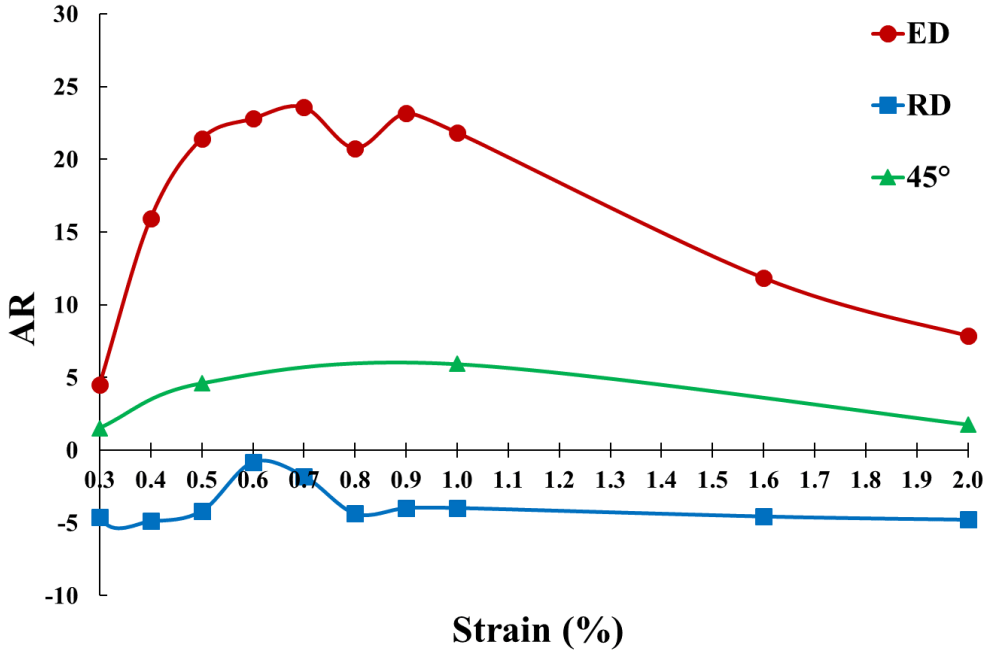

Figure 74. Ratio of cyclic asymmetry at different strain amplitudes ranging from 0.3 to 2% for different sample orientations

The RD asymmetry levels do not change remarkably, remaining close to zero, and so manifesting more symmetric behavior than other directions. As discussed, this symmetric behavior arises from the crystallographic texture of ZK60 extrusion, in which the c-axes of grains are randomly orientated on a plane normal to ED. Hence, twinning happens under both tension and compression along RD. Lastly, along 45°, like the deformation curves, the level of asymmetry lies between the ones for ED and RD, signifying that the deformation behavior of 45° is a combination of ED and RD behaviors. Moreover, while the asymmetry level for 45° is not as high as ED's owing to different texture, it decreases like ED's at high strain amplitudes. A finding that can be attributed to the tension peak stress drop at high strain amplitudes (Figure 67).

In Figure 75, the tension and compression cyclic behavior of ZK60 is plotted against the quasi-static behavior under tension and compression loadings along different material directions. At low strain amplitudes, where the material response is nearly elastic, the quasi-static and cyclic behaviors are very similar. However, at higher strain amplitudes, cyclic

hardening occurs due to the resistance built up by dislocation-dislocation, dislocation-twin, and twin-twin interactions [41]. Hence, cyclic curves are harder than quasi-static curves for RD and 45°. However, as previously stated, for ED, softening occurs at strain amplitudes higher than 1%, probably due to the formation of micro-cracks, and affects fatigue modeling, as discussed later.

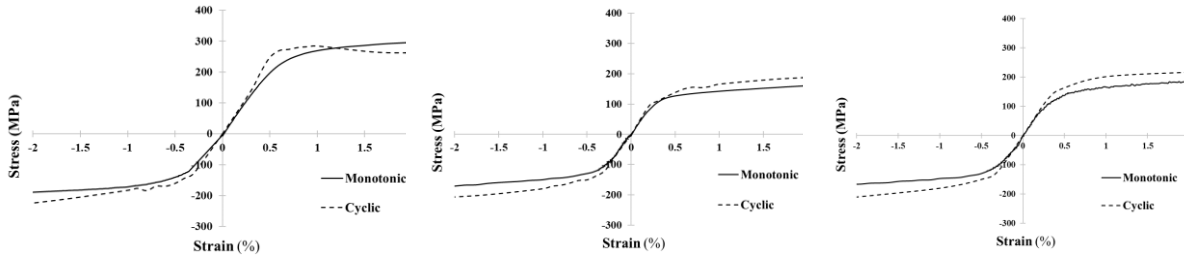

Figure 75. Comparison between quasi-static and cyclic curves for ZK60 extrusion along (a) ED, (b) RD, and (c) 45°

6.4.2 Effect of loading on the fatigue performance

Figure 68 showed that the fatigue life of ZK60 is not sensitive to the material direction in the LCF regime, i.e., $\varepsilon_a \geq 0.4\%$, although the deformation behavior differs. In other words, the cyclic deformations for RD and 45° are almost symmetric, whereas the deformation for ED involves profound twinning happening only under compressive loading. Thus, significant asymmetry is evident. On the other hand, according to Figure 68, fatigue life within the HCF regime, i.e., $\varepsilon_a < 0.4\%$, is distinct in spite of similar symmetric deformation behavior.

Figure 76 demonstrates the hysteresis loops at two different strain amplitudes, 0.5% and 1%, both corresponding to the LCF regime, for different directions. Although the tensile peak stresses for ED are the highest among all directions for both strain amplitudes, the areas inside the ED hysteresis loop are less than those of RD and 45°. The area inside a hysteresis loop represents the energy being dissipated in each cycle. Therefore, less energy would dissipate along ED in each cycle than along the other two directions, both of which show relatively similar loop areas. On the other hand, the larger tensile peak stress causes wider stress ranges and higher tensile mean stresses, which are more damaging for ED samples.

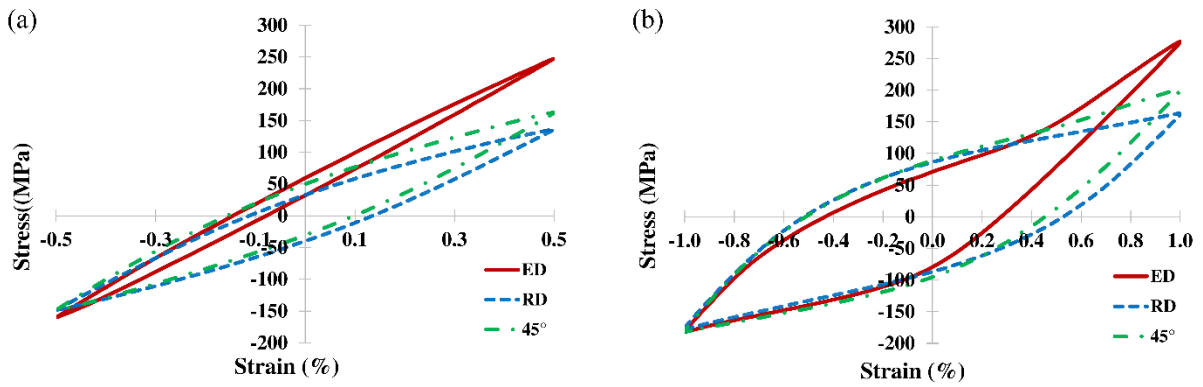

Figure 76. Stabilized hysteresis loops for ED, RD, and 45° at (a) ε_a =0.5% and (b) ε_a =1%

Profound residual twins can affect the fatigue life of ED samples in two ways. Firstly, interactions between twin-twin bands and twin-dislocations can initiate cracks, leading to premature fatigue failure [47][197]. On the other hand, some studies have suggested that the surface roughness as a result of extension-twinning can retard crack growth, due to roughness-induced crack closure [198]. The overall result of competing factors, namely strength, twin-twin bands interactions, twin-dislocations interactions, and surface roughness resulting from extension-twinning, is that the fatigue lives in the LCF regime are similar. However, in the HCF regime where twinning does not happen, material's strength governs deformation. In fact, at these strain amplitudes, the area inside the hysteresis loop is small, indicating little plasticity in the deformation. The deformation thus tends to be more elastic, and so the governing fatigue life factor in the HCF regime would be the strength of the alloy, suggesting a remarkably higher fatigue life for ED samples in HCF because cracks initiation occurs later due to the higher strength along this direction [199].

6.5 Fatigue modeling

As discussed, ZK60 extrusion exhibits identical behavior in the LCF regime along three different directions in terms of the strain-life curve; however, in the HCF regime, their fatigue response shows segmental deviation. Furthermore, along the ED, there is a partial softening in the high strain amplitude, e.g., ε_a =1.6% compared to 1 %, which causes nonlinearity in the

elastic strain response of the material, when plotted with respect to the number of reversals (Figure 77 (a)). As a consequence, the fatigue modeling of ZK60 can be complex. A goal in fatigue modeling of anisotropic materials is to discover a set of universal parameters that can be employed for life prediction of the material regardless of the orientation. To this intent, RD was selected as the primary direction, and the universal parameters required for two different damage criteria were extracted from the experiments in this specific direction. Eventually, these parameters were used to predict the life in other directions. In what follows, SWT, as a critical plane model, and JV, as an energy-based damage criterion, are assessed for the fatigue life prediction of ZK60.

6.5.1 SWT

The SWT parameter was founded on the principal strain range and maximum stress on the principal strain plane, namely $\Delta\varepsilon_1$ and $\sigma_{n,max}$, respectively, in the following formulation:

$$SWT = \sigma_{n,max}\frac{\Delta\varepsilon_1}{2} \tag{6-1}$$

This parameter was originally suggested to account for the mean stress effect and has been extensively employed in many efforts to estimate the fatigue life of Mg alloys [18], [42], [43], [47], [70], [80]. Although the SWT parameter was defined the same in all those studies, its correlation with fatigue life was made differently. In the present study, the correlation is formulated by integrating SWT with the Coffin-Manson relation as follows:

$$SWT = \frac{{\sigma'_f}^2}{E}\left(2N_f\right)^{2b} + \sigma'_f\varepsilon'_f\left(2N_f\right)^{b+c} \tag{6-2}$$

where:

σ'_f: Fatigue strength coefficient

ε'_f: Fatigue toughness coefficient

b: Fatigue strength exponent

c: Fatigue toughness exponent

and E is the modulus of elasticity and $2N_f$ is the number of reversals to failure. Other components on the right side of the equation are based on the Coffin-Manson approximation and will be extracted by employing strain-life and hysteresis curves along RD. In this approach, the strain range is decomposed into elastic and plastic parts ($\Delta\varepsilon_e$ and $\Delta\varepsilon_p$), which are calculated from the stabilized hysteresis loop for each strain amplitude:

$$\frac{\Delta\varepsilon_e}{2} = \frac{\sigma'_f}{E}\left(2N_f\right)^b \quad 6\text{-}3$$

$$\frac{\Delta\varepsilon_p}{2} = \varepsilon'_f\left(2N_f\right)^c \quad 6\text{-}4$$

The elastic and plastic strain ranges with respect to the number of reversals to failure are depicted in Figure 77 (b). The Coffin-Manson parameters, as presented in Table 13, were extracted from the experimental results in the reference direction (RD) using the aforementioned equations.

Table 13. Coffin-Manson parameters for SWT model

σ'_f (MPa)	360.73
ε'_f	1.862
b	-0.110
c	-0.780

Finally, by substituting these parameters into the SWT model (Equations 5-1 and 5-2), the predicted lives in all three directions were found through a numerical solution.

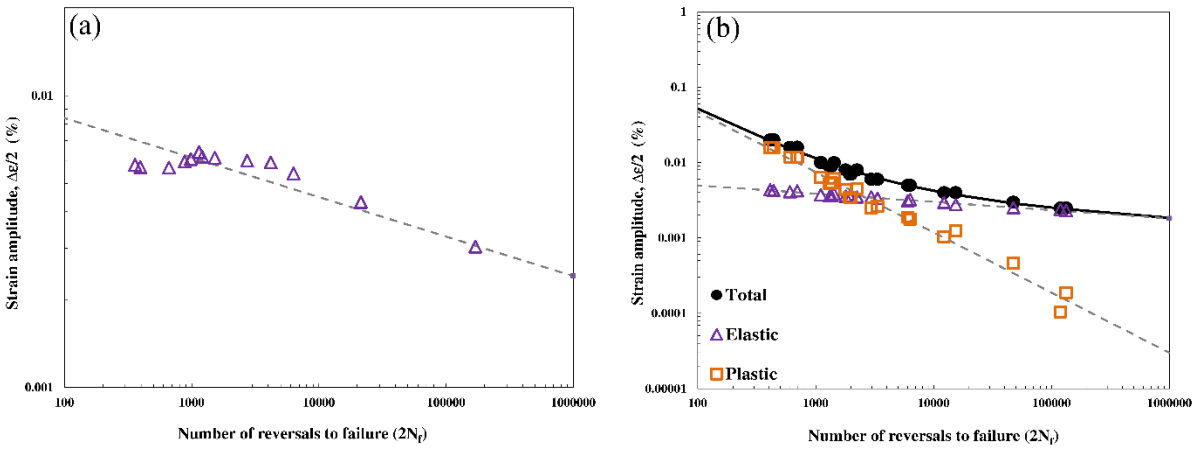

Figure 77. (a) Nonlinear elastic response of the strain for ED and (b) decomposition of strain into elastic and plastic strain in RD

The predicted lives in contrast to the experimental ones are illustrated in Figure 78. A diagonal solid line denotes the ideal prediction, while the dashed and dashed-dot lines specify the area where predicted life over experimental life rests within the factors of 2 and 2.5, respectively. Along RD, life prediction meets expectation in accordance with the fact that the Coffin-Manson parameters were extracted in this direction. For both 45° and ED specimens, SWT underpredicts the life; however, the prediction is more conservative for ED. The observed drop in the life prediction accuracy of ED might be attributed to the reported nonlinear elastic strain of the material, which is fitted by the linear regression in the Coffin-Manson relation (Figure 77 (a)).

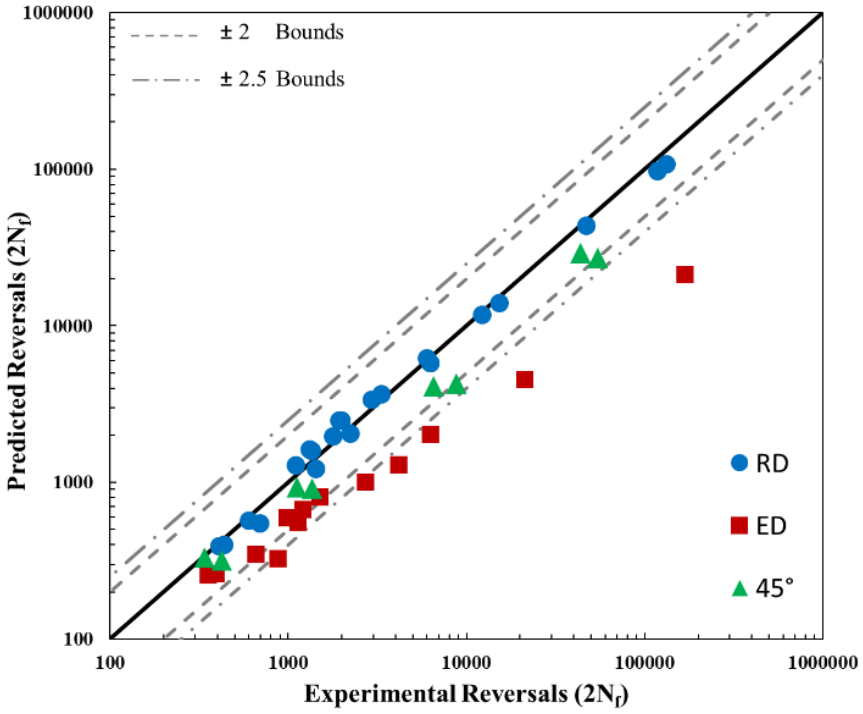

Figure 78. SWT predicted vs. experimental reversals for all directions

6.5.2 Jahed-Varvani

As was pointed out and discussed earlier, the anisotropic properties of wrought Mg alloys could make their fatigue modeling challenging. Due to the scalar nature and resulting direction independency of energy, the longstanding approach to tackling this exceptional characteristic is implementing energy-based damage parameters, including JV, Jiang, and Ellyin [18], [46], [47], [50], [70], [80], [139], [200], [201]. In JV, total strain energy, as the damage parameter, is expressed by two terms: i) the positive elastic strain energy density (ΔE_e^+), and ii) the plastic energy density (ΔE_p). The latter is defined as the area inside the hysteresis loop, and the former is obtained by the following equation:

$$\Delta E_e^+ = \frac{{\sigma_{max}}^2}{2E} \qquad 6\text{-}5$$

where σ_{max} is the tensile peak stress. By assembling the elastic and plastic parts of strain energy, the JV parameter is formulated thus:

$$JV = \Delta E_e^+ + \Delta E_p \quad \text{6-6}$$

and will be correlated to life as follows [91]:

$$JV = E_e'(2N_f)^B + E_f'(2N_f)^C \quad \text{6-7}$$

where the four parameters on the right side of the equation are

E_e' = Energy-based fatigue strength coefficient

E_f' = Energy-based fatigue ductility coefficient

B = Energy-based fatigue strength exponent

C = Energy-based fatigue ductility exponent

These parameters are determined from curves fitted to the elastic and plastic portions of the energy along the radial direction, as depicted in Figure 79 (a).

Table 14. JV model parameters

E'_e (MJ/m^3)	1.4875
E'_f (MJ/m^3)	1604.3
B	-0.219
C	-0.920

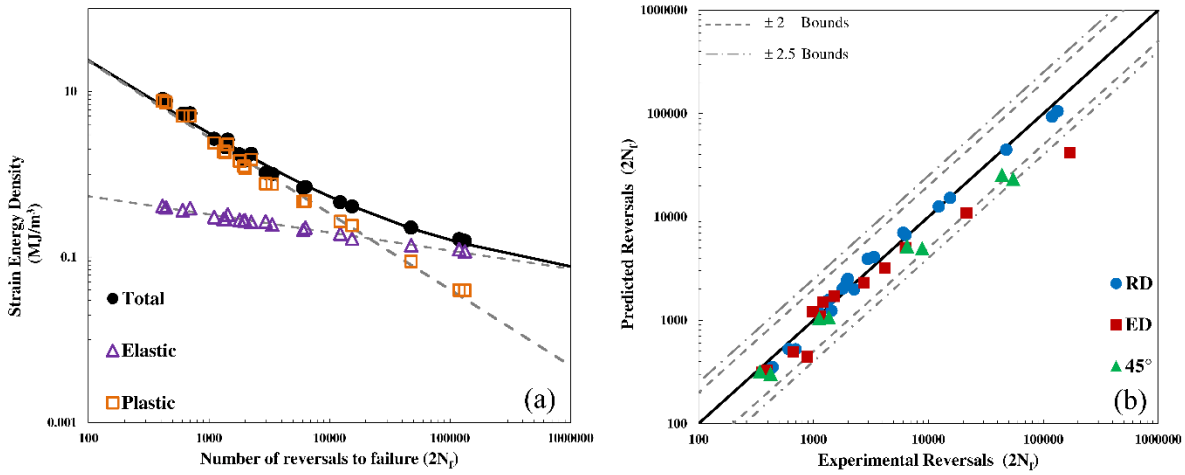

Figure 79. (a) Decomposition of total strain energy into elastic and plastic energies in RD and (b) JV predicted vs. experimental reversals for all directions

By employing the JV model in conjunction with the parameters extracted for RD, Table 14, fatigue lives in different directions are predicted numerically similar to the SWT approach and plotted against the experimental life in Figure 79 (b). The data-points congregating about the solid line and almost within the bound of factor 2.5 in both LCF and HCF regions demonstrate the capability of the JV parameter to model the fatigue of ZK60 with anisotropic behavior. However, some deviation is observed along the ED direction as the lives increases to more than 10000 cycles. This deviation is possibly attributed to exhausted plastic energy decapitation through the hysteresis loops in HCF where the model relies solely on the elastic part of the strain energy. Comparing the Figure 78 and Figure 79 (b) suggests that the SWT model yields to more conservative life predictions than the JV model.

6.5.3 Further discussion

The total strain energy density, as a fatigue damage parameter, is determined at each strain amplitude at the stabilized cycle to discern the underlying reason for similar LCF lives, but different HCF ones. Figure 80 depicts the total strain energy density against the total strain amplitude for the different directions. It is observed that at high strain amplitudes, although the deformation behaviors are dissimilar, the fatigue damage parameters are roughly the same. Therefore, the fatigue lives in the LCF regime are identical in the wake of similar fatigue

damage occurring. On the other hand, under small strain amplitudes, i.e., the HCF regime, the amount of damage at the stabilized cycle is marginal and close to zero, implying elastic deformation.

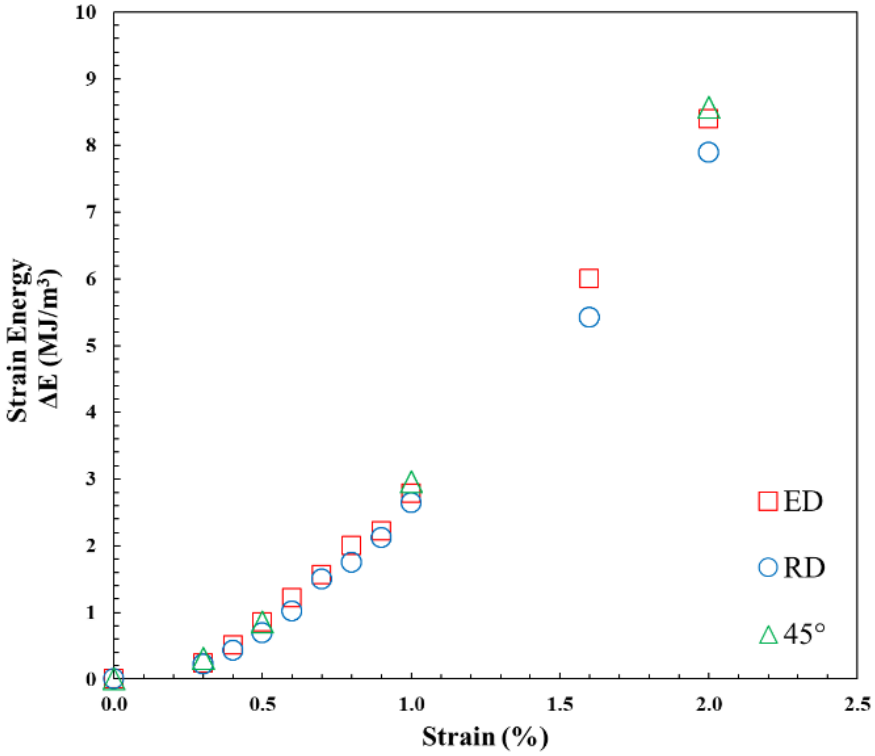

Figure 80. Total strain energy density as the fatigue damage parameter at different strain amplitudes along different directions for ZK60 extrusion

6.6 Conclusions

This study explored the mechanical behavior of ZK60 extrusion Mg alloy in three different directions: extrusion (ED), radial (RD), and 45°. From the results and discussions, the following conclusions can be made:

1. The extruded alloy exhibited a sharp basal texture in the microstructure such that the hexagonal crystals were randomly orientated with their c-axes perpendicular to the extrusion direction.
2. The quasi-static behavior of ZK60 extrusion depended on the material's direction in the light of the developed texture. Indeed, while the static behavior along ED was

asymmetric in tension and compression, the RD and 45° samples exhibited symmetric behaviors.

3. In spite of dissimilar quasi-static behaviors along the different directions, the cyclic behavior in the LCF regime was not sensitive to the direction. However, the behaviors in the HCF regime were distinct.
4. JV, as an energy-based model, provides acceptable fatigue life predictions for ZK60 extrusion with anisotropic behavior.

Chapter 7

Multiaxial fatigue behavior of extruded and thermo-mechanically low-temperature close-die forged ZK60 Mg alloys

7.1 Introduction

Transportation sector has been attempting to adopt lightweight alloys in the vehicles' components in the light of the necessity to cut down the fuel consumption rates of automobiles. One such material being magnesium (Mg) alloy was found to be a proper candidate for this purpose due to its low density, high specific strength, and excellent machinability [9], [193], [202]. However, Mg's applications have been limited largely to the non-load-bearing components such as seat frames and housing parts [12]. To achieve the abovementioned mass-saving target, Mg's applications need to be broadened to load-bearing parts such as the suspension system, too. On the other hand, such components are subjected to multiaxial loadings during their service life. Thereby, it is important to characterize the mechanical behavior of Mg alloys under multiaxial loadings.

Die casting is the prevalent processing method of Mg alloys for its economic advantages [15]. However, this manufacturing technique brings in abundant of defects and porosities in the microstructure of the material that affect the cyclic behavior adversely [16][17]. Therefore, for structural applications, wrought Mg alloys are introduced, which have shown promising mechanical properties and fatigue behavior comparing to the cast alloys [17][18][19][20].

One of the most examined features of the multiaxial loading is the materials' sensitivity to the non-proportionality. Non-proportionality of loading leads to the rotation of the principal axes during the load history, which might affect the fatigue life [66]. It was shown in a study by Pejkowski et al that phase angle shifts under the same stress ratio can influence two different materials differently [67]. The multiaxial fatigue behavior characterization of different wrought Mg alloys has recently been investigated. Albinmousa et al. studied the multiaxial fatigue characteristics of AZ31B Mg alloys extrusion in [69][46][70][71]. They carried out proportional and non-proportional multiaxial fatigue tests in different phase angles. It was

found that non-proportionality exhibits additional hardening, but it does not change the fatigue response significantly. Moreover, it was noted that the twinning mode of deformation has a key role in the multiaxial behavior of the alloy. Due to the intrinsically scalar nature of energy, an energy-based model was employed that effectively correlated the different damages of axial and torsional loadings to the fatigue life. In another study, Xiong et al. [75] investigated the tension-compression asymmetric behavior of AZ31B extrusion under the combined axial-torsional loading. Two critical-plane multiaxial fatigue models were used to predict the cyclic life successfully. Li et al. [79] studied the multiaxial ratcheting in AZ31B extrusion, and reported the dependency of the ratcheting strain on the shape of multiaxial locus. Moreover, it was noted that the traditional equivalent stress-strain responses cannot be exploited for AZ31B Mg alloys, for the contribution of different modes of deformation in the axial and torsional modes of loading. Aside from the AZ31B Mg alloy extrusion, the mechanical behavior of AZ61 Mg alloy extrusion was studied by Yu et al. [68]. They performed fully reversed axial, torsional, proportional axial-torsional, and 90° out-of-phase multiaxial cyclic tests, while the proportional and non-proportional tests exhibited the highest and the shortest lives for the same equivalent strain amplitude, respectively. In another study, Roostaei et al. [81] studied the multiaxial fatigue behavior of AM30 under different phase angles, namely , 0° (in phase), 45°, and 90°. The effect of non-proportionality was observed to be depended on the applied axial strain amplitude. Moreover, the interaction of the axial and torsional loading was studies. Lastly, two critical-plane models and an energy-based model were employed to predict the multiaxial fatigue life.

As discussed above, the main attention in multiaxial fatigue research has been dedicated to the AZ- and AM- series. On the other hand, ZK- series Mg alloys have shown superb mechanical behavior due to the presence of Zr as a grain refiner [32][84]. The mechanical behavior of ZK60 extrusion has been studied under uniaxial loading [41][45] [203]. Also, recently, Albinmousa et al. investigated the multiaxial behavior of ZK60-T5 magnesium extrusion [83]. However, to the best knowledge of the authors, no study has been done on the mechanical behavior of ZK60 extrusion under torsional and combined axial-torsional loadings. Therefore, in the current study, we investigated the torsional behavior of

ZK60 extrusion as well as the effects of combined axial-torsional loading on its fatigue characteristics at different phase angles in the light of the material's sensitivity to the non-proportionality. Also, an energy-based model and a critical-plane model, that have shown their merits in predicating fatigue life, were employed to consider the fatigue damages contributed to the axial and torsional loadings.

7.2 Material and experiment

This study employed both as-extruded and extruded-forged ZK60 alloys. The extrusion material was an extruded ZK60 cylinder with the diameter of 127 mm and length of 400 mm, supplied by Luxfer MEL Technologies. Table 15 represents the chemical composition of the alloy. Also, the starting material for the forged alloy was supplied by the same company in the form of cylindrical billets with 300 mm diameter, which were subsequently cut into smaller billets of 65 mm in length and 63.5 mm in diameter. The billets were heated for 3 hours in a furnace to the temperature of 250° C, which was the lowest temperature to obtain a crack-free forging [59]. Then, the billets were placed in a hydraulic press, and isothermally pressed into an I-beam [100] at the ram speed of 20 mm/sec in a single step. Graphite was the employed lubricant to reduce the friction during the process. Eventually, the forged samples were air-cooled to the room temperature. Figure 81 (a) schematically shows the configuration of the forging dies and the billet. The final forged part is depicted in Figure 81 (b). FD, LD, and TD denote the forging, longitudinal, and transverse directions in Figure 81 (b). Smooth dog-bone samples were machined out of the two flanges of the forgings (Figure 81 (b)) and exploited for the quasi-static and cyclic axial tests. The mechanical behavior of ZK60 extrusion along ED has already been studied in Chapter 6. To conduct cyclic pure shear and multiaxial fatigue tests, thin-walled tubular samples with the geometry in accordance with the ASTM E2207 standard [101] were machined out of the as-extruded cylinder billet along the longitudinal direction. To ensure the consistency in the extruded samples, all the tubular samples were extracted at the distance equivalent to the 85% of the cylinder radius. Figure 81 (c) and (d) depict the geometry and location of the collected tubular samples in the as-extruded ZK60

billet, respectively. Due to the geometry restrictions in the forging width, the geometry of the tubular samples was modified for the forged material under the guidance of the ASTM E2207 standard. Figure 81 (e) and (f) illustrate the geometry of the forging samples and the location of them in the I-beams, respectively. Also, the microstructure in the I-beam's flanges, where the samples are extracted from, were compared with one each other to make assure the consistency.

Table 15. Chemical composition of ZK60 extrusion alloy (wt%)

Element	Zn	Zr	others	Mg
Composition	5.3	0.69	<0.30	balance

Quasi-static tests were performed in the standard laboratory conditions under the rotation-controlled mode using an Instron 8874 servo-hydraulic frame having axial and torsional load capacities of ±25 kN and ±100 N.m, respectively. The crosshead of the machine was rotating at the angular velocity of 0.18 deg/sec, and the shear strain was measured using the ARAMIS 3D Digital Image Correlation (DIC) system equipped with 5-megapixel resolution cameras having the frame rate of 15 fps. Three quasi-static tests were delivered to ensure the consistency of the result.

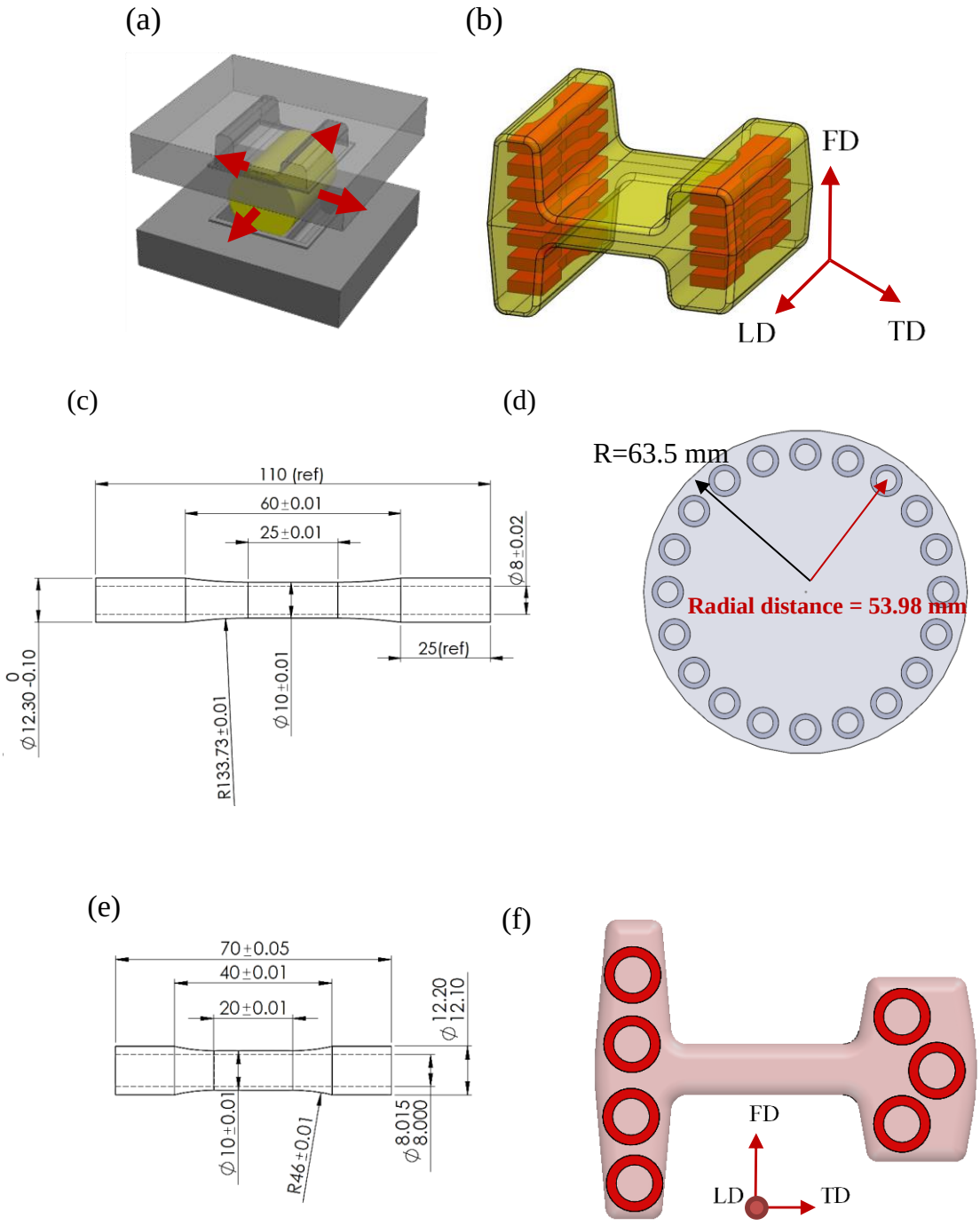

Figure 81. (a) Thin-walled tubular specimen's geometry; (b) the location of the collected tubular samples along the extrusion direction of the ZK60 Mg cylinder in the billet's cross section

Fully reversed cyclic pure shear tests as well as proportional, 45° and 90° out-of-phase multiaxial experiments were conducted on the same Instron loading frame under the standard laboratory conditions. Uniaxial tension-compression results along the extrusion direction (ED) were taken from the previous article [203]. Axial and shear strains were controlled for all the fatigue tests. Strain was being measured using an epsilon biaxial extensometer with the axial and shear strain travels of ±5% and ±1.5°. The frequency during the tests were in the range of 0.1-0.5 Hz, depending on the applied strain amplitude. Higher frequencies were applied for the tests at lower strain amplitudes which exhibit longer fatigue lives. At very small strain amplitudes during the pure shear tests, once the material's behavior was stabilized, the test was stopped, and the extensometer was removed. Subsequently, the experiment was resumed under the torque mode of control at higher frequencies up to 10 Hz. The failure criterion was assumed to be either the final rupture, or 50% drop in the maximum load, whichever came first. Moreover, each test was at least once duplicated to verify the reproducibility of the results. Lastly, the hysteresis loop at the half-life cycle was considered to represent the stabilized cyclic response.

For microstructural observation, samples were prepared through the following standard metallographic procedure. First, they were ground using silicon-carbide papers with grit No. up to 1200 and polished sequentially with 6-, 3-, 1- and 0.1-micron diamond pastes. An etchant made of 4.2 g picric acid, 70 ml ethanol, 10 ml acetic acid, and 10 ml distilled water was applied to the sample surface later.

The crystallographic texture was characterized by means of X-ray diffraction employing Bruker D8 Discover X-ray diffractometer equipped with an advanced 2D-detector. The characterization started with incomplete pole figures measurement in the back-reflection mode applying CuKα radiation at 40 kV-40 mA. The complete pole figures were calculated using DIFFRAC.texture software. The EBSD measurement was delivered in the CanmetMATERIAL center in Hamilton, Canada, using an EDAX EBSD detector, mounted to an FEI NovaSEM-650 (FEG-SEM), at an operating voltage of 20 kV. The step size for the measurement was chosen to be 0.35 μm. The step size was chosen such that a minimum of 25 measurements were done per grain, considering a minimum grain size of 2 μm. The data was

post processed using TSL OIM 8.0 software. The data was initially filtered using the grain dilation approach. An orientation difference of 10 degrees or more between adjacent pixels was used to create grain boundaries. For the sake of sample preparation, samples were polished till 3µm diamond paste and then polished with oxide polishing suspensions (OPS) for improving the polishing results. Subsequently, the samples were chemically polished in a 5% Nital solution for 30 seconds. Further details regarding the EBSD setup and data processing can be found in [102].

7.3 Results

7.3.1 Microstructure and texture

Figure 82 shows the typical microstructure and texture of the starting alloy and the forged material at different locations throughout the cross section of the I-beam following a standard procedure for Mg alloys. Both alloys exhibit bi-modal grain morphology, where large island-shaped grains are surrounded by fine equiaxed grains. These islands are solid solution material that involve less Zn and Zr resulting in their resistance to the hot deformation and recrystallization, while the equiaxed grains are formed by partial recrystallization (DRX) [145][116]. The average grain size for the DRXed grains in the starting material was determined to be 8.1±1.9 µm, following the linear intercept method, while the forged alloy demonstrated an average value of 4.6±1.6 µm for the fine grains, which is 43% smaller than the parent grains. It is also noted that the microstructure of the material in both flanges, where the samples are extracted from, are approximately similar (Figure 82 (d) and (e)).

The texture measurement shows that the forging operation has modified the texture of the starting alloy in the I-beam flanges. While the starting alloy showed a preferred crystallographic orientation suggesting the majority of the c-axes were oriented perpendicular to the extrusion direction, the same pole figures for the forged alloys indicate that the c-axes of the magnesium unit cells have slightly reoriented toward the radial (RD) and longitudinal (LD) directions. This delay the extension-twin formation in the cyclic response of the forged material, as will be discussed thoroughly later.

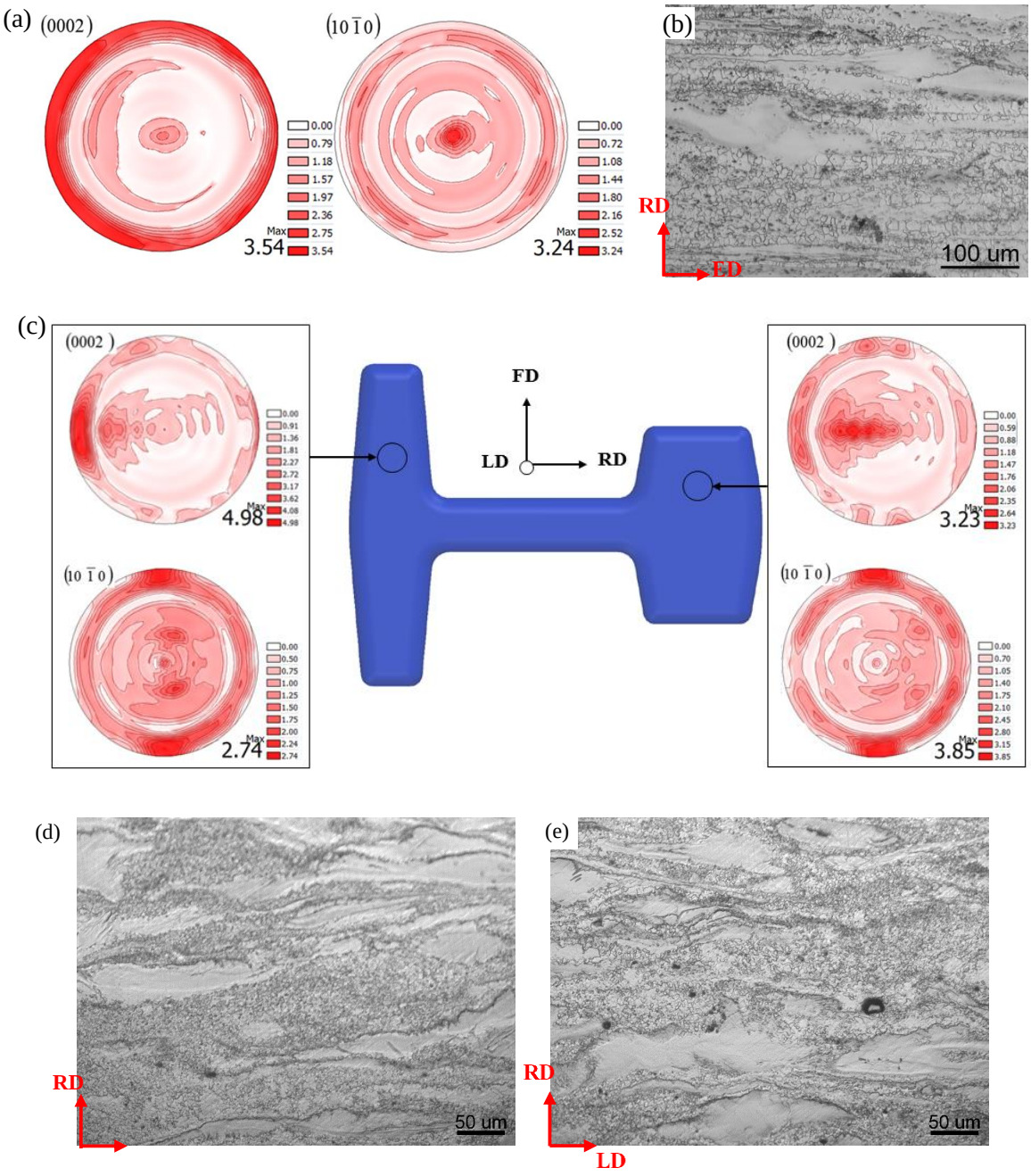

Figure 82. Microstructure (b,d,e) and pole figures (a,c) of ZK60 extrusion (a,b) and forged ZK60 (c,d,e)

7.3.2 Quasi-static behavior

Figure 83 plots the quasi-static axial and torsional behavior of ZK60 before and after forging. As expected, the forging process has improved the mechanical properties. However, this effect is more pronounced in the axial response. The increase in the mechanical properties is attributed to the grain refinement achieved after the forging process. To be more specific, the forged material exhibits 13% increase of the axial yield and 10% increase of the ultimate strength besides the significant 64% improvement of the elongation. However, the change in the shear response is not as remarkable as the one in the axial. The average shear yield strength and ultimate shear strength increased slightly by 3%, while the strain to failure was increased a little more by 16%. The axial and shear properties of extruded and forged materials are summarized in Table 16. The standard deviation numbers for the shear properties are relatively large. This, as will be discussed later, is because extension twinning is accommodating the shear strains at high strains. Due to the orientation-dependent nature of twinning, shear properties depend on the crystallographic orientation of unit cells which varies across the cross section of the I-beam according to the texture measurements. Thereby, the shear properties show large standard deviations.

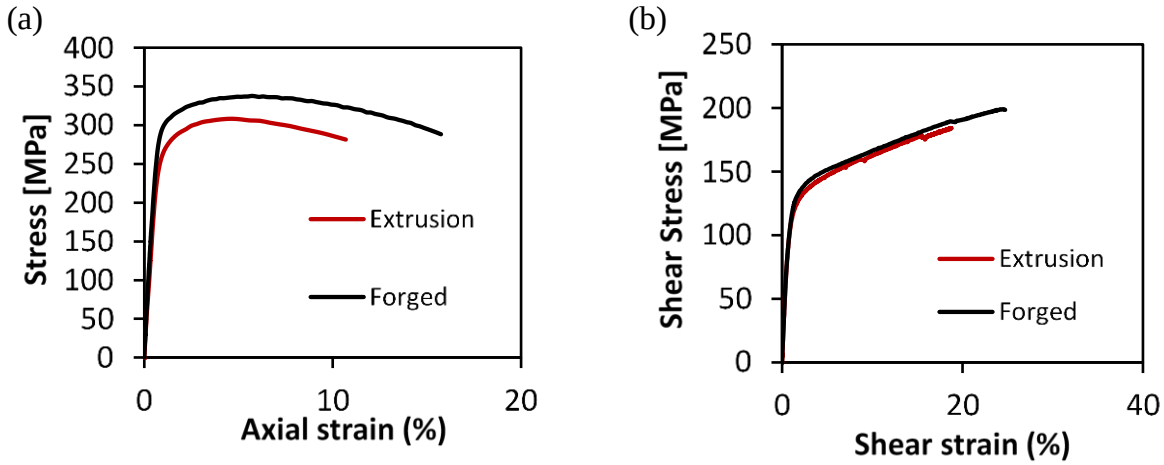

Figure 83. Effect of forging process on the (a) axial and (b) shear quasi-static behavior

Table 16. Quasi-static mechanical properties of ZK60 extrusion and forged under axial and shear loading

Material	Axial				Shear			
	E [GPa]	σ_y [MPa]	σ_{UTS} [MPa]	$\varepsilon_{failure}$ (%)	G [GPa]	σ_y [MPa]	σ_{UTS} [MPa]	$\varepsilon_{failure}$ (%)
Extrusion	43 ± 1	251 ± 0	309 ± 1	11 ± 0	17	94	183	19
Forged	45 ± 0	284 ± 1	339 ± 1	18 ± 2	16 ± 1	97 ± 7	190 ± 13	22 ± 4

7.3.3 Texture and microstructure evolution during the shear loading

Figure 84 depicts the evolution of texture in ZK60 extrusion after final failure under quasi-static shear loading at ~20% strain. Comparing this texture with that of undeformed alloy, Figure 60, it is noted that texture in the deformed material has changed considerably, and the majority of the grains have possessed new orientation which indicates the activation of twinning at such a high shear strain. The microstructure of the failed sample was also analyzed under optical microscope. Figure 85 clearly demonstrates the existence of twinning after applying shear loading (It had already shown in Figure 59 that the undeformed material's microstructure was twin-free).

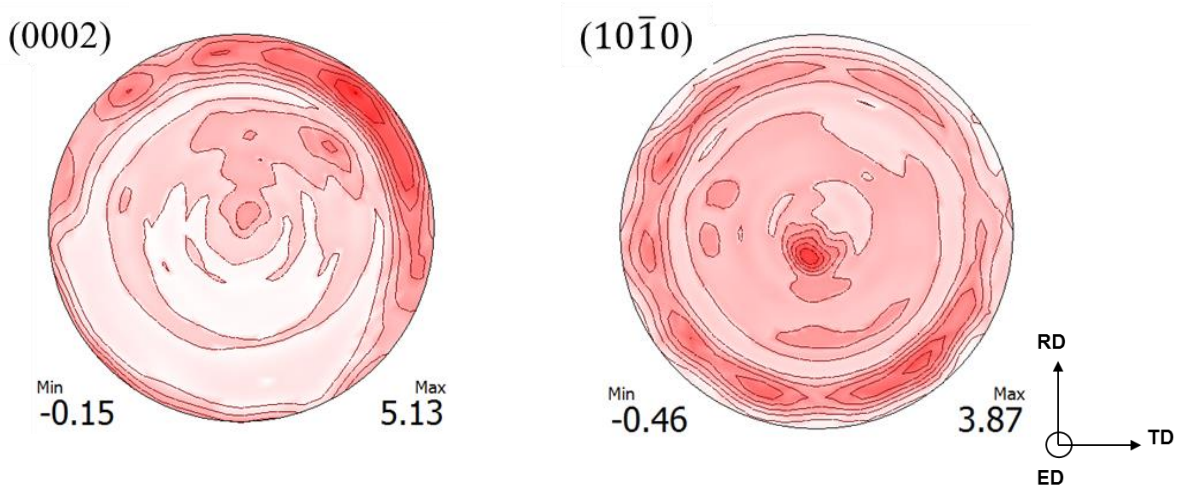

Figure 84. (0002) and $(10\bar{1}0)$ pole figures of deformed ZK60 extrusion under 20% shear strain

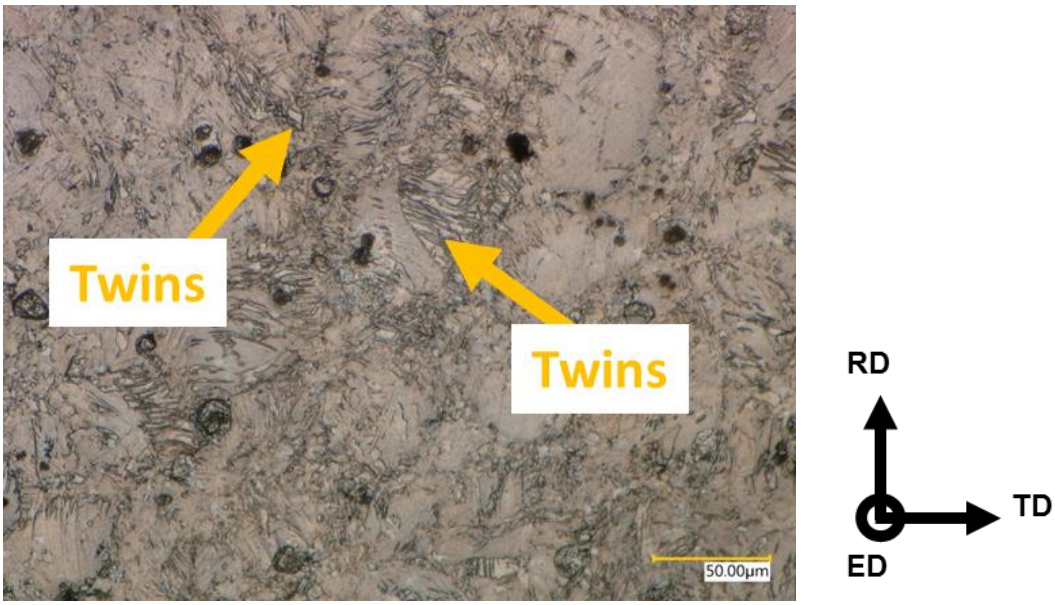

Figure 85. Microstructure of deformed sample under shear loading illustrating the traces of twins obtained at 20% shear strain

EBSD measurement is conducted on both undeformed and deformed samples to identify the type(s) of twinning deformation that is/ are involved in the quasi-static shear loading. Figure 86 illustrates the extrusion EBSD inverse pole figure maps (IPF) and the misorientation angle plot of ZK60 extrusion before applying the shear loading. The results show that twins are not present in the undeformed material.

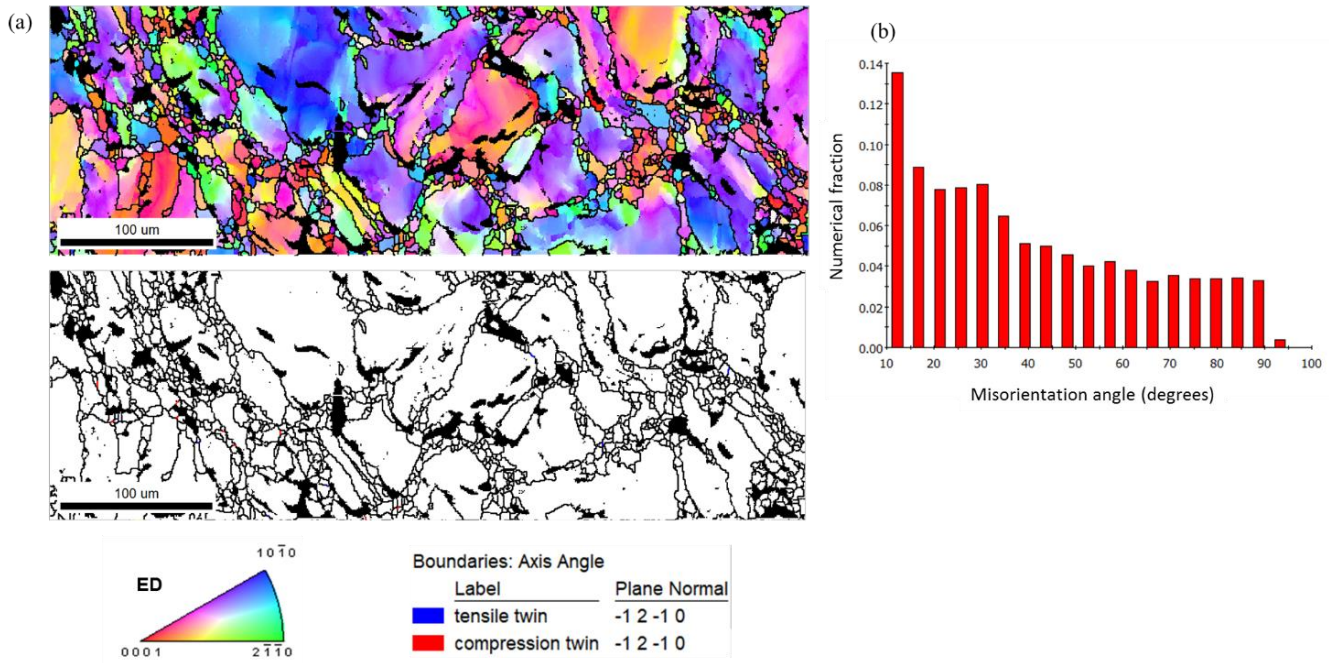

Figure 86. (a) EBSD inverse pole figure of undeformed ZK60 extrusion; (b) misorientation angle plot for undeformed ZK60 extrusion

The EBSD IPF results for deformed ZK60 extrusion are depicted in Figure 87, and tensile twins are marked with blue lines. It is noted that the microstructure contained extensive amount of tensile twinning. Figure 87 (b) also shows the misorientation angle plot for deformed material and the peak at ~86.3° confirms the $\{10\bar{1}2\}$ tensile twinning. Therefore, considering the change in the texture and the results from EBSD, it is concluded that extension twinning is involved in the shear failure of Mg alloys.

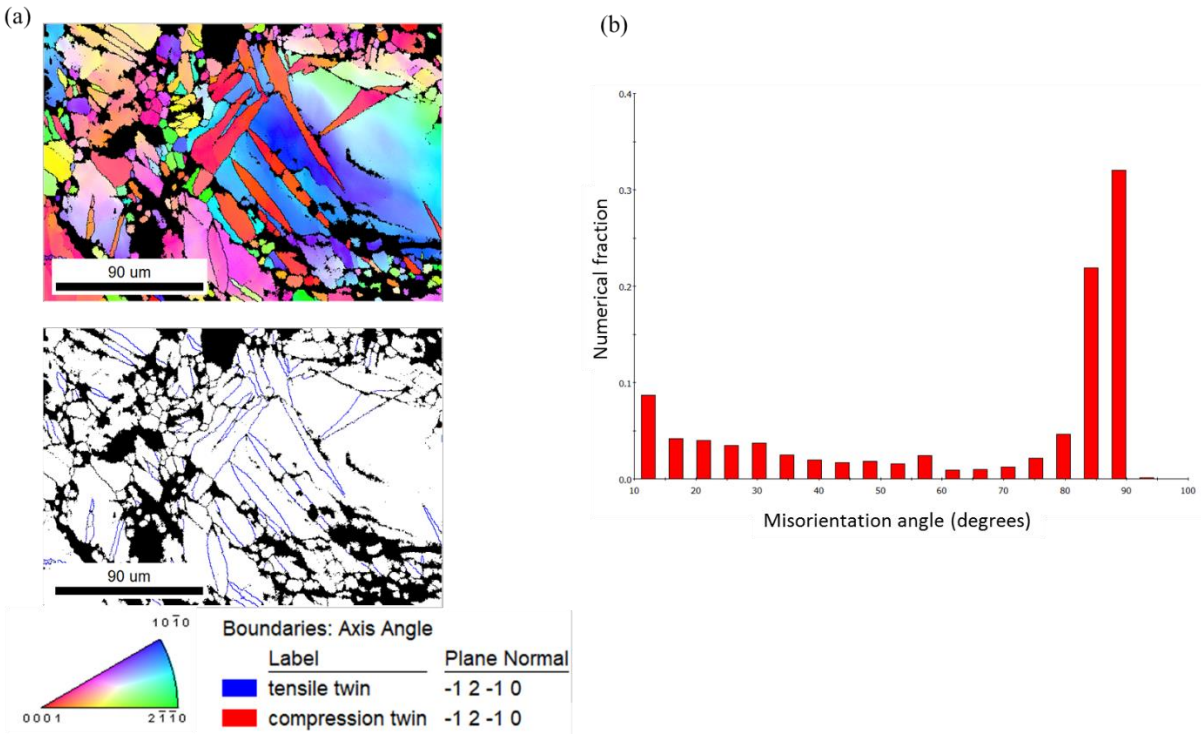

Figure 87. (a) EBSD inverse pole figure of deformed ZK60 extrusion; (b) misorientation angle plot for deformed ZK60 extrusion

7.3.4 Cyclic loading

Figure 88 illustrates the effect of the forging process on the cyclic axial and pure shear loading. Once again, like the quasi-static behavior, the impact of forging process on the axial response was more conspicuous than that on the shear response. Under axial loading, for strain amplitudes higher than 0.6%, both materials display similar fatigue lives. However, at lower strain amplitudes, the forged alloy shows higher fatigue lives. For instance, while the fatigue life of as-extruded alloy at the axial strain amplitude of 0.5% was 3367 cycles, that for the forged material was improved to 8561 cycles. The increase in the fatigue life of the forged alloy is a two-fold: (i) At low strain amplitudes, that plasticity is modest, the fatigue response is ascribed to the material's strength against the crack initiation, whereas in the low cycle fatigue (LCF) regime, the cyclic life corresponds to the material's tolerance to the defects and assessing its resistance to the crack propagation [156]. Hence, an empirically traditional strategy says the higher the quasi-static strength, the better the fatigue response in the high

cycle fatigue (HCF) regime; on the other hand, higher ductility under quasi-static loading leads to a better performance in the LCF regime [53]. In this context, the forged material is showing better HCF response, as its higher yield strengths demand for more cycles to accumulate the damage required for the crack initiation. This is in analogy to the results obtained in Chapter 6 for investigating the uniaxial fatigue behavior of ZK60 extrusion along different directions, where the extrusion direction having the highest yield strength was exhibiting the highest fatigue lives among all directions, whereas the fatigue behavior was insensitive to the loading direction in the LCF regime.

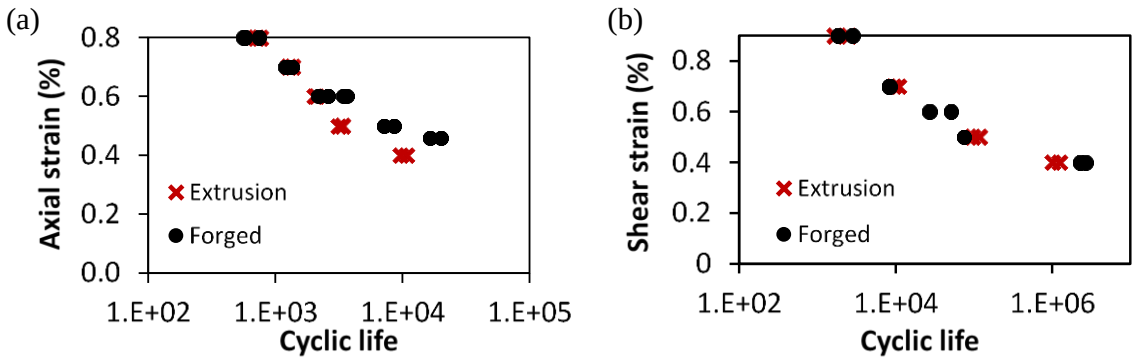

Figure 88. The impact of the forging process on the strain-controlled cyclic behavior of ZK60 under (a) axial and (b) pure shear loading

(ii) At the axial strain amplitude of 0.5%, another factor contributing to the higher fatigue life for the forged alloy in addition to the yield strength is the material's texture. Figure 89 depicts the hysteresis loop of the extruded material and the forged one at the second and half-life cycles. As discussed in Chapter 6 and also shown in Figure 89 (a) for ZK60 extrusion, at the strain amplitude of 0.5%, extension twinning and detwinning are active under the compression and tension reversals, respectively, at the second cycle along the extrusion direction. However, the twinned grains in the compression reversals are not fully detwinned in the next tension reversal; hence, some residual twins remain in the microstructure. As the twinning mode exhausts its capacity to accommodate the strain in the following cycles, it is reported that slip modes of system will accommodate the deformation and the material hardens rapidly

[18][42][148]; thereby, the hysteresis loop at the half-life cycle will not be sigmoidal anymore, however, the interaction of the slip systems with the residual twins brings about tensile mean stress in the following cycles that can affect the fatigue life adversely. On the contrary, the basal texture in the forged alloy is weaker comparing to the as-extruded one leading to a symmetric hysteresis loop at the second cycle, and no twinning-detwinning is involved for accommodating the strain during the deformation. Therefore, the tensile mean stress at the half-life cycle is lower than that for the extruded material, i.e. 1 MPa for the forged alloy vs 43 MPa for the extruded alloy. The higher tensile mean stress for the extruded ZK60 is detrimental to its fatigue life leading to a lower fatigue life at the strain amplitude of 0.5%.

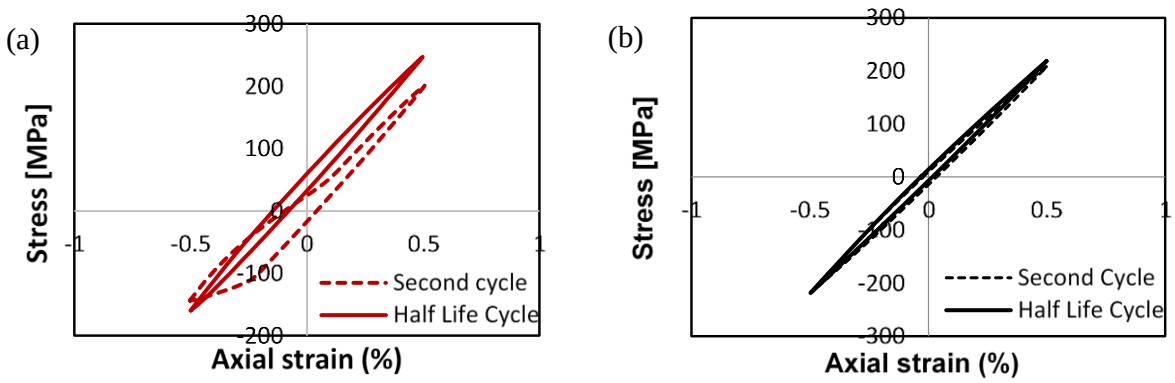

Figure 89. Evolution of hysteresis loops for the second and half-life cycles at the strain amplitude of 0.5% under axial loading for (a) ZK60 extrusion and (b) ZK60 forged

Figure 90 illustrates the axial response of the extrusion and forged alloys at a relatively high strain amplitude of 0.8% at which twinning/ detwinning is active for both materials. It is noted that while the tensile peak stress of the forged alloy is marginally more than that of the extruded alloy, which can cause slightly more damage during the tensile reversal, the area inside the hysteresis loop of the forged material representing the dissipated energy during a cycle is lightly less than that of the extruded one. Consequently, the overall result of the competing factors, namely, the tensile stress' damage and the dissipated energy due to plasticity, is the equal fatigue life for both materials at high strain amplitudes.

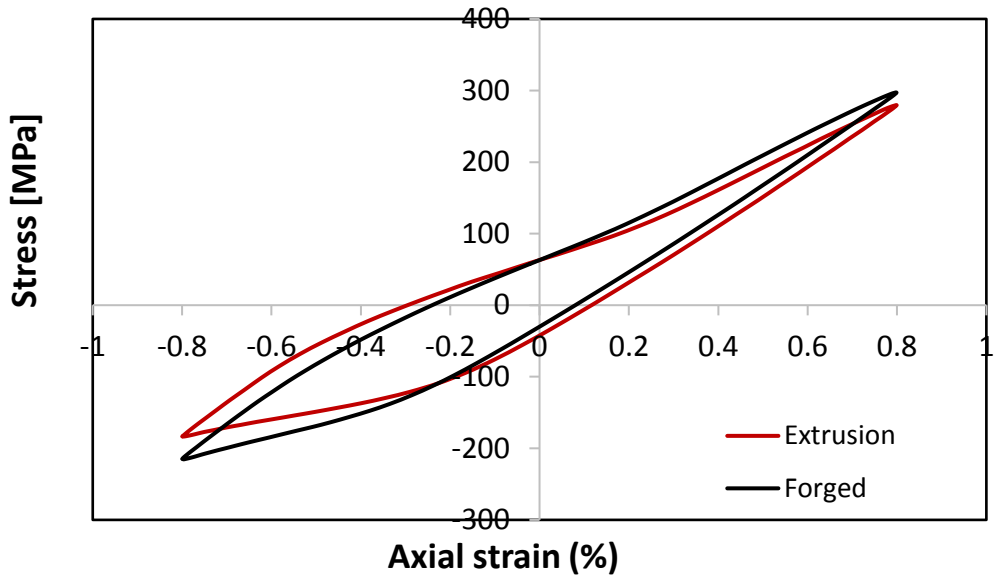

Figure 90. Half-life hysteresis loops for the extruded and forged alloy at the strain amplitude of 0.8%

The stabilized hysteresis loops for the various tested shear strain amplitudes are presented in Figure 91 at the half-life cycle. It is noteworthy that unlike the hysteresis loops obtained for the axial direction along ED, Figure 62, the shear hysteresis loops are relatively symmetric at all tested shear strain amplitudes for both materials which can be ascribed to the slip dominated plasticity during the loading. Figure 92 illustrates the basal (0002) and prismatic $(10\bar{1}0)$ pole figures of ZK60 extrusion samples tested at 1.1% shear strain amplitude under fully reversed cyclic loading. The XRD measurement was done on a section far away from the final crack to suppress the effects of stress localization on the texture and microstructure of the material around the fatigue crack. From this figure, it can be seen that the texture has not changed considerably, and there is no change in the orientation of basal planes (0002), which is an evidence for the dominancy of slip deformation at the tested range of shear strain amplitudes. Lastly, the microstructure of the deformed sample was studied under optical microscope, which is depicted in Figure 93. It is clear from this figure that the microstructure is twin-free after applying 1.1% cyclic shear strain. Albeit, some tiny twins are visible in Figure 93 which are believed to be made during the polishing process.

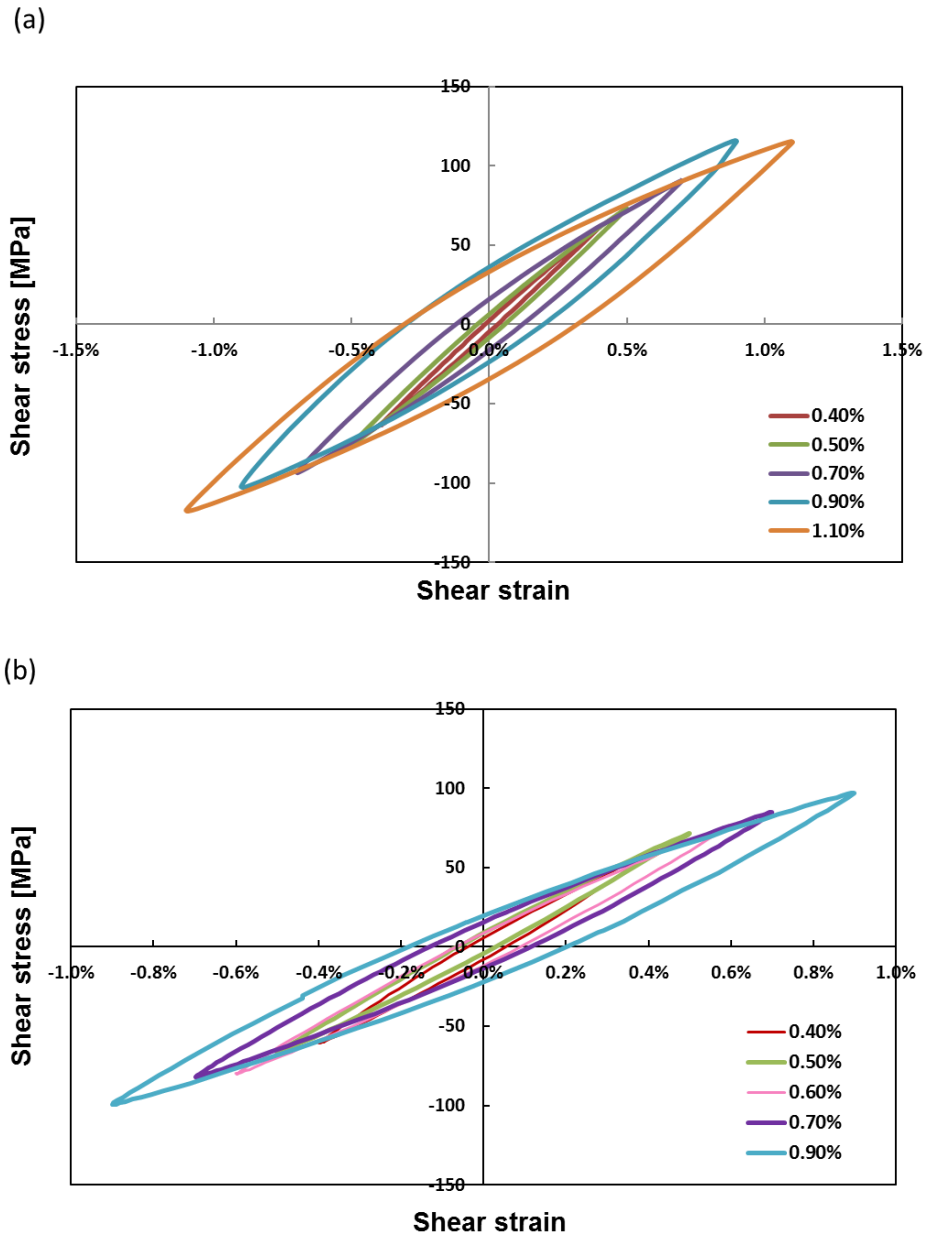

Figure 91. Stabilized shear hysteresis loops at various shear strain amplitudes for (a) ZK60 extrusion (b) ZK60 forged

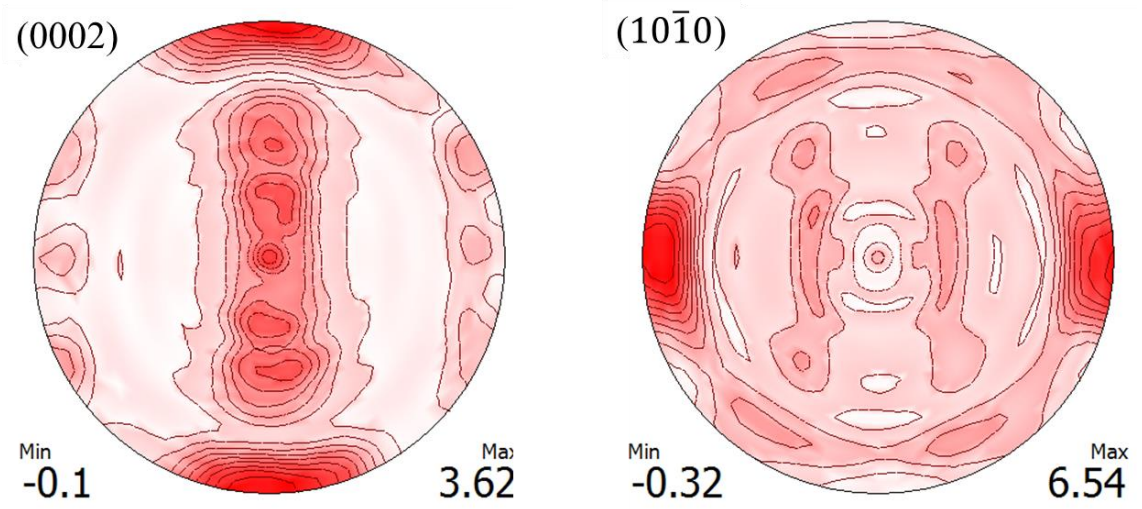

Figure 92. (0002) and (10$\bar{1}$0) pole figures of ZK60 extrusion obtained from samples tested at 1.1% fully reversed shear strain

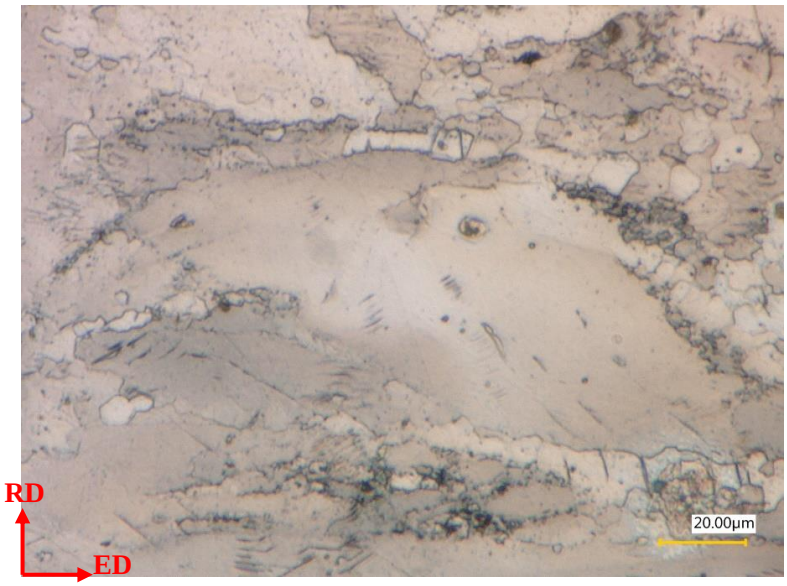

Figure 93. Typical microstructure of deformed ZK60 extrusion at 1.1% fully reversed shear strain

Another considerable feature of cyclic shear loading for both ZK60 extrusion and forged is the significantly lower degree of cyclic hardening. The evolution of shear stress amplitude during the cyclic history is shown for both materials in Figure 94 which illustrates moderate cyclic hardening even at high shear strain amplitudes. These results are in accordance with the cyclic shear behavior reported for AZ31B extrusion [69] and AZ31B extruded-forged [204], however, more severe cyclic hardening was reported for AZ61 extrusion [68] and AM30 extrusion [81]. The overall cyclic shear hardening response may also be inferred better in the cyclic shear-strain plot in Figure 95. In this figure, the stabilized shear stress response is plotted against the corresponding quasi-static one up to the final tested shear strain amplitude. It is clear that for both materials, the extent of cyclic hardening is moderate.

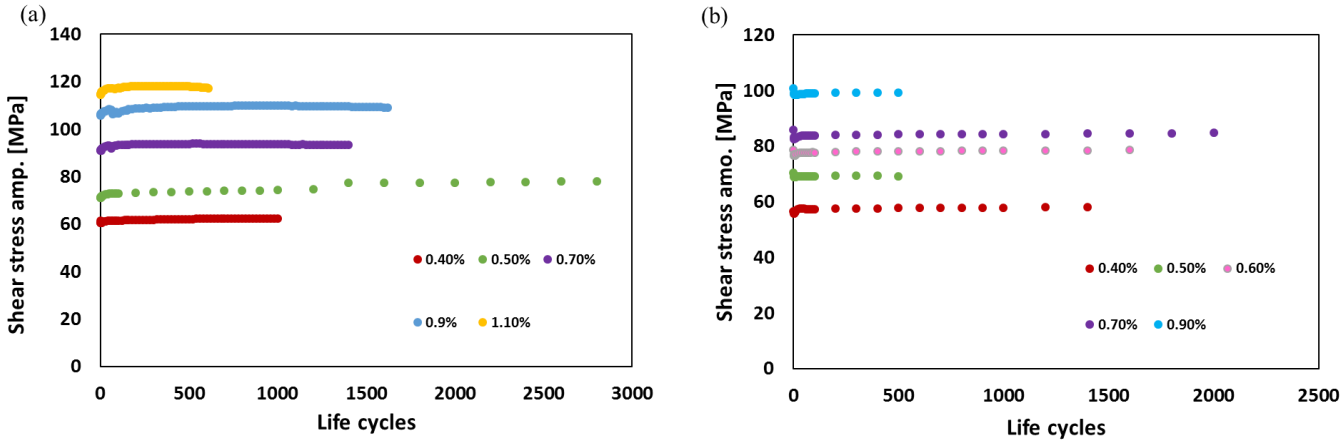

Figure 94. evolution of the shear stress amplitude vs. number of cycles for ZK60 (a) extrusion and (b) forged

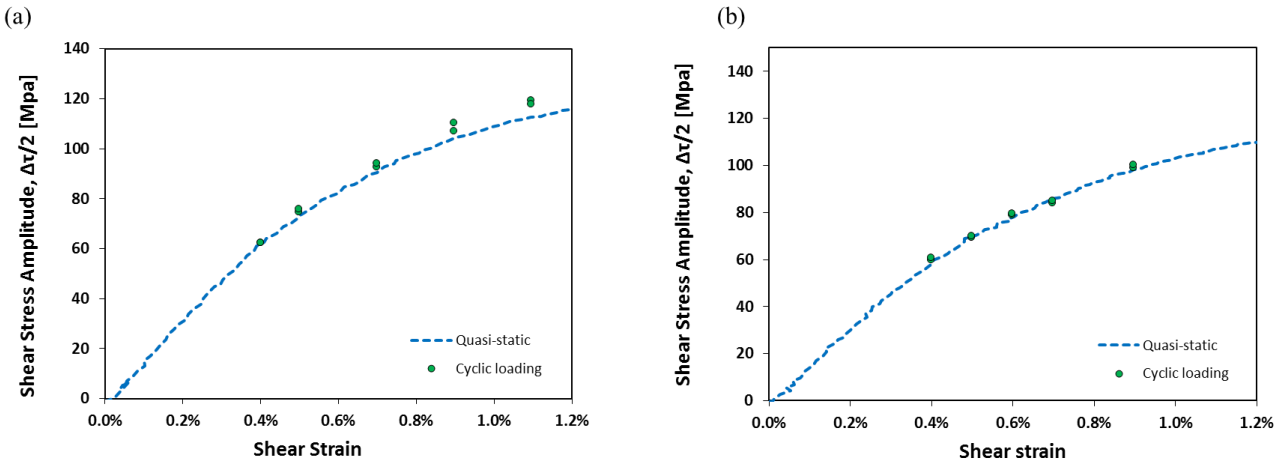

Figure 95. Comparison of the cyclic shear response and the quasi-static response for (a) ZK60 extrusion and (b) ZK60 forged

7.3.5 Multiaxial fatigue behavior

Fully reversed proportional and non-proportional multiaxial fatigue tests are conducted at various strain and shear strain amplitudes along with different phase angles. A summary of all the fatigue results are presented in Table 17. The strain amplitudes, shear strain amplitudes, and phase angles were selected so as to study the multiaxial fatigue behavior from two perspectives: (i) The interaction of axial and shear loading and the effect of these loadings on different modes of deformation in ZK60 extrusion and forged, and (ii) the materials' multiaxial fatigue behavior's sensitivity to the phase angle shift.

Table 17. Fatigue results under proportional and non-proportional multiaxial cyclic tests for ZK60 extrusion and ZK60 forged

	Spec. ID	ε_a (%)	γ_a (%)	σ_{max} [MPa]	σ_{min} [MPa]	σ_m [MPa]	τ_{max} [MPa]	τ_{min} [MPa]	τ_m [MPa]	N_f Cycles
Extrusion	IN2	0.7	1.0	212	-174	19	89	-78	6	380
	IN3	0.7	1.0	113	-126	-6	70	-73	-1	9312
	IN4	0.3	0.5	112	-122	-5	69	-71	-1	12660
	IN5	0.3	0.5	108	-107	1	108	-101	3	901
	IN6	0.3	1.0	104	-105	0	112	-104	4	947
	IN7	0.3	1.0	192	-162	15	98	-88	5	425
	IN8	0.6	1.0	213	-172	21	92	-81	5	374
	IN9	0.7	0.5	245	-191	27	53	-46	4	909
	IN10	0.7	0.5	249	-190	30	57	-49	4	736
	45_1	0.7	0.5	257	-193	32	62	-66	-2	777
	45_2	0.3	0.5	103	-137	-17	77	-69	4	8435
	45_3	0.7	0.5	262	-195	34	64	-68	-2	879
	45_4	0.3	0.5	116	-129	-7	72	-75	-1	15412
	45_5	0.3	1.0	115	-107	4	113	-109	2	834
	45_6	0.3	1.0	113	-108	3	109	-108	0	1017
	90_1	0.7	0.5	254	-200	27	74	-78	-2	768
	90_3	0.3	0.5	122	-128	-3	74	-82	-4	34595
	90_5	0.3	0.5	135	-114	11	73	-79	-3	23641
	90_6	0.3	1.0	118	-121	-2	110	-112	-1	1681
	90_7	0.3	1.0	114	-123	-4	111	-110	1	1278
	90_8	0.7	0.5	255	-197	29	70	-78	-4	771
Forged	IN2	0.4	0.5	161	-155	3	62	-63	0	4966
	IN1	0.4	0.5	162	-154	4	62	-64	-1	3248
	IN3	0.7	0.5	240	-210	15	51	-51	0	505

	IN4	0.7	0.5	250	-214	18	49	-46	2	383
	45_1	0.4	0.5	149	-165	-8	66	-70	-2	5046
	45_2	0.4	0.5	153	-157	-2	63	-67	-2	4883
	45_3	0.7	0.5	257	-220	18	53	-57	-2	383
	45_4	0.7	0.5	249	-225	12	58	-63	-2	483
	90_1	0.4	0.5	171	-156	7	62	-63	-1	1729
	90_2	0.4	0.5	165	-158	3	65	-66	-1	2098
	90_3	0.7	0.5	247	-221	13	66	-68	-1	413
	90_4	0.7	0.5	251	-230	10	65	-67	-1	410

7.3.5.1 Effect of load multiaxiality

Proportional multiaxial fatigue tests were delivered on the extruded and the forged ZK60 alloy at low and high strain amplitudes. The lower strain amplitudes of 0.3% and 0.4% cannot activate twinning/detwinning modes of deformation under pure axial loading in the extruded and forged materials, respectively, whereas the 0.7% strain amplitude is high enough to trigger these modes profusely. The shear strain amplitude was chosen relatively small as 0.5% so that the strain would be accommodated dominantly by the slip modes of deformation. Hence, any effects associated with the interactions of slipping and twinning resulting from the co-occurrence of the imposed shear and axial strains can be considered by examining any changes in the stabilized half-life hysteresis loops.

Figure 96 illustrates the stabilized half-life axial hysteresis loops under pure axial and variety of different load multiaxiality combinations for ZK60 extrusion (a,c) and ZK60 forged (a,b). The findings suggest that while the imposed shear strain affects the slip, twining, and detwinning modes of deformation differently, this effect is similar in both alloys. In particular, the shear strain does not change the stress required to activate the extension twining and detwinning for accommodating the applied axial strain significantly in both alloys. In contrary, it brings about less resistance against the slip mode of deformation. Therefore, the hardening rate of the slip-dominated part of the hysteresis loops (end of the tensile reversal in (a) and

both peaks in (b and c)) is decreased leading to lower tensile peaks, whereas a near identical twining- and detwinning-dominated portions are observed at the end of the compressive and onset of the tensile reversals of the hysteresis loops of both materials in Figure 96 (a) that twining/ and detwinning are involved significantly, whereas the hardening rate of the slip-dominated part of the hysteresis loops (end of the tensile reversal in (a) and both peaks in (b and c)) is decreased leading to a lower tensile peaks. In other words, the shear strain which is mostly accommodated by the slip mode of deformation does not affect the twinning/ and detwinning behavior considerably, whereas the slip occurring in the shear direction reduces the stress needed to activate slip in the other direction (axial direction). A similar multiaxiality effect is observed in [81] for AM30 extrusion.

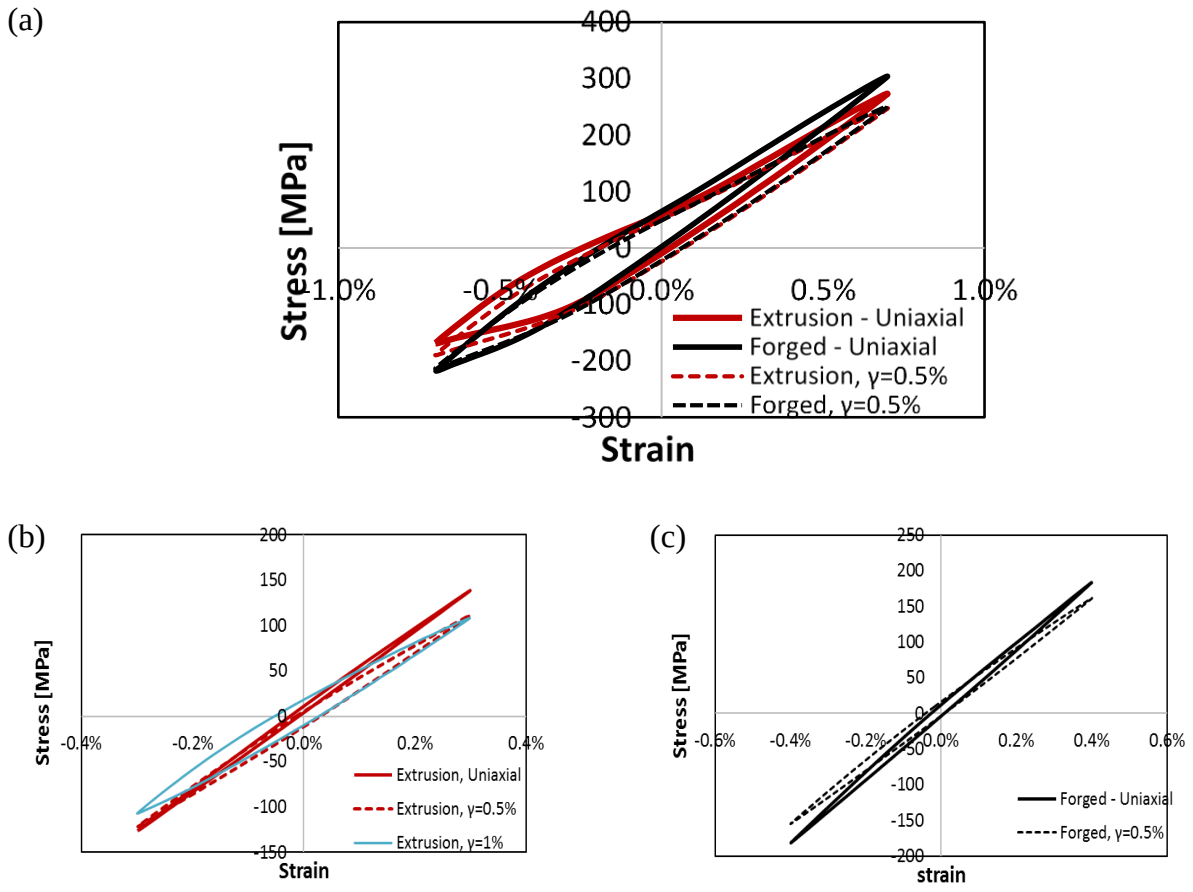

Figure 96. Effect of the imposed shear strain on the slip, twining and detwinning modes of deformation under axial loading at the strain amplitude of (a) 0.7%, twining/ detwinning active, and (b) 0.3%, slip active in ZK60 extrusion and (c) 0.4%, slip active in forged ZK60

Another significant effect of the combined shear-axial strain is the increase of the axial dissipation energy in each cycle. In fact, the area inside a hysteresis loop refers to the energy being dissipated during a cycle, and despite the reduction in the hardening rate during the slip-dominated sections of the hysteresis loops, the area inside them has increased. This is more pronounced once a large shear strain amplitude such as 1% is accompanying a small axial strain amplitude such as 0.3%. Under such low strain amplitudes, rarely is plasticity involved in the deformation, and the limited amount of plasticity is dominantly accommodated by

slipping. However, the addition of a relatively high shear strain results in the activation of some extension twins by lowering the CRSS on the twin planes. Consequently, more plasticity is involved in the deformation [81]. On the other hand, high axial strain amplitudes such as 0.7% sufficiently activate extension twining and addition of a high shear strain would not contribute substantially to the increase of the overall twin volume fraction. Consequently, the dissipated energy in Figure 96 (a) has not varied dramatically by adding the shear strain.

In a manner analogous to what presented above, Figure 97 delineates the effect of the axial loading on the shear response at the stabilized half-life cycle under slip dominated and twin-dominated strain amplitudes. In general, low axial strains which would be driven largely by slipping contribute to the small lowering of positive and negative peaks by reducing the resistivity against slipping along the shear axis, Figure 97 (a), like the reduction occurring in the axial response, Figure 96 (b) and (c). For example, in the case of proportional 0.4%-axial strain and 0.5%-shear strain test on the ZK60 forged, tensile and compressive peaks are lessened by 12% and 16%, respectively, and the positive and negative peaks in the shear response are reduced by 12% and 6%, respectively. It is possible, therefore, that the slip occurring in one direction, facilitates the activation of slipping in the other direction. On the other hand, the company of high strain amplitudes such as 0.7%, that activate extension twining along the axial axis reduces the positive and negative peaks as it is done under slip-dominated strain amplitudes; however, this reduction is much more considerable when twining is happening (Figure 97 (b)). In fact, extension twining rotates the basal planes of the grains by 86.3° [36]. This reorientation allows easier movements of slip planes leading to lowering the required shear stress for activating slipping along shear axis.

Lastly, it is noted that the area inside the hysteresis has increased which denotes higher dissipated energy during each cycle. This increase in the strain energy density is more remarkable when twinning is considerably happening. For instance, while the shear plastic strain energy for a pure shear fatigue test at the amplitude of 0.5% was increased by 79% after introducing 0.4% concurrent axial strain, that will be augmented by 179% in the presence of proportional 0.7% axial strain that promote the activation of extension twinning.

(a)

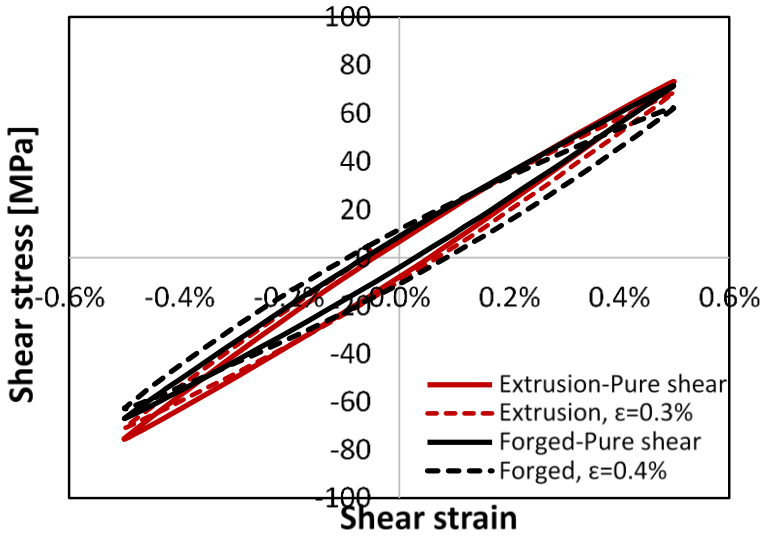

(b)

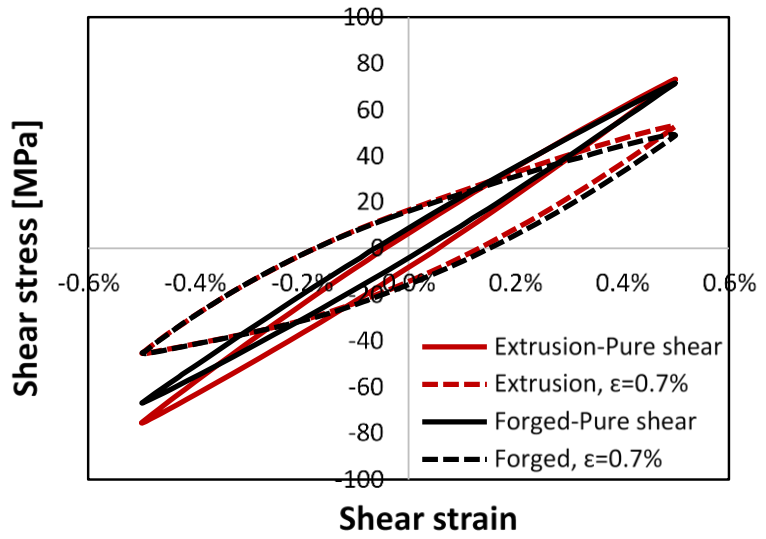

Figure 97. Shear response of ZK60 extrusion and forge under pure shear and multiaxial loadings at shear strain amplitude of 0.5% and axial strain amplitudes of (a) 0.3% and 0.4% (no twining) and (b) 0.7% (twinning)

7.3.5.2 Phase angle effects

Multiaxial fatigue tests were conducted at various phase angle shifts, namely 0° in phase, 45° out-of-phase, and 90° out-of-phase. Figure 98 illustrates the influence of the phase angle shifts on the axial and shear response of ZK60 extrusion and forged at the stabilized half-life cycle. In general, the effect of non-proportionality on the hysteresis loops was similar for

both materials. To be more specific, the axial response is not sensitive to phase angle whether or not twinning is happening, but shear shows pronounced sensitivity to the phase angle at some strain amplitudes. In fact, the axial and shear hysteresis loops for each alloy are near identical regardless of the phase angle degrees when the dominant mode of deformation is slipping at both loading axes (Figure 98 (a, b, c, d)). However, when the axial strain amplitude is increased to 0.7%, which means that the extension twinning is happening abundantly along the axial axis, the corresponding shear loops exhibit substantial sensitivity to the phase angle in both alloys, while the axial responses remained alike at various phase angles. From the peak and valley stress perspective, increasing the phase angles results in the increase of the shear stresses. Similar results were recognized by Gryguc et al for forged AZ80 [82]. This pronounced change in the shear response can be related to the variation of the overall twin volume fraction by changing the phase angle between the load waveforms. In fact, as discussed in the previous section and reported elsewhere [81], twinning facilitates the occurrence of slipping under shear loading by reorienting the grains toward a favorable orientation that lowers the CRSS for the basal slips. Hence, the less twin volume fraction, the higher the required stress required for slipping. On the other hand, in the case of in phase multiaxial loading, the highest twin volume amount (compressive peak point) coincides with the peak of shear strain, while the superposition of shear strain by 90° out-of-phase leads to the least twin volume fraction at shear strain peaks, which yields in the highest amount of shear stress peaks for 90° non-proportionality.

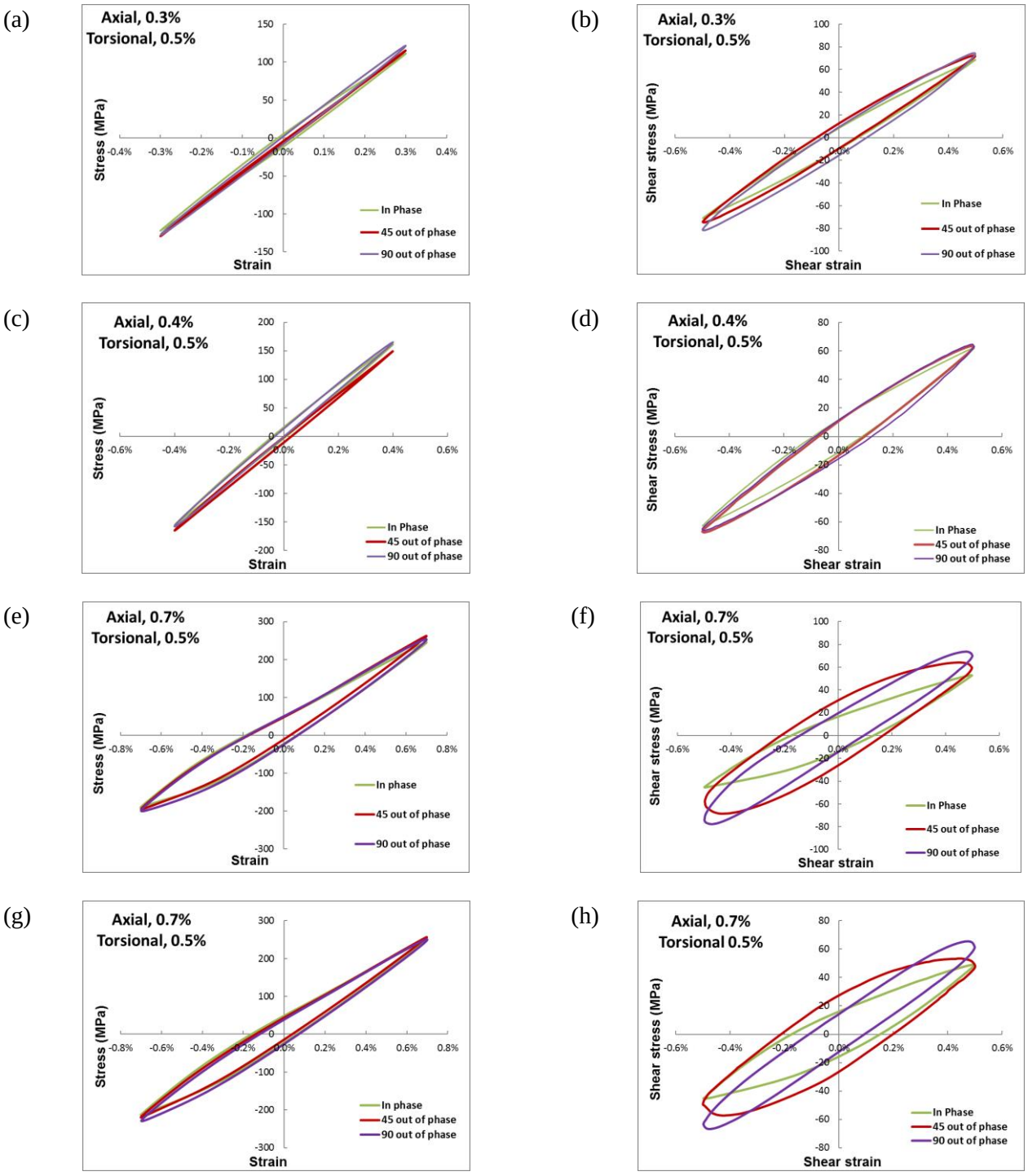

Figure 98. evolution of hysteresis loops at different phase angles at axial strain amplitudes of 0.3% (a), 4% (c), and 0.7 % (e,g) and shear strain amplitudes of 0.5% (b,d,f,h) for ZK60 extrusion (a,b,e,f) and forged (c,d,g,h) at different phase angles

Figure 99 highlights the axial and shear stress amplitudes and the average obtained fatigue lives for ZK60 extrusion and forged under multiaxial fatigue loading at the shear strain amplitude of 0.5% and variety of axial strains and phase angles. It is noted that under the twin-dominated strain amplitudes, i.e, ε_a=0.7% and γ_a=0.5%, no considerable effect of phase angle on the cyclic life can be observed for neither of the alloys. On the other hand, under the slip-dominated strains, ε_a=0.3% and γ_a=0.5% for extrusion and ε=0.4% and γ_a=0.5% for the forged Mg, while the proportional and 45° out-of-phase multiaxial tests exhibit similar fatigue results, 90-degree non-proportionality increases the cyclic life of the extruded alloy and decreases that for the forged material. Moreover, a comparison of the two results from Figure 98 and Figure 99 together reveal that the biaxial fatigue response is somewhat dominated by the axial loading at such loadings that the shear strain amplitude is "small" for two major reasons: (i) the shape of shear hysteresis loops changes dramatically at different phase angles, while the axial response stays fairly invariant to the shift of phase angle; (ii) the fatigue lives are rather similar, especially when twinning is activated under axial loading, despite the remarkable change in the shear stress amplitude. For example, in the case of ε_a=0.7% and γ_a=0.5%, Figure 99 (b) and (c), both alloys show similar fatigue lives at proportional and non-proportional loadings, but the shear stress amplitudes change by more than 20 MPa. A possible hypothesis is the dominancy of the axial response in these loading conditions, which requires more investigations. These findings concur with the findings of literature in [69][46][205] for AZ31B and [82] for AZ80 forged.

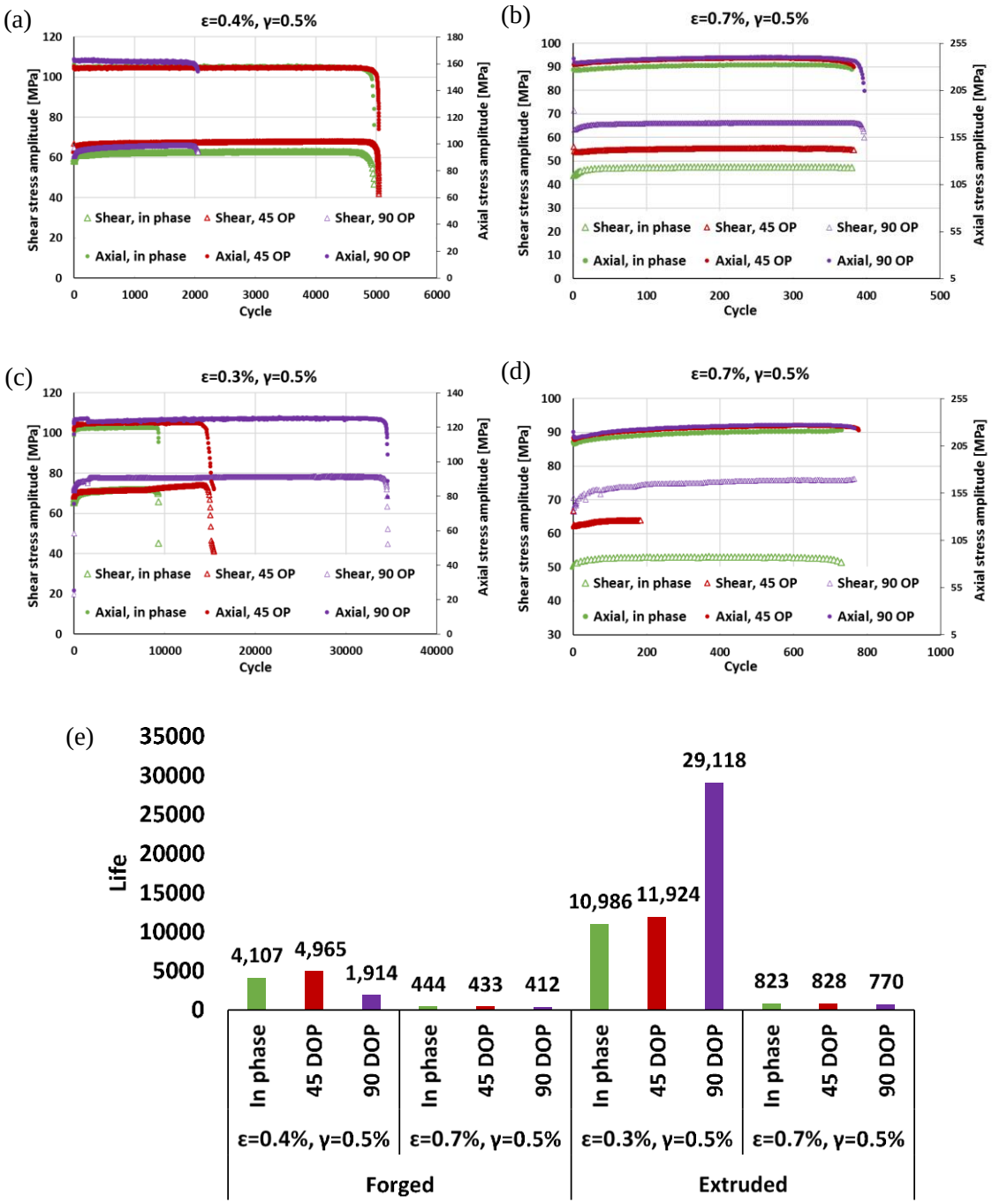

Figure 99. Axial and shear stress amplitudes for ZK60 forged (a,b) and extrusion (c,d) and the average fatigue lives for both alloys (e) at different phase angles of 0°, 45°, and 90°

From crack propagation perspective, Figure 100 illustrates the macroscopic fracture morphology for ZK60. An examination of the crack growth behavior confirms that axial

loading is dominating the multiaxial response under ε_a=0.7% and γ_a=0.5%, Figure 100 (a), due to presence of transverse crack growth which is a typical axial cracking feature. On the other hand, under 0.3% axial and 1% shear strain amplitude, i.e. "small" axial and "high" shear strains, a longitudinal crack is observed which indicates the characteristics of shear loading failure. Figure 101 is showing the variation of axial and shear stress amplitudes during the loading history for 0.3% axial and 1% shear strain amplitude loading. It is observed that unlike Figure 99, shear stress is invariant to the phase angle shift and the axial stress amplitude varies dramatically. Hence, in this case, it is possible that the shear loading is governing the cyclic response to obtain somewhat similar fatigue lives. Lastly, early crack growth is examined under a "high"-"high" combination of strain ratios, ε_a=0.7% and γ_a=1%. At such loading scenario, an oblique early crack growth behavior is seen that tends to be transvers at the moment of final fracture. Therefore, the orientation of earl crack propagation highly depends on the strain ratios.

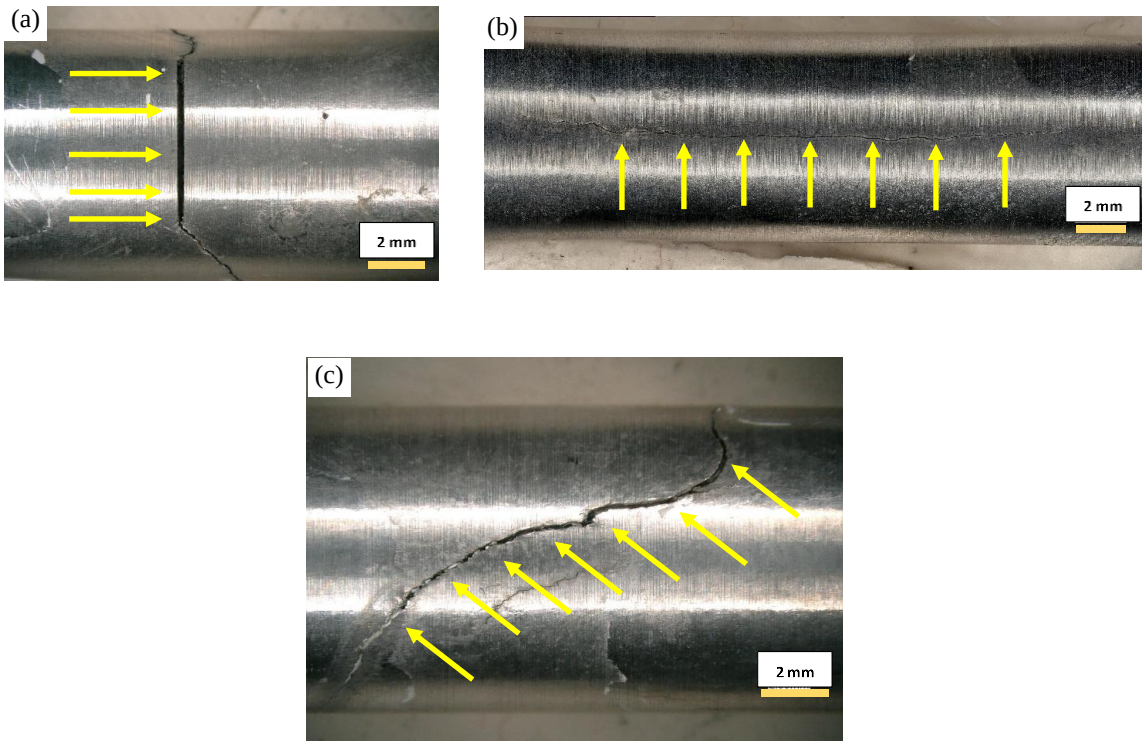

Figure 100. Macroscopic fracture morphology for a ZK60 sample failed under (a) 0.7% axial and 0.5% shear, (b) 0.3% axial and 1% shear, (c) 0.7% axial and 1% shear

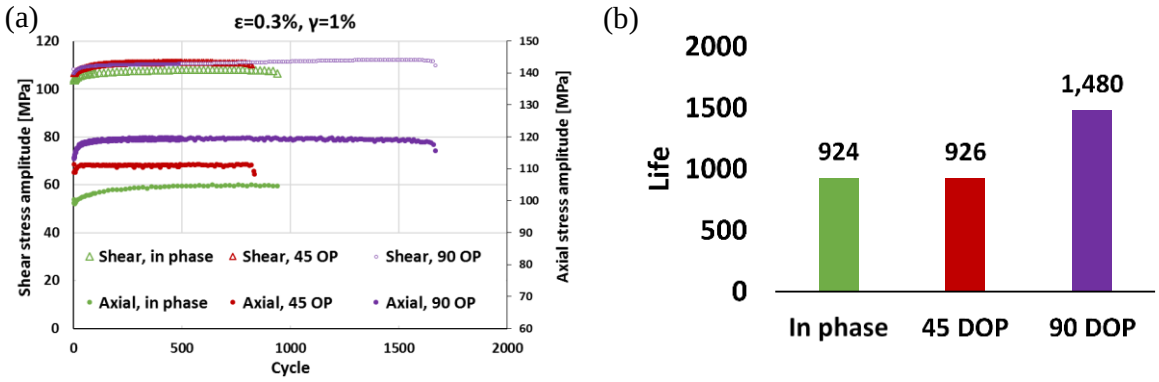

Figure 101. (a) Axial and shear stress amplitudes for ZK60 extrusion under multiaxial loading at ε_a=0.3% and γ_a=1%; (b) average fatigue lives at different phase angles of 0°, 45°, and 90°

7.4 Fatigue modeling

7.4.1 MSWT

The Smith, Watson, Topper (SWT) parameter [206] was modified by Socie with a critical plane interpretation to predict the multiaxial fatigue [86]. However, the model's accuracy was insufficient to correlate the fatigue data under pure torsional loading, as it was designed for materials cracking under tensile loading. Therefore, Jiang and Sehitoglu [89] proposed a modification to the SWT parameter (MSWT) to consider a general cracking mode:

$$MSWT\ Parameter = 2b\Delta\varepsilon\langle\sigma_{max}\rangle + \frac{1-b}{2}\Delta\tau\Delta\gamma \qquad 7\text{-}1$$

where σ_{max} and $\Delta\tau$ are the maximum normal stress and shear stress range in the half-life cycle on a material plane, respectively. Also, $\Delta\varepsilon$ and $\Delta\gamma$ are normal strain range and shear strain range, respectively, corresponding to the normal stress and shear stress. The symbol $\langle\ \ \rangle$ denotes the MacCauley bracket, which is defined as $\langle x\rangle = 0.5(x + |x|)$. In fact, employing the MacCauley bracket makes sure that no compressive damage is incorporated in the model. Lastly, the parameter b is a material constant which represents the cracking mode and varies from 0 to 1. For b=1, the modified SWT parameter becomes the original parameter defined by Socie. It has been stated that $b \geq 0.5$ suggest tensile cracking mode. On the other hand, b

values less than 0.37 suggest the shear cracking behavior, and the values between 0.37 and 0.5 evaluate mixed cracking. Theoretically, the parameter b is determined by setting the pure shear and pure axial responses coincide on a single curve. However, due to the texture influence, it is not possible to have cyclic tension-compression and cyclic shear curves of ZK60 coincide on a curve. Therefore, the value b was varied to get the best fit regression curve of both data set, and subsequently the fatigue parameter was correlated to the fatigue life by a non-linear equation that best fits the experimental data. Based on this method, the value of b for the current alloy was obtained to be 0.245, as shown in Figure 102 (a). Figure 102 (b) plots the baseline fatigue parameter-fatigue life (N_f) curve which is:

$$(MSWT - 0.322)^{1.883}\left(2N_f\right) = 6286.121 \qquad 7\text{-}2$$

The critical plane is defined as the plane where the MSWT parameter is maximum. Equations (1) and (2) can be combined to predict the fatigue life for different multiaxial fatigue loading scenarios. A plot of the predicted fatigue life vs. the experimental life is included in Figure 102 (c). It is clear that the obtained model predicts the cyclic life under different loading scenarios with sufficient accuracy up to the cyclic life of 2×10^4, with the majority of data within a factor of ±2. However, when the fatigue life is more than 2×10^4, the model exhibits "conservative" predictions. This model was employed to predict the fatigue of AZ61A Mg alloys, and the estimations were reasonable in the same life range ($N_f < 2 \times 10^4$) [68]. The same procedure was adopted for ZK60 forged with the material constant b equals to 0.22. The predicted life vs. the experimental life is plotted in Figure 102 (d). the model yields acceptable predictions with the majority of estimations falling within a factor of ±2

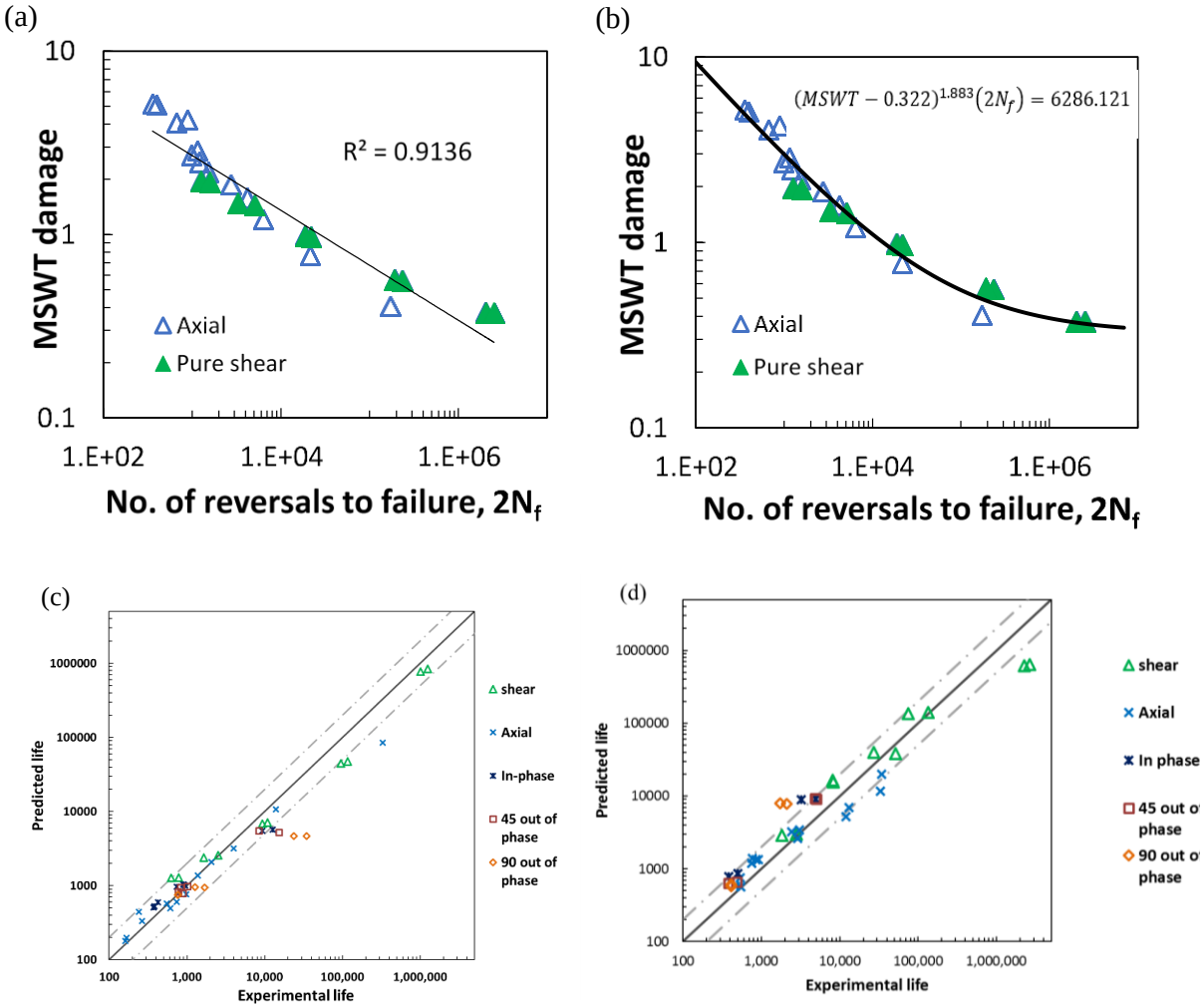

Figure 102. (a) Calculated MSWT damage parameter under axial and shear loading for ZK60 extrusion; (b) the baseline MSWT-N_f relationship for ZK60 extrusion; (c) The correlation of the predicted life by the MSWT model with the obtained experimental life for ZK60 extrusion, (d) the correlation of the predicted life by the MSWT model with the obtained experimental life for ZK60 forged

7.4.2 Jahed-Varvani (JV)

Jahed-Varvani [168] is an energy-based fatigue model which has shown its merits in predicting the multiaxial fatigue behavior of wrought Mg alloys in many researches [46][70][71][82][205]. In this model, the total strain energy density is implemented as the

fatigue damage parameter, which is comprised of the elastic and plastic strain energy densities. The latter is the area inside the axial and shear hysteresis loops. The former elastic part is defined as follows:

$$\Delta E_e^+ = \frac{\sigma_{max}^2}{2E} \qquad Axial \qquad\qquad \Delta E_e^+ = \frac{\tau_{max}^2 + \tau_{min}^2}{2G} \qquad Shear \tag{7-3}$$

where σ_{max} is the axial stress at the positive tip of the hysteresis loop, τ_{max} and τ_{min} are the peak and valley stresses of the shear hysteresis loop at the stabilized half-life cycle, and E and G are the elastic axial and shear modulus, respectively. Subsequently, the strain energy density is correlated to the fatigue life for the pure axial and shear tests with a direct-fit approach to a formula like the Coffin-Manson equation. The modeling parameters are tabulated in Table 18.

$$\Delta E \quad = C_1\left(2N_f\right)^{d_1} + C_2\left(2N_f\right)^{d_2} \tag{7-4}$$

Lastly, the total strain energy density is implemented to the uniaxial fatigue life predictions independently to determine Na and Ns. The final life is determined using the following linear equation:

$$N_f = \frac{\Delta E_A}{\Delta E_T} N_a + \frac{\Delta E_s}{\Delta E_T} N_s \tag{7-5}$$

where the N_f is the final estimated life and ΔE_A and ΔE_s are the axial and shear strain energy density.

Figure 103 shows the estimated fatigue lives under different loading scenarios for ZK60 extrusion and forged. The long-dashed lines denote a factor of 1.5 zone. It is clear that the majority of estimations lie down in this area that denotes the merits of the model in predicting the proportional and non-proportional cyclic life.

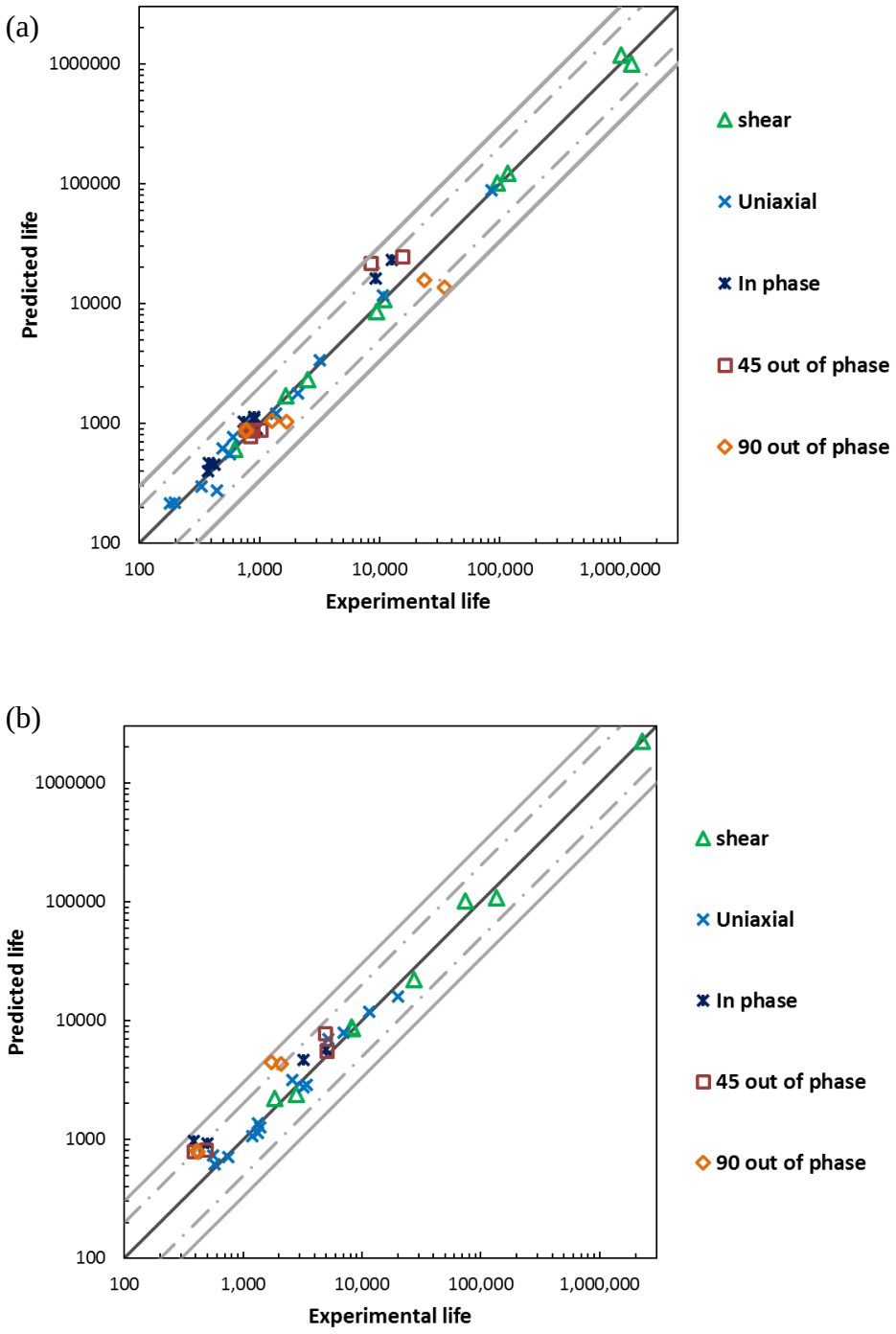

Figure 103. The correlation of the predicted life by the JV model with the obtained experimental life for (a) ZK60 extrusion and (b) ZK60 forged

Table 18. Energy-based fatigue parameters used in JV model

	parameter	Extrusion	Forged
Shear	C_1	1.122	0.374
	d_1	-0.117	-0.035
	C_2	36.860	52.557
	d_2	-0.447	-0.499
Axial	C_1	17.746	65.045
	d_1	-0.357	-0.476
	C_2	64984.935	60680.001
	d_2	-1.523	-4.000

7.4.3 Further discussion

The total strain energy density, as a fatigue damage parameter, is determined for the samples the fracture surfaces of which were shown in Figure 100. Figure 104 depicts the damage contributions from the axial and axial loading from the strain energy perspective. It is observed that for the transverse crack growth mode, the axial damage is considerable, i.e. 79% of total strain energy density is from the axial loading, while the shear loading contributes to 21 % of the total strain energy density. On the other hand, for the sample showing longitudinal cracking, torsional damage is 87% of the total damage, whereas in the case of oblique crack growth mode, both axial and torsional loadings show somewhat equal portions of the total damage.

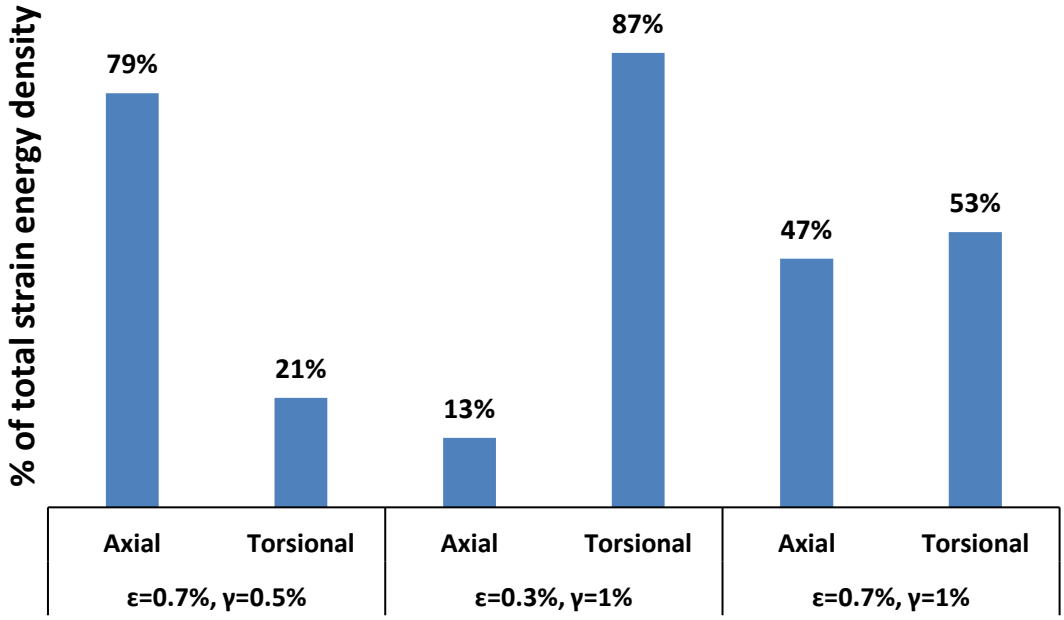

Figure 104. The axial and torsional portions of the total strain energy density

7.5 Conclusion

Multiaxial fatigue characteristics of the starting as-extruded and I-beams forged ZK60 Mg alloys have been studied through conducting quasi-static and fully-reversed strain controlled cyclic experiments including uniaxial, pure torsional, and combined axial-torsional tests at different phase angles, namely 0° proportional, and 45° and 90° out-of-phase non-proportional tests. Based on the results, the following conclusions can be drawn:

1. The forging process refined the grains of the as-extruded alloy. While the average grain size for the fine DRXed grains in the starting material was 8.1±1.9 μm, that for the forged alloy was decreased to an average value of 4.6±1.6 μm, which is 43% smaller than the parent grains. It is also observed that the microstructure is uniform in both flanges of the I-beam forgings.
2. The forging process modified the texture of the extruded alloy in the I-beam flanges. While the majority of the unit cells in the starting alloy were oriented perpendicular to the longitudinal extrusion direction, which was loading direction

in this study, the pole figures of forgings suggest that c-axis of Mg unit cells was reoriented toward the radial (RD) and longitudinal (LD) directions subsequent the thermo-mechanical process.

3. The current forged alloy exhibited an overall improvement in the mechanical behavior, especially under uniaxial loading in the light of grain refinement and texture modification.
4. The texture developed in the forged ZK60 resulted in asymmetric axial response; however, the level of asymmetry was reduced due to texture modification.
5. EBSD measurements showed that shear deformation is causing $\{10\bar{1}2\}$ tensile twinning in the material.
6. Cyclic shear tests showed almost symmetric hysteresis loops at all strain amplitudes for both materials.
7. Combining the shear strain with the axial strain did not change the twin-dominated portion of the axial hysteresis loop in both alloys. However, it reduced the stress required to activate slipping.
8. The company of a high axial strain amplitude that triggers extension twinning reduces the stress needed to accommodate shear strain along the other loading axis for both extruded and forged ZK60.
9. The multiaxial fatigue behavior of ZK60, both extrusion and forged, is somewhat dominated by the axial component once the dominant mode of deformation under shear loading is slipping.
10. For both alloys, the shape of shear hysteresis loop changed drastically by changing the phase angle. Also, fatigue lives were invariant to the phase angle shift, especially when twinning was activated under axial loading, despite the considerable change in the shear stress amplitude.
11. Generally, non-proportionality did not change the fatigue life considerably, particularly, at high strain amplitudes that twinning is involved in the deformation.
12. The early crack growth behavior in both alloys depended on the ratio of axial and shear strain amplitudes. At low shear strain amplitude such as 0.4% and 0.5%, that

slipping is dominant under shear loading, the crack growth is transverse to the axial loading which testifies the dominancy of axial loading.

13. The initial crack growth mode for a low axial and high shear strain amplitude loading is longitudinal cracking, which is a shear cracking feature. Furthermore, the high-high combination of strain ratios led to oblique crack propagation mode.
14. JV, as an energy-based model, showed its merits to predict fatigue lives under various loading paths.

Chapter 8
Summary, conclusions, contributions, and future works

8.1 Summary

The objectives of this research have been fulfilled thorough launching a comprehensive campaign of experimental studies, made by making extensive use of state-of-the-art mechanical and material science facilities, and fatigue modelling. The focus was to establish a link between the material, structure, process, and performance. The extensive experimental characterization of the original and forged materials that has been made through this study is critical for the design and validation of the forging process of Mg alloys in future.

A thorough introduction was proposed at the beginning of the thesis that covers the motivations behind conducting this study, and addresses the objectives of this research, which highlight its novelty and usefulness. In the second chapter, a complete literature review has been made that summarizes the research works surrounding the fatigue behavior of ZK60 Mg alloys. The next four chapters cover the results and findings of this research that have been published in three reputable international journals. Moreover, this work has been disseminated at three well-known international conferences on the material science, fatigue, and multiaxial fatigue, namely, TMS2017 [145], IFC12 [207], and ICMFF12 [208], respectively. Furthermore, several presentations of this work have been delivered in the form of monthly update meetings, project annual meetings, and university seminars for both academic and industry partners to foster transferring the developed discovery-level knowledge to real-world applications.

8.2 Conclusions

The conclusions of each stage of the research work is presented at the end of each chapter. However, for convenient reading, a summary of them is reiterated in this chapter:

1. To characterize the quasi-static and cyclic behavior of cast ZK60 before and after open-die forging

2. To characterize and model the mechanical behavior of ZK60 extrusion in different directions
3. To investigate the effects of close-die forging on the fatigue behavior of ZK60 extrusion

Quasi-static and uniaxial strain-controlled fatigue tests were delivered on the as-cast and open-die forged ZK60. The fatigue tests were conducted at variety of strain amplitudes ranging from 0.2% to 0.9% to investigate the effects of induced sharp texture on the fatigue response of the alloys. Also, the fracture surfaces were analyzed using the SEM and EDX to discern the reasons underlying the failure mechanism of the materials. Lastly, an energy-based model was employed effectively to predict the cyclic lives. Based on the results, the following conclusions were drawn that address the research objective #1:

1. Microstructural analysis demonstrated bimodal refined grains with a significant reduction of casting defects after conducting the forging process on the cast alloy. However, the dendritic morphologies still existed, demonstrating that completed recrystallization (DRX) did not occur.
2. Texture analysis revealed a random texture for the cast material; however, in the case of forged ZK60, grains were orientated mostly toward the forging direction (FD). The intensified texture causes the activation of extension twinning under compression loading along the forging direction that leads to a lower yield strength in compression along this direction; thereby, a significant tension-compression asymmetry was exhibited in the quasi-static and fatigue responses of ZK60 forged comparing to the starting cast alloy.
3. The ductility of the forged ZK60 Mg alloy tested in tension loading increased significantly by 72%, while the ultimate strength remained about the same. The improvement of ductility depends heavily on the presence of defects in the alloy, which was reduced extensively in the forgings. However, the tensile strength in the forged condition remained the same due to the occurrence of incomplete DRX.

4. Fracture surface analysis showed the brittle fracture behavior of as-cast ZK60, while the forged material was showing some dimples which is a typical feature of ductile failure. In fact, this indicates that more plastic deformation was occurring during the test on the forged sample, meaning that material was more ductile after performing the forging.
5. From the fatigue response perspective, as-cast ZK60 displayed symmetric hysteresis loops at different strain amplitudes. On the other hand, the shape of hysteresis loops for the forged material depended on the applied strain amplitude and showed substantial asymmetry when extension twinning was occurring in the compression reversal and subsequent detwinning followed by slip was happening in the tensile reversal (sigmoidal hysteresis loops).
6. Forged ZK60 exhibited superior fatigue response compared to the as-cast alloy owing to the grain refinement and the lower amount of porosities and second-phase particles inside its microstructure.
7. Different mechanisms of crack initiation for the forged material were proposed. At high cycle fatigue regime, persistent slip bands (PSB) and intermetallic particles are the major cause of crack nucleation. On the other hand, for the strain amplitudes higher than 0.4%-0.5%, at which twinning is occurring considerably, the interactions between twin-twin bands besides twin-dislocation interactions can also form cracks leading to the final fracture.
8. The JV model, as an energy-based model, yielded reliable fatigue life prediction for both cast and forged materials within the range of tested strain amplitudes.

Quasi-static and strain-controlled fatigue characteristics of ZK60 extrusion have been investigated in three directions: the extrusion direction (ED), the radial direction (RD), and 45° direction. Fatigue tests were conducted at various strain amplitudes up to 2%. The microstructure examination and texture measurement as well as fracture surface analysis were delivered to establish fundamental links between the microstructure and bulk material response. Based on the results and discussions, the following conclusions can be drawn in the

context of process-structure-property-performance relationships that directly addresses objective #2, and provides the foundation to the realization of objective #3:

1. The extruded alloy revealed a sharp basal texture such that the majority of the HCP grains were perpendicular to the ED direction. This can favor favor $\{10\bar{1}2\}$ extension-twinning under compression loading in ED samples.
2. The microstructure of the extruded alloy was featured by large bright islands surrounded by fine equiaxed grains. These islands are reported to be solid solution material that lacks Zn and Zr, which show resistance against hot deformation and recrystallization.
3. The quasi-static properties of ZK60 extrusion was sensitive to the loading direction. While ED samples showed drastic tension-compression asymmetry, RD and 45° samples had symmetric behavior. Moreover, ED has the highest tensile strength and the least ductility in the light of the material's microstructure and texture characteristics.
4. Under cyclic loading, profound asymmetry was evident along ED at strain amplitudes at which appreciable amount of twinning occurs under compression loading. In contrast, RD and 45° samples revealed symmetric hysteresis loops at all strain amplitudes due to the concurrent occurrence of twinning and detwinning.
5. Fatigue lives were identical amongst all directions in the low cycle fatigue (LCF) regime, though the fatigue response for ED samples was asymmetric, and that for the RD and 45° sample was almost symmetric. Several factors contribute to this behavior which are comprised of material's strength, twin-twin band interactions, twin dislocation interactions, and surface roughness resulting from the extension twinning.
6. In the high cycle fatigue (HCF) regime, ED samples showed an order of magnitude higher cyclic lives. The reason for this increase is thought to be two-fold: i) due to the material's higher strength along ED that retards crack initiation cycle and ii) for finer grains in the ED plane that delay the crack growth.

7. JV, as an energy-based model, was employed to predict the fatigue lives along different directions using single set of material properties.
8. The total strain energy density, as a fatigue damage parameter, was similar along the three directions in the LCF regime, concurring with the similar fatigue lives in this zone.
9. The fracture surface along each direction was examined under SEM. While at the strain amplitude of 0.3% that corresponds to the HCF regime, the fatigue striation (FS) marks were finer for the ED samples, denoting a higher fatigue live for ED, at the strain amplitude of 2%, HCF regime, the average distance along FS marks were statistically similar for all directions.
10. The microstructure of the fractured samples was examined, and profuse twinned grains were observed along ED.

As-extruded billets were close-die forged at 250°C, which was the lowest temperature to achieve a crack free forging. The forging operation yielded in "I-beam" shaped forgings. Multiaxial fatigue characteristics of the starting as-extruded and I-beams forged ZK60 Mg alloys have been studied through conducting quasi-static and fully-reversed strain controlled cyclic experiments including uniaxial, pure torsional, and combined axial-torsional tests at different phase angles, namely 0° proportional, and 45° and 90° out-of-phase non-proportional tests. Based on the results, the following conclusions can be drawn that highlight the objective #3, and enrich the findings of objectives #2:

15. The forging process refined the grains of the as-extruded alloy. While the average grain size for the fine DRXed grains in the starting material was 8.1±1.9 μm, that for the forged alloy was decreased to an average value of 4.6±1.6 μm, which is 43% smaller than the parent grains. It is also observed that the microstructure is uniform in both flanges of the I-beam forgings.
16. The forging process modified the texture of the extruded alloy in the I-beam flanges. While the majority of the unit cells in the starting alloy were oriented perpendicular to the longitudinal extrusion direction, which was loading direction

in this study, the pole figures of forgings suggest that c-axis of Mg unit cells was reoriented toward the radial (RD) and longitudinal (LD) directions subsequent the thermo-mechanical process.

17. The current forged alloy exhibited an overall improvement in the mechanical behavior, especially under uniaxial loading in the light of grain refinement and texture modification.
18. The texture developed in the forged ZK60 resulted in asymmetric axial response; however, the level of asymmetry was reduced due to texture modification.
19. EBSD measurements showed that shear deformation is causing $\{10\bar{1}2\}$ tensile twinning in the material.
20. Cyclic shear tests showed almost symmetric hysteresis loops at all strain amplitudes for both materials.
21. Combining the shear strain with the axial strain did not change the twin-dominated portion of the axial hysteresis loop in both alloys. However, it reduced the stress required to activate slipping.
22. The company of a high axial strain amplitude that triggers extension twinning reduces the stress needed to accommodate shear strain along the other loading axis for both extruded and forged ZK60.
23. The multiaxial fatigue behavior of ZK60, both extrusion and forged, is somewhat dominated by the axial component once the dominant mode of deformation under shear loading is slipping.
24. For both alloys, the shape of shear hysteresis loop changed drastically by changing the phase angle. Also, fatigue lives were invariant to the phase angle shift, especially when twinning was activated under axial loading, despite the considerable change in the shear stress amplitude.
25. Generally, non-proportionality did not change the fatigue life considerably, particularly, at high strain amplitudes that twinning is involved in the deformation.
26. The early crack growth behavior in both alloys depended on the ratio of axial and shear strain amplitudes. At low shear strain amplitude such as 0.4% and 0.5%, that

slipping is dominant under shear loading, the crack growth is transverse to the axial loading which testifies the dominancy of axial loading.

27. The initial crack growth mode for a low axial and high shear strain amplitude loading is longitudinal cracking, which is a shear cracking feature. Furthermore, the high-high combination of strain ratios led to oblique crack propagation mode.
28. JV, as an energy-based model, showed its merits to predict fatigue lives under various loading paths.

At the end, these discovery-level contributions were exploited in the design and build of a load-bearing vehicle component successfully. The forged component was 37% lighter than the benchmark cast Aluminum front lower control arm and passed the structural tests.

8.3 Scientific contributions

This research has made original and significant contributions to fundamental discovery-level knowledge on the mechanical behavior of cast, extruded, and forged ZK60 and its engineering applications by conducting complete systematic material characterization and fatigue life modeling. The key novel contributions of this undertaking are summarized below:

1. **Characterizing the effects of open-die forging on the mechanical behavior of ZK60 cast:**

   Available studies on the characterization of the mechanical behavior of wrought ZK60 Mg alloys have mostly focused on the extruded alloy. The present research addressed the characteristics of quasi-static and fatigue behavior of cast-forged ZK60 for the first time, and provided the following specific new contributions that were not available before:

   1. Quasi-static and fatigue properties were extracted for both as-cast and cast-forged ZK60
   2. The effect of open-die forging on the mechanical properties of cast ZK60 was the drastic improvement of ductility and mild increase of strength (Figure 105).

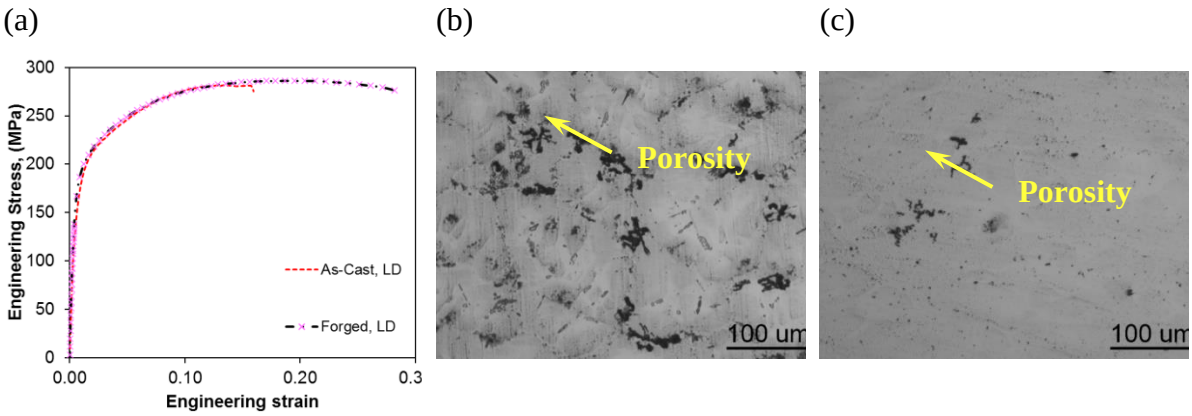

Figure 105. (a) Effect of open-die forging on the quasi-static behavior of ZK60 cast; (b,c) reduction of porosity volume was the major reason for the ductility improvement

2. Finding the drives behind the uniaxial failure mechanism in the as-cast and cast-forged ZK60

The present study thoroughly analyzed the fracture surfaces of the as-cast and cast-forged materials (Figure 106 and Figure 107). The drives behind the uniaxial fatigue failure mechanisms in ZK60 cast and forged are proposed for the first time. For the forged material, in the HCF regime, persistent slip bands (PSB) and intermetallic particles are the major cause of crack nucleation. In the LCF regime, where twinning is occurring considerably, the interactions between twin-twin bands besides twin-dislocation interactions can also form cracks leading to the final fracture. For the cast material, porosities adversely affected the fatigue life. Cracks were also observed next to the intermetalics and slip bands.

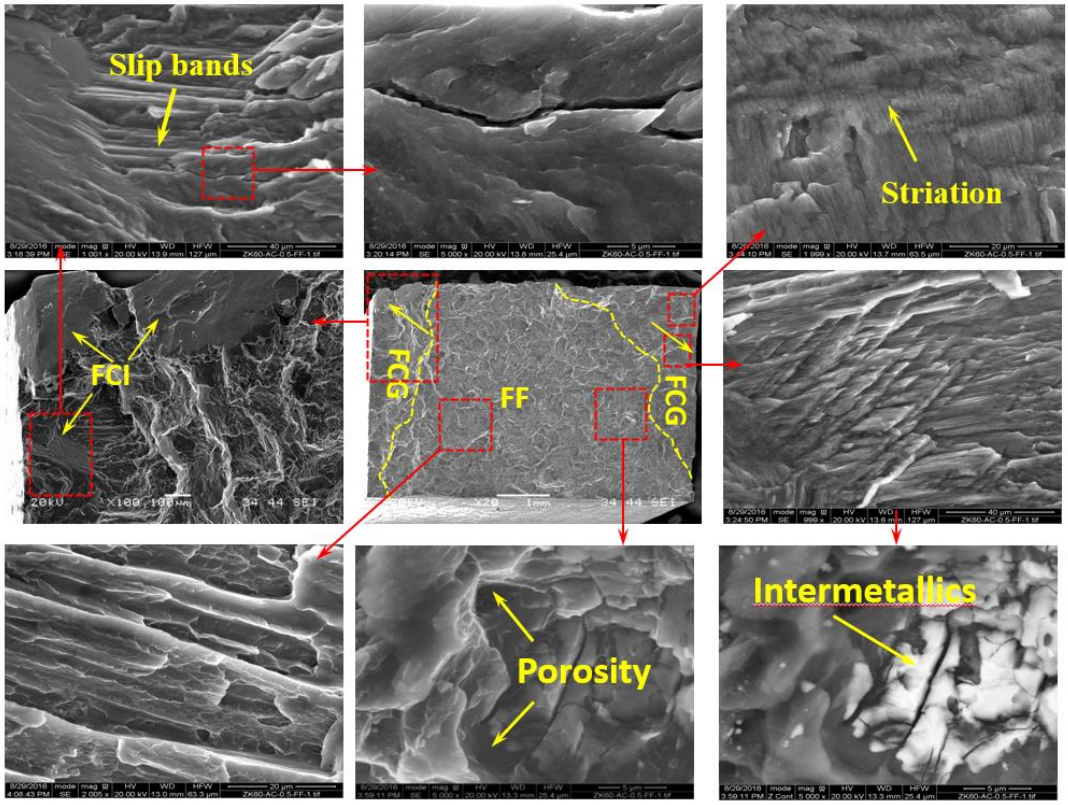

Figure 106. Fatigue fracture of ZK60 Mg alloy cast tested at 0.5% strain amplitude

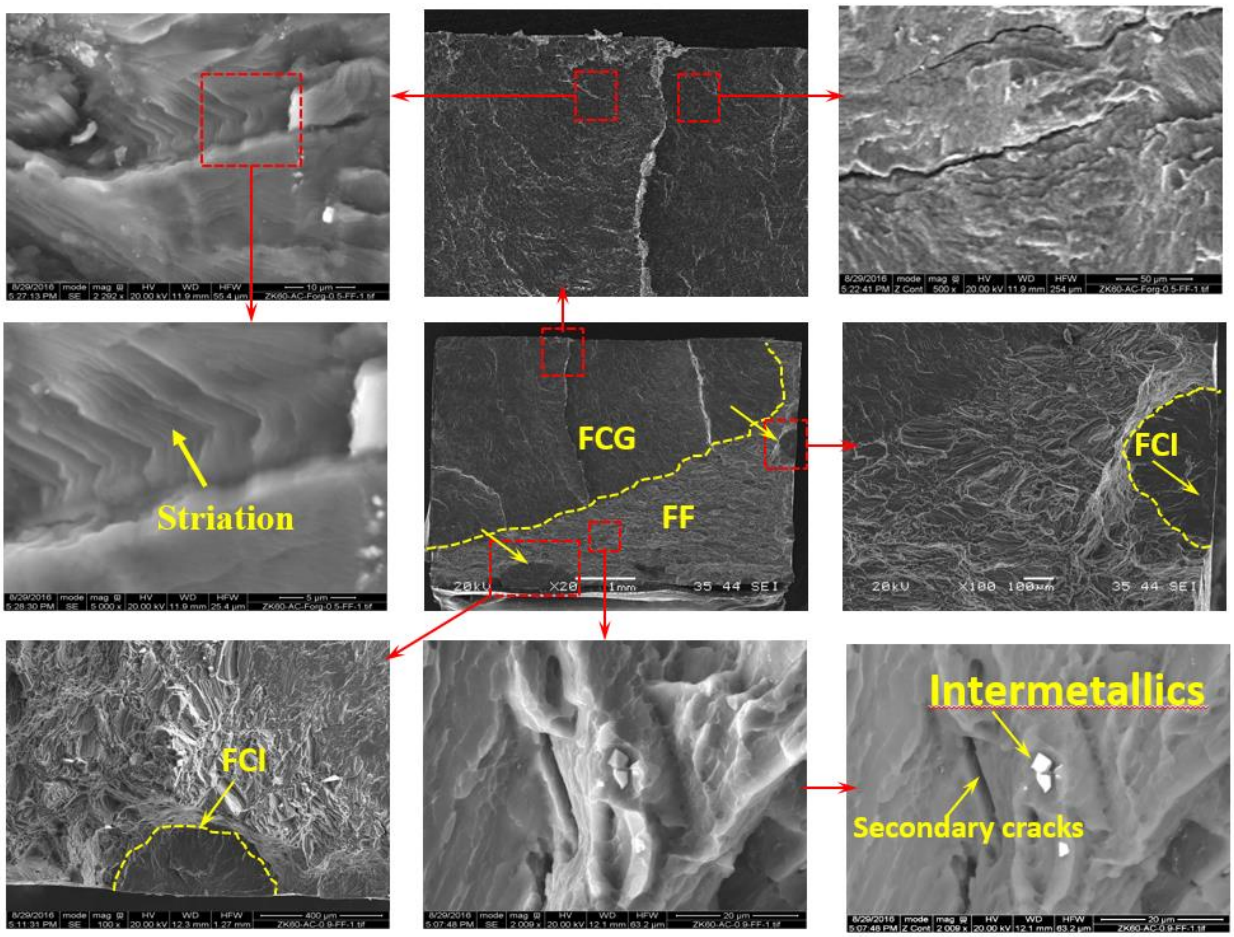

Figure 107. Fatigue fracture of forged ZK60 Mg alloy tested at 0.5% strain amplitude

3. Complete mechanical behavior characterization and fatigue life modeling along various material orientations for ZK60 extrusion

A few studies are available in the literature on the characterization of the mechanical behavior of ZK60 extrusion. However, all of them focus only on the extrusion direction. In this study, for the first time, a comprehensive investigation was performed along different directions and the following contributions have been made:

1. Quasi-static and fatigue properties were produced along different material directions in a wide range of strain amplitudes, for the first time (Figure 108)
2. This question was answered: "Why is the quasi-static behavior of ZK60 extrusion asymmetric along ED, but is symmetric along RD and 45°?"
3. For the first time, the fatigue behavior in both LCF and HCF regimes were investigated and the following question was addressed: "Why are the fatigue lives similar along different directions in the LCF regime and dissimilar in the HCF regime?"
4. For the first time, an energy-based model was used to predict the fatigue life along different directions with a single set of material parameters (Figure 108).
5. Through fractographic and microstructural analyses, it was discovered that twin lamellas are responsible for to the final failure along ED, while slip bands are the main drive for the fracture along RD (Figure 109).

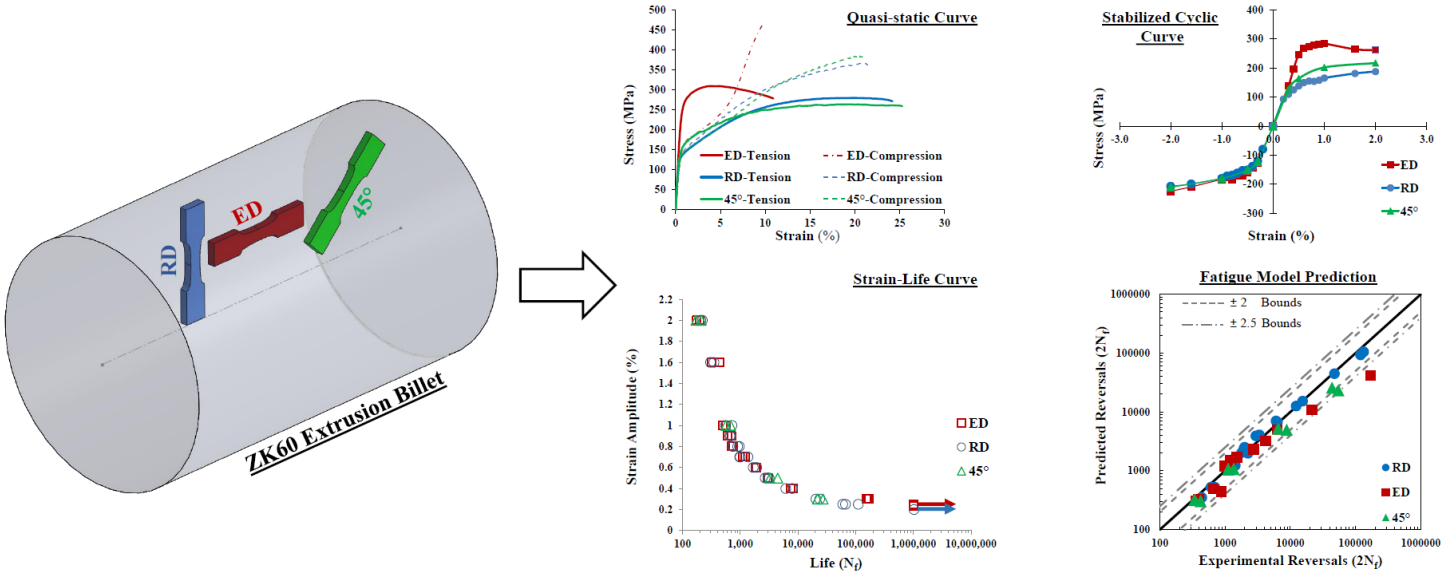

Figure 108. Quasi-static and fatigue behavior of ZK60 extrusion along different directions and fatigue modeling

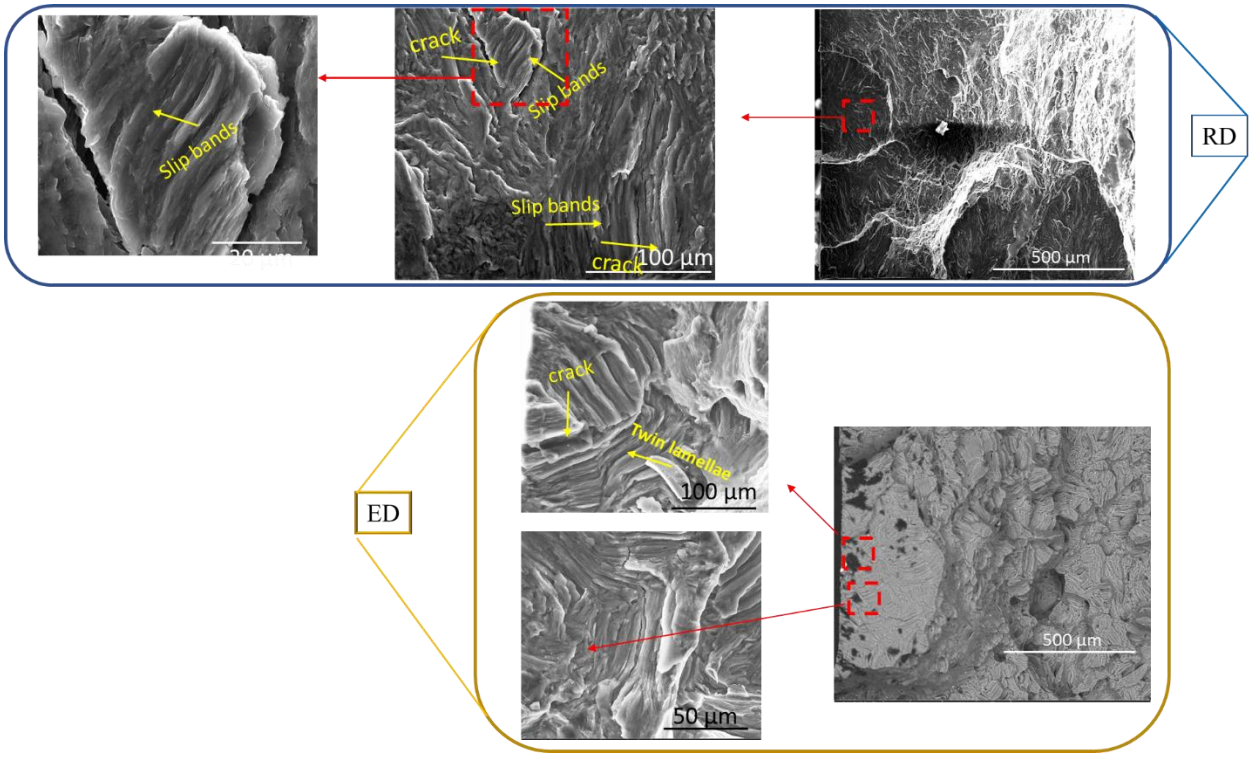

Figure 109. Slip bands on the fracture surface of RD samples and twin lamellas on the fracture surface of ED samples

4. Characterizing the multiaxial fatigue behavior of as-extruded and extruded-forged ZK60

The present study is the pioneer in studying the multiaxial fatigue behavior of ZK60 extrusion and forged. All the findings in chapter 6 are original and novel, and the major ones are summarized as:

1. Mechanical properties of ZK60 extrusion and forged were extracted under different load paths.
2. Forging brings about the improvement of uniaxial fatigue response in the HCF regime by delivering grain refinement and texture modification. The effect of forging on the strain-controlled response within the LCF is not pronounced.
3. High shear strains can change the texture and activate extension twinning (Figure 110).
4. Changing the phase angle does not affect the axial component during the multiaxial loading. On the contrary, the shear response is influenced extremely by shifting the phase angle (Figure 111).
5. The multiaxial fatigue behavior of ZK60 is somewhat dominated by the axial loading when the shear loading is dominated by slipping (Figure 111).

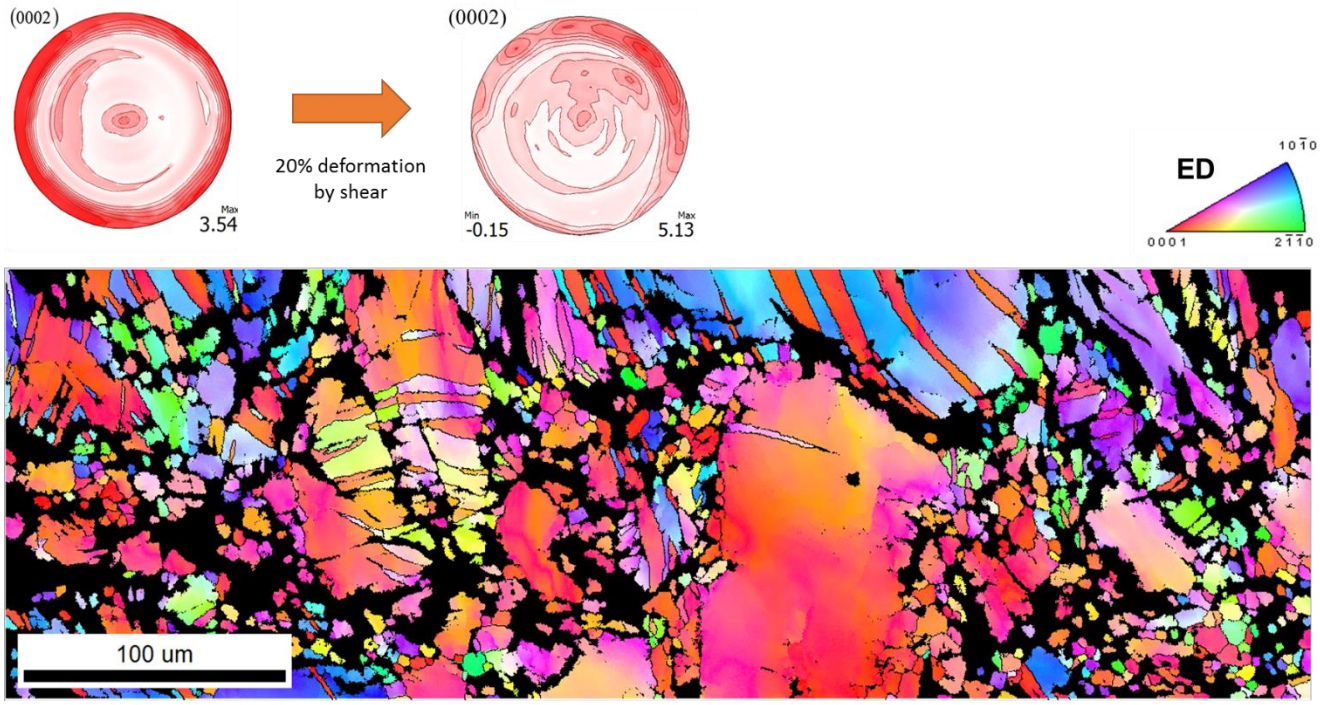

Figure 110. 20% shear strain has changed the texture and nucleated extension twinning

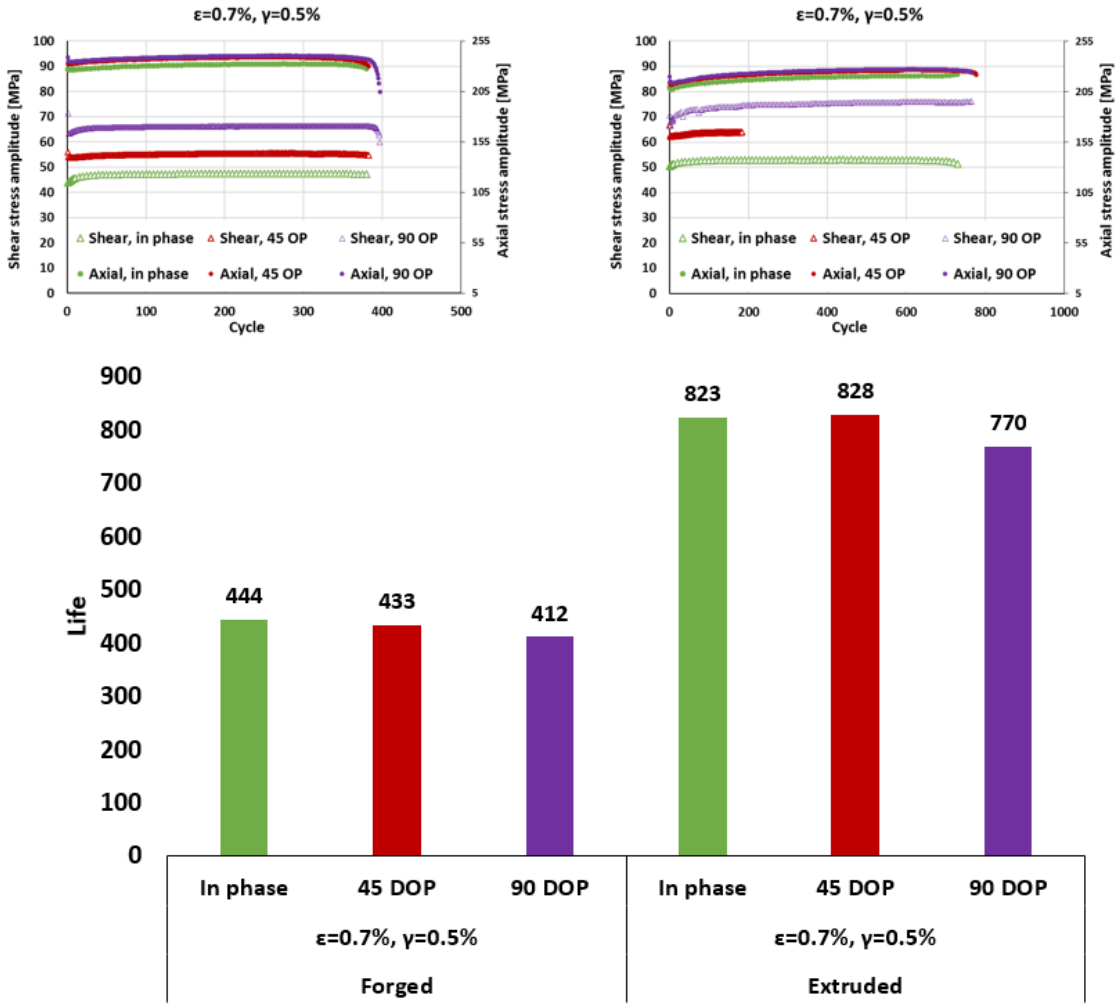

Figure 111. Effect of axial loading vs shear loading on the multiaxial fatigue life of ZK60 forged and extruded

8.4 Future works

Despite the prolific scientific contributions of the current research undertaking, there still exist ample of gaps in the research area to be explored. The following future research is recommended and discussed:

1. To conduct EBSD and fracture surface analysis on the shear samples fractured under quasi-static and cyclic loading at different shear strains:

   While many studies have been made on the uniaxial and multiaxial fatigue behavior of different wrought Mg alloys such as AZ31B, AZ80, AM30, etc., very limited studies have been made on the pure shear response of Mg alloys. Therefore, it is recommended to perform quasi-static and cyclic shear tests at different strain amplitudes and characterize the shear response along the shear curve at different shear strains.

2. To develop an equivalent strain relationship for wrought Mg alloys:

   Currently, an overwhelming fact to study the multiaxial fatigue behavior of wrought Mg alloys is the lack of a relationship for determining the equivalent strain. In fact, some studies have employed the von-Mises relation; however, this equation is valid for materials with symmetric response. On the contrary, wrought Mg alloys, in particular forged ZK60, show asymmetric behavior. In the current study, von-Mises was valid only in the slip-dominated portion of the fatigue life curves, where the hysteresis loops were symmetric, but at higher strains that were high enough to activate extension twinning appreciably, von-Mises did not work. Hence, a prominent step in studying the fatigue behavior of wrought Mg alloys including forged ZK60 would be developing a general equation for calculating the equivalent shear.

3. Studying the mechanical behavior under more complex variable amplitude loading scenarios:

   The current research is pioneering the study of multiaxial fatigue behavior of forged ZK60. Future works should focus on characterizing the material's behavior under more complicated load paths such as variable amplitude loading (VAL). In particular, under

VAL, the effects of load sequence and overload/ or underloads can be studied. Also, variable amplitude multiaxial loading is another complicated loading scenario that involves plenty of knowledge gaps and need comprehensive studies to filling the gaps.

Bibliography

[1] National Aeronautics and Space Administration, “GISS Surface Temperature Analysis (v4).” [Online]. Available: https://data.giss.nasa.gov/gistemp/graphs/. [Accessed: 21-Jan-2020].

[2] United States Environmental Protection Agency, “Greenhouse Gas Inventory Data Explorer.” [Online]. Available: https://cfpub.epa.gov/ghgdata/inventoryexplorer/. [Accessed: 21-Jan-2020].

[3] T. Gayer and W. K. Viscusi, “Overriding consumer preferences with energy regulations,” *J. Regul. Econ.*, vol. 43, no. 3, pp. 248–264, 2013.

[4] M. GEUSS, “CARS — EPA reaffirms 54.5mpg target fuel economy by 2025; automakers turn to Trump.” [Online]. Available: https://arstechnica.com/cars/2016/12/epa-reaffirms-55-4mpg-target-fuel-economy-by-2025-automakers-turn-to-trump/. [Accessed: 21-Jan-2020].

[5] G. Fontaras, N. G. Zacharof, and B. Ciuffo, “Fuel consumption and CO2 emissions from passenger cars in Europe – Laboratory versus real-world emissions,” *Prog. Energy Combust. Sci.*, vol. 60, pp. 97–131, 2017.

[6] G. Fontaras and Z. Samaras, “On the way to 130 g CO2/km-Estimating the future characteristics of the average European passenger car,” *Energy Policy*, vol. 38, no. 4, pp. 1826–1833, 2010.

[7] S. Kobayashi, S. Plotkin, and S. K. Ribeiro, “Energy efficiency technologies for road vehicles,” *Energy Effic.*, vol. 2, no. 2, pp. 125–137, 2009.

[8] International Magnesium Association, “MAGNESIUM SUSTAINABILITY.” [Online]. Available: https://www.intlmag.org/page/mg_sustain_ima#:~:targetText=Magnesium is highly recyclable and,it a very sustainable material. [Accessed: 21-Jan-2020].

[9] B. L. Mordike and T. Ebert, “Magnesium Properties - applications - potential,” *Mater. Sci. Eng. A*, vol. 302, no. 1, pp. 37–45, 2001.

[10] D. Eliezer, E. Aghion, and F. H. Froes, “Magnesium science, technology and applications,” *Adv. Perform. Mater.*, vol. 5, no. 3, pp. 201–212, 1998.

[11] M. Easton, A. Beer, M. Barnett, C. Davies, and G. Dulop, “Magnesium Alloy Applications in Automotive Structures,” *JOM*, vol. 60, no. 11, pp. 57–60, 2008.

[12] M. K. Kulekci, “Magnesium and its alloys applications in automotive industry,” *Int. J. Adv. Manuf. Technol.*, vol. 39, no. 9–10, pp. 851–865, 2008.

[13] G. S. Cole, “Magnesium vision 2020-a north american automotive strategic vision for magnesium.,” *IMA-PROCEEDINGS-. Int. Magnes. Assoc.*, p. 13, 2007.

[14] H. Friedrich and S. Schumann, “Research for a ‘new age of magnesium’ in the automotive industry,” *J. Mater. Process. Technol.*, vol. 117, no. 3, pp. 276–281, 2001.

[15] F. Pan, M. Yang, and X. Chen, “A Review on Casting Magnesium Alloys : Modification of Commercial Alloys and Development of New Alloys,” *J. Mater. Sci. Technol.*, vol. 32, no. 12, pp. 1211–1221, 2016.

[16] H. Mayer, M. Papakyriacou, B. Zettl, and S. E. Stanzl-tschegg, “Influence of porosity on the fatigue limit of die cast magnesium and aluminium alloys,” *Int. J. Fatigue*, vol. 25, pp. 245–256, 2003.

[17] S. M. H. Karparvarfard, S. K. Shaha, S. B. Behravesh, H. Jahed, and B. W. Williams, “Fatigue characteristics and modeling of cast and cast-forged ZK60 magnesium alloy,” *Int. J. Fatigue*, vol. 118, no. November 2017, pp. 282–297, 2019.

[18] A. A. Roostaei and H. Jahed, “Role of loading direction on cyclic behaviour characteristics of AM30 extrusion and its fatigue damage modelling,” *Mater. Sci. Eng. A*, vol. 670, pp. 26–40, 2016.

[19] Y. Estrin and A. Vinogradov, “Extreme grain refinement by severe plastic deformation: A wealth of challenging science,” *Acta Mater.*, vol. 61, no. 3, pp. 782–817, 2013.

[20] S. R. Agnew, J. A. Horton, T. M. Lillo, and D. W. Brown, “Enhanced ductility in

strongly textured magnesium produced by equal channel angular processing," *Scr. Mater.*, vol. 50, no. 3, pp. 377–381, 2004.

[21] G. R. Argade, S. K. Panigrahi, and R. S. Mishra, "Effects of grain size on the corrosion resistance of wrought magnesium alloys containing neodymium," *Corros. Sci.*, vol. 58, pp. 145–151, 2012.

[22] W. H. Sillekens, G. Kurz, and R. J. Werkhoven., *Magnesium forging technology: state-of-the-art and development perspectives*. IOS Press, 2010.

[23] N. M. L. S. Gupta, Manoj, *Magnesium, magnesium alloys, and magnesium composites*. John Wiley & Sons, 2011.

[24] H. B. Avedesian, Michael M., *ASM specialty handbook: magnesium and magnesium alloys*. ASM international, 1999.

[25] S. R. Agnew, M. H. Yoo, and C. N. Tomé, "Application of texture simulation to understanding mechanical behavior of Mg and solid solution alloys containing Li or Y," *Acta Mater.*, vol. 49, no. 20, pp. 4277–4289, 2001.

[26] M. H. Yoo, "Slip, twinning, and fracture in hexagonal close-packed metals," *Metall. Trans. A*, vol. 12, no. 3, pp. 409–418, 1981.

[27] D. Sarker, J. Friedman, and D. L. Chen, "De-twinning and Texture Change in an Extruded AM30 Magnesium Alloy during Compression along Normal Direction," *J. Mater. Sci. Technol.*, vol. 31, no. 3, pp. 264–268, 2015.

[28] D. Sarker, J. Friedman, and D. L. Chen, "Twin Growth and Texture Evolution in an Extruded AM30 Magnesium Alloy During Compression," *J. Mater. Sci. Technol.*, vol. 30, no. 9, pp. 884–887, 2014.

[29] F. Novy, M. Janecek, V. korik, J. Muller, and L. Wagner, "Very high cycle fatigue behaviour of as-extruded AZ31, AZ80, and ZK60 magnesium alloys," *Int. J. Mater. Res.*, vol. 100, no. 3, pp. 288–291, 2009.

[30] Y. Snir, G. Ben-Hamu, D. Eliezer, and E. Abramov, "Effect of compression

deformation on the microstructure and corrosion behavior of magnesium alloys," *J. Alloys Compd.*, vol. 528, pp. 84–90, 2012.

[31] C. Bettles and M. Gibson, "Current wrought magnesium alloys: Strengths and weaknesses," *Jom*, vol. 57, no. 5, pp. 46–49, 2005.

[32] J. D. Robson and C. Paa-Rai, "The interaction of grain refinement and ageing in magnesium–zinc–zirconium (ZK) alloys," *Acta Mater.*, vol. 95, pp. 10–19, 2015.

[33] Z. Huang, W. Qi, and J. Xu, "Effect of microstructure on impact toughness of magnesium alloys," *Trans. Nonferrous Met. Soc. China*, vol. 22, no. 10, pp. 2334–2342, 2012.

[34] S. R. Agnew, P. Mehrotra, T. M. Lillo, G. M. Stoica, and P. K. Liaw, "Texture evolution of five wrought magnesium alloys during route a equal channel angular extrusion: Experiments and simulations," *Acta Mater.*, vol. 53, no. 11, pp. 3135–3146, 2005.

[35] S. R. Agnew and Ö. Duygulu, "Plastic anisotropy and the role of non-basal slip in magnesium alloy AZ31B," *Int. J. Plast.*, vol. 21, no. 6, pp. 1161–1193, 2005.

[36] L. Wu, A. Jain, D. W. Brown, G. M. Stoica, S. R. Agnew, B. Clausen, D. E. Fielden, and P. K. Liaw, "Twinning–detwinning behavior during the strain-controlled low-cycle fatigue testing of a wrought magnesium alloy, ZK60A," *Acta Mater.*, vol. 56, no. 4, pp. 688–695, 2008.

[37] C. H. Cáceres, T. Sumitomo, and M. Veidt, "Pseudoelastic behaviour of cast magnesium AZ91 alloy under cyclic loading–unloading," *Acta Mater.*, vol. 51, no. 20, pp. 6211–6218, Dec. 2003.

[38] D. W. Brown, A. Jain, S. R. Agnew, and B. Clausen, "Twinning and Detwinning During Cyclic Deformation of Mg Alloy AZ31B," *Mater. Sci. Forum*, vol. 539–543, pp. 3407–3413, 2007.

[39] X. Y. Lou, M. Li, R. K. Boger, S. R. Agnew, and R. H. Wagoner, "Hardening evolution of AZ31B Mg sheet," *Int. J. Plast.*, vol. 23, no. 1, pp. 44–86, 2007.

[40] Y. Liu, P. Z. Tang, M. Y. Gong, R. J. Mccabe, J. Wang, and C. N. Tomé, "Three-dimensional character of the deformationtwin in magnesium," *Nat. Commun.*, no. 2019, pp. 1–7.

[41] Y. Xiong, Q. Yu, and Y. Jiang, "An experimental study of cyclic plastic deformation of extruded ZK60 magnesium alloy under uniaxial loading at room temperature," *Int. J. Plast.*, vol. 53, pp. 107–124, 2014.

[42] Q. Yu, J. Zhang, Y. Jiang, and Q. Li, "An experimental study on cyclic deformation and fatigue of extruded ZK60 magnesium alloy," *Int. J. Fatigue*, vol. 36, no. 1, pp. 47–58, 2012.

[43] Y. Xiong and Y. Jiang, "Fatigue of ZK60 magnesium alloy under uniaxial loading," *Int. J. Fatigue*, vol. 64, pp. 74–83, 2014.

[44] S. Dong, Y. Jiang, J. Dong, F. Wang, and W. Ding, "Cyclic deformation and fatigue of extruded ZK60 magnesium alloy with aging effects," *Mater. Sci. Eng. A*, vol. 615, pp. 262–272, 2014.

[45] W. C. Liu, J. Dong, P. Zhang, Z. Y. Yao, C. Q. Zhai, and W. J. Ding, "High cycle fatigue behavior of as-extruded ZK60 magnesium alloy," *J. Mater. Sci.*, vol. 44, no. 11, pp. 2916–2924, 2009.

[46] J. Albinmousa, H. Jahed, and S. Lambert, "Cyclic behaviour of wrought magnesium alloy under multiaxial load," *Int. J. Fatigue*, vol. 33, no. 8, pp. 1127–1139, 2011.

[47] D. Toscano, S. K. Shaha, B. Behravesh, H. Jahed, and B. Williams, "Effect of forging on the low cycle fatigue behavior of cast AZ31B alloy," *Mater. Sci. Eng. A*, vol. 706, no. May, pp. 342–356, 2017.

[48] H. Somekawa, Singh Alok, and T. Mukai, "Effect of precipitate shapes on fracture toughness in extruded Mg–Zn–Zr magnesium alloys," *J. Mater. Res.*, vol. 22, no. 4, pp. 965–973, 2007.

[49] R. Jahadi, M. Sedighi, and H. Jahed, "ECAP effect on the micro-structure and mechanical properties of AM30 magnesium alloy," *Mater. Sci. Eng. A*, vol. 593, pp.

178–184, 2014.

[50] A. Gryguc, S.K. Shaha, H. Jahed, M. Wells, B. Williams, J. McKinley, “Tensile and fatigue behaviour of as-forged AZ31B extrusion,” *Fract. Struct. Integr.*, vol. 38, pp. 251–258, 2016.

[51] A. Gryguc, H. Jahed, B. Williams, and J. McKinley, “Magforge – Mechanical behaviour of forged AZ31B extruded magnesium in monotonic compression,” *Mater. Sci. Forum*, vol. 828–829, pp. 291–297, 2015.

[52] Y. Z. Wu, H. G. Yan, J. H. Chen, S. Q. Zhu, B. Su, and P.-L. Zeng, “Microstructure and mechanical properties of ZK60 magnesium alloy fabricated by high strain rate multiple forging,” *Mater. Sci. Technol.*, vol. 29, no. 1, pp. 54–59, 2013.

[53] E. Vasilev, M. Linderov, D. Nugmanov, O. Sitdikov, M. Markushev, and A. Vinogradov, “Fatigue Performance of Mg-Zn-Zr Alloy Processed by Hot Severe Plastic Deformation,” *Metals (Basel).*, vol. 5, no. 4, pp. 2316–2327, 2015.

[54] D. R. Nugmanov, O. S. Sitdikov, and M. V Markushev, “Texture and anisotropy of yield strength in multistep isothermally forged Mg-5.8Zn-0.65Zr alloy,” *IOP Conf. Ser. Mater. Sci. Eng.*, vol. 82, no. 1, p. IOP Publishing, 2015.

[55] J. Q. Tao, Y. S. Cheng, S. D. Huang, F. F. Peng, W. X. Yang, M. Q. Lu, Z. M. Zhang, and X. Jin, “Microstructural evolution and mechanical properties of ZK60 magnesium alloy prepared by multi-axial forging during partial remelting,” *Trans. Nonferrous Met. Soc. China 22*, vol. 22, pp. 428–434, 2012.

[56] P. Moldovan, G. Popescu, D. Bojin, D. Constantinescu, and M. Pana, “Improving the fatigue resistance of magnesium alloys for forged parts in automotive industry,” *Metal. Int.*, vol. 14, pp. 23–26, 2009.

[57] H. Miura, G. Yu, and X. Yang, “Multi-directional forging of AZ61Mg alloy under decreasing temperature conditions and improvement of its mechanical properties,” vol. 528, pp. 6981–6992, 2011.

[58] Y. Xu-yue, S. U. N. Zheng-yan, and X. Jie, “Grain size and texture changes of

magnesium alloy AZ31 during multi-directional forging," *Trans. Nonferrous Met. Soc. China*, vol. 18, pp. s200–s204, 2008.

[59] N. Ogawa, M. Shiomi, and K. Osakada, "Forming limit of magnesium alloy at elevated temperatures for precision forging," *Int. J. Mach. Tools Manuf.*, vol. 42, no. 5, pp. 607–614, 2002.

[60] R. Matsumoto and K. Osakada, "Development of Warm Forging Method for Magnesium Alloy," *Mater. Trans.*, vol. 45, no. 9, pp. 2838–2844, 2004.

[61] R. Matsumoto and K. Osakada, "Lubrication and friction of magnesium alloys in warm forging," *CIRP Ann. Technol.*, vol. 51, no. 1, pp. 223–226, 2002.

[62] Y. Kwon, Y. Lee, S. Kim, and J. Lee, "Effect of initial microstructure on hot forging of Mg alloys," *Int. J. Mod. Phys. B*, vol. 22(31n32), pp. 6064–6069, 2008.

[63] G. Kurz, B. Clauw, W. H. Sillekens, D. Letzig, and P. Manufacturing, "Die Forging of the Alloys Az80 and Zk60," *Magnes. Technol. 2009, 15 Febr. 2009 through 19 Febr. 2009, San Fr. CA, USA, Conf. code 76923, 197-202, TMS*, 2009.

[64] M. Noban, H. Jahed, E. Ibrahim, and A. Ince, "Load path sensitivity and fatigue life estimation of 30CrNiMo8HH," *Int. J. Fatigue*, vol. 37, pp. 123–133, 2012.

[65] M. Noban, H. Jahed, S. Winkler, and A. Ince, "Fatigue characterization and modeling of 30CrNiMo8HH under multiaxial loading," *Mater. Sci. Eng. A*, vol. 528, no. 6, pp. 2484–2494, 2011.

[66] D. Socie and G. Marquis, *Multiaxial Fatigue*. SAE International, 1999.

[67] Ł. Pejkowski, D. Skibicki, and J. Sempruch, "High-cycle fatigue behavior of austenitic steel and pure copper under uniaxial, proportional and non-proportional loading," *J. Mech. Eng.*, vol. 60, no. 9, pp. 549–560, 2014.

[68] Q. Yu, J. Zhang, Y. Jiang, and Q. Li, "Multiaxial fatigue of extruded AZ61A magnesium alloy," *Int. J. Fatigue*, vol. 33, no. 3, pp. 437–447, 2011.

[69] J. Albinmousa, H. Jahed, and S. Lambert, "Cyclic axial and cyclic torsional behaviour

of extruded AZ31B magnesium alloy," *Int. J. Fatigue*, vol. 33, no. 11, pp. 1403–1416, 2011.

[70] J. Albinmousa and H. Jahed, "Multiaxial effects on LCF behaviour and fatigue failure of AZ31B magnesium extrusion," *Int. J. Fatigue*, vol. 67, pp. 103–116, 2014.

[71] H. Jahed and J. Albinmousa, "Multiaxial behaviour of wrought magnesium alloys – A review and suitability of energy-based fatigue life model," *Theor. Appl. Fract. Mech.*, vol. 73, pp. 97–108, 2014.

[72] J. Albinmousa, H. Jahed, and S. Lambert, "An Energy-Based Fatigue Model for Wrought Magnesium Alloy under Multiaxial Load," in *ICMFF9*, 2010, pp. 471–478.

[73] J. Albinmousa, H. Jahed, and S. Lambert, "Estimation of Fatigue Crack Orientation using Critical Plane Parameters: An Experimental Investigation," in *ICMFF10*, 2013.

[74] F. Ellyin, "Multiaxial Fatigue," *J. Enginnering Mater. Technol.*, vol. 113, no. 1, pp. 112–118, 1991.

[75] Y. Xiong, Q. Yu, and Y. Jiang, "Multiaxial fatigue of extruded AZ31B magnesium alloy," *Mater. Sci. Eng. A*, vol. 546, pp. 119–128, 2012.

[76] Y. Jiang, "A fatigue criterion for general multiaxial loading," *Fatigue Fract. Eng. Mater. Struct.*, vol. 23, no. 1, pp. 19–32, 2000.

[77] L. G. Reis, V. Anes, and M. de Freitas., "AZ31 magnesium alloy multiaxial LCF behavior: theory, simulation and experiments," *Adv. Mater. Res.*, vol. 891, pp. 1366–1371, 2014.

[78] Y. Jiang and H. Sehitoglu, "Modeling of Cyclic Ratchetting Plasticity , Part I : Development of Constitutive Relations," *J. Appl. Mech.*, vol. 63, no. 3, pp. 720–725, 1996.

[79] H. Li, G. Kang, Y. Liu, and H. Jiang, "Non-proportionally multiaxial cyclic deformation of AZ31 magnesium alloy : Experimental observations," *Mater. Sci. Eng. A*, vol. 671, pp. 70–81, 2016.

[80] F. Castro and Y. Jiang, “Fatigue life and early cracking predictions of extruded AZ31B magnesium alloy using critical plane approaches,” vol. 88, pp. 236–246, 2016.

[81] A. A. Roostaei and H. Jahed, “Multiaxial cyclic behaviour and fatigue modelling of AM30 Mg alloy extrusion,” *Int. J. Fatigue*, vol. 97, pp. 150–161, 2017.

[82] A. Gryguć, S. B. Behravesh, S. K. Shaha, H. Jahed, M. Wells, B. Williams, and X. Su, “Multiaxial cyclic behaviour of extruded and forged AZ80 Mg alloy,” *Int. J. Fatigue*, vol. 127, pp. 324–337, 2019.

[83] J. Albinmousa, M. J. Adinoyi, and N. Merah, “Multiaxial fatigue of extruded ZK60 magnesium alloy,” *Fatigue Fract. Eng. Mater. Struct.*, vol. 42, pp. 2276–2289, 2019.

[84] J. S. Chun and J. G. Byrne, “Precipitate Sterngthening Mechanisms in Magnesium Zinc Alloy Single Crystal,” *J. Mater. Sci.*, vol. 4, pp. 861–872, 1969.

[85] R. I. Stephens, A. Fatemi, R. R. STEPHENS, and H. 0. FUCHS, *Metal Fatigue in Engineering (second Edition)*. 2001.

[86] D. Socie, “Multiaxial Fatigue Damage Models,” *J. Eng. Mater. Technol.*, vol. 109, no. 4, pp. 293–298, 1987.

[87] A. Fatemi and D. Socie, “A Critical Plane Approach to Multiaxial Fatigue Damage Including out-of-Phase Loading,” *Fatigue Fract. Eng. Mater. Struct.*, vol. 11, no. 3, pp. 149–165, 1988.

[88] Kn. Smith, T. H. Topper, and P. Watson, “A stress-strain function for the fatigue of metals(Stress-strain function for metal fatigue including mean stress effect),” *J. Mater.*, vol. 5, no. January 1970, pp. 767–778, 1970.

[89] Y. Jiang and H. Sehitoglu, “Fatigue and stress analysis of rolling contact. Report no. 161, UILU-ENG 92-3602.,” College of Engineering, University of Illinois at Urbana-Champaign, 1992.

[90] Y. Ling, “Characterization and Modeling of Smooth and Notched Rolled ZEK100-O under Cyclic Load,” 2018.

[91] H. Jahed and A. Varvani-farahani, “Upper and lower fatigue life limits model using energy-based fatigue properties,” *Int. J. Fatigue*, vol. 28, pp. 467–473, 2006.

[92] A. A. Roostaei, A. Pahlevanpour, S. B. Behravesh, and H. Jahed, “On the de fi nition of elastic strain energy density in fatigue modelling,” *Int. J. Fatigue*, vol. 121, no. October 2018, pp. 237–242, 2019.

[93] H. J. Seyed Behzad Behravesh, S. B. Lambert, and M. Chengji, “Constitutive modeling for cyclic behavior of AZ31B magnesium alloy and its application,” *Adv. Mater. Res.*, vol. 891, pp. 809–814, 2014.

[94] A. A. Roostaei and H. Jahed, “A cyclic small-strain plasticity model for wrought Mg alloys under multiaxial loading: Numerical implementation and validation,” *Int. J. Mech. Sci.*, vol. 145, no. July, pp. 318–329, 2018.

[95] S. B. Behravesh, “Fatigue Characterization and Cyclic Plasticity Modeling of Magnesium Spot-Welds,” 2013.

[96] A. A. Roostaei, “Cyclic Characterisation and Plasticity Modelling of AM30 Magnesium Alloy Extrusion,” 2017.

[97] M. Noban, J. Albinmousa, H. Jahed, and S. Lambert, “A Continuum-Based Cyclic Plasticity Model for AZ31B Magnesium Alloy under Proportional loading,” *Procedia Eng.*, vol. 10, pp. 1366–1371, 2011.

[98] A. A. Roostaei, Y. Ling, H. Jahed, and G. Glinka, “Applications of Neuber ’ s and Glinka ’ s notch plasticity correction rules to asymmetric magnesium alloys under cyclic load,” *Theor. Appl. Fract. Mech.*, vol. 105, p. 102431, 2020.

[99] L. Qian, F. Victor, A. A. Roostaei, U. Dighrasker, G. Glinka, and H. Jahed, “Notch Plasticity and Fatigue Modelling of AZ31B-H24 Magnesium Alloy Sheet,” *SAE Tech. Pap.*, no. NO. 2019-01-0530, 2019.

[100] G. Yu, “Forging Specimen Design for Magnesium Alloys,” *(Master’s Thesis), Retrieved from Univ. Waterloo Database*, 2016.

[101] "ASTM E2207 - Standard Practice for Strain-Controlled Axial-Torsional Fatigue Testing with Thin-Walled Tubular Specimens," *ASTM Int.*

[102] P. Prakash, "Microstructure and texture evolution during hot deformation of AZ80 magnesium alloy," University of Waterloo, 2019.

[103] Z. A. Luo, G. M. Xie, Z. Y. Ma, G. L. Wang, and G. D. Wang, "Effect of yttrium addition on microstructural characteristics and superplastic behavior of friction stir processed ZK60 alloy," *J. Mater. Sci. Technol.*, vol. 29, no. 12, pp. 1116–1122, 2013.

[104] M. Kaseem, B. K. Chung, H. W. Yang, K. Hamad, and Y. G. Ko, "Effect of Deformation Temperature on Microstructure and Mechanical Properties of AZ31 Mg Alloy Processed by Differential-Speed Rolling," *J. Mater. Sci. Technol.*, vol. 31, no. 5, pp. 498–503, 2015.

[105] M. R. Barnett, M. D. Nave, and C. J. Bettles, "Deformation microstructures and textures of some cold rolled Mg alloys," vol. 386, pp. 205–211, 2004.

[106] J. Xu, B. Guan, H. Yu, X. Cao, Y. Xin, and Q. Liu, "Effect of Twin Boundary–Dislocation–Solute Interaction on Detwinning in a Mg–3Al–1Zn Alloy," *J. Mater. Sci. Technol.*, vol. 32, no. 12, pp. 1239–1244, 2016.

[107] R. Z. Valiev, Y. Estrin, Z. Horita, T. G. Langdon, M. J. Zehetbauer, and Y. Zhu, "Producing Bulk Ultrafine-Grained Materials by Severe Plastic Deformation: Ten Years Later," *JOM*, vol. 68, no. 4, pp. 1216–1226, 2016.

[108] J. Lin, X. Wang, W. Ren, X. Yang, and Q. Wang, "Enhanced Strength and Ductility Due to Microstructure Refinement and Texture Weakening of the GW102K Alloy by Cyclic Extrusion Compression," *J. Mater. Sci. Technol.*, vol. 32, no. 8, pp. 783–789, 2016.

[109] D. L. Yin, H. L. Cui, J. Qiao, and J. F. Zhang, "Enhancement of mechanical properties in a Mg – Zn – Zr alloy by equal channel angular pressing at warm temperature," *Mater. Res. Innov.*, vol. 19, pp. 28–31, 2015.

[110] M. Madaj, M. Greger, and V. Karas, "MAGNESIUM-ALLOY DIE FORGINGS FOR

AUTOMOTIVE APPLICATIONS," *Mater. Tehnol.*, vol. 49, no. 2, pp. 267–273, 2015.

[111] Y. Yuan, A. Ma, X. Gou, J. Jiang, F. Lu, D. Song, and Y. Zhu, "Superior mechanical properties of ZK60 mg alloy processed by equal channel angular pressing and rolling," *Mater. Sci. Eng. A*, vol. 630, pp. 45–50, 2015.

[112] W. Z. Chen, W. C. Zhang, L. X. Zhang, and E. D. Wang, "Property improvements in fine–grained Mg–Zn–Zr alloy sheets produced by temperature–step–down multi–pass rolling," *J. Alloys Compd.*, vol. 646, pp. 195–203, 2015.

[113] Y. H. Kim, H. T. Sohn, and W. J. Kim, "Ductility enhancement through texture control and strength restoration through subsequent age-hardening in Mg-Zn-Zr alloys," *Mater. Sci. Eng. A*, vol. 597, pp. 157–163, 2014.

[114] F. Fereshteh-Saniee, N. Fakhar, F. Karami, and R. Mahmudi, "Superior ductility and strength enhancement of ZK60 magnesium sheets processed by a combination of repeated upsetting and forward extrusion," *Mater. Sci. Eng. A*, vol. 673, pp. 450–457, 2016.

[115] W. Yu, Z. Liu, H. He, N. Cheng, and X. Li, "Microstructure and mechanical properties of ZK60 – Yb magnesium alloys," *Mater. Sci. Eng. A*, vol. 478, no. 1–2, pp. 101–107, 2008.

[116] A. Hadadzadeh, M. A. Wells, S. Kumar, H. Jahed, and B. W. Williams, "Role of compression direction on recrystallization behavior and texture evolution during hot deformation of extruded ZK60 magnesium alloy," *J. Alloys Compd.*, vol. 702, pp. 274–289, 2017.

[117] H. Watanabe, K. Moriwaki, T. Mukai, T. Ohsuna, K. Hiraga, and K. Higashi, "Materials processing for structural stability in a ZK60 magnesium alloy," *Mater. Trans.*, vol. 44, no. 4, pp. 775–781, 2003.

[118] C. Y. Wang, X. J. Wang, H. Chang, K. Wu, and M. Y. Zheng, "Processing maps for hot working of ZK60 magnesium alloy," *Mater. Sci. Eng. A*, vol. 464, no. 92, pp. 52–

58, 2007.

[119] Y. Wu, H. Yan, S. Zhu, J. Chen, A. Liu, and X. Liu, “Flow behavior and microstructure of ZK60 magnesium alloy compressed at high strain rate,” *Trans. Nonferrous Met. Soc. China*, vol. 24, no. 4, pp. 930–939, 2014.

[120] H. Chen, S. B. Kang, H. Yu, J. Cho, H. W. Kim, and G. Min, “Effect of heat treatment on microstructure and mechanical properties of twin roll cast and sequential warm rolled ZK60 alloy sheets,” *J. Alloys Compd.*, vol. 476, no. 1–2, pp. 324–328, 2009.

[121] D. Sarker and D. L. Chen, “Dependence of compressive deformation on pre-strain and loading direction in an extruded magnesium alloy: Texture, twinning and de-twinning,” *Mater. Sci. Eng. A*, vol. 596, pp. 134–144, 2014.

[122] S. K. Shaha, F. Czerwinski, W. Kasprzak, and D. L. Chen, “Tensile and compressive deformation behavior of the Al-Si-Cu-Mg cast alloy with additions of Zr, V and Ti,” *Mater. Des.*, vol. 59, pp. 352–358, 2014.

[123] X. Li, S. M. Xiong, and Z. Guo, “Correlation between Porosity and Fracture Mechanism in High Pressure Die Casting of AM60B Alloy,” *J. Mater. Sci. Technol.*, vol. 32, no. 1, pp. 54–61, 2016.

[124] S. D. Wang, D. K. Xu, B. J. Wang, E. H. Han, and C. Dong, “Effect of solution treatment on the fatigue behavior of an as-forged Mg-Zn-Y-Zr alloy,” *Sci. Rep.*, vol. 6, p. 23955, 2016.

[125] I. Ulacia, S. Yi, M. T. Pérez Prado, N. V. Dudamell, F. Galvez Diaz-Rubio, D. Letzig, and I. Hurtado, “Texture Evolution of AZ31 Magnesium Alloy Sheet at High Strain Rates,” *Proc. 4th Int. Conf. High Speed Form. | 4th Int. Conf. High Speed Form. | 09/03/2010 - 10/03/2010 | Columbus, Ohio, EEUU*, pp. 189–197, 2010.

[126] G. Proust, C. N. Tomé, A. Jain, and S. R. Agnew, “Modeling the effect of twinning and detwinning during strain-path changes of magnesium alloy AZ31,” *Int. J. Plast.*, vol. 25, no. 5, pp. 861–880, 2009.

[127] Č. Jan, K. Máthis, B. Clausen, J. Stráská, and P. Luká, “Study of the loading mode

dependence of the twinning in random textured cast magnesium by acoustic emission and neutron diffraction methods," *Mater. Sci. Eng. A*, vol. 602, pp. 25–32, 2014.

[128] K. Máthis, P. Beran, J. Čapek, and P. Lukáš, "In-situ neutron diffraction and acoustic emission investigation of twinning activity in magnesium," *J. Phys. Conf. Ser.*, vol. 340, no. 1, p. 12096, 2012.

[129] A. Vinogradov, D. Orlov, A. Danyuk, and Y. Estrin, "Deformation mechanisms underlying tension – compression asymmetry in magnesium alloy ZK60 revealed by acoustic emission monitoring," *Mater. Sci. Eng. A*, vol. 621, pp. 243–251, 2015.

[130] T. Al-Samman and G. Gottstein, "Dynamic recrystallization during high temperature deformation of magnesium," *Mater. Sci. Eng. A*, vol. 490, no. 1–2, pp. 411–420, 2008.

[131] R. D. Doherty, "Recrystallization and texture," *Prog. Mater. Sci.*, vol. 42, pp. 39–58, 1997.

[132] R. D. Doherty, D. a. Hughes, F. J. Humphreys, J. J. Jonas, D. Juul Jensen, M. E. Kassner, W. E. King, T. R. McNelley, H. J. McQueen, and a. D. Rollett, "Current issues in recrystallization: A review," *Mater. Today*, vol. 1, no. 2, pp. 14–15, 1998.

[133] G. M. Xie, Z. Y. Ma, and L. Geng, "Effect of microstructural evolution on mechanical properties of friction stir welded ZK60 alloy," *Mater. Sci. Eng. A*, vol. 486, no. 1–2, pp. 49–55, 2008.

[134] X. Chen, X. Huang, F. Pan, A. Tang, J. Wang, and D. Zhang, "Effects of heat treatment on microstructure and mechanical properties of ZK60 Mg alloy," *Trans. Nonferrous Met. Soc. China 21*, vol. 21, no. 4, pp. 754–760, 2011.

[135] W. S. Miller, L. Zhuang, J. Bottema, A. J. Wittebrood, and P. De Smet, "Recent development in aluminium alloys for the automotive industry," *Mater. Sci. Eng. A*, vol. 280, no. 1, pp. 37–49, 2000.

[136] R. von Mises, "Mechanik der plastischen Formanderung von Kristallen," *ournal Appl. Math. Mech. für Angew. Math. und Mech.*, vol. 8, no. 3, pp. 161–185, 1928.

[137] E. Meza-garc, P. Dobroˇ, J. Bohlen, D. Letzig, and K. Ulrich, “Deformation mechanisms in an AZ31 cast magnesium alloy as investigated by the acoustic emission technique,” *Mater. Sci. Eng. A*, vol. 462, no. 1–2, pp. 297–301, 2007.

[138] A. Chapuis and J. H. Driver, “Temperature dependency of slip and twinning in plane strain compressed magnesium single crystals,” *Acta Mater.*, vol. 59, no. 5, pp. 1986–1994, 2011.

[139] S. H. Park, S. G. Hong, W. Bang, and C. S. Lee, “Effect of anisotropy on the low-cycle fatigue behavior of rolled AZ31 magnesium alloy,” *Mater. Sci. Eng. A*, vol. 527, no. 3, pp. 417–423, 2010.

[140] S. Hasegawa, Y. Tsuchida, H. Yano, and M. Matsui, “Evaluation of low cycle fatigue life in AZ31 magnesium alloy,” *Int. J. Fatigue*, vol. 29, no. 9–11, pp. 1839–1845, 2007.

[141] D. Toscano, S. . Shaha, S. B. Behravesh, H. Jahed, M. A. Wells, B. W. Williams, and J. McKinley, “Effect of Forging on Microstructure, Texture and Compression Behavior of Extruded AZ31B,” *J. Mater. Eng. Perform.*, pp. 1–14, 2017.

[142] A. Gryguc, S. K. Shaha, S. B. Behravesh, H. Jahed, M. Wells, B. Williams, and X. Su, “Monotonic and cyclic behaviour of cast and cast-forged AZ80 Mg,” *Int. J. Fatigue*, vol. 104, pp. 136–149, 2017.

[143] S. M. H. Karparvarfard, S. K. Shaha, S. B. Behravesh, H. Jahed, and B. W. Williams, “Microstructure , texture and mechanical behavior characterization of hot forged cast ZK60 magnesium alloy,” *J. Mater. Sci. Technol.*, 2017.

[144] A. Hadadzadeh, S. K. Shaha, M. A. Wells, H. Jahed, and B. Williams, “Recrystallization behavior and texture evolution during hot deformation of extruded ZK60 magnesium alloy,” in *Conference: Materials Science and Technology 2016, MS&T 2016, Location Salt Lake City, UT, USA, Date: Oct 23-27*, 2016, pp. 281–288.

[145] S. M. H. Karparvarfard, S. K. Shaha, A. Hadadzadeh, S. B. Behravesh, H. Jahed, M. A. Wells, and B. W. Williams, “Characterization of Semi-Closed Die-Forged ZK60

Mg Alloy Extrusion," *Magnes. Technol. 2017. Springer Int. Publ.*, pp. 329–334, 2017.

[146] J. B. Jordon, J. B. Gibson, M. F. Horstemeyer, H. El Kadiri, J. C. Baird, and A. A. Luo, "Effect of twinning, slip, and inclusions on the fatigue anisotropy of extrusion-textured AZ61 magnesium alloy," *Mater. Sci. Eng. A*, vol. 528, no. 22–23, pp. 6860–6871, 2011.

[147] W. R. Osorio, P. R. Goulart, S. G. A, N. C. Moura, and A. Garcia, "Effect of Dendritic Arm Spacing on Mechanical Properties and Corrosion Resistance of Al 9 Wt Pct Si and Zn 27 Wt Pct Al Alloys," *Metall. Mater. Trans. A*, vol. 37, pp. 2525–2538, 2006.

[148] S. R. Agnew and and J. J. B. Christopher A. Calhoun, "What is in a Strain Hardening 'Plateau'?," in *Magnesium Technology 2016, Springer International Publishing*, 2016, pp. 189–194.

[149] L. Wu, S. R. Agnew, D. W. Brown, G. M. Stoica, B. Clausen, A. Jain, D. E. Fielden, and P. K. Liaw, "Internal stress relaxation and load redistribution during the twinning–detwinning-dominated cyclic deformation of a wrought magnesium alloy, ZK60A," *Acta Mater.*, vol. 56, no. 14, pp. 3699–3707, 2008.

[150] S. Kim, S. Hong, J. Lee, C. Soo, J. Yoon, and H. Yu, "Materials Science & Engineering A Anisotropic in-plane fatigue behavior of rolled magnesium alloy with { 10 − 12 } twins," *Mater. Sci. Eng. A*, vol. 700, no. May, pp. 191–197, 2017.

[151] X. Z. Lin and D. L. Chen, "Strain controlled cyclic deformation behavior of an extruded magnesium alloy," *Mater. Sci. Eng. A*, vol. 496, pp. 106–113, 2008.

[152] Z. Keshavarz and M. R. Barnett, "EBSD analysis of deformation modes in Mg-3Al-1Zn," *Scr. Mater.*, vol. 55, no. 10, pp. 915–918, 2006.

[153] S. R. Agnew, D. W. Brown, and C. N. Tomé, "Validating a polycrystal model for the elastoplastic response of magnesium alloy AZ31 using in situ neutron diffraction," *Acta Mater.*, vol. 54, no. 18, pp. 4841–4852, 2006.

[154] N. a. Fleck, G. M. Muller, M. F. Ashby, and J. W. Hutchinson, "Strain gradient plasticity: Theory and experiment," *Acta Metall. Mater.*, vol. 42, no. 2, pp. 475–487,

1994.

[155] Q. Yu, J. Zhang, and Y. Jiang, “Fatigue damage development in pure polycrystalline magnesium under cyclic tension-compression loading,” *Mater. Sci. Eng. A*, vol. 528, no. 25–26, pp. 7816–7826, 2011.

[156] Y. Estrin and A. Vinogradov, “Fatigue behaviour of light alloys with ultrafine grain structure produced by severe plastic deformation: An overview,” *Int. J. Fatigue*, vol. 32, no. 6, pp. 898–907, 2010.

[157] J. Casey and H. Jahedmotlagh, “THE STRENGTH-DIFFERENTIAL EFFECT IN PLASTICITY,” *Int. J. Solids Struct.*, vol. 20, no. 4, pp. 377–393, 1984.

[158] H. Mughrabi, R. Wang, K. Differt, and C. Fatigue, “Fatigue Crack Initiation by Cyclic Slip Irreversibilities in High-Cycle Fatigue,” *Fatigue Mech. Adv. Quant. Meas. Phys. Damage, STP30551S, J. Lankford, D. Davidson, W. Morris, R. Wei, Ed., ASTM Int. West Conshohocken, PA*, pp. 5–45, 1983.

[159] U. Essmann, U. Gösele, and H. Mughrabi, “A model of extrusions and intrusions in fatigued metals I . Point-defect production and the growth of extrusions,” *Philos. Mag. A*, vol. 44, no. 2, pp. 405–426, 1981.

[160] K. Gall, G. Biallas, H. J. Maier, P. Gullett, M. F. Horstemeyer, D. L. Mcdowell, and J. Fan, “In-situ observations of high cycle fatigue mechanisms in cast AM60B magnesium in vacuum and water vapor environments,” *Int. J. Fatigue*, vol. 26, pp. 59–70, 2004.

[161] K. E. N. Gall, G. Biallas, H. J. Maier, P. Gullett, M. F. Horstemeyer, and D. L. Mcdowell, “In-Situ Observations of Low-Cycle Fatigue Damage in Cast AM60B Magnesium in an Environmental Scanning Electron Microscope METHODS,” *Metall. Mater. Trans. A*, vol. 35, no. January, pp. 321–331, 2004.

[162] S. K. Shaha, F. Czerwinski, W. Kasprzak, J. Friedman, and D. L. Chen, “Monotonic and cyclic deformation behavior of the Al-Si-Cu-Mg cast alloy with micro-additions of Ti, V and Zr,” *Int. J. Fatigue*, vol. 70, 2015.

[163] K. N. Smith, P. Watson, and T. H. Topper, “Stress-Strain Function for the Fatigue of Metals,” *Journal of Materials,* vol. 5. pp. 767–778, 1970.

[164] J. Dallmeier, O. Huber, H. Saage, and K. Eigenfeld, “Uniaxial cyclic deformation and fatigue behavior of AM50 magnesium alloy sheet metals under symmetric and asymmetric loadings,” *Mater. Des.*, vol. 70, pp. 10–30, 2015.

[165] Y. C. Lin, Z. H. Liu, X. M. Chen, and J. Chen, “Stress-based fatigue life prediction models for AZ31B magnesium alloy under single-step and multi-step asymmetric stress-controlled cyclic loadings,” *Comput. Mater. Sci.*, vol. 73, pp. 128–138, 2013.

[166] J. Dallmeier, O. Huber, H. Saage, K. Eigenfeld, and A. Hilbig, “Quasi-static and fatigue behavior of extruded ME21 and twin roll cast AZ31 magnesium sheet metals,” *Mater. Sci. Eng. A*, vol. 590, pp. 44–53, 2014.

[167] S. Begum, D. L. Chen, S. Xu, and A. A. Luo, “Low cycle fatigue properties of an extruded AZ31 magnesium alloy,” *Int. J. Fatigue,* vol. 31, no. 4, pp. 726–735, 2009.

[168] H. Jahed, A. Varvani-Farahani, M. Noban, and I. Khalaji, “An energy-based fatigue life assessment model for various metallic materials under proportional and non-proportional loading conditions,” *Int. J. Fatigue*, vol. 29, no. 4, pp. 647–655, 2007.

[169] F. Ellyin, K. Golos, and Z. Xia, “In-Phase and Out-of-Phase Multiaxial Fatigue,” *J. Eng. Mater. Technol.*, vol. 113, no. 1, pp. 112–118, 1991.

[170] G. Liu, R. Xin, F. Liu, and Q. Liu, “Twinning characteristic in tension of magnesium alloys and its effect on mechanical properties,” *Mater. Des.*, vol. 107, pp. 503–510, 2016.

[171] F. Mokdad, D. L. Chen, and D. Y. Li, “Single and double twin nucleation, growth, and interaction in an extruded magnesium alloy,” *Mater. Des.*, vol. 119, pp. 376–396, 2017.

[172] E. I. Galindo-Nava, “Modelling twinning evolution during plastic deformation in hexagonal close-packed metals,” *Mater. Des.*, vol. 83, pp. 327–343, 2015.

[173] F. A. Mirza, D. L. Chen, D. J. Li, and X. Q. Zeng, “Low cycle fatigue of an extruded Mg-3Nd-0.2Zn-0.5Zr magnesium alloy,” *Mater. Des.*, vol. 64, pp. 63–73, 2014.

[174] F. Mokdad and D. L. Chen, “Strain-controlled low cycle fatigue properties of a rare-earth containing ZEK100 magnesium alloy,” *Mater. Des.*, vol. 67, pp. 436–447, 2015.

[175] F. Lv, F. Yang, Q. Q. Duan, Y. S. Yang, S. D. Wu, S. X. Li, and Z. F. Zhang, “Fatigue properties of rolled magnesium alloy (AZ31) sheet: Influence of specimen orientation,” *Int. J. Fatigue*, vol. 33, no. 5, pp. 672–682, 2011.

[176] S. Ishihara, S. Taneguchi, H. Shibata, T. Goshima, and a. Saiki, “Anisotropy of the fatigue behavior of extruded and rolled magnesium alloys,” *Int. J. Fatigue*, vol. 50, pp. 94–100, 2013.

[177] Z. Bin Sajuri, Y. Miyashita, Y. Hosokai, and Y. Mutoh, “Effects of Mn content and texture on fatigue properties of as-cast and extruded AZ61 magnesium alloys,” *Int. J. Mech. Sci.*, vol. 48, no. 2, pp. 198–209, 2006.

[178] J. B. Jordon, H. R. Brown, H. El Kadiri, H. M. Kistler, R. L. Lett, J. C. Baird, and A. A. Luo, “Investigation of fatigue anisotropy in an extruded magnesium alloy,” *Int. J. Fatigue*, vol. 51, pp. 8–14, 2013.

[179] C. Wang, T. J. Luo, J. X. Zhou, and Y. S. Yang, “Anisotropic cyclic deformation behavior of extruded ZA81M magnesium alloy,” *Int. J. Fatigue*, vol. 96, pp. 178–184, 2017.

[180] Y. Xiong and Y. Jiang, “Cyclic deformation and fatigue of rolled AZ80 magnesium alloy along different material orientations,” *Mater. Sci. Eng. A*, vol. 677, pp. 58–67, 2016.

[181] H. T. Zhou, Z. D. Zhang, C. M. Liu, and Q. W. Wang, “Effect of Nd and Y on the microstructure and mechanical properties of ZK60 alloy,” *Mater. Sci. Eng. A*, vol. 445–446, pp. 1–6, 2007.

[182] Y. Xiong, Q. Yu, and Y. Jiang, “Deformation of extruded ZK60 magnesium alloy under uniaxial loading in different material orientations,” *Mater. Sci. Eng. A*, vol. 710,

no. July 2017, pp. 206–213, 2018.

[183] M. W. Brown and K. J. Miller, “A Theory for Fatigue Failure under Multiaxial Stress-Strain Conditions,” *Proc. Inst. Mech. Eng.*, vol. 187, no. 1, pp. 745–755, 1973.

[184] Y. Y. Wang and W. X. Yao, “Evaluation and comparison of several multiaxial fatigue criteria,” *Int. J. Fatigue*, vol. 26, no. 1, pp. 17–25, 2004.

[185] A. Carpinteri and A. Spagnoli, “Multiaxial high-cycle fatigue criterion for hard metals,” *Int. J. Fatigue*, vol. 23, no. 2, pp. 135–145, 2001.

[186] A. Varvani-Farahani, “New energy-critical plane parameter for fatigue life assessment of various metallic materials subjected to in-phase and out-of-phase multiaxial fatigue loading conditions,” *Int. J. Fatigue*, vol. 22, no. 4, pp. 295–305, 2000.

[187] E. Macha and C. M. Sonsino, “Energy criteria of multiaxial fatigue failure,” *Fatigue Fract. Eng. Mater. Struct.*, vol. 22, no. 12, pp. 1053–1070, 1999.

[188] I. Papadopoulos, “A comparative study of multiaxial high-cycle fatigue criteria for metals,” *Int. J. Fatigue*, vol. 19, no. 3, pp. 219–235, 1997.

[189] D. Socie, “Critical plane approaches for multiaxial fatigue damage assessment,” *ASTM Spec. Tech. Publ.*, vol. 1191, pp. 7–36, 1993.

[190] J. A. Bannantine, “A review of mutiaxial fatigue damage model and observed material behavior,” pp. 213–237, 1991.

[191] K. Lieb, R. Horstman, K. Peters, C. Enright, R. Meltzer, M. Bruce Vieth, and Y. Garud, “Multiaxial Fatigue: A Survey of the State of the Art,” *J. Test. Eval.*, vol. 9, no. 3, p. 165, 1981.

[192] E. Krempl, *The Influence of State of Stress on Low-Cycle Fatigue of Structural Materials. A Literature Survey and Interpretive Report*. 1974.

[193] S. Zheng, Q. Yu, and Y. Jiang, “An experimental study of fatigue crack propagation in extruded AZ31B magnesium alloy,” *Int. J. Fatigue*, vol. 47, pp. 174–183, 2013.

[194] Y. S. Garud, “A New Approach to the Evaluation of Fatigue Under Multiaxial

Loadings," *J. Eng. Mater. Technol.*, vol. 103, no. 2, p. 118, 1981.

[195] ASTM Int., *Standard Test Methods for Tension Testing of Metallic Materials 1*, no. C. 2009.

[196] Y. Xiong, X. Gong, and Y. Jiang, "Effect of initial texture on fatigue properties of extruded ZK60 magnesium alloy," *Fatigue Fract. Eng. Mater. Struct.*, vol. 274–276, no. I, pp. 193–198, Feb. 2018.

[197] H. Yu, Y. Xin, A. Chapuis, X. Huang, R. Xin, and Q. Liu, "The different effects of twin boundary and grain boundary on reducing tension-compression yield asymmetry of Mg alloys," *Nat. Publ. Gr.*, no. May, pp. 4–11, 2016.

[198] Y. J. Wu, R. Zhu, J. Tao, and W. Qing, "Role of twinning and slip in cyclic deformation of extruded Mg – 3 % Al – 1 % Zn alloys," *Scr. Mater.*, vol. 63, no. 11, pp. 1077–1080, 2010.

[199] F. Yang, S. M. Yin, S. X. Li, and Z. F. Zhang, "Crack initiation mechanism of extruded AZ31 magnesium alloy in the very high cycle fatigue regime," *Mater. Sci. Eng. A*, vol. 491, pp. 131–136, 2008.

[200] S. H. Park, S. G. Hong, J. Yoon, and C. S. Lee, "Influence of loading direction on the anisotropic fatigue properties of rolled magnesium alloy," *Int. J. Fatigue*, vol. 87, pp. 210–215, 2016.

[201] F. Castro and Y. Jiang, "Fatigue of extruded AZ31B magnesium alloy under stress- and strain-controlled conditions including step loading," *Mech. Mater.*, vol. 108, pp. 77–86, 2017.

[202] G. Huang, J. Li, T. Han, H. Zhang, and F. Pan, "Improving low-cycle fatigue properties of rolled AZ31 magnesium alloy by pre-compression deformation," *Mater. Des.*, vol. 58, pp. 439–444, 2014.

[203] A. H. Pahlevanpour, S. M. H. Karparvarfard, S. K. Shaha, S. B. Behravesh, S. Adibnazari, and H. Jahed, "Anisotropy in the quasi-static and cyclic behavior of ZK60 extrusion: Characterization and fatigue modeling," *Mater. Des.*, vol. 160, pp. 936–948,

2018.

[204] D. Toscano, “Characterization of the Quasi-Static and Fatigue Behavior of Forged AZ31B Magnesium Alloy by,” University of Waterloo, 2018.

[205] J. Albinmousa, H. Jahed, and S. Lambert, “Multiaxial Fatigue Life Prediction of AZ31B Extrusion,” *23 rd Can. Congr. Appl. Mech.*, pp. 5–8, 2011.

[206] Sm. RN, W. P, and T. TH, “A stress–strain parameter for the fatigue of metals,” *J. Mater.*, vol. 5, no. 4, pp. 767–78, 1970.

[207] S. M. H. Karparvarfard, S. K. Shaha, S. B. Behravesh, H. Jahed, and B. Williams, “Fatigue life improvement of cast ZK60 Mg alloy through low temperature closed-die forging for automotive applications,” *MATEC Web Conf.*, vol. 165, p. 06009, 2018.

[208] S. M. H. Karparvarfard, S. B. Behravesh, S. K. Shaha, and H. Jahed, “On the phase angle role in the shear response of ZK60 Mg alloys under multiaxial fatigue,” *MATEC Web Conf.*, vol. 08005, 2019.

Appendix A

Cyclic test summary on ZK60 at different conditions

Table 19. Cyclic axial test summary

Specimen condition	Strain amplitude (%)	Max stress [MPa]	Min stress [MPa]	Life	Elastic strain energy density [MJ/m3]	Plastic strain energy density [MJ/m3]
As-cast	0.9	198	-197	750	0.44	1.95
	0.9	203	-183	709	0.46	1.95
	0.8	191	-188	1338	0.40	1.47
	0.8	192	-186	818	0.41	1.48
	0.7	187	-167	1563	0.39	0.99
	0.7	187	-171	1194	0.39	0.99
	0.6	185	-167	1388	0.38	0.67
	0.6	179	-166	2040	0.36	0.67
	0.5	164	-160	2858	0.30	0.49
	0.5	164	-163	2321	0.30	0.49
	0.4	160	-123	4149	0.28	0.24
	0.4	149	-134	4996	0.25	0.23
	0.3	122	-121	14417	0.17	0.07

	0.3	128	-114	15299	0.18	0.07
	0.3	114	-117	27137	0.15	0.06
	0.2	81	-84	516579	0.07	0.01
	0.2	85	-87	165385	0.08	0.01
	0.175	73	-74	>10000000	0.06	0.00
	0.15	66	-64	>10000000	0.05	0.00
Forged	0.9	197	-179	832	0.43	1.81
	0.7	220	-161	1707	0.54	1.01
	0.7	221	-164	1674	0.54	0.99
	0.5	180	-144	3976	0.36	0.37
	0.5	176	-143	7041	0.34	0.38
	0.4	154	-139	13090	0.26	0.28
	0.4	138	-130	17152	0.21	0.28
	0.3	125	-116	58490	0.17	0.11
	0.3	115	-117	82445	0.15	0.11
	0.25	105	-110	105616	0.12	0.03
	0.25	97	-104	536971	0.10	0.03
	0.22	92	-93	>10000000	0.09	0.00
	0.2	88	-88	>10000000	0.09	0.00

Extruded (ED)	0.3	139	-127	85,100	0.209	0.028
	0.4	197	-143	10,697	0.424	0.079
	0.5	247	-160	3,157	0.665	0.192
	0.6	269	-169	2,090	0.790	0.419
	0.7	273	-169	1,364	0.813	0.742
	0.8	280	-183	759	0.851	1.144
	1.6	259	-203	332	0.727	4.986
	2.0	260	-222	197	0.735	7.510
	1.6	271	-215	440	0.800	5.477
	1.0	277	-182	493	0.832	1.832
	1.0	292	-183	570	0.930	2.016
	2.0	264	-226	179	0.760	7.787
	0.9	282	-176	605	0.865	1.352
Extrusion (RD)	0.2	93	-79	>1000000	-	-
	0.25	104	-104	128000	-	-
	0.25	101	-103	66466	-	-
	0.3	110	-121	30000	-	-
	0.4	129	-134	6140	-	-
	0.4	121	-141	7700	-	-

	0.5	141	-152	3100	-	-
	0.6	147	-157	1925	-	-
	0.7	156	-164	1357	-	-
	0.8	156	-169	995	-	-
	0.9	158	-171	897	-	-
	1.0	163	-176	553	-	-
	1.6	179	-197	303	-	-
	2.0	186	-203	220	-	-
Extrusion (45°)	0.3	1224	-124	21754	-	-
	0.3	127	-119	27267	-	-
	0.5	166	-151	3260	-	-
	0.5	162	-149	4400	-	-
	1.0	204	-178	680	-	-
	1.0	201	-181	560	-	-
	2.0	214	-208	170	-	-
	2.0	221	-212	211	-	-

Table 20. Cyclic pure shear test on ZK60 summary

Specimen condition	Shear Strain amplitude (%)	Max stress [MPa]	Min stress [MPa]	Life	Elastic strain energy density [MJ/m3]	Plastic strain energy density [MJ/m3]
Extrusion	0.500	73.2	-75.6	116719	0.309	0.098
	0.500	72.9	-77.8	95194	0.318	0.107
	0.700	90.8	-93.5	10892	0.475	0.300
	0.700	102.6	-84.3	9339	0.493	0.341
	0.900	115.9	-102.7	1649	0.671	0.736
	0.900	106.1	-106.1	2518	0.630	0.636
	1.100	115.0	-121.2	626	0.781	1.248
	1.100	115.4	-117.9	784	0.761	0.989
	0.400	60.9	-63.4	1012534	0.216	0.038
	0.400	60.2	-63.8	1255157	0.215	0.048
Forged	0.500	71.5	-67.0	135760	0.272	0.085
	0.700	84.9	-82.2	8207	0.395	0.270
	0.500	68.5	-70.7	74563	0.275	0.086
	0.400	58.4	-60.9	2655460	0.349	0.159
	0.600	76.9	-80.1	27294	0.207	0.035
	0.600	78.7	-79.5	51376	0.547	0.501
	0.400	58.4	-62.5	2281955	0.559	0.519
	0.900	97.1	-99.4	2800	0.405	0.267
	0.900	98.9	-99.7	1845	0.272	0.085
	0.700	82.6	-86.4	8308	0.395	0.270

Table 21. Multiaxial fatigue test on ZK60 summary

Condition	Test #	Strain Amp (%)	Shear Strain Amp. (%)	Phase angle	Axial				Torsional				Total Life (Nf)
					Max. Stress (MPa)	Min. Stress (MPa)	Positive Elastic Energy (MJ/m3)	Plastic Strain Energy (MJ/m3)	Max. Stress (MPa)	Min. Stress (MPa)	Positive Elastic Energy (MJ/m3)	Plastic Strain Energy (MJ/m3)	
Extrusion	IN2	0.7	1	0	212	-174	0.490	0.876	89	-78	0.384	0.911	380
	IN3	0.7	1	0	113	-126	0.137	0.061	70	-73	0.280	0.166	9312
	IN4	0.3	0.5	0	112	-122	0.130	0.063	69	-71	0.265	0.120	12660
	IN5	0.3	0.5	0	108	-107	0.119	0.116	108	-101	0.600	0.815	901

	IN6	0.3	1	0	104	-105	0.109	0.127	112	-104	0.636	0.909	947
	IN7	0.3	1	0	192	-162	0.361	0.644	98	-88	0.470	1.096	425
	IN8	0.6	1	0	213	-172	0.436	0.918	92	-81	0.413	1.086	374
	IN9	0.7	0.5	0	245	-191	0.568	0.728	53	-46	0.134	0.209	909
	IN10	0.7	0.5	0	249	-190	0.573	0.747	57	-49	0.155	0.254	736
	45_1	0.7	0.5	45	257	-193	0.598	0.619	62	-66	0.226	0.418	777
	45_2	0.3	0.5	45	103	-137	0.095	0.026	77	-69	0.291	0.196	8435
	45_3	0.7	0.5	45	262	-195	0.603	0.621	64	-68	0.240	0.424	879
	45_4	0.3	0.5	45	116	-129	0.115	0.012	72	-75	0.295	0.161	15412
	45_5	0.3	1	45	115	-107	0.113	0.048	113	-109	0.672	1.032	834
	45_6	0.3	1	45	113	-108	0.107	0.018	109	-108	0.643	1.016	1017
	90_1	0.7	0.5	90	254	-200	0.529	0.780	74	-78	0.313	0.295	768
	90_3	0.3	0.5	90	122	-128	0.120	0.048	74	-82	0.333	0.188	34595
	90_5	0.3	0.5	90	135	-114	0.145	0.050	73	-79	0.314	0.144	23641
	90_6	0.3	1	90	118	-121	0.109	0.098	110	-112	0.671	0.806	1681
	90_7	0.3	1	90	114	-123	0.100	0.092	111	-110	0.666	0.819	1278
	90_8	0.7	0.5	90	255	-197	0.495	0.776	70	-78	0.299	0.294	771
Forged	IN2	0.4	0.5	0	161	-155	0.284	0.105	62	-63	0.221	0.151	4966
	IN1	0.4	0.5	0	162	-154	0.286	0.109	62	-64	0.223	0.209	3248
	IN3	0.7	0.5	0	240	-210	0.631	0.736	51	-51	0.146	0.236	505
	IN4	0.7	0.5	0	250	-214	0.686	0.691	49	-46	0.128	0.215	383
	45_1	0.4	0.5	45	149	-165	0.243	0.053	66	-70	0.262	0.215	5046
	45_2	0.4	0.5	45	153	-157	0.255	0.016	63	-67	0.245	0.165	4883
	45_3	0.7	0.5	45	257	-220	0.722	0.570	53	-57	0.176	0.385	383
	45_4	0.7	0.5	45	249	-225	0.677	0.578	58	-63	0.208	0.353	483
	90_1	0.4	0.5	90	171	-156	0.320	0.098	62	-63	0.243	0.184	1729
	90_2	0.4	0.5	90	165	-158	0.299	0.092	65	-66	0.268	0.194	2098
	90_3	0.7	0.5	90	247	-221	0.667	0.694	66	-68	0.279	0.236	413
	90_4	0.7	0.5	90	251	-230	0.688	0.660	65	-67	0.273	0.230	410